A Study of Oscillations in Solar Active Regions

A THESIS

submitted for the award of Ph.D. degree of

MOHANLAL SUKHADIA UNIVERSITY

in the

Faculty of Science

by

Ram Ajor Maurya

Under the Supervision of

Dr. Ashok Ambastha

Professor

UDAIPUR SOLAR OBSERVATORY

PHYSICAL RESEARCH LABORATORY, UDAIPUR

DEPARTMENT OF PHYSICS

FACULTY OF SCIENCE

MOHANLAL SUKHADIA UNIVERSITY

UDAIPUR

2010

DECLARATION

I hereby declare that the work incorporated in the present thesis entitled ***"A Study of Oscillations in Solar Active Regions"*** *is my own work and is original. This work (in part or in full) has not been submitted to any University for the award of a Degree or a Diploma.*

Date:

Ram Ajor Maurya
(Author)
Udaipur Solar Observatory
Physical Research Laboratory
Dewali, Badi Road
Udaipur 313 001
India.

CERTIFICATE

I feel great pleasure in certifying that the thesis entitled ***"A Study of Oscillations in Solar Active Regions"*** *embodies a record of the results of investigation carried out by* ***Mr. Ram Ajor Maurya*** *under my guidance. I am satisfied with the analysis of data, interpretation of results and conclusions drawn.*

He has completed the residential requirement as per the rules.

I recommend the submission of thesis.

Date:

Prof. Ashok Ambastha
(Thesis Supervisor)
Udaipur Solar Observatory
Physical Research Laboratory
Dewali, Badi Road
Udaipur 313 001
India.

Countersigned by
Head of the Department

To my parents

Contents

List of Figures

List of Tables

Acknowledgments

It is my great pleasure to express sincere thanks to my supervisor Prof. Ashok Ambastha for his valuable guidance and encouragement in carrying out this work. I am grateful to him for giving me this opportunity to work with him. Thank you sir, for your patience, your help and your care. Thank you for teaching me so much about solar physics and for accepting to take me as your PhD. student.

I am thankful to Prof. J.N. Goswami, Director PRL, for providing the necessary facilities required during this work. I would like to express my sincere gratitude to Prof. H.M. Antia of TIFR, Mumbai, for kindly giving me an opportunity to work with him for a month at TIFR during the initial stages of my research and for valuable discussions and help whenever needed. I am also thankful to Prof. P. Venkatakrishnan for many useful discussions on various concepts of solar physics.

I would like to record my sincere thanks to Dr. Frank Hill (NSO, USA), Dr. R. Komm (NSO, USA), Prof. M. Thomson (University of Sheffield, UK), Prof. Sarbani Basu (Yale University, USA), and Prof. J. Christensen-Dalsgaard (Danish AsteroSeismology Centre, Denmark) for their valuable communications on helioseismology at various stages of my work. Dr. J. Harvey (NSO, USA) was very kind in describing the basic principles of GONG and MDI observations and providing their comparisons. I am thankful to Dr. Sushant Tripathy (NSO, USA) for providing the required GONG data during my thesis work.

It is a pleasure for me to express my heartfelt thanks to all the faculty members of USO; Dr. Nandita Srivastava, Dr. Shibu Mathew, Dr. Sanjay Gosain, Dr. Brajesh Kumar, Dr. Bhuwan Joshi, Mr. Raja Bayanna and Dr. R. Bhattacharyya for providing their help whenever required. I would like to thank my friends Sanjeev, Vinay, Rohan, Jayant, Anand, Vema and Babulal for giving me their good company and sharing the moments of happiness. I am very much thankful to the families of Prof. Ambastha and Prof. Venkatakrishnan for their help and encouragement during my research, and to the families of Mr. Sudhir Gupta, Dr. Brajesh Kumar, Dr. Sanjay Gosain, Mr. Raja Bayanna, Dr. Bhuwan Joshi, Mr. Babulal Madhukar and Mr. Manoj Bhatnagar for helping me out whenever I faced problems.

The administrative staff of USO had been very supportive all through and I *wish to express my sincere thanks to them, particularly, to Mr. Raju Koshy, Mr. Rakesh Jaroli, Mr. Pinakin Shikari and Mr. Shankarlal Paliwal. I am thankful to Mr. Naresh Jain for providing the USO Hα data used in this study. I thanks to USO staff, Mr. Laxmilal Suthar, Mr. Jagdish Singh Chauhan, Mr. Dalchand Purohit, Mr. Ramchandra Carpenter and Mukesh Bhai Saradawa for their help at various stages of my work. I am thankful to all those members of USO and PRL staff who have helped me directly or indirectly in this study and helped in completing my thesis.*

I am deeply indebted to the GONG and SOHO/MDI teams for providing their data, i.e., magnetograms, dopplergrams and intensitygrams. My work has made extensive use of MLSO, TRACE, GOES, MSFC, RHESSI and Hinode data, which I would like to acknowledge here.

Finally, words fail me in expressing the deep sense of gratitude to my parents for their continuous encouragement to work in science and undertake the long and arduous journey of a research scholar. I am grateful to my late grand mother for her inspiration and to my sister for her affection. My wife Shashikala has been very helpful and understanding throughout and provided me with delicious food when I came back home after a long and hard day's work. My lovely daughter Divya gave me her delightful company to play with and to make me happy and relaxed.

My life at Udaipur included moments of happiness and sadness, comfort and hardship, laughter and depression. However, all these moments shall be cherished by me as beautiful lifelong memories.

Ram Ajor Maurya

Abstract

Solar active regions (ARs) are three-dimensional magnetic structures extending from deep sub-photosphere to coronal heights. These ARs are responsible for producing most of the energetic transients, such as flares and Coronal Mass Ejections (CMEs), due to a complex interplay of their magnetic and velocity fields. Therefore, accurate high spatial and temporal measurements of solar magnetic and velocity fields are essential ingredients for the understanding of the evolution and energetic activities of ARs. However, availability of these measurements is limited only to the photosphere and to some extent, to the chromosphere. The energetic charged particles released during these transients may also affect the measurements of magnetic and Doppler velocity fields. In addition, the energetic transients are expected to excite *p*-mode oscillations in ARs by imparting a mechanical impulse associated with their thermal expansion on the photosphere.

While studying the magnetic and velocity fields in AR NOAA 10486, we detected some puzzling moving transient features during the X17/4B and the X10/2B flares of 28 and 29 October 2003, respectively. Both these flares were extremely energetic white-light events. The transient features appeared during impulsive phases of the flares and moved with speeds ranging from 30 to 50 km s^{-1}. These features were located near the previously reported compact acoustic (Donea and Lindsey, 2005) and seismic sources (Zharkova and Zharkov, 2007). We have examined the origin of these features and their relationship with various other aspects of the flares, *viz.*, hard X-ray emission sources and flare kernels observed at different layers - *i)* photosphere (white-light continuum), *ii)* chromosphere (Hα 6563Å), *iii)* temperature minimum region (UV 1600Å), and *iv)* transition region (UV 284Å).

We have determined the characteristic properties of local oscillation modes by applying the ring diagram technique to 3-D power spectra of NOAA 10486. Strong evidence of substantial increase in mode amplitude and systematic variations in sub-surface flows are found from comparison of the pre- to the post-flare phases of the energetic X17/4B flare of 28 October 2003. Furthermore, we have found statistically significant association between the mode energy and flare energy from

the study of several ARs of Solar Cycle 23.

Our study has revealed the prevalence of strongly twisted flows in the interior of ARs having complex magnetic fields. Using the Doppler data obtained by the Global Oscillation Network Group (GONG) project for a sample of 74 ARs, we have discovered the presence of steep gradients in meridional velocity at depths ranging from 1.5 to 5 Mm in flare productive ARs. The gradients showed an interesting hemispheric trend of negative (positive) sign in the northern (southern) hemispheres.

We have discovered presence of three sheared layers in the depth range of 0–10 Mm in many flare productive ARs, providing an evidence of their complex flow structures as compared to the dormant or less productive ARs. An important inference derived from our analysis is that the location of the deepest zero vertical vorticity is correlated with the remaining lifetime of ARs. These new findings may be employed as important tool for predicting the life expectancy of an AR and space weather predictions.

Finally, we have studied the kinetic helicity in sub-photospheric flows and magnetic helicity in photospheric magnetic fields of 91 ARs of solar cycle 23. We have investigated the hemispheric trend in the kinetic helicity of sub-photospheric flows averaged over depths 2.5-12 Mm. This has been examined with magnetic helicity parameter obtained for the ARs by using photospheric vector magnetic fields. However, any significant association between the twists of sub-photospheric flows and photospheric magnetic fields is not found.

Chapter 1

Introduction

Our Sun is the closest star, and due to its proximity it is possible to observe its surface with very high spatial and temporal resolutions, not possible for any other star. These observations help in our understanding of the physics of stellar structure and dynamics. The visible surface, or the “skin” of the Sun, *i.e.*, the photosphere, is about a hundred kilometer thick. Due to its large opacity a direct view of the solar interior is not allowed. By tracking the motion of surface features, such as the sunspots, it is determined that the Sun rotates around its axis once in around 28 days. But it does not rotate as a solid body, as the rotation is faster near the equator as compared to the higher latitudes. The rice like patterns, or granules, observed in high spatial resolution photospheric images change their shape in short time scales of a minute and demonstrate the presence of convection in the solar interior. Other fine structures and phenomena visible at the photosphere are surface expressions of the physical processes taking place in the interior. The oscillatory patterns observed on the photosphere are another very important signs of turbulent phenomenon occurring beneath the surface. These oscillations provide us a new tool to study the opaque interior of the Sun.

1.1 The Discovery of Solar Oscillations

The possibility of oscillatory motions in the solar atmosphere was first theoretically investigated by Whitney (1958), and observationally discovered in the 1960's by Leighton, Noyes and Simon (1962) by measuring Doppler shifts of spectral lines on the solar disk. These observations revealed oscillatory motions of gas parcels on solar photosphere and the existence of wave packets or patches, both in space and time. These periodic oscillations attained peak velocity of $\sim$1 km s^{-1} with average period around five minute. The size of excursion of each patch was estimated to be of the order of a few tens of kilometer but an insignificant fraction of the solar radius. Soon thereafter, other researchers detected similar periodicity in their data obtained by different instruments (Evans and Michard, 1962; Noyes and Leighton, 1963; Simon and Leighton, 1964; Orrall, 1965; Gonczi and Roddier, 1969). Various theoretical interpretations were put forward to explain these oscillations. There were suggestions that they may be compressions of gas caused by sound waves in the solar atmosphere (Meyer and Schmidt, 1967). Some attributed it to the atmosphere being bobbing up and down like a buoyant cork on water (Schmidt and Zirker, 1963; Ulmschneider, 1968). Others thought that the matter was not so organized – the atmosphere was being buffeted by turbulence (Jones, 1969).

After a decade of the observational report, Ulrich (1970) and Leibacher and Stein (1971) came independently with their radical ideas to explain the observations. They suggested that oscillations lie not in the atmosphere but rather in the deep interior of the Sun. They explained that these oscillations were caused by acoustic waves (or p-modes), which are trapped in different cavities of the solar interior. As the waves move outward they are reflected back at the Sun's surface (the photosphere) where the density and pressure decrease very rapidly. Inward moving waves are then refracted (their direction of motion bent) by the increase in the speed of sound, as the temperature increases with depth, and eventually return back to the surface. Thus trapped sound waves set the Sun vibrating in millions of different patterns or modes. These waves are most readily observed as primarily vertical velocities at the solar surface by Doppler shift techniques. The vertical velocities vary harmonically in time and in space across the solar surface. The observations by Deubner (1975), and independently by Rhodes, Ulrich and Simon (1977) confirmed the hypothesis of p-modes as the power was found to be concentrated in a series of ridges in the $k - \omega$ diagram. It is generally believed that these modes may be either intrinsically overstable or stochastically excited by turbulence in the near-surface convection zone immediately beneath the photosphere (Gough *et al.*, 1996).

Once the exact nature of these oscillations was established, it was realized that these can be used for probing the "invisible" solar interior. The study of solar interior using oscillations has been referred as helioseismology (Deubner and Gough, 1984; Gough and Toomre, 1991) essentially in analogy with geoseismology. Methods of helioseismology are divided into two classes, "global" and "local", depending on whether the study involves the whole Sun or areas of smaller spatial scales, such as, the ARs.

1.2 Global Helioseismology

Global helioseismology utilizes properties of global waves that propagate throughout the Sun: they have lifetimes that are long enough for a wave to travel completely around the solar circumference and self interfere without suffering a loss of phase coherency greater than $\pi/2$ (Hill, 1995). Global helioseismology consists of measuring the frequencies of p-mode oscillations and searching for a seismic solar model whose oscillation frequencies match the observed ones. As solar global modes of oscillations propagate inside the Sun, their oscillation periods are affected by the temperature, composition and motions, thus yield insights into conditions in the solar interior. Accurate determination of these modes provides a powerful diagnostic tool for probing the structure and dynamics of the solar interior.

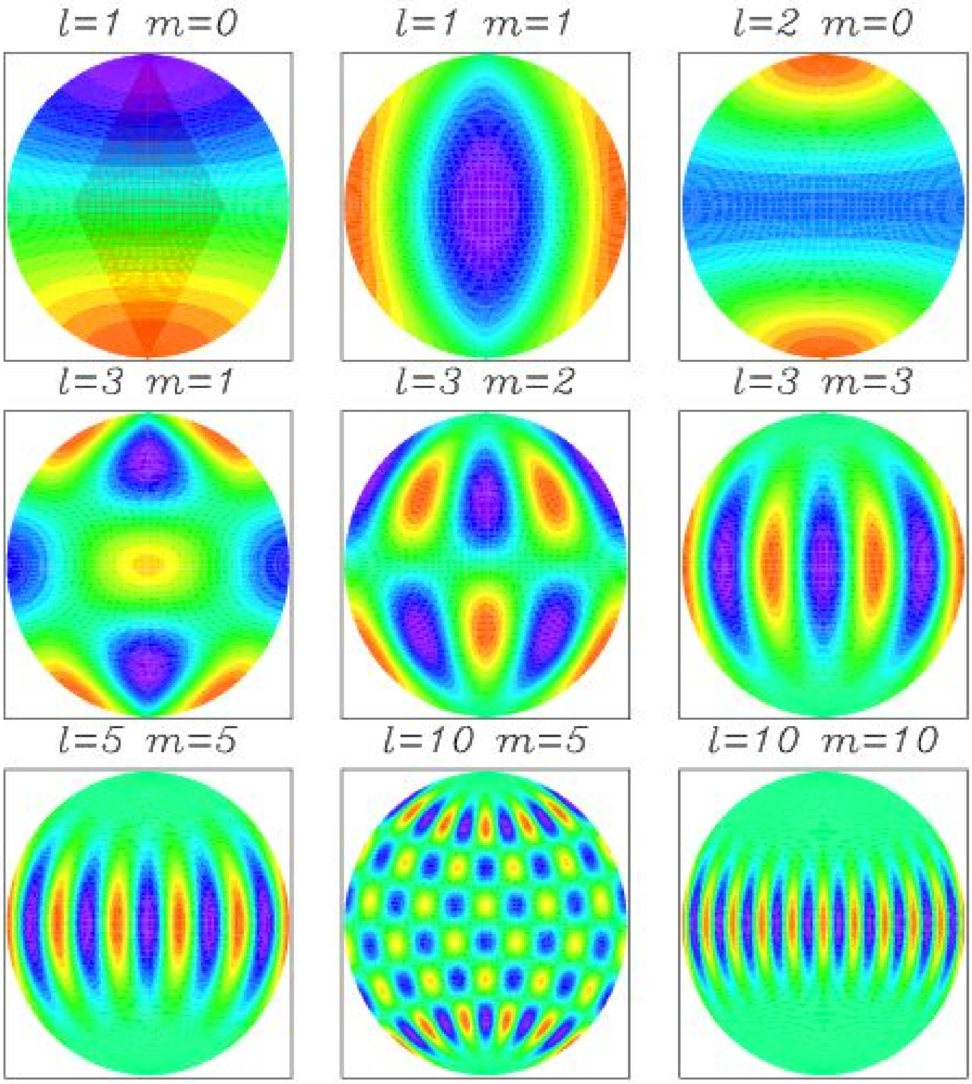

Figure 1.1 Spherical harmonic representation of the solar oscillations for different ℓ and m. The axis is assumed to be vertical as seen from the Earth. Red (blue) patches represent positive (negative) values of spherical harmonics.

The global analysis decomposes a time series of intensity and Doppler velocity images into spherical harmonics Y_l^m (Figure 1.1), where ℓ is the harmonic degree representing the total number of node circles around the sphere and m is the azimuthal number representing the number of node circles passing through the North (or South) pole. The number of nodes from the Sun's surface to its central core are termed as the radial order n.

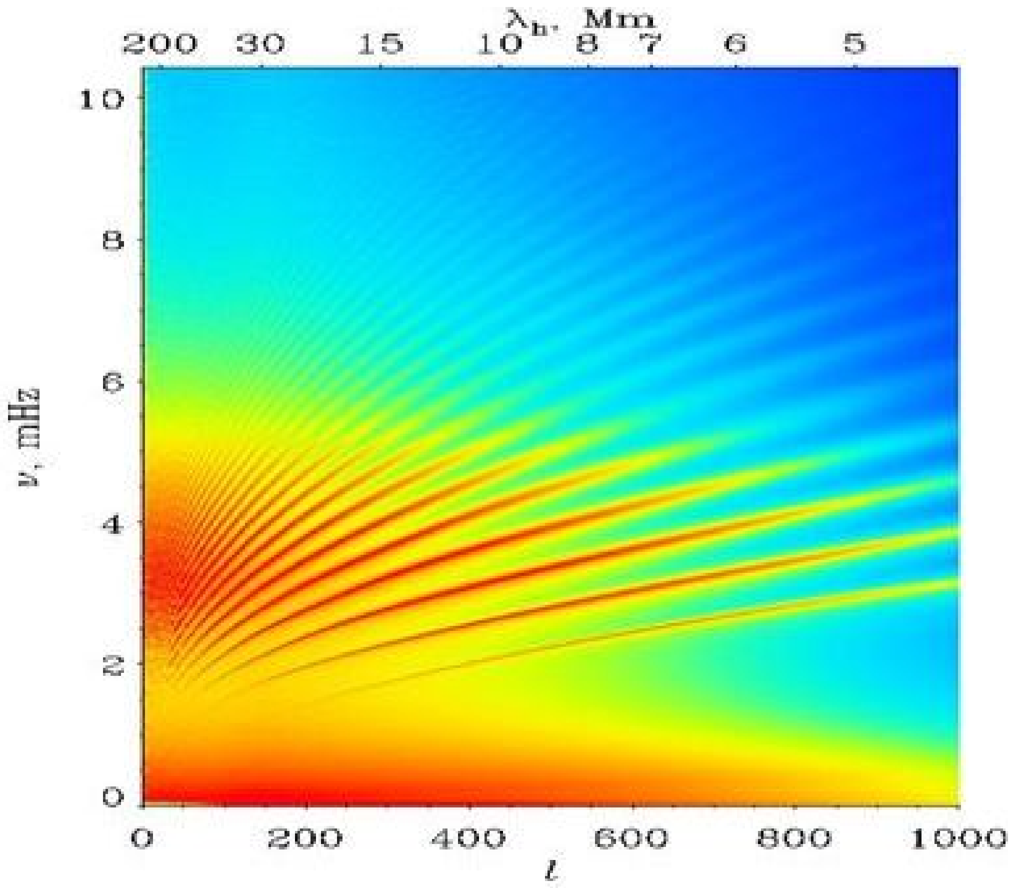

Figure 1.2 The $\ell - \nu$ diagram for mode frequencies up to 10 mHz and $\ell = 1000$ derived from MDI high-cadence full disk data (courtesy: SOHO/MDI).

1.2.1 Modes of Solar Oscillation

Global oscillations are essentially divided into three categories based on restoring forces that drive them: acoustic (p-modes), gravity (g-modes), and surface-gravity (f-modes). The spectrum of the detected oscillations arises from modes with periods ranging from about 1.5 min to about 20 min and with horizontal wavelengths in the range between less then a few thousand kilometers to the size of the solar globe (Gough and Toomre, 1991). There are about 10^7 p- and f-modes alone (Harvey, 1995); each oscillation mode sampling different depths of the solar interior.

The restoring force that causes acoustic waves in the solar interior is pressure, hence the name 'p-modes'. These oscillations are very strong in the frequency range 2–5 mHz (see Figure 1.2), where they are often referred to as '5-minute oscillations'. These oscillations are readily detectable with Doppler imaging or sensitive spectral line intensity imaging. The observed velocity at any time on the photosphere is a superposition of millions of p-modes, with ℓ values ranging from zero to over one thousand. Thousands of p-modes of high and intermediate degree ℓ have been detected by the GONG (Harvey *et al.*, 1988) project and the MDI (Scherrer *et al.*, 1995) instrument aboard the SOHO spacecraft. The modes with the degree ℓ below 200 are clearly separated while the higher degree modes are ridged together (Rabello-Soares, Korzennik and Schou, 2001). Very few p-modes are there at frequencies below 1.5 mHz which have been detected by the Global Oscillations at Low Frequency (GOLF, Gabriel *et al.*, 1995) instrument aboard the SOHO spacecraft (García *et al.*, 2001).

The restoring force that drives the gravity waves (or g-modes) are density waves which have negative buoyancy of displaced material. These oscillation modes have low frequencies (0–0.4 mHz), and are confined in the deep solar interior below the convection zone. It is believed that the restoring force for the g-modes is caused by adiabatic expansion. In the deep interior of the Sun, the temperature gradient is weak, and a small packet of gas that moves upward will be cooler and denser than the surrounding gas. Therefore, it will be pulled back to its original position by buoyancy; this restoring force drives the g-modes. In the solar convection zone, the temperature gradient is slightly greater than the adiabatic lapse rate, so that there is an anti-restoring force (that drives convection) and g-modes cannot propagate. Therefore the g-modes are are evanescent through the entire convection zone. They are believed to have very small residual amplitudes of only a few millimeters at the photosphere, hence, they are extremely difficult to detect. Since the 1980s, several claims of g-mode detection have been made but none of them are confirmed. More recently, again a claim of g-mode detection has been made using GOLF data (García *et al.*, 2007).

Surface gravity waves or f-modes are also gravity waves, but occur at or near the photosphere, where the temperature gradient again drops below the adiabatic lapse rate. Some f-modes of moderate and high degree, between $\ell = 117$ and $\ell = 300$, have been observed by MDI (Corbard and Thompson, 2002).

1.2.2 Results of Global Helioseismology

Helioseismology has became a unique diagnostic observational tool in the field of solar physics to study the solar interior which provides proofs of several theoretical interpretations. In the past three decades, global 5 minute p-mode oscillations have provided valuable information about the physics inside the Sun. The eigen frequencies of p-modes have helped in determining the sound speed profile as well as the density profile inside the Sun. Some of the most important results of global analysis are presented below.

The most historical result of global helioseismology was the explanation of the solar neutrino problem by providing the proofs to the incorrect models of the solar interior (Bahcall *et al.*, 1997). Other features revealed by helioseismology include: outer convective zone and the inner radiative zone rotate at different speeds which is thought to generate the global magnetic field of the Sun by a dynamo effect (Thompson *et al.*, 2003; Ossendrijver, 2003), and that the convective zone has "jet streams" of plasma (more precisely, torsional oscillations) thousands of kilometers below the surface (Vorontsov *et al.*, 2002). These jet streams form broad fronts at the equator, breaking into smaller cyclonic storms at higher latitudes. Torsional oscillations represent the time variation in solar differential rotation. They are alternating bands of faster and slower rotation. So far there is no generally accepted theoretical explanation for the torsional oscillations. However, a close relation to the solar cycle is evident, as they also have a period of eleven years, as known since their discovery in 1980 (Howard and Labonte, 1980).

1.2.3 Limitations of Global Helioseismology

Although global helioseismology provides several important results about the solar interior, it has some limitation for the study of near surface properties, *viz.*, flows, transient activities, *etc.* The global modes extend over all longitudes, thus analysis of their frequencies provides essentially no information about the longitudinal variations of solar properties. They depend only on the component of rotation which is symmetric around the equator. The properties of global modes have little sensitivity to meridional or more complex flows, such as large convective eddies, which may be present in the solar convection zone. It became possible to explore the properties of relatively shallower layers underneath small spatial scales of ARs only after the advent of local helioseismology.

1.3 Local Helioseismology

Local helioseismology, a term first used by Lindsey, Braun and Jefferies in 1993, is a technique to interpret the full wave field observed at the solar photosphere, not just the mode frequencies (more precisely, eigenmode). It uses high degree ($\ell > 300$) acoustic waves which are damped over the time scales much shorter than the time required to circumnavigate the Sun. Therefore, their frequencies are local measures of the Sun's properties. Local helioseismology uses these short wavelength acoustic waves measured on small patches of the solar surface. It provides a three-dimensional view of the solar envelope, which is important to understand large-scale flows, magnetic structures, and their interactions in the solar interior. It is also possible to study their relationship with transient energetic events such as flares, CMEs, *etc.* Three main techniques of local helioseismology are generally used, *viz.*, ring diagram analysis, time-distance method and acoustic holography.

1.3.1 Ring Diagram Analysis

The technique of ring diagram analysis was first introduced by Hill (1988). Its basic aim was to infer the speed and direction of horizontal flows over small patches (typically $16° \times 16°$) below the solar surface. It uses the Doppler shift observations over these small patches and derives the average properties of ambient acoustic waves from power spectra of solar oscillations. For example, sound speed, and adiabatic index can be compared within magnetically active and inactive regions (Basu, Antia and Bogart, 2004). Thus the ring analysis is a generalization of global helioseismology applied to local areas on the Sun (as opposed to half of the Sun). A detailed description of this technique is given in Chapter 5.

1.3.2 Time-Distance Analysis

The method of time-distance helioseismology was introduced by Duvall *et al.* (1993b) to measure and interpret the travel times of the solar waves between any two locations on the solar surface. A travel time anomaly contains the seismic signature of buried inhomogeneities within the proximity of the ray path that connects two surface locations. An inverse problem must then be solved to infer the local structure and dynamics of the solar interior (Jensen, 2003). The time-distance technique can be used in the study of photospheric and sub-photospheric structures of the AR and provides spatially and temporally resolved informations.

1.3.3 Helioseismic Holography

Helioseismic holography was introduced by Lindsey and Braun (1990) for the main purpose of far-side (magnetic) imaging, *i.e.*, a special case of phase-sensitive holography. In simple terms, sunspots absorb helioseismic waves, which causes a seismic deficit that can be imaged at the antipode of the sunspot. Helioseismic holography uses the wavefield on the visible disk to learn about ARs present on the far-side of the Sun. The basic idea is that the wavefield, *e.g.*, the line-of-sight (LOS) Doppler velocity, observed at the solar surface, can be used to make an estimate of the wavefield at any location in the solar interior at a given instant in time.

1.3.4 Results of Local Helioseismology

Local helioseismology has become very important tool for the study of small patches of the size of ARs. A major practical application in space weather predictions is to provide images of the far side of the Sun from the Earth (Braun and Lindsey, 2001), including sunspots. To facilitate spaceweather forecasting, seismic images of the central portion of the solar far side are being produced nearly continuously by analyzing data from the GONG and SOHO. Since 2001 the entire far side has been imaged with this data.

This technique has been used to give seismic images of solar flares. Acoustic holography, applied to MDI data, is ideal for the detection of sources and sinks of acoustic waves on the Sun. Braun and Fan (1998) discovered a region of lower acoustic emission in the 3 - 4 mHz frequency band which extends far beyond the sunspots (the acoustic moat). Acoustic moats extend beyond magnetic regions into the quiet Sun. In addition, Braun and Lindsey (1999) discovered high-frequency emission, termed as ‘acoustic glories’, surrounding ARs.

Activity related effects on p-mode parameters have been reported by many researchers (Chaplin *et al.*, 2000; Rajaguru, Basu and Antia, 2001; Hindman *et al.*, 2000). Kosovichev and Zharkova (1998, 1999) and Donea, Braun and Lindsey (1999) have reported excitation of flare-related waves on the solar surface. It is to note that any mode amplification induced by transient energetic events has to compete with absorption effects associated with sunspots. Therefore, it has been difficult to detect flare-related effects in magnetically complex ARs. Rajaguru, Basu and Antia (2001) found that the presence of intense magnetic fields in and around sunspots absorbs the power associated with solar oscillations, while, Ambastha, Basu and Antia (2003) found that the power in high-degree p-modes is amplified during the period of high flare activity as compared to non-flaring regions of similar magnetic fields. For the X17/4B flare of 28 October 2003, acoustic sources were detected by Donea, Braun and Lindsey (1999), Donea and Lindsey (2005) and seismic waves were found to originate from the flare-site by Kosovichev and Zharkova (1998, 1999), Kosovichev (2006).

On the other hand, at the global scale of the whole solar disk, Ambastha and Antia (2006) found a poor correlation between the running means of Flare Index and low-ℓ mode power. A similar result was found for CME Index also. However, Karoff and Kjeldsen (2008) have recently reported that there is a stronger correlation between flares and energy in the acoustic spectrum of disk-integrated sunlight for high-frequency waves than for p-modes. Basu and Antia (1999) using local helioseismic technique found a difference of 5 m s^{-1} near the surface in the zonal flows of North and South hemisphere. Ambastha *et al.* (2004), using same technique, found indications that the meridional velocity in a flaring AR possesses steeper gradient below a depth of 5 Mm as compared to dormant ARs. This feature was found in several other flaring ARs, and after major flares the gradients were found to reduce. However, it remains to be established whether this is a general feature of flare-productive ARs.

1.4 Motivations and Organization of the Thesis

The motivation of the thesis work is to study the internal and external characteristics of ARs derived from the local oscillations and observed energetic transient activities. Our main motivations are to investigate the following important problems: Variations in magnetic and Doppler velocity fields of ARs associated with energetic transients; Characteristics of photospheric p-modes in active, dormant and quiet regions; Influence of energetic transients vis-a-vis p-mode characteristics; Relationship of sub-photospheric flow topology with flare (and CME) productivity of ARs; Association of sub-photospheric flows with lifetime of ARs, and with their photospheric magnetic fields.

It is of particular interest to investigate how the oscillation modes are modified by strong magnetic fields and energetic transients occurring in ARs. Physical parameters are required to be determined with depth in sub-photospheric layers under ARs to infer the differences in active and quiet regions. Maps of flows in the solar interior should be constructed using high resolution helioseismic data as an AR evolves and emerges upward to the photosphere. These maps, combined with observations of external layers, are expected to provide knowledge about the behaviour of ARs extending from their deep interior to the observable layers, *i.e.*, the photosphere, chromosphere and corona.

It would be interesting to examine flaring and non-flaring (dormant) ARs in order to identify any distinct features in their internal structures and dynamics distinguishing these regions. In particular, there were some highly complex and extremely flare productive ARs observed during Solar Cycle 23. Can we draw some inferences on what features set apart these super-active regions (SARs), *e.g.*, NOAA 9393, 10486, *etc.* from other ARs ? High quality helioseismic data is now available from GONG and MDI for a large number of ARs observed during the last Solar Cycle 23. Corresponding high resolution observations of solar transients are also available from both ground-based and space-borne instruments. We expect that a comprehensive analysis of a large set of ARs would help in addressing these important problems. We expect to establish whether (or not) the steep gradients in meridional velocity found at 4–5 Mm depth by Ambastha *et al.* (2004) in NOAA 10486 is a general feature of all major flaring ARs. These findings could have important role in understanding the mechanism of flare productivity, characterization of ARs, and in space-weather predictions.

The thesis is organized as follows:

Chapter 2 describes the observational data obtained from various sources. We also present brief descriptions about the instrumentation principles of different observations.

In Chapter 3, we discuss an automated method based on mathematical morphology to extract the solar features, *e.g.*, flare ribbons, magnetic features, *etc.* This is required for the determination of flare ribbon expansion velocity, reconnection rate, and energy release in flares. To illustrate the technique, we carry out the computations for the X17/4B flare of 28 October 2003 in NOAA 10486. This method is applied to other flares in the ARs studied here.

In Chapter 4, we present variations in magnetic and Doppler velocity fields observed during extremely energetic transients. In particular, we discuss the physical properties of rapidly moving transient magnetic and Doppler features detected during the X17/4B and X10/2B super-flares of 28 and 29 October 2003, respectively. Associated with these moving transients, magnetic polarity reversals, or magnetic anomalies, were also observed. We have investigated the association of these transients with the expansion of the white-light flare ribbons using multi-wavelength data corresponding to successively higher layers of solar atmosphere. We have provided an interpretation of these transients on the basis of the available flare models.

In chapter 5, we describe the local helioseismology method used in this thesis for studying the ARs, *i.e.*, the ring diagram analysis. The physical parameters of p-modes derived from this analysis are then used to infer the sub-surface flows with depth using inversion techniques. We present a comparison of the results obtained from two different ring fitting techniques. We also examine the applicability of our inversion techniques by testing the results on simulated data, obtained using a “forward” method.

Variations in p-mode parameters observed during energetic transients have been presented in Chapter 6. We demonstrate the validity of ring diagram analysis for the study of energetic transients. A statistical study of p-mode energy and flare energy has been carried out for deriving general properties of flaring and dormant ARs.

Chapter 7 describes sub-photospheric flows in active and dormant regions. Variations in the sub-photospheric flow topology are examined with the level of flaring activity in ARs. We study a large set of ARs observed during Solar Cycle 23 to further establish the association of flare productivity with meridional velocity gradients previously reported by Ambastha *et al.* (2004), and to infer whether the sub-photospheric flow topology has a relation with the lifetime of ARs.

In Chapter 8, we study the latitudinal distribution of kinetic helicities of sub-photospheric flow and magnetic helicities of photospheric magnetic fields in several ARs of Solar Cycle 23 and attempt to examine their association. In particular, we discuss the daily evolution of kinetic and magnetic helicities in NOAA 10930 of December 2006.

Finally, we present the summary and conclusions of our study in Chapter 9. Limitations of some of the present techniques and observational data are highlighted. Scope for future work is also discussed.

Chapter 2

The Observational Data and Methods of Analysis

2.1 Introduction

Solar active regions, where most of the energetic transients occur, are three-dimensional magnetic structures extending from deeper sub-photospheric layers crossing through the photosphere to the coronal heights. The sites of primary energy release associated with these transients are essentially located in the corona while their secondary effects are observed in the lower, denser layers of the solar atmosphere as flare brightening and the outward propagating CMEs. A detailed study of energetic transient and its signatures in various atmospheric layers and in the sub-photospheric depths of the ARs requires different types of multi-wavelength observations and related tools of analysis.

In the following, we provide a list of various observations used in our study of the ARs along with the details of their sources, data reduction and analysis tools.

2.2 The Observational Data

For our study, we have used both ground- and space-based observations of ARs. Space-based observations are free from the degrading influence of atmospheric seeing. However, they have constrains due to limited availability and inadequate coverage. Therefore, it is still required to use the data obtained from ground-based instruments.

We have divided the observational data used in this study in two main categories: *i)* Data for helioseismic studies, and *ii)* Data for the study of solar transient activities. A brief description of the data, instrumentation principles and analysis techniques are given below.

2.2.1 Data for Helioseismic Studies

As discussed in the Chapter 1, the Sun oscillates in 10 million modes. Helioseismic data, used for their study, consists of spatially unresolved (or unimaged), and resolved (or imaged) Doppler shift observations of the Sun. For studying the low degree modes, we record the Doppler shifts of integrated, unimaged Sun. In these observations, the signal corresponding to the high degree modes, which have small structures, are essentially canceled out. On the other hand, the low degree modes produce radial motion that is in phase across much of the solar disk. This yields a detectable spectral shift in the unimaged sunlight. However, we are interested in the study of local oscillations in ARs, which are much smaller in size than the whole solar disk. These studies correspond to the high degree modes, possible only by spatially resolved, imaged observations of the Sun.

The maximum value of harmonic degree ℓ that can be studied depends on the spatial resolution of the observations, while the maximum value of the frequencies that can be studied depends on the temporal cadence of the observations. For example, a spatial resolution of $\Delta x = 0.125°$ will give a Nyquist value of harmonic degree $\ell = 1440$[1]. However, atmospheric seeing, leakage, foreshortening and other errors in the observations cause difficulty in estimating the maximum values of harmonic degree up to Nyquist ℓ. If the observations have a cadence of $\Delta t = 1$ min, it gives a Nyquist frequency of $1/(2\Delta t) = 8.3$ mHz and only frequencies below this limit can be measured.

The frequency resolution in the power spectrum is determined by the length of the time series or the time duration over which the observations are made. If the observations extend over one full day then we can expect a frequency resolution of 11.6 μHz. In order to obtain higher spectral resolution we need observations covering much longer periods. However, it is not possible to observe the Sun continuously for more than 16 hrs from a single site on the Earth. Observations over successive days will necessarily have gaps during the nights. These gaps in the data introduce artificial frequencies in the power spectrum, rendering it nearly impossible to unambiguously identify the real solar modes. Thus it is desirable to have continuous observations covering several days or even months.

There are three possible ways for achieving nearly continuous long observations of the Sun: (i) Observations from the South pole of the Earth (*e.g.*, Duvall *et al.*, 1991), which in principle, can give a few months observations, but in practice it is difficult to have continuous observations extending over more than a few weeks because of weather conditions, (ii) Network of sites around the globe (*e.g.*, GONG), and (iii) Space-borne instrument in a Sun-lit Lagrangian point (*e.g.*, SOHO/MDI). For our studies, we have used the observations obtained from the later two instruments which are described below.

GONG Data

The Global Oscillation Network Group (GONG) is a community-based project, designed around two decades ago, for detailed study of the internal structure and

[1] $k_{nyq} = k_h \Rightarrow \frac{\pi}{\Delta x} = \frac{\sqrt{\ell(\ell+1)}}{R_\odot} \approx \frac{\ell}{R_\odot} \Rightarrow \ell = \frac{\pi}{\Delta x} R_\odot$

dynamics of the Sun using helioseismic techniques (Harvey *et al.*, 1988). It consists of six ground-based stations located around the Earth to obtain near-continuous observations of the Sun. It uses Ni I 6767.8 Å spectral line (see Figure 2.1) and works on the principle of phase shift interferometry (Harvey 2008, private communication). It makes 60 full disk images per second of the Sun as transmitted from 0.7 Å pass band filter centered on the Ni I line. An interferometer produces a sinusoidal transmission function of wavelength across the passband having a period of about 0.3 Å. This transmission function is swept in wavelength smoothly at a rate of 1/3 fringe per 1/60 second camera frame time in synchronism with the camera. Thus we get three images (I_1, I_2, I_3) of the Sun in 1/20 second that have different intensities (or modulated) depending on the position of the transmission profile relative to the solar spectral line. The observed intensity at time t can be written as,

$$I(t) = I_0[1 + M\cos(5\omega t - \phi)] \tag{2.1}$$

From these three images, I_1, I_2 and I_3, one can derive the average intensity I_0 and the phase ϕ of the intensity modulation,

$$\phi = \tan^{-1}\left(\sqrt{3}\,\frac{I_2 - I_3}{I_2 + I_3 - 2I_1}\right), \tag{2.2}$$

and the strength of the modulation (M),

$$M = \frac{1}{I_0}\left[\frac{2}{3}\sum_{i=1}^{3}(I_i - I_0)^2\right]^{1/2} \tag{2.3}$$

The phase depends on the Doppler shift of the spectral line and is therefore the basic velocity information produced by the GONG instrument. The relation between relative Doppler velocity (v) and measured phase ($\delta\phi$) is

$$v = c\,\frac{\delta\phi}{\phi} \tag{2.4}$$

For the magnetic field information, it works as follows: Intensity is integrated for one second using right circularly polarized (RCP) input light. Then a liquid crystal modulator changes the retardation so that left circularly polarized (LCP) light images are integrated separately for the next second. These steps are repeated for total integration time of 60 seconds. The integrated RCP and LCP images produce two velocity images and their difference gives the longitudinal Zeeman splitting (related to magnetic field) plus some noise from the evolution of the real velocity field over one second and image degradation caused by the atmospheric seeing.

The GONG observations for global helioseismology studies began in 1995 from the full network of six ground-based stations located around the world initially with 256×256 pixel^2 imaging device for full disk observations. These were upgraded to 1024×1024 pixel^2 format in 2001 which is providing high spatial resolution data since then. The primary and raw data obtained from GONG instrument consists of full disk solar velocity field images taken every minute in fits format. In the data reduction procedures, images obtained from different sites are corrected for instrumental, photometric, geometric and known motion effects and then remapped into a standard image frame which adjusts for optical and atmospheric distortions. Finally, images obtained from six stations are merged to make full day time series (1440 images) using method described by Toner *et al.* (2003).

These high resolution corrected time series of data have increased the range of the degree ℓ of p-modes, and also made it suitable for local helioseismology studies. Different data products are available and can be downloaded from the GONG archive: `http://gong2.nso.edu/archive/`. It provides full disc magnetograms, dopplergrams and white-light images with the spatial and temporal resolutions of 2.5 arcsec pixel^{-1} and 1 min, respectively. The per pixel measurement accuracy for the Doppler and magnetic field observations are 5 m s^{-1} and 10 G, respectively.

SOHO/MDI Data

In addition to the GONG data, we have also used the data obtained from the space-borne instrument SOHO/MDI[2] (Scherrer *et al.*, 1995) as and where needed. SOHO was launched on 2 December 1995 and is observing the Sun since then from the Sun-lit Lagrangian point L1 except for an interruption in data from June 1998 to February 1999 when contact with the satellite was temporarily lost. The SOHO/MDI data has the advantage of no atmospheric degradation as compared to the GONG data obtained from the ground-based network. We have also used the SOHO/MDI data to inter-compare the results obtained from GONG data.

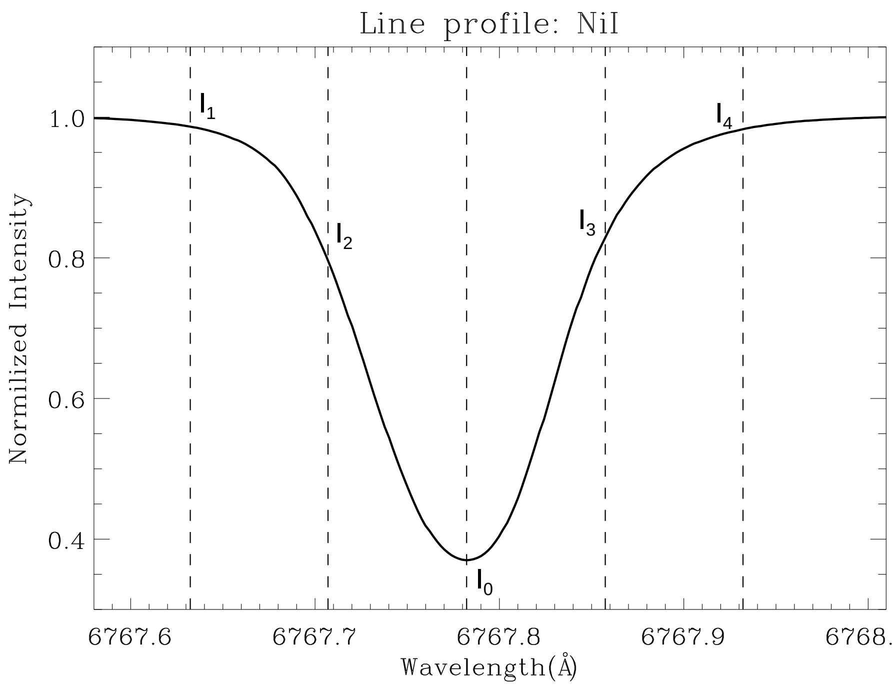

Figure 2.1 Ni I line profile (solid) used in the SOHO/MDI instrument. Vertical lines correspond to five fixed positions separated by 75 mÅ, across the Ni I line profile (the spectral data was obtained from BASS2000[a]).

[a] http://bass2000.obspm.fr/sobr_spect.php

The MDI instrument on board SOHO uses the same photospheric absorption line Ni I 6767.8 Å as is used by the GONG instruments. But its basic observa-

[2] Solar and Heliospheric Observatory, Michelson Doppler Imager

tional principle is different from GONG. The center of the wavelength bandpass is tunable in steps of about 8 mÅ over a range of 377 mÅ centered on the 6767.8 Å. The width of bandpass is fixed at 94 mÅ. The incident light can be in any of the four polarization states: s-wave, p-wave, right-hand circular, and left-hand circular. Camera readout time limits the rate at which successive filtergrams can be taken to about 1 every 3 seconds. They all involve sets of filtergrams at five fixed wavelengths separated by 75 mÅ (see Figure 2.1), denoted by I_0, I_1, I_2, I_3, and I_4. The filtergrams are combined on-board by an image processor to produce the secondary observables, which can then be sampled, binned, and/or filtered depending on the observing program.

The Doppler shift is calculated as a tabulated nearly linear function of the filtergram difference ratios:

$$r_1 = \frac{I_1 + I_2 - I_3 - I_4}{I_1 - I_3} \qquad \text{for} \qquad I_1 + I_2 > I_3 + I_4 \tag{2.5}$$

and,

$$r_2 = \frac{I_1 + I_2 - I_3 - I_4}{I_4 - I_2} \qquad \text{for} \qquad I_1 + I_2 < I_3 + I_4 \tag{2.6}$$

The line shift parameter is then converted to the velocity using an empirical lookup table (Scherrer *et al.*, 1995). Finally, the Doppler velocity (magnetic field strength) is determined by the mean (difference) between the velocities (V_l and V_r) calculated at the left and right circular modes,

$$V = \frac{V_l + V_r}{2}, \qquad B = \frac{V_l - V_r}{2.84} \tag{2.7}$$

The MDI full disc magnetograms, dopplergrams and white-light images are available on request from the MDI archive: `http://soi.stanford.edu/sssc/datasets.html`. The MDI data have spatial resolution of 2.0 arcsec pixel^{-1} and temporal cadence of 1 min. The per pixel measurement accuracy for the Doppler and magnetic fields observations are 20 m s^{-1} and 30 G, respectively.

2.2.2 Data for the Study of Solar Transients

To study the association of energetic transients with photospheric p-modes and sub-photospheric flows, we need observations of solar atmosphere where energetic transients occur. These observations include photospheric magnetic fields and flares observations in different wavelengths corresponding to different heights of the solar atmosphere. In the following, we describe the observational data used in this study.

USO Hα Data

We have used Hα filtergrams obtained from Udaipur Solar Observatory (USO) for studying the chromospheric activities in ARs. These filtergrams were taken by a 15-cm aperture f/15 spar telescope. Digital observations are available since 1998 with different spatial and temporal resolutions depending upon the camera and observing conditions. For example, the X17/4B flare of 28 October 2003 was observed at a cadence of 30 s during the quiet phase, and 3 s in flare mode, with spatial resolution of 0.4 arcsec pixel^{-1} at the CCD detector plane.

The raw Hα filtergrams are subjected through several steps of image processing for various corrections. From the large set of available images for an event, first we selected the best images taken in good "seeing" conditions. We then applied standard corrections of (a) dark-subtraction to remove the signal due to dark current and (b) flat-fielding for equalization of the CCD pixels' response. These images were then subjected to the following:

- *Image alignment (or registration)*: The image motion effects due to random telescope tracking errors were removed by spatial registration of images with a reference image. This is done in two steps: First, the images were manually registered with respect to a compact feature such as a sunspot, used as a fixed reference during the period of observation. Then, a second-step registration was carried out using a Fourier technique based on a cross-correlation method applied on the manually registered images to achieve a higher order registration to a sub-pixel accuracy. All the images used in our study were aligned and registered using these procedures.

- *Intensity level normalization (or atmospheric correction)*: The average intensity level of solar images changes with the time of the day, and also due to local effects such as the change of observing conditions caused by varying dust and cloud coverages. To remove these effects and obtain normalized images, we carried out the following correction:

$$I_{\text{out}} = (I_{\text{in}} - I_{\text{min}}) \left(\frac{F_{\text{max}} - F_{\text{min}}}{I_{\text{max}} - I_{\text{min}}} \right) + F_{\text{min}}$$

  where, I_{in} is the input image obtained from the previous steps, I_{min} and I_{max} are desired minimum and maximum intensity values in the output image I_{out}, respectively.

We can set the value of F_{min} to 0 and F_{max} to 255 for eight-bit images. But, the problem with this is that a single outlying pixel with either a high or low value can severely affect the value of F_{min} or F_{max} and this could lead to inappropriate scaling. Therefore we first take a histogram of the image and then select F_{min} and F_{max} at, say, the 5th and 95th percentile values in the histogram. That is, 5% of the pixel in the histogram will have values lower than F_{min}, and 5% of the pixels will have values higher than F_{max}. This helps in preventing the outlier pixels affecting the scaling significantly.

MLSO Hα Data

The Mauna Loa Solar Observatory (MLSO) is located on the island of Hawaii, and is operated by the High Altitude Observatory (HAO). We have used the processed

MLSO[3] Hα filtergrams for the events that occurred during the night-time of the USO, Udaipur site. These images are acquired by the telescope named Digital Prominence Monitor (DPM) on the Kodak Megaplus 1.6 CCD with spatial and temporal resolutions of 2.9 arcsec pixel^{-1} and 3 min, respectively.

TRACE UV Data

The Transition Region and Coronal Explorer (TRACE, Handy *et al.*, 1999; Schrijver *et al.*, 1999) was a NASA Small Explorer (SMEX) mission launched on 2 April 1998 to image the solar corona and transition region at high angular and temporal resolution. The major objective of the TRACE was to investigate the connections between fine scale magnetic fields and the associated plasma structures on the Sun. The TRACE mission obtained its last science image on 21 June 2010/23:56 UT.

We have obtained the data from the archives of TRACE[4] for the temperature minimum and transition regions which correspond to the wavelengths of 1600 Å and 284 Å, respectively. The 1600 Å images correspond to the UV Cont, C I and Fe II emissions forming at the temperature range $(4.0 - 10) \times 10^3$K while 284 Å images correspond to the Fe XV emissions forming at the temperature range $(1.25 - 4) \times 10^6$ K. The raw format images obtained from the TRACE archives were further processed using the Interactive Data Language (IDL) routines provided in the Solar Software[5] (SSW). The spatial and temporal resolutions of TRACE observations are 0.5 arcsec pixel^{-1} and 35 s, respectively.

RHESSI HXR Data

The Reuven Ramaty High Energy Solar Spectroscopic Imager (RHESSI) is a NASA small explorer mission which was launched on 5 February 2002 to explore the basic physics of particle acceleration and explosive energy release in solar flares (Lin

[3]http://mlso.hao.ucar.edu/cgi-bin/mlso_data.cgi
[4]http://trace.lmsal.com/trace_cat.html
[5]http://sohowww.nascom.nasa.gov/solarsoft/

et al., 2002). RHESSI is designed to image solar flares in energetic photons from soft X-rays (∼3 keV) to gamma rays (up to ∼20 MeV) and to provide high resolution spectroscopy up to gamma ray energies of ∼20 MeV. Its imaging is based on a Fourier-transform technique using a set of 9 Rotational Modulation Collimators (RMCs, grid pairs). Its imaging capability is achieved with fine tungsten and/or molybdenum grids that modulate the solar X-ray flux as the spacecraft rotates at ∼15 rpm. Each RMC consist of two widely-spaced, fine-scale linear grids, which temporally modulate the photon signal from sources in the field of view as the spacecraft rotates around an axis parallel to the long axis of the RMC. The modulation can be measured with a detector placed behind the RMC. The modulation pattern over half a rotation for a single RMC provides the amplitude and phase of many spatial Fourier components over a full range of angular orientations but for a small range of spatial source dimensions. Multiple RMCs, each with different slit widths, can provide coverage over a full range of flare source sizes.

An image is reconstructed from the set of measured Fourier components in exact mathematical analogy to multi-baseline radio interferometry. The raw format data (*i.e.*, modulated Fourier components) for different events were obtained from the RHESSI data site[6]. HXR maps for the events were then constructed using Pixon method (Hurford *et al.*, 2002) provided under the SSW for the dimension of 64×64 pixel^2 centered at the flaring regions. The spatial and temporal resolutions of the constructed images are 4 arcsec pixel^{-1} and 1 min, respectively. Different energy bands of flares of different energetics can be chosen. For example, we have used a higher energy (100-200 keV) band for the highly energetic X17/4B flare of 28 October 2003 as compared to the lower energy (50-100 keV) band for the less energetic X10/2B flare of 29 October 2003.

[6] ftp://hercules.ethz.ch/pub/hessi/data/

GOES SXR Data

The Geostationary Operational Environmental Satellite (GOES) system, operated by the United States National Environmental Satellite, Data, and Information Service (NESDIS), supports the weather forecasting, severe storm tracking, and meteorology research. GOES-14 satellite provides continuous monitoring of the solar integrated flux in soft X-rays[7]. We have used GOES data for identifying the solar transient activity and its association with p-mode oscillations.

MSFC VMG Data

The Marshall Space Flight Center (MSFC) solar vector magnetograph (VMG) facility was built by NASA to understand the role of solar magnetism in processes such as solar flares. The magnetic field measurements are based on Zeeman splitting of Fe I 5250.2 Å spectral line. MSFC[8] vector magnetograms are available for the period September 2000 - October 2004 with an improved spatial resolution of 0.64 arcsec pixel^{-1}. The measurement accuracy of MSFC vector magnetic fields is 100 G pixel^{-1}. We have used these data sets for comparative study of the topologies of the photospheric magnetic fields and the sub-photospheric flows.

Hinode/SOT Data

In addition to the MSFC vector magnetograms, we have also used the recent Hinode/SOT[9] data to cover ARs observed from November 2006 onwards. Hinode is a joint project of Japan, US and UK launched on 22 September 2006 to improve the understanding of mechanisms that power the solar atmosphere and drive solar eruptions. The Solar Optical Telescope (SOT) on board Hinode is a 50 cm Gregorian optical telescope with an angular resolution of about 0.2 arcsec over the field of view of about 400×400 arcsec^2 which produces images of the solar photosphere and

[7] http://goes.ngdc.noaa.gov/data/
[8] http://magaxp1.msfc.nasa.gov/
[9] http://sot.lmsal.com/sot-data

chromosphere in different interference filters. The SOT Spectropolarimeter (SP) produces one of the most sensitive vector magnetograph maps of the photosphere to date.

We have used the Stokes parameters (I, Q, U and V) provided by Hinode/SOT, to derive the three magnetic field components (B_x, B_y, B_z). Initially, the Stokes profiles were calibrated using the IDL routines provided in SSW. Then other magnetic field parameters, *e.g.*, total magnetic field (B_t), inclination angle (γ), azimuth angle (ϕ), *etc.*, were derived using the Unno-Rachkowsky (Unno and Kato, 1962; Rachkowsky, 1967) inversion code of SSW. We resolved the 180° azimuth ambiguity using acute angle method (Sakurai, Makita and Shibasaki, 1985). Then these parameters were transformed to the disc center to avoid projection effects (Venkatakrishnan, Hagyard and Hathaway, 1988).

2.3 Summary and Conclusions

For our study of ARs, we have obtained the observational data from various ground-based and space-borne instruments. The photospheric *p*-mode and subphotospheric properties of ARs have been studied using dopplergrams observations obtained from GONG and SOHO/MDI. Energetic transient activity related properties of ARs were studied using multi-wavelength observations obtained from other data sources, *e.g.*, USO, TRACE, RHESSI, *etc.*

For the analysis of the observational data, we have developed several image processing and other routines in IDL and Fortran. We have also used the available SSW packages provided with corresponding data to study the solar transients.

As discussed in the Chapter 1, it is important to estimate the energy released during a flare as it can modify solar oscillations at local as well as global scales. In order to understand the extent of these flare-induced modifications, we compared the characteristics of oscillations in flaring and dormant ARs of varying magnetic complexities. Such a study of spatial and temporal variations in oscillations involves appropriate methods of time series analysis of Doppler images.

We have used ring diagram analysis technique to obtain the flare-induced variations in p-mode oscillation characteristics. The photospheric p-mode parameters have been further used in deriving sub-photospheric flow properties in active and quiet regions by inversion techniques. We have presented details of these methods in Chapter 5.

Chapter 3

Flare Ribbon Separation and Energy Release

3.1 Introduction

It is believed that catastrophic changes in the magnetic field configuration of ARs occurring at coronal heights trigger energetic transients such as flares and CMEs (Sturrock, 1966; Hirayama, 1974; Kopp and Pneuman, 1976). When a coronal flux rope loses equilibrium and moves upwards, an extreme reconnection current sheet (RCS) is formed underneath. The magnetic reconnection in RCS releases large amount of energy stored in the magnetic field configurations (Forbes and Priest, 1984; Lin and Forbes, 2000). Electric fields of RCS effectively accelerate charged particles, *i.e.*, electrons, protons and ions. Accelerated charged particles gyrate around magnetic field lines and propagate toward the underlying footpoints, losing their energy in the lower atmosphere and producing flare ribbons (Martens and Young, 1990; Litvinenko and Somov, 1995). It has also been suggested that these gyrating charged particles produce microwave radiation by gyrosynchrotron process and hard X-ray (HXR) emission through a thick-target bremsstrahlung process (Brown, 1971; Emslie, 1978).

Using observations from *Yohkoh*/Soft X-ray Telescope (SXT), Masuda, Kosugi and Hudson (2001) first reported a two ribbon structure associated with HXR energy range above 30 keV and suggested that electrons are accelerated in the whole system of a flare arcade. They analyzed the motions of two HXR ribbons assuming these to be the footpoints of reconnected loops. Zhou, Ji and Huang (2008) studied footpoint motion of the M5.7 and X10 flares of 14 March 2002 and 29 October 2003, respectively. Using observations in UV/EUV by TRACE and HXR by RHESSI, they found that the UV/EUV flare ribbons and HXR footpoints showed converging motion during the impulsive phases of both the events.

Nonthermal or accelerated particles, specifically quasi-relativistic electrons, produce white-light flares (WLF) by direct heating of photosphere (Rust and Hegwer, 1975; Hudson *et al.*, 1992; Neidig and Kane, 1993). This is observationally supported by the HXR footpoints (sites of nonthermal particle acceleration) matching well with WLF ribbons (Fletcher and Hudson, 2001; Metcalf *et al.*, 2003). However, only very high energy electrons, having energy exceeding a few MeV, are expected to penetrate to deeper photospheric layers due to the increasing density. Only these high energy electrons can contribute to direct heating which may not be adequate to produce WLF emission. It was inferred from the TRACE WL and *Yohkoh*/HXT data that WLF ribbons originate in the chromosphere and the temperature minimum region, and that the enhanced WL emission is caused by ionization and subsequent recombination of hydrogen. Energy thus deposited in the chromosphere by the electron beam is then transported to the lower atmosphere by a back-warming process (Wang, 2006).

Evolution of two ribbon flares is morphologically characterized by separation with time of the flare ribbons in the chromosphere, as traditionally observed in Hα . This usually occurs during solar eruptive phenomena (eruptive filaments, flares and CMEs) and is believed to be the lower atmospheric signature of magnetic reconnection occurring at higher levels subsequent to the energy release in the corona. As the magnetic field lines at coronal heights progressively reconnect, their footprints move farther out from the already reconnected field lines. This

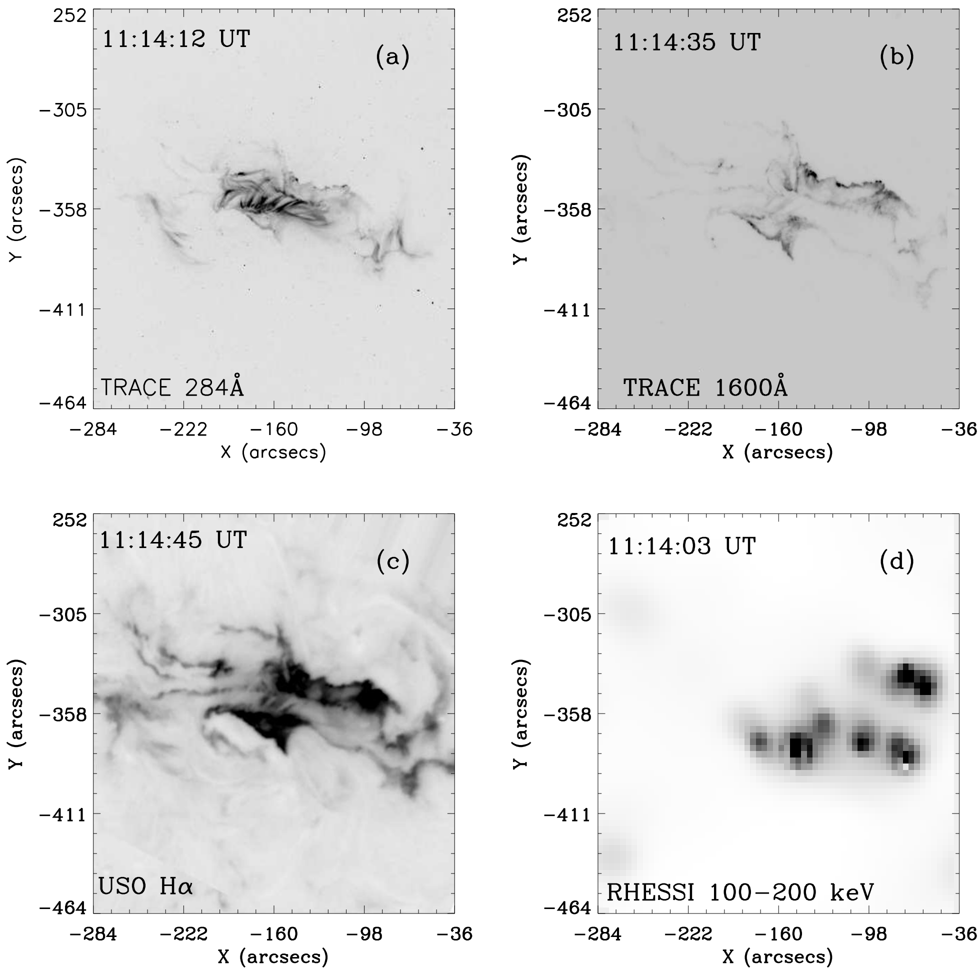

Figure 3.1 Images (in negative) of NOAA 10486 taken on 28 October 2003 during the X17/4B superflare: (a) TRACE UV 284 Å at 11:14:12 UT, (b) TRACE UV 1600 Å at 11:14:35 UT, (c) USO H α at 11:14:45 UT showing post-flare loops, and (d) RHESSI HXR at 11:14:03 UT in the energy range 100 – 200 keV.

successive reconnection process causes the apparent increase of separation of the flare–ribbons.

As a result of magnetic reconnection, loop arcades are produced below the reconnection site during the decay or post-flare phase. These loops are initially very hot and visible in EUV (*cf.* Figure 3.1a, b), and only the footpoints of the loops are observed in Hα (*cf.* Figure 3.1c). The two sets of footpoints at each side of the loop arcade appear as two elongated ribbons. As the loops cool down, the whole or parts of loops may become temporarily visible in Hα . These are called Hα post-flare loops. The separation velocity of flare ribbons depends on the reconnection rate of magnetic field lines, indicating a close relationship between the flare ribbon separation and energy release processes.

The main requirement in determining the flare reconnection rate and energy release is to detect and obtain flare characteristics by image processing and pattern recognition techniques. Several methods have been proposed for tracking of the apparent separation motion of two ribbon flares (Qu *et al.*, 2004b; Asai *et al.*, 2006). We have developed a simple technique for automatic detection of flare, its characterization and determination of various independent parts of flare ribbons, and not the flare as a whole, which might be misleading.

In Section 3.2, we briefly discuss the basic formalism of the problem. We present an automated image processing technique for developing various features of a transient, *e.g.*, flare ribbon, magnetic structures, *etc*, on the basis of mathematical morphology in Section 3.3. Sections 3.4 describes the technique developed and used in the study of flare ribbon separation and energy released during a flare. Finally, Section 3.5 provides the summary and conclusions of the analysis.

3.2 Basic Formalism

Solar flares are signatures of magnetic reconnection at coronal heights (*e.g.*, Forbes and Lin, 2000). The energy released during a flare can be estimated from the reconnection rate of field lines. This requires measurement of photospheric magnetic fields and flare ribbon separation speeds which can be used to derive the two physical terms for determination of magnetic reconnection rates: the rate of magnetic flux change involved in magnetic reconnection in the low corona and the electric field inside the RCS that is generated during magnetic reconnection. Isobe *et al.* (2002), suggested that the energy release rate can be estimated using the formula

$$\frac{\mathrm{d}E}{\mathrm{d}t} = SA_\mathrm{r}f_\mathrm{r} = \frac{1}{2\pi}B_\mathrm{c}^2 v_\mathrm{in} A_\mathrm{r} f_\mathrm{r} \tag{3.1}$$

where, S is the Poynting flux into the reconnection region, B_c, $v_{\rm in}$, A_r, and $f_{\rm r}$ are coronal magnetic field strength, inflow velocity, area of the reconnection region and filling factor of reconnection inflow, respectively.

Isobe *et al.* (2002) have discussed the importance of filling factors in the estimation of energy release rate, because not all magnetic field lines reconnect. They suggested that it is best to use $f_r = 0.3$. However, it is difficult to measure the coronal magnetic field and a recourse to magnetic field extrapolation is usually made. The reconnection area can be deduced from extreme ultraviolet (EUV) images. Estimation of inflow velocity ($v_{\rm in}$) is another difficult issue, as there are very few direct observations for obtaining the inflow velocities (Yokoyama *et al.*, 2001; Narukage and Shibata, 2006). Following an indirect method to determine the inflow velocity from magnetic flux conservation theorem, we can write

$$B_{\rm c} v_{\rm in} = B_{\rm chro} v_{\rm ribb} = B_{\rm phot} v_{\rm ribb} \tag{3.2}$$

where, $B_{\rm phot}$ and $B_{\rm chro}$ are the photospheric and chromospheric magnetic field strengths, respectively, and $v_{\rm ribb}$ is the velocity of Hα ribbon separation. Here, we have assumed that $B_{\rm chro} \approx B_{\rm phot}$.

The inflow velocity ($v_{\rm in}$) in the RCS can thus be calculated from Equation 3.2 using the values of $B_{\rm c}$, $B_{\rm phot}$, and $v_{\rm ribb}$. We can estimate the separation velocities of flare ribbons using the method presented in the Section 3.4. Using the derived separation velocities for the flare ribbons, it is possible to estimate the magnetic reconnection rate and energy released during a flare.

Magnetic reconnection theories predict how fast reconnection can occur. Accordingly, the speed of magnetic reconnection can be expressed in terms of the inflow velocity ($v_{\rm in}$) or the dimensionless ratio of $v_{\rm in}$ to the Alfvén velocity ($v_{\rm A}$) in the inflow region and can be written as

$$M_i = \frac{v_{\rm in}}{v_A}$$

where, the Alfvén velocity is given by $v_A = B_{\rm c}/\sqrt{4\pi\rho}$ and ρ is density near the reconnection region, which can be taken as a free parameter from an atmospheric model. Therefore, the reconnection rate using Equation (3.2) can be written as,

$$M_i = \frac{v_{\rm ribb} B_{\rm phot} \sqrt{4\pi\rho}}{B_{\rm c}^2} \tag{3.3}$$

An alternative measure of the reconnection rate is the electric field strength in the RCS. It shows how violently the magnetic reconnection progresses. It is defined as the reconnected magnetic flux per unit time and is expressed as,

$$\dot{\Phi} = B_{\rm c} v_{\rm in}$$

From Equation (3.2), it can be written as

$$\dot{\Phi} = B_{\rm phot} v_{\rm ribb} \tag{3.4}$$

The rate of magnetic energy release, *i.e.*, energy released per unit time during a flare is the product of Poynting flux and the area of RCS given by Equation (3.1). If we assume that the area of magnetic reconnection remains fixed during the flare (*cf.* Asai *et al.*, 2004), the energy release rate will be proportional to the Poynting flux only and hence independent of the filling factor ($f_{\rm r}$). Using Equations (3.1) and (3.2), Poynting flux can be written as,

$$S = \frac{1}{2\pi} B_{\rm c} B_{\rm phot} v_{\rm ribb} \tag{3.5}$$

It must be noted that the amount of energy reaching at a footpoint is not the total energy because a part of the reconnection energy will go outward and only the rest will come downward to the solar photosphere. Further, the downward energy coming to the solar photosphere is distributed into two footpoints. Therefore, the energy at a footpoint can be written as,

$$S = \frac{\epsilon}{2\pi} B_{\rm c} B_{\rm phot} v_{\rm ribb} \tag{3.6}$$

where, we have $0 \leq \epsilon \leq 0.5$. In the above equation, the coronal magnetic field ($B_{\rm c}$) is yet to be determined, which is required in the numerical calculation of M_i and S. To express $B_{\rm c}$ in terms of the photospheric magnetic field $B_{\rm phot}$, Asai *et al.* (2004) used $B_{\rm c} = aB_{\rm phot}$, where a is a constant to be deduced. The Poynting flux then can be written as,

$$S = \frac{\epsilon\, a}{2\pi} B_{\rm phot}^2 v_{\rm ribb}. \tag{3.7}$$

One can determine the constant a using magnetic field extrapolation by IDL package MAGPACK2[1] (Sakurai, 1982).

Finally, to calculate the magnetic reconnection (Equation 3.4) and energy-release rates (Equation 3.7), we require the strength of the photospheric magnetic field ($B_{\rm phot}$) along the path (or direction) of the ribbon separation. This can be obtained from the GONG and SOHO/MDI line-of-sight magnetograms at the centroid locations of Hα flare ribbons.

3.3 Feature Development using Mathematical Morphology

Flare ribbons are usually the brightest features observed in Hα filtergrams, however, they show a variety of structural variations. Therefore, a careful extraction of flare features is essential, using suitable image processing techniques, to precisely analyze the motions of flare-kernels.

As a first step, we set an appropriate threshold minimum intensity value to select the flare ribbons in a filtergram. For example, a pixel value is set to zero, if it lies below 70% of the maximum value (*cf.* Figure 3.2b). The threshold

[1] `http://solarwww.mtk.nao.ac.jp/sakurai/en/magpack2.shtml`

is chosen from a plage whose intensity does not show much variation during the period of the flare. The flare intensity is taken to be larger than this threshold. A larger threshold than the plage intensity will lose details of the flare while a smaller threshold value will include undesired regions lying outside the flare ribbons. In the case of lower (upper) threshold the flare ribbon will be thicker (thinner) but will not affect the centroid of the ribbon from which the position measurements are carried out. Therefore, the calculation of flare ribbon separation and velocity is not sensitive to the threshold value (see, Section 3.4). It is, however, a difficult task to decide on the boundary of flare ribbons for which one can use boundary-based methods. We have used a Sobel edge detector adopted in IDL. Edges of flare ribbons in Figure 3.2(b) are shown in Figure 3.2(c) as detected using this method.

3.3.1 Feature Extraction

After obtaining the pre-processed images, *e.g.*, USO Hα (Section 2.2.2), we enhanced and extracted the features of interest, *e.g.*, flare ribbons, using Mathematical Morphological Operations (MMO), which is a powerful tool to extract the main features of a digitized image (Gonzalez and Woods, 2008). This tool was first used in image processing by Serra (1983) to find geometrical structures in images. More recently, it has been used in solar physics for detection of flares (Qu *et al.*, 2004a,b), filaments (Shih and Kowalski, 2003; Qu *et al.*, 2005; Aboudarham *et al.*, 2008), sunspots (Zharkov *et al.*, 2005; Zharkova *et al.*, 2005), and prominences (Fu, Shih and Wang, 2007). A further description of the structuring element with different MMO can be found in Gonzalez and Woods (2008). Another technique based on neural networks has also been used for the detection of solar flares by Fernandez Borda *et al.* (2002).

The method of MMO is based on set theory. A binary image is a complete morphological description of the image in 2D integer space (Z^2), where elements are either “0” or “1”. The fundamental MMO are “erosion” and “dilation”.

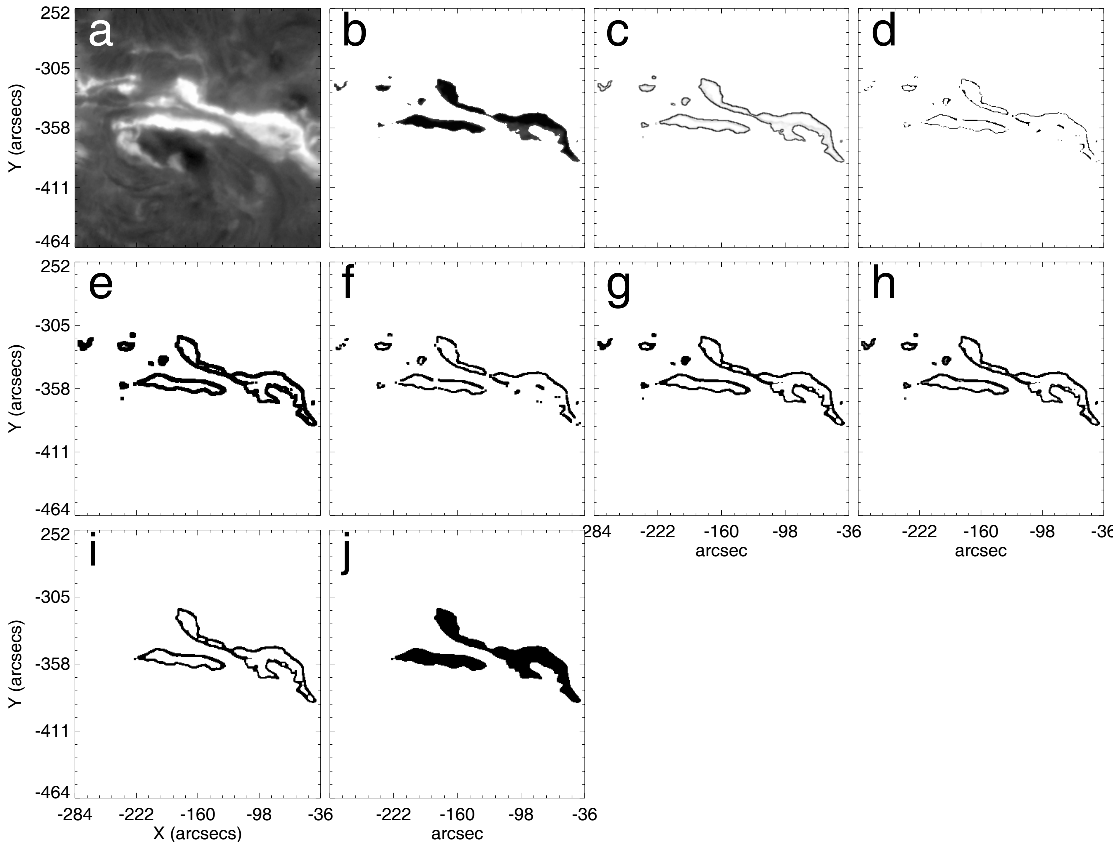

Figure 3.2 Results of image processing steps applied to a typical Hα filtergram for the X17/4B flare event of 28 October 2003 at 11:03 UT: (a) image obtained after preprocessing (see Section 2.2.2), (b) region-growing, (c) edge-detection using the Sobel, (d) erosion of b, (e) dilation of b, (f) opening of b, (g) closing of b, (h) morphological closing of c, (i) small parts removed from h and (j) hole filled in i. Images b−j are presented in negative for clarity.

If A and B are sets in Z^2 space then, "erosion" of A by B is given by

$$A \ominus B = \{z : (B)_z \subseteq A\} \tag{3.8}$$

In our study, A is the image (*e.g.*, Figure 3.2b) which is to be eroded and B is the structuring element chosen to be a 3×3 matrix. In erosion, a smaller size of structuring element will eliminate the small components while a larger size will eliminate the large components. A larger size will also deform the shape of flare ribbons, changing their centroid. The "erosion" operator shrinks the components of the image. It consists of replacing each pixel of an image by the minimum of its neighbours (Figure 3.2d).

The "dilation" operator expands the components of the image. It consists of replacing each pixel of an image by the maximum of its neighbours (Figure 3.2e). The "dilation" of A by B in Z^2 space is given by

$$A \oplus B = \{z : (\hat{B})_z \cap A \neq \phi\} \tag{3.9}$$

There are two other morphological operators, *viz.*, "opening" and "closing". The "opening" generally smoothens the contour of an object, breaks narrow isthmuses, and eliminates thin protrusions. The "closing" also tends to smooth sections of contours but, as opposed to "opening", it generally fuses narrow breaks and long thin gulfs, eliminates small holes, and fills gaps in the contour. The "opening" of a set A by structuring element B is defined as

$$A \circ B = (A \ominus B) \oplus B \tag{3.10}$$

i.e., opening of A by B is the erosion of A by B, followed by a dilation of the result by B, Figure 3.2(f). Similarly, "closing" of set A by structuring element B is defined as

$$A \bullet B = (A \oplus B) \ominus B \tag{3.11}$$

i.e., closing of A by B is the dilation of A by B, followed by an erosion of the result by B (Figure 3.2g).

We applied morphological "closing" to the image (*e.g.*, Figure 3.2c) to erase the gaps and smooth the contours. A binary image after this operation is shown in Figure 3.2(h). The images after applying MMO consist of many small features. These are removed using "region labeling" methods. The region labeling method gives labels to each components of an image. We count the number of pixels in each label and remove those component by "0", which have values less than a set threshold (Figure 3.2i).

3.3.2 Hole Filling

The MMO is a very nice tool to extract and enhance features of interest as described above. However, image obtained after MMO bears small holes or background regions surrounded by a connected border of foreground pixels within selected components, *i.e.*, large area components as seen in Figure 3.2(i). In fact, the holes in between the flare ribbons are parts of the flare ribbons, created due to edge detection by the Sobel operator. Since we are interested only in the edge, area, *etc.*, of flare ribbons, these holes should be removed by "1" from binary images. For this purpose, we have used an automatic procedure based on morphological reconstruction (Gonzalez and Woods, 2008). This procedure uses "geodesic dilation" described as follows.

Let $I(x, y)$ be a binary image having small holes. We form a marker image F, which is "0" everywhere except at the image border, where it is set to $1 - I$; *i.e.*,

$$F(x,y) = \begin{cases} 1 - I(x,y) & \text{if } (x,y) \text{ is on the border of } I \\ 0 & \text{otherwise} \end{cases} \tag{3.12}$$

Then, the binary image with holes filled will be,

$$H = \left[R_{I^c}^{(n)}(F)\right]^c, \tag{3.13}$$

where superscript c represents the complement and $\left[R_{I^c}^{(n)}(F)\right]^c$ is "geodesic dilation" of size n of the marker image F with respect to the mask image I^c. The "geodesic dilation" is defined by,

$$\left[R_{I^c}^{(n)}(F)\right] = R_{I^c}^{(1)}\left[R_{I^c}^{(n-1)}(F)\right], \tag{3.14}$$

where, $R_{I^c}^{(1)}(F) = (F \oplus B) \cap I^c$, $\cap$ represents the "intersection" operator and B

is the structuring element as described above. The image after removing holes is shown in Figure 3.2(j).

We have used the aforementioned technique of feature extraction in our studies of flare ribbons, magnetic and Doppler features, *etc.*

3.4 Determination of Flare Ribbon Separation

We extract the flare ribbons using MMO described in Section 3.3. Once the flare ribbons are extracted, we can measure their separation from a reference, such as the magnetic neutral line. Some questions that arise in the determination of flare ribbon separation are: Can we use a straight line representing the magnetic polarity reversal or neutral line passing between the flare ribbons? Do the flare ribbons move perpendicularly to the neutral line? Do the flare ribbons on either side move with the same velocity? The visual inspection of the Hα flare (*cf.* Figure 3.2a) shows that the flare ribbons were nearly parallel to each other, but curved in shape. Therefore, a straight line representing the neutral line can not be drawn through the ribbons. Also, various components of the flare ribbons are curved in different directions. Therefore, it is important to know the direction of neutral line in order to infer the direction of motion of a given part of the flare ribbon.

Figure 3.3 shows cartoon of a two ribbon flare to illustrate our method for distance measurement between the flare ribbons and the neutral line (NL). Here, R_1 and R_2 represent two ribbons of the flare, and the dotted line NL represents the magnetic neutral line. Solid lines, drawn perpendicular to the neutral line, mark the directions of motion of different portions of ribbons, assuming that the apparent motion of flare ribbons is perpendicular to the neutral line. Therefore, the velocity derived at a given point on the flare ribbon may be the same in magnitude, but not necessarily be so in direction.

It is well-known that the overlying arcades are usually sheared, which decreases with increasing distance from the magnetic polarity reversal boundary and

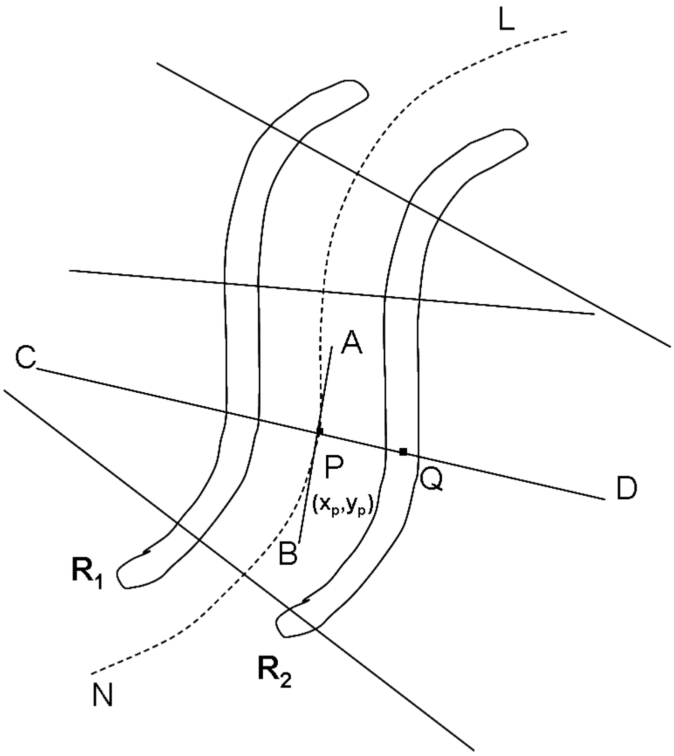

Figure 3.3 Cartoon of a two ribbon flare illustrating our method to determine flare ribbon separation. Dotted line represents the magnetic polarity reversal, *i.e.*, neutral line. The contours around the dotted line represent the ribbons R_1 and R_2 of the flare. Solid line AB is tangent to the neutral line NL at point P. Other solid lines are drawn perpendicularly to the neutral line at different points.

with increasing coronal height. Thus it follows that footpoints of the reconnected flare loops will move not only from the polarity reversal boundary, but also along it. To address this issue, we need to obtain the 3D topology of magnetic reconnection region. We should also be able to identify the conjugate points of flare ribbons across the neutral line, seen to be connected by post-flare loops, which is not an easy task. However, some information about it can be obtained from magnetic field extrapolations and the observed post-flare loops in Hα and EUV images. For example, to find the conjugate points in Hα flare ribbons, Asai *et al.* (2006) divided the regions of flare ribbons lying over magnetic polarities opposite to each other into fine meshes. Then, they drew light curves of total intensity for each box in both meshes, and identified the highly correlated pairs (conjugated pairs) by calculating the cross-correlation functions. This is a good approach to find the conjugate points. But for a complex region the field lines may be highly sheared on small scales which poses difficulty in identifying these points. Magnetic field extrapolation may be a better approach to get closer to the conjugate pairs.

But, again, the inherent errors in extrapolations may pose difficulty in identifying correct conjugate points in complex ARs.

In order to address the above-mentioned issues, we have adopted a simple assumption of flare ribbon motion perpendicular to the neutral line. We have implemented an algorithm in IDL for the detection of flare ribbon separation based on an automated technique. It calculates the ribbon separation measured from the neutral line at specified points of the neutral line. The main steps of the technique are:

- *Locating the magnetic neutral line between the flare ribbons*: Contours of co-temporal photospheric LOS magnetograms are overlaid on the corresponding Hα filtergrams obtained at the time of maximum phase of the flare. The magnetic neutral line (NL) is obtained by fitting an appropriate polynomial over several points within the region of magnetic field lines

- *Finding the direction of motion of flare ribbons*: We assume for simplicity that flare ribbons move perpendicularly to the neutral line, NL, passing through the flare ribbons R_1 and R_2 (*cf.* Figure 3.3). Let AB be tangent at point P on NL, CD is drawn perpendicular to AB at P. Let Q be the centroid of the flare ribbon R_2 that is assumed to follow the path PD. To obtain the direction of PD with respect to the x-axis, we find the gradient (say, m_p) at point P derived by the Lagrange interpolation method, and the gradient of line PD, *i.e.*, $m'_p = -1/m_p$. The direction of motion as measured from the horizontal or x-axis is then $\theta_p = \tan^{-1}(m'_p)$. The direction of motion of a flare ribbon at any desired point along NL can be obtained by following a similar procedure.

- *Measuring the distance of flare ribbon from the neutral line*: At a given time t, the distance of a point, $Q(x_k, y_k)$ from $P(x_p, y_p)$ on the neutral line is given by

$$d_t = \sqrt{(x_k - x_p)^2 + (y_k - y_p)^2}$$

Using the measured flare ribbon distances from the neutral line, one can find their velocities simply by taking their time derivatives. But this would be noisy due to the errors involved in the measured distances using the above procedures. We use an appropriate function to fit the measured distances so that the errors are reduced.

3.4.1 Energy Release during the X17/4B Flare

To make an estimate of the energy released during the X17/4B flare of 28 October 2003 (for the details of the flare, please see Section 4.4), we have used the method described in Section 3.2-3.3. This requires first the determination of flare ribbon separation from the magnetic neutral line along different directions.

An USO Hα filtergram for this two ribbon white-light flare obtained at 11:03 UT is shown in Figure 3.4(left panel). The overlaid solid and dashed contours represent positive and negative magnetic polarities, respectively, obtained from longitudinal magnetograms. The dotted contours represent the magnetic neutral lines. Straight lines drawn perpendicularly to a segment of neutral line, marked in green color, represent the directions of motion of different parts of flare ribbons from the corresponding point P of the neutral line. Here, we have selected six points P_i over the magnetic neutral line and corresponding directions of flare ribbon motion are shown in different colors. The centroids of the flare ribbon are followed along these directions to measure the flare ribbon separation from the corresponding points (*i.e.*, $P_{\rm i}$) on NL. The measured distances corresponding to different components are shown by "×" symbol in panels (a) of Figures 3.5.

Temporal derivative of computed distances $d(t)$ is taken to determine the separation velocity of the moving transients. However, the direct derivative of $d(t)$ reveals a noisy velocity profile because of scattered data points. To overcome this problem, we fit a Boltzmann sigmoid (best fitting) to smoothen the observed

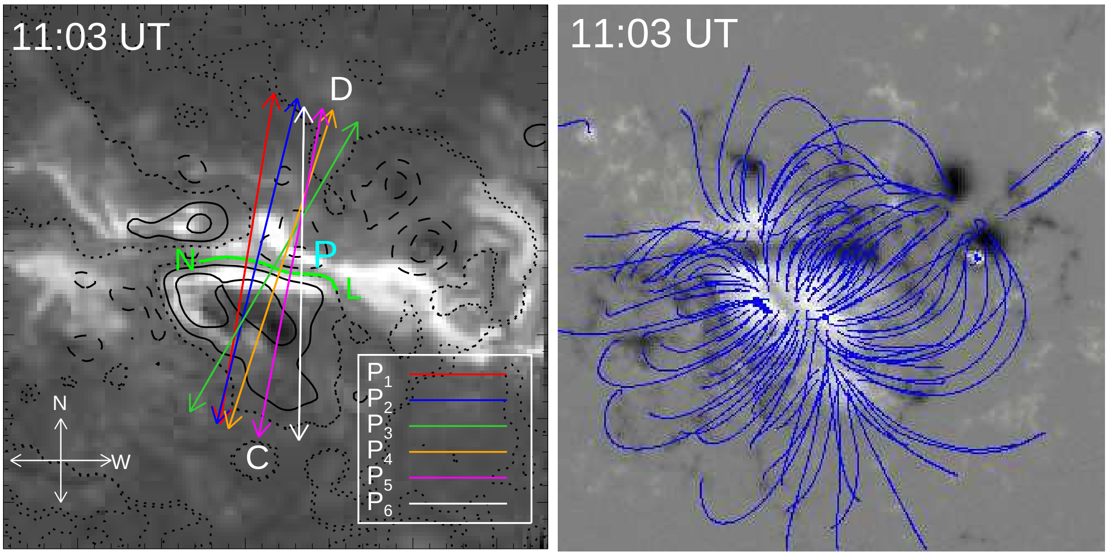

Figure 3.4 (Left) NOAA 10486 Hα filtergram overlaid with the contours of LOS magnetic fields during the X17/4B flare of 28 October 2003. Solid (dashed) contours represent positive (negative) polarities, respectively. Dotted contours represent the polarity reversal lines. A part of the neutral line NL passing through the flare ribbons is highlighted in green color. (Right) The extrapolated magnetic field lines plotted over the GONG LOS magnetogram.

distance points. This is given by

$$d(t) = A_0 + \frac{A_1 - A_0}{1 + e^{(t-A_2)/A_3}} \tag{3.15}$$

where, A_0, A_1, A_2 and A_3 are the fitting parameters corresponding to the following: A_0 - top (*i.e.*, maximum of $d(t)$), A_1 - bottom (*i.e.*, minimum of $d(t)$), A_2 - the time at which distance is halfway between bottom and top, and A_3 - the steepness of the curve, with a larger value denoting a shallower curve. The solid curves in Figure 3.5 panels (a) show the fitted distances while the dotted ones represent the separation velocities.

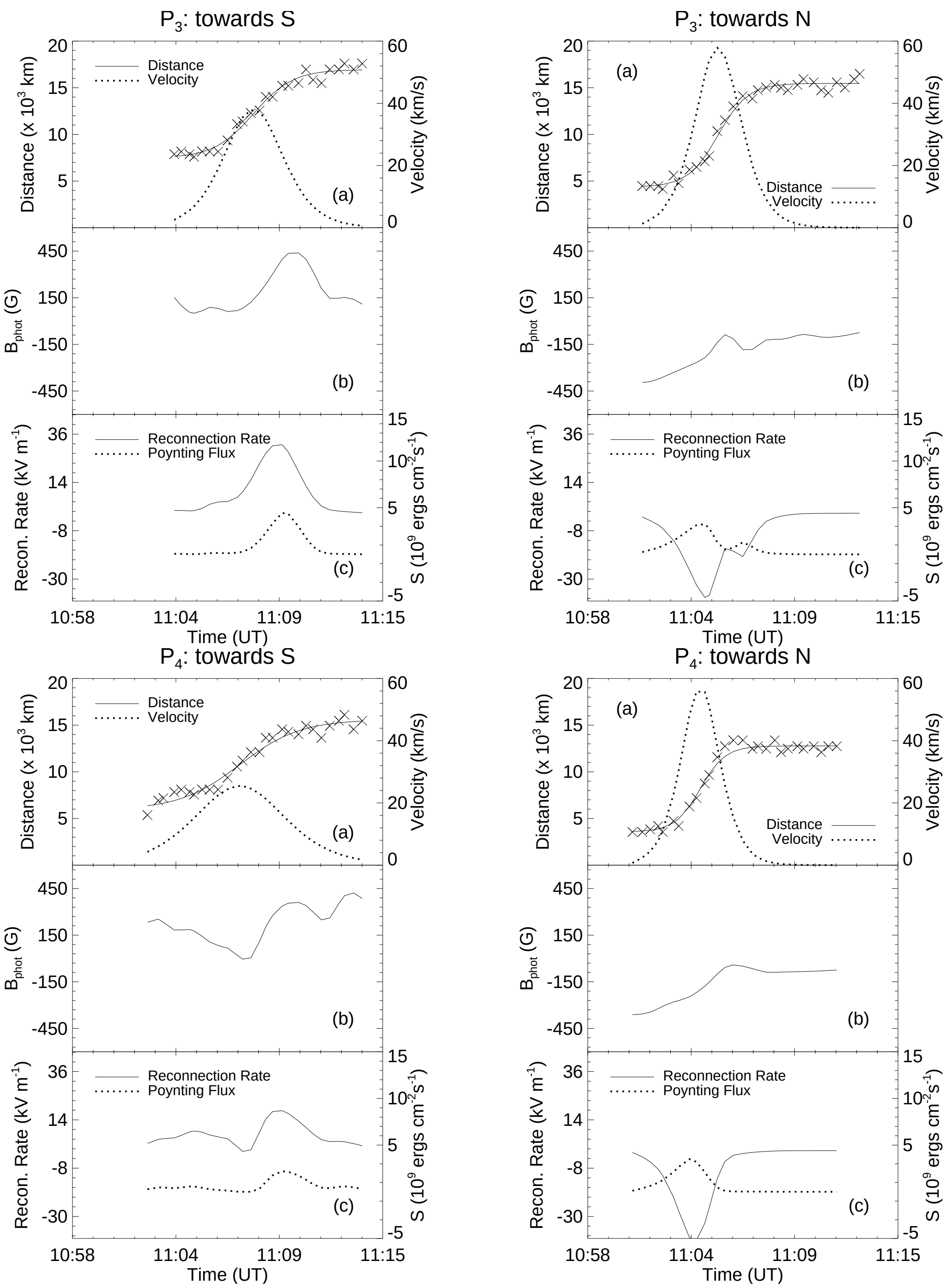

Figure 3.5 Top and bottom panels correspond to the measurement of different parameters along the lines P_3 and P_4, respectively (*cf.* Figure 3.4): (a) "×"(solid) represents the measured (fitted) distances with time, and dotted lines represent the velocity profiles ($v(t)$) derived by taking temporal derivative of the fitted distances. (b) magnetic flux ($B_{\rm phot}$) at the points used for distance measurement. (c) Reconnection rate ($\dot{\Phi}$) (solid line) and Poynting flux (S) (dotted lines).

We extrapolated the LOS component of magnetic fields using the IDL package MAGPACK2 for estimating the energy constant a (see Equation 3.7). The results are shown in Figure 3.4 (right panel). The value for a is found to be ≈ 0.09, which is an average value over the whole region, but it is smaller in strong-field areas. From the observed photospheric magnetic field B_{phot}, calculated energy constant a and the flare ribbon separation velocity v_{ribb}, we have determined the reconnection rate at different locations.

Figure 3.5 shows the parameters determined from the aforementioned procedures along PC (left panel) and PD (right panel) directions of ribbon motions. We find a weak negative correlation between the ribbon-separation speed and the longitudinal magnetic flux density for the X17/4B flare. Xie, Zhang and Wang (2009) have also reported a similar result for the flare of 10 April 2001. However, contrary to the event studied by them, we do not find similarity in temporal profiles of the magnetic reconnection rate and the flare ribbon separation speed during the evolution of the X17/4B flare. In fact, we find that the magnetic reconnection rate is better correlated with the photospheric LOS magnetic field strength.

The X17/4B flare of 28 October 2003 showed both extended ribbon structures as well as several fragmentary kernels. The flare was associated with a filament eruption, two ribbon separation, and a very fast propagating CME. We determined the temporal evolution of the separation between different portions of the two main ribbons. Nearly all of these showed a rapid increase of velocity reaching a maximum in the range 20 – 60 km s^{-1} in the impulsive phase, *i.e.*, 10:58 – 11:05 UT. Thereafter, during the next ten minutes, the separation speed decreased at different rates depending on the magnetic field structure and strength in the region of flare expansion. Interestingly, magnetic flux showed a rapid decrease/increase in some locations at the time of maximum velocity of ribbon separation.

Average Poynting flux over the entire RCS during the flare studied here is found to be of the order of 10^9. This flare was a long duration event lasting for 10^4 seconds. The approximate area of RCS estimated from EUV data is 10^{19} cm^2.

Therefore, the energy-release is estimated to be of the order of $\approx 10^{32}$ ergs, which is sufficient to produce the observed HXR sources.

3.5 Summary and Conclusions

We developed an automated technique to extract the flare ribbons on the basis of MMO. This is based on an automatic algorithm to compute the motion of flare ribbons under the assumption that the flare ribbons separate perpendicularly to the neutral line. Using flare ribbon separation and photospheric magnetic field data, we have computed the magnetic reconnection and energy release rates during a flare. We have applied these tools for the study of the energetic solar flares observed in NOAA AR 10486, *i.e.*, the X17/4B and X10/2B flares of 28 and 29 October 2003, respectively (see Chapter 4).

The magnetic reconnection rate in corona, as represented by the electric fields (E_c) in the reconnecting current sheet, has been estimated from the measured ribbon separation speed and magnetic fields obtained from GONG. Electric fields reaching up to 35 kV m^{-1} were found in some locations. Evolution of these parameters provides an evidence that the impulsive flare energy release is indeed governed by the fast magnetic reconnection in the corona. The magnetic energy release rate (*i.e.*, Poynting flux) has been deduced for various parts of the flare. An average Poynting flux during the flare is found to be of the order of 10^9, which gives the energy release of the order of $\approx 10^{32}$ ergs over the entire flare duration of over 10^4 seconds.

In summary, we have found for the X17/4B flare that: *i*) the flare ribbons did not move with the same velocity, but different parts moved with widely varying speeds in different directions, *ii*) flare ribbon separation is observed to decelerate in the regions of strong magnetic fields, and *iii*) magnetic field reconnection (*i.e.*, electric field strength) and energy-release rate (*i.e.*, Poynting flux) increased with increasing separation velocity, and *iv*) the temporal profile of magnetic reconnection rate showed a better correlation with LOS magnetic field strength than with the flare ribbon separation speed during the evolution of the flare.

Most of the methods suggested in literature for the determination of flare energy release are based on certain assumptions and, therefore, provide only approximate estimates. A complete and accurate flare-energy release calculation is beyond the capability of presently available observational and theoretical techniques. The 3D topology of ARs is only now beginning to be observed by recent projects such as the STEREO spacecraft. Therefore, our aim in the present study is limited to providing a relatively simple, automated approach for the estimation of an approximate level of energy-release in two ribbon flares.

Chapter 4

Flare Associated Variations in Magnetic and Velocity Fields of Active Region NOAA 10486

4.1 Introduction

It is known that catastrophic changes in the magnetic field configuration of ARs at coronal heights trigger energetic transients such as fares and CMEs. Therefore, velocity and magnetic field variations are expected to accompany these transients. It was first suggested by Giovanelli (1939) that energy release in flares should be associated with observable magnetic field changes. Extensive efforts have been made since then to detect such changes using photospheric magnetic field measured. However, the observed changes in magnetic field parameters during the impulsive phase of a flare are expected to be related to a variety of effects that could introduce ambiguity in the reported results. One major concern is that flare associated modification of spectral line profiles, used for the measurement of photospheric magnetic fields, may affect the estimation of magnetic fields. Some other physical processes accompanying the sudden energy release occurring in the solar corona may also influence the measurements and adequate care must be taken in interpreting the "observed" changes.

Several types of changes in the observed magnetic fields from pre- and post-phases of flares have been reported by ground-based instruments (Patterson and Zirin, 1981; Patterson, 1984; Wang *et al.*, 1992; Ambastha, Hagyard and West, 1993; Chen *et al.*, 1994; Hagyard, Stark and Venkatakrishnan, 1999), and more recently, by space-borne instruments (Kosovichev and Zharkova, 2001; Qiu and Gary, 2003; Wang, 2006). These changes in observed magnetic fields can be divided into two main categories, "permanent" and "transient". The first type is irreversible change which has been observed during pre- to post phases of flares. Such changes occur due to flux emergence and cancelation process and may be considered as real changes. The later, "transient" changes are reversible that occurs only during energetic events. Therefore, it is difficult to interpret these changes as real or artifact of observations, and have been termed as "magnetic transient" (Patterson, 1984; Kosovichev and Zharkova, 2001) or "magnetic anomaly" (Qiu and Gary, 2003).

Some numerical models have been carried out to confirm magnetic field changes attributed to the observed transient change in the spectral line profile, used for magnetic field measurements, from absorption to emission (Machado *et al.*, 1980; Vernazza, Avrett and Loeser, 1981; Ding and Fang, 1989; Ding, Qiu and Wang, 2002). However, non-LTE calculations for the spectral line Ni I 6768 Å, used in GONG and SOHO/MDI instruments, have shown that this line can turn into emission only by a large increase of electron density and not by heating of the atmosphere by thermal or any other means. Consistent with this report, Qiu and Gary (2003) discovered sign reversals in locations of strong HXR emission formed by energetic electron beams near cooler, strong magnetic field areas of sunspot umbra/penumbra. Injection and transport of high-energy electrons were observationally inferred also from a M9.8 flare observed in microwave by Owens Valley Solar Array, and in HXR by hard X-ray telescope on board *Yohkoh* (Lee *et al.*, 2002).

The GONG and MDI instruments use the same spectral line, *i.e.*, Ni I 6768 Å, but different in principles of observations (see Section 2.2.1). Edelman *et al.* (2004) simulated the GONG and MDI observations for solar flares and concluded that magnetic field measurements are less sensitive to the line shape changes as compared to the Doppler velocity measurements. In addition, their numerical simulation showed that the observed transient sign reversal may be produced when the Ni I 6768 Å line profile turns into emission as a result of non-thermal beam impact on the atmosphere in regions of strong magnetic fields. The effect of line profile changes on magnetic field estimates has also been reported by Abramenko and Baranovsky (2004). They studied six different photospheric absorption spectral lines using spectrograph during flaring and quiet Sun. Their studies showed that the flare profiles are shallower in the line core as compared to quiet Sun profiles and are less steep in the wings too. It was concluded that the magnetic field measurements can be underestimated by 18-25% in areas of Hα ribbons of moderate solar flare. They suggested that the enhanced core emission may be related with heating of the photosphere by the flare while decrease of the slope near wings due to inhomogeneity of the photospheric magnetic fields.

The super active region NOAA 10486 produced extremely energetic X17/4B and X10/2B flares on 28 and 29 October 2003, respectively. We have carried out a detailed investigation of the evolution of magnetic and Doppler velocity fields with the expectation that flares of such magnitude should provide detectable and unambiguous changes. Both abrupt and gradual changes in velocity and magnetic fields were found from GONG and MDI dopplergram movies. More interestingly, we detected rapidly "moving" magnetic/ Doppler velocity transient features (MFs) during the impulsive phases of these flares.

We found that the MFs moved away from the flare site with large velocities ranging from 30 to 50 km s^{-1}, comparable in magnitude to the classic seismic waves detected during the impulsive phase of the X2.6/1B flare of 9 July 1996 (Kosovichev and Zharkova, 1998). These MFs did not appear to be instrumental artifacts as both GONG and MDI movies exhibited similar features. Therefore, it is required to understand the characteristics and mechanism of these peculiar MFs which are generally not seen in other flares.

There are several questions related to the MFs. If they were indeed associated with the white-light flare (WLF) by way of the absorption line profile turning into emission, we expect them to be spatially and temporally correlated with the observed WLF kernels. If not, whether these MFs were associated with HXR sources, produced by nonthermal electron beams directed from the primary flare site to the denser photospheric layer? Whether they were associated with sign-reversal anomalies as reported by Qiu *et al.* (2002)?

In this chapter, we discuss the evolution of magnetic and Doppler fields, spatial and temporal correlations of the magnetic and Doppler velocity MFs, and then attempt to understand their correlations with observed flare kernels. We have used flare data obtained in the lower atmosphere, *i.e.*, photosphere and chromosphere, and in the upper layers using multi-wavelength observations. In Section 4.2, we briefly describe the observational characteristics of SAR NOAA 10486. In Section 4.3, we discuss the observational data and methods of analysis. Properties of MFs and their association with flare kernels are described in Sections 4.4 –4.5. Finally, summary and discussions are presented in Section 4.6.

4.2 The Super Active Region NOAA 10486 and its Flares

In the declining phase of the solar cycle 23, three active regions NOAA 10484, 10486 and 10488 appeared during the period of 17 October-4 November 2003. NOAA 10486 was one of the biggest and complex $\beta\gamma\delta$ configuration ARs of solar cycle 23. It made its disk transit from 22 October to 4 November 2003. During this transit, it produced several flares of unprecedented magnitudes a large number of energetic X-class flares including X5/1B, X17/4B, X10/2B, X8/2B. The super flare X28/3B of 4 November 2003 from this SAR was the largest X-ray flare in the recorded history.

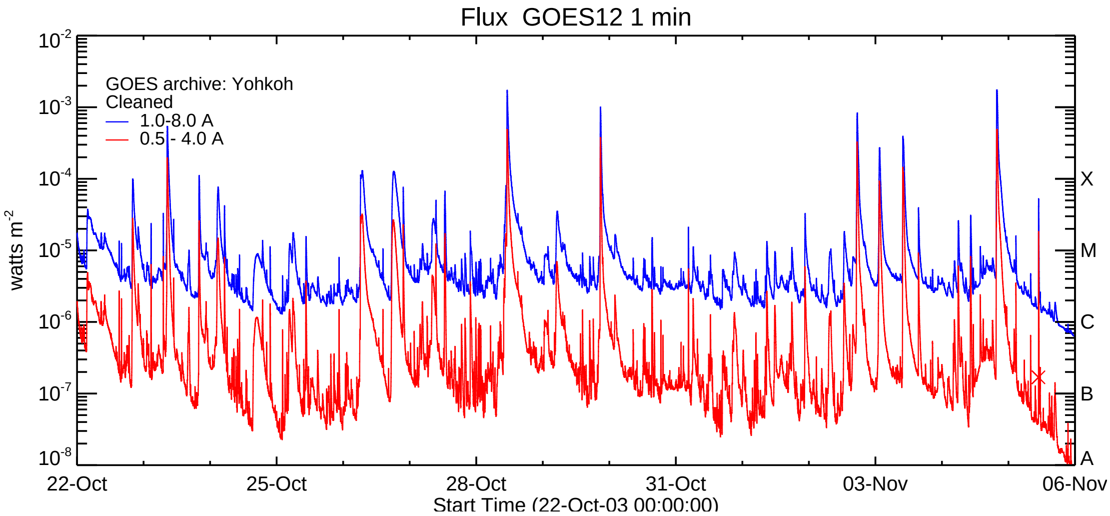

Figure 4.1 Disk integrated GOES X-ray flux observed during 22 October - 6 November 2003, where, Red (Blue) curve represents X-ray flux in the wavelength range 0.5-4.0 Å(1.0-8.0 Å).

It saturated the GOES X-ray detectors, and was later re-classified as X45 $\pm$ 5 flare based on its ionospheric response. Figure 4.1 shows the disk integrated GOES flux observed during the period 22 October - 6 November 2003, where red (blue) curves correspond to the GOES flux observed in the wavelength range 0.5 – 4.0 Å(1.0 – 8.0 Å). Most of these energetic flares were associated with fast moving CMEs and produced large geomagnetic effects.

The energetic flares of NOAA 10486 have been extensively studied during the past few years. Using Huairou Solar Observatory Station (HSOS) vector magnetograms, Zhang, Liu and Zhang (2005) reported highly sheared transverse field structures that gradually evolved around both sides of the magnetic neutral line. They found submerging and emerging magnetic features in the vicinity of the flare onset sites along with rotating penumbra with large horizontal velocity $\sim$ 50 km s^{-1}. Using Hα observations, Ambastha (2006) reported evolutionary changes in the SAR during 26-31 October 2003 along with the changes associated with magnetic/velocity fields. It has been further reported that these flares helioseismically affected the sub-photospheric layers underneath the SAR, as inferred from the detection of acoustic (Donea and Lindsey, 2005) and seismic sources

(Kosovichev, 2006) during the X17/4B and X10/2B flares of 28 and 29 October 2003. Ambastha *et al.* (2004) reported enhancement in the acoustic mode amplitude during the post-flare phases of the flare of 28 October 2003. Zharkova and Zharkov (2007) found the seismic sources to be located near the acoustic sources discovered earlier by Donea and Lindsey (2005).

4.3 The Observational Data and Analysis

We have used full disk time series of magnetograms and Dopplergrams images obtained by GONG and SOHO/MDI instruments to study the evolution of magnetic and Doppler velocity fields in NOAA 10486 during the X17/4B and X10/2B flares of 28 and 29 October 2003, respectively. We also used the white-light photospheric intensity images from GONG and MDI. For the data corresponding to the upper atmospheric layers, we have used TRACE UV 1600 Å for the temperature minimum region, USO and MLSO Hα observations for the chromosphere, and TRACE UV 284 Å for the transition region. To compare the locations of flare kernels and MFs with HXR sources, we have used HXR data obtained by RHESSI (details of the data is given in Section 2.2).

All the images were aligned by de-rotating with the solar rotation. We ignored the effect of solar differential rotation while correcting the images, since (i) the SAR was located close to the solar equator and (ii) selected areas-of-interest were much smaller than the disk. The raw Hα filtergrams obtained for our study were processed using the methods described in Section 2.2.2. Finally, to align images obtained in different wavelengths, we overlaid contours of magnetic flux on the images which were then used for identifying and selecting corresponding areas-of-interest by visual inspection of features, such as, filaments and sunspots. Figures 4.2 and 4.11 show the selected areas of NOAA 10486 from TRACE UV 1600 Å, USO Hα, TRACE UV 284 Å, MDI magnetogram/Dopplergram, and GONG white-light images for the flares of 28 and 29 October 2003, respectively.

4.4 The X17/4B Flare of 28 October 2003

The X17/4B flare of 28 October 2003 in NOAA 10486 was one of the most energetic two ribbon white-light events ever observed. At the time of the occurrence of this flare, the SAR was located near the disk center at S16E18. According to the GOES X-ray flux data, the flare started at 09:51 UT and ended at 11:24 UT, with the maximum phase at 11:10 UT (see Figure 4.1). However, as observed in Hα, the flare was a long duration event (LDE) that lasted over a considerably longer period of several hours.

Figure 4.2 shows multi-wavelength images corresponding to different layers of solar atmosphere obtained during the peak phase of this flare. The top row, from the left to right columns, shows the flare kernels as observed in the temperature minimum region, the chromosphere and the transition region. It may be noted that the flare kernels displayed structural similarities in these layers. Images corresponding to the photospheric layer are shown in the bottom row, from the left to right columns: MDI magnetogram, MDI Dopplergram and GONG white-light image which clearly shows emission kernels of this energetic WLF.

A movie of GONG magnetograms showed interesting but puzzling "magnetic" transient features (MFs) moving rapidly away from the flare site during the X17/4B super-flare. Figure 4.2 shows the MFs as seen at 11:06 UT. One of the MFs was observed to be moving toward the leading sunspot (marked by a rectangular box), while, the other moved perpendicularly to the magnetic neutral line (marked by an arrow). These features, detected in both GONG and MDI movies, appeared and faded in a few minutes' period during the impulsive phase of the flare (Ambastha, 2007a, 2008; Maurya and Ambastha, 2008). Faint Doppler velocity transients were also detected with the flare, similar to the localized Doppler velocity enhancements reported earlier by Venkatakrishnan, Kumar and Uddin (2008). Figure 4.2 reveals these transient features to be associated with the flare ribbons.

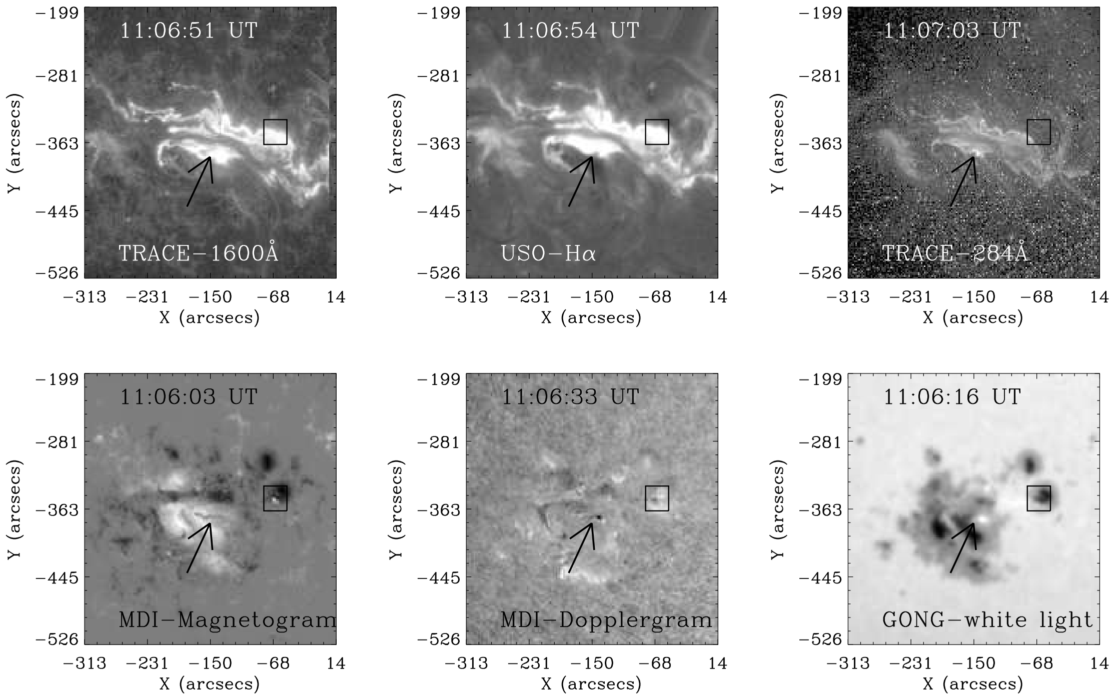

Figure 4.2 Multi-wavelength observations of NOAA 10486 during the impulsive phase of the white-light X17/4B flare of 28 October 2003: TRACE UV 1600 Å, USO Hα and TRACE UV 284 Å (top row, from left to right columns), and MDI magnetogram, Dopplergram and GONG white-light image (bottom row, from left to right columns). The arrow and the box mark the locations of observed MFs.

4.4.1 Evolution of Magnetic and Doppler Velocity Fields

Using the high cadence GONG magnetogram and dopplergram data of NOAA 10486 for the period of 12:46 UT 27 October - 16:09 UT 28 October 2003, it is possible to examine the temporal and spatial evolution in magnetic and velocity fields at flaring and non-flaring sites. We have evaluated the average mean magnetic flux and Doppler velocity over nine selected areas of size 10×10 pixel^2 as marked in Figure 4.3. These boxes were selected along the neutral lines forming narrow channels of strong magnetic field gradients around the location of flare ribbons, and in quiet regions far away from the flare for reference.

Figure 4.4 shows temporal profiles of mean magnetic flux and Doppler velocity evaluated at different box positions. Peak phase of the X17/4B flare of 28 October

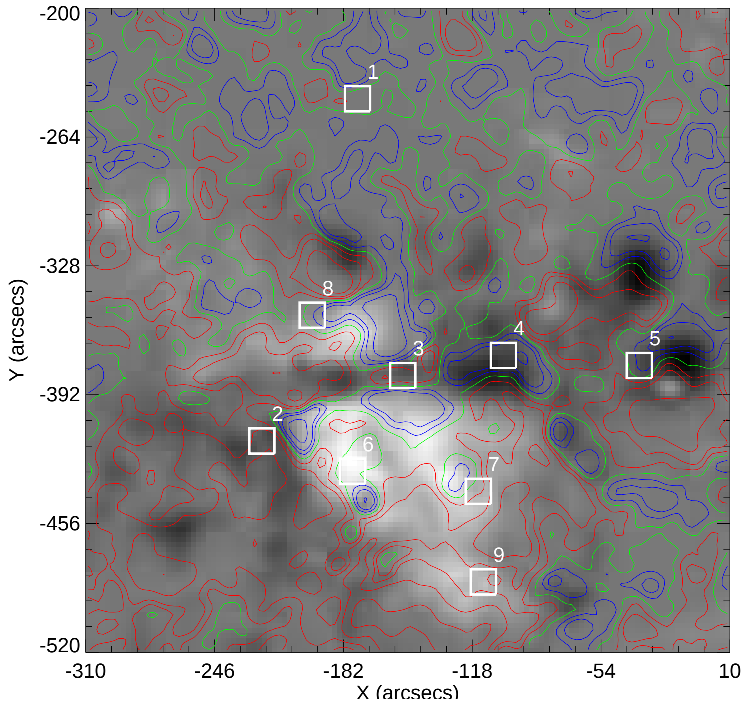

Figure 4.3 Magnetogram of the NOAA 10486 overlaid with the contours of dopplergram observed at 11:10 UT. Red/blue contours represent the upward/downward motions with velocities $\pm100, \pm200, \pm400, \pm800$ m s^{-1} while zero values are shown in green. The boxes of sizes 10×10 pixel^2 are drawn at selected areas of interest.

2003 is marked at 11:10 UT by the arrow. Gradual, or evolutionary, as well as, abrupt changes around the time of the flare are both discernible from the profiles of mean magnetic flux (top panel) and Doppler velocity (bottom panel) at different locations of the AR. For comparison, the profile obtained at a quiet reference area, "1", located far away from the flaring site is also plotted. It is clear that there are no changes in the reference box throughout the period of the plot. On the other hand, along with gradual evolution, abrupt changes at the peak phase of the flare occurred in the boxes 6, 7, 9 (2, 4) located near the flaring site having positive (negative) polarities. Mean Doppler velocity evolved gradually with time at these locations and showed similar abrupt changes during the peak phase of the flare. Interestingly, the downward flow at box 4 turned to upward direction just after the peak phase of the flare. This agrees well with the earlier report of similar feature found at the site of seismic sources by Zharkova and Zharkov (2007).

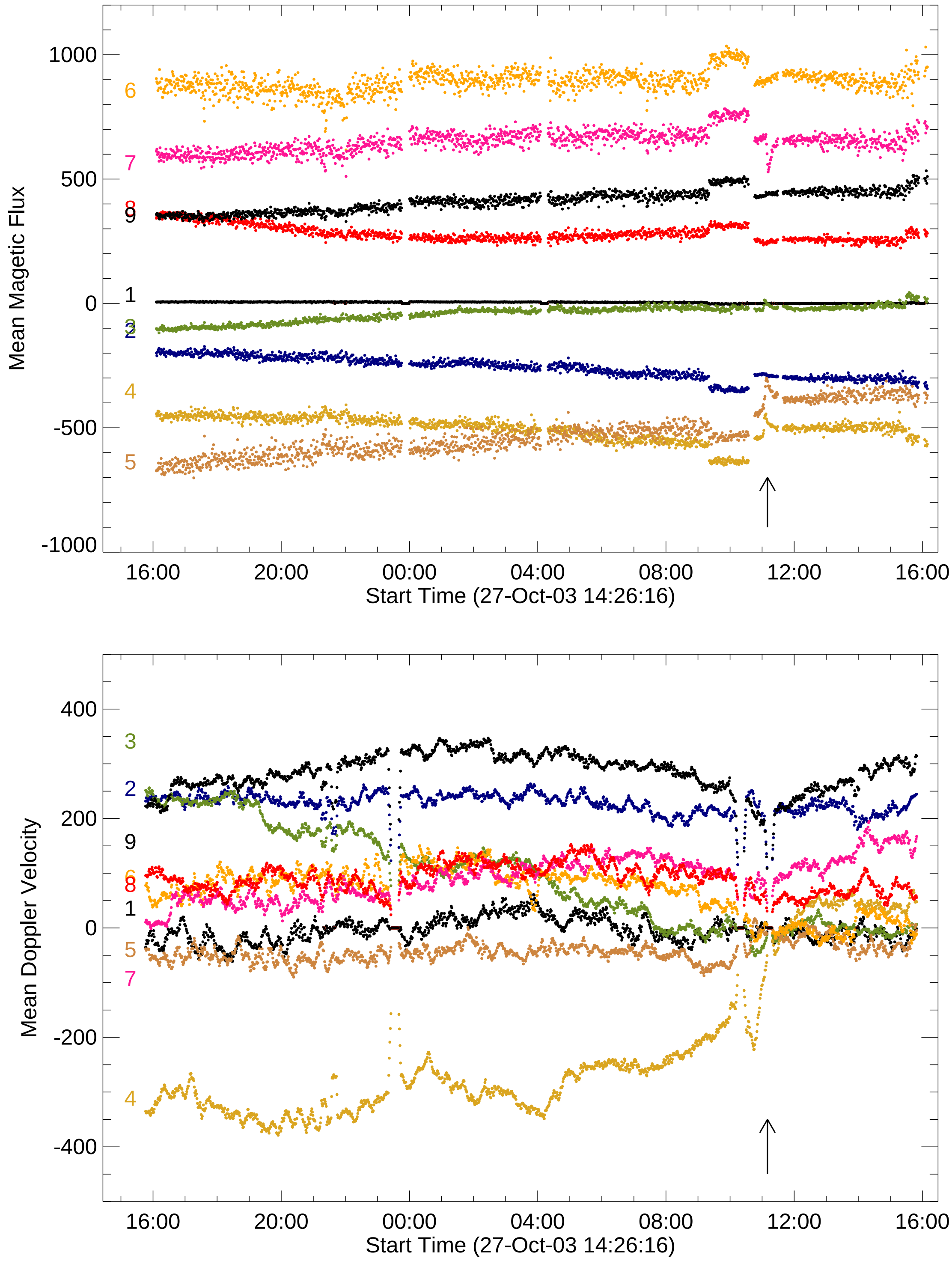

Figure 4.4 Temporal profiles showing variations in the net magnetic and Doppler velocity fields of NOAA 10486 at selected box positions of Figure 4.3 during 27-28 October 2003. The arrow marks the time of the peak phase of the X17/4B flare.

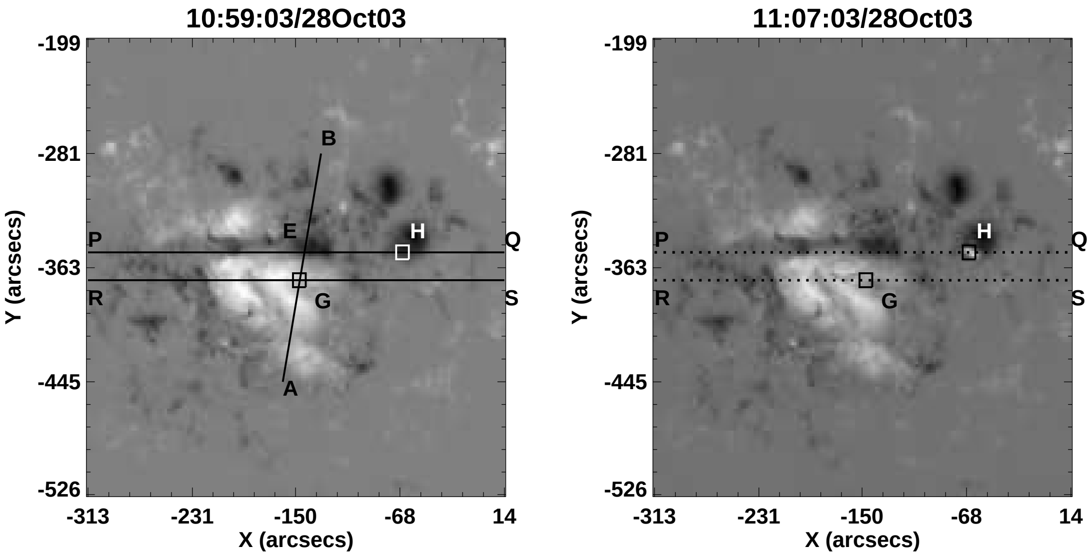

Figure 4.5 MDI magnetograms taken around the pre- and peak phases of the 28 October 2003 flare at 10:59:03 UT (left panel) and 11:07:03 UT (right panel), respectively.

4.4.2 Magnetic Polarity Reversal during the X17/4B Flare

From the analysis of magnetic and Doppler velocity fields corresponding to the moving transients, we noticed sign reversal of magnetic polarity (and Doppler velocity) at some locations during the impulsive phase of the flare. To precisely identify these locations, we plotted magnetic flux profiles along a horizontal raster moving from the bottom to the top of selected magnetograms during the pre- and peak-phases of the flare. We found two locations G and H around which magnetic polarity sign reversals occurred (Figure 4.5). We have drawn lines RS and PQ passing through these two points over the magnetograms at 10:59:03 UT (solid lines) and 11:07:03 UT (dotted lines), respectively. AB marks the direction of motion of WLF kernels and MFs. Distances are estimated from a reference point E (left panel).

The corresponding magnetic flux profiles along RS and PQ are shown in Figure 4.6. Solid and dotted profiles represent magnetic flux at 10:59:03 UT and 11:07:03 UT, respectively. It is evident that magnetic polarity reversals occurred

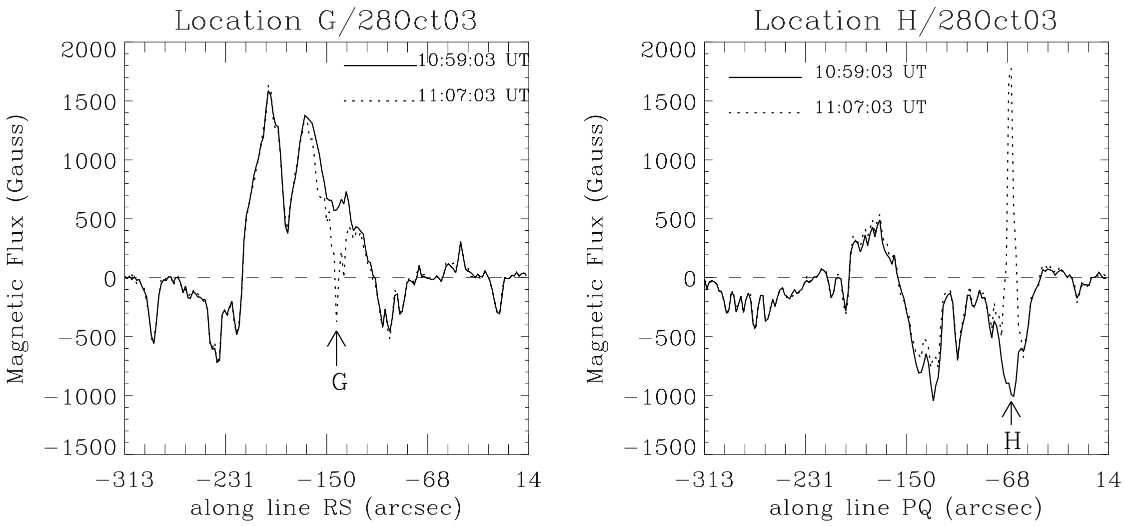

Figure 4.6 Magnetic flux along lines RS (left panel) and PQ (right panel) shown in Figure 4.5.

at G and H as the moving "magnetic" features passed over these locations at 11:07:03 UT, *i.e.*, around the peak phase of the flare. Elsewhere, magnetic flux matched fairly well along these lines at the two time instants.

Using the Big Bear Solar Observatory (BBSO) videomagnetograph data, Zirin and Tanaka (1981) had earlier reported such sign reversals spatially and temporally associated with the large flares of 1 and 5 July 1980. But they gave no explanation about the cause of sign reversals. Later, it was attributed to thermal heating of lower atmosphere by the flare, turning the core of the line used for measurement from absorption to emission (Patterson, 1984).

More recently, this effect was reported for a large X-class flare of 6 April 2001 using MDI magnetograms (Qiu and Gary, 2003). However, the sign reversals observed by MDI instrument are difficult to explain by sudden heating of the lower atmosphere. This is because Ni I 6768 Å line (used by MDI and GONG instruments) is formed in the temperature minimum region and is rather stable against any temperature changes (Bruls, 1993). Another important point to note is that the measurement of strong magnetic fields by MDI instrument is affected by saturation effect and hence, incorrect (Liu and Norton, 2001). They showed for strong magnetic fields, *e.g.*, in umbral regions, that the resulting Zeeman effect may exceed the working range of MDI algorithm. However, the observed sign reversal can not be produced by this difficulty alone.

Interestingly, Qiu and Gary (2003) noted that sign-reversals occurred near locations of strong magnetic field, or the cooler sunspot umbrae, that are exactly co-aligned with HXR sources. This suggested that the sign reversal anomaly was associated with non-thermal electron beam precipitating to the lower atmosphere near the cool sunspots. This inference was further supported by a numerical simulation of MDI measurements incorporating the flare effects.

The transient sign-reversals observed during the impulsive phase of the X17/4B flare in NOAA 10486 appear to be similar in nature as reported by Qiu and Gary (2003). However, in this case (*cf.* Figure 4.5), we found two locations that somewhat differed in their basic characteristics – (i) the sign reversal at H was located in strong magnetic field region of the leading, negative polarity umbra; similar to that reported by Qiu and Gary (2003), and remained nearly stationary during the entire impulsive phase, (ii) the sign reversal at G first appeared near the neutral line, *i.e.*, in a weak field location, and subsequently moved rapidly toward stronger magnetic field region of the following, positive polarity sunspots.

In the next section, we discuss in detail the motion and properties of the magnetic and Doppler transients and their association with flare kernels as observed at various solar atmospheric layers.

4.4.3 Motion of the Magnetic/Doppler Transients and Flare Kernels

From Figure 4.2, we may infer that the magnetic/Doppler transients are spatially correlated with the flare kernels observed at different heights of the solar atmosphere. For further establishing this relationship, we enhanced the transients using Maximum Entropy Method (MEM) (Skilling and Bryan, 1984; Narayan and

Nityananda, 1986). It is a deconvolution algorithm that operates by minimizing a smoothness function ("entropy") in an image. Before applying this tool for each type of observation, we subtracted the square root of a reference image from the square root of corresponding images obtained at different instants of time. Figure 4.7 (a–e) shows contours of suitably enhanced features observed during, 11:00-11:12 UT, the impulsive phase of the flare in different sets of images, *i.e.*, MDI magnetograms and Dopplergrams, GONG white-light, TRACE UV 1600 Å, USO Hα and TRACE UV 284 Å. These contours display the spatial and temporal evolution of magnetic/Doppler transients and flare kernels observed at various atmospheric layers with increasing height from the photosphere to the transition region. The solid line in the figure represents an arbitrary reference line, RS, drawn along the neutral line from where distances of various features were measured (*cf.* Figure 4.5). The arrows and rectangular boxes mark the positions of magnetic and Doppler transients.

Figure 4.7 shows that the magnetic transients and flare kernels separated away from the neutral line with time during the impulsive phase of the flare (rows a–e, in each column). This follows the usual behavior of two ribbon flares. We note that the evolution of magnetic and Doppler transients (columns 1 and 2) is spatially and temporally well correlated with the flare kernels observed in different layers of solar atmosphere (columns 3–6). Locations of observed transients are marked by arrows and boxes in each frame. Along with magnetic transients, comparatively fainter Doppler transients are discernible during this period (column 2), similar to the Doppler-ribbons reported by Venkatakrishnan, Kumar and Uddin (2008). Magnetic and Doppler transients are observed to be correlated with WLF kernels observed during the impulsive phase of the flare. In the following, we determine the separation velocities of the transients and flare kernels.

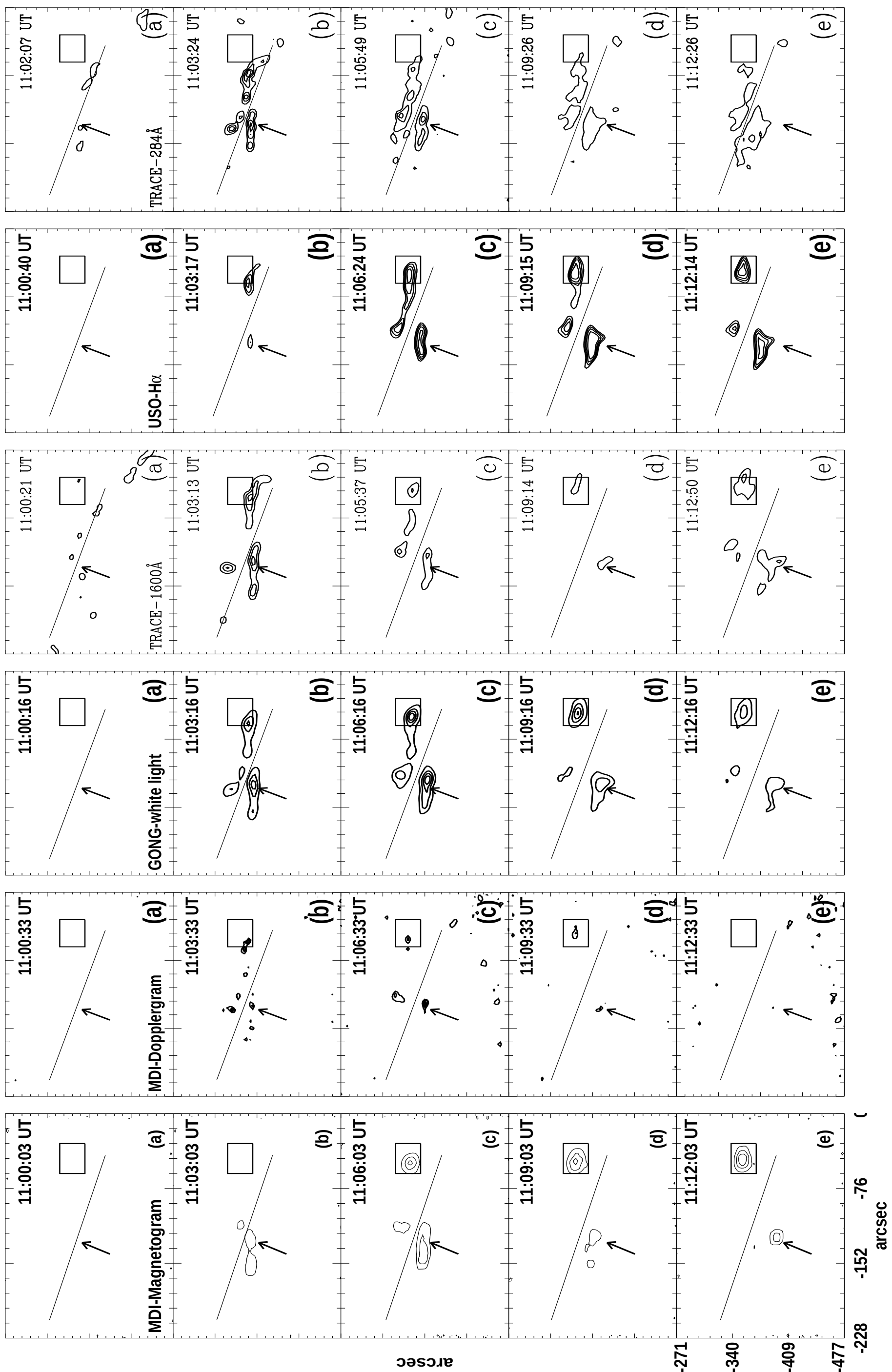

Figure 4.7 A mosaic of multi-wavelength observations showing the moving transients and flare kernels during the X17/4B super-flare of 28 October 2003. Contours are drawn at 20, 40, 60 and 80% levels of the maximum values in the enhanced images: MDI magnetograms, MDI Dopplergrams, GONG white-light, TRACE UV 1600 Å, USO Hα and TRACE UV 284 Å (from left to right columns). Arrows and rectangular boxes mark locations of the transients.

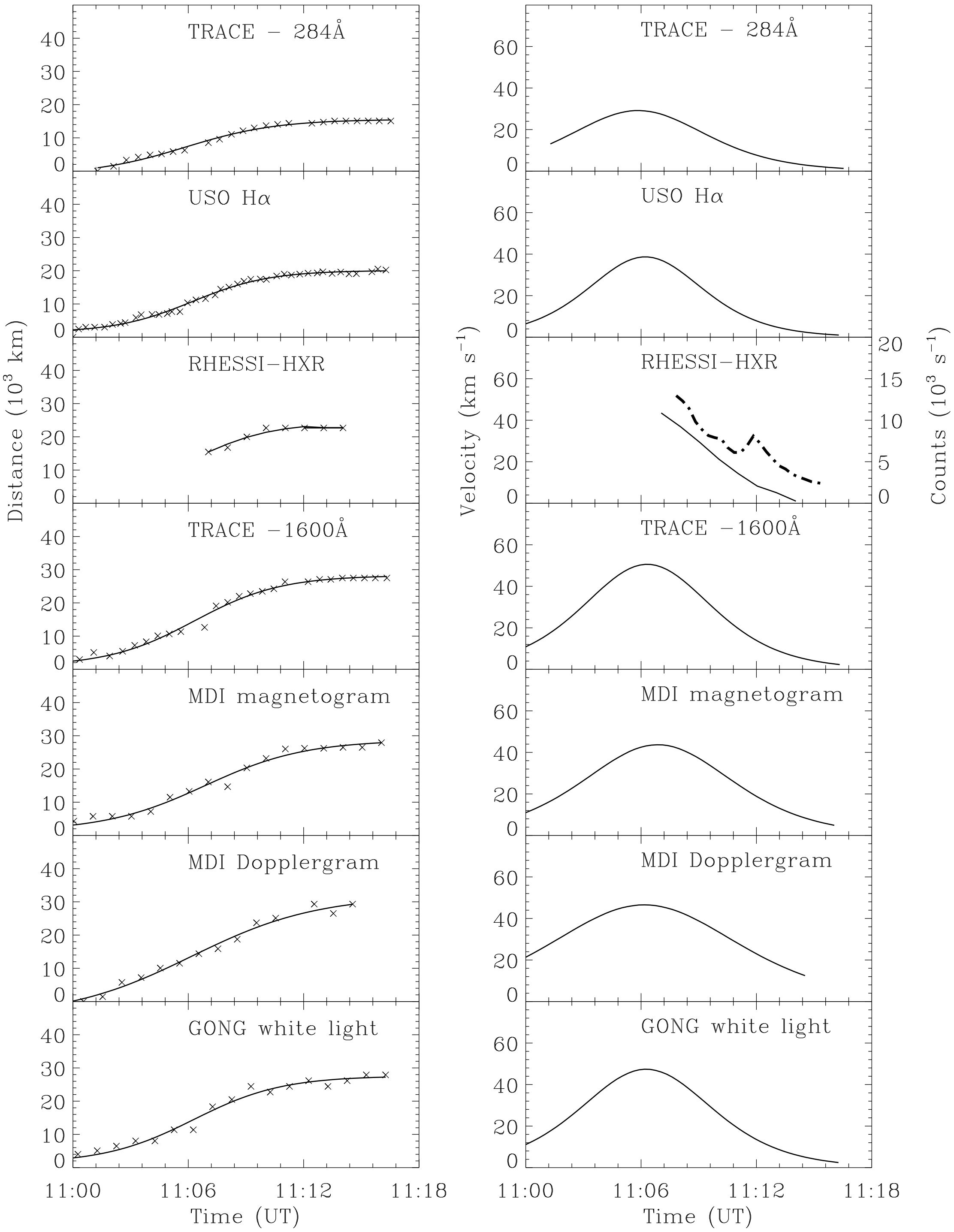

Figure 4.8 Separation of flare kernels and magnetic/Doppler transients from a reference line during 11:00-11:15 UT. Left panel with marked "×"(solid line) shows measured (fitted) distances. Right panel shows the separation velocities of flare kernels and MFs obtained from the fitted distances corresponding to the left panel. The dash-dotted line in RHESSI velocity panel shows the HXR light curve.

Velocities of MFs and Flare Ribbons

We carried out the following procedure to quantitatively examine the motion of various observed features.

First, we selected a reference point E (Figure 4.5) on the neutral line to determine the feature motions from the co-aligned images. We implemented an automated algorithm based on method described in Section 3.4 in IDL to determine the separation of observed transients. The maximum value of a feature was followed along EA, *i.e.*, the direction of motion of the features. Distance between the point of maximum value within a given feature (say E′: x_1, y_1) and the reference point E (x_2, y_2) was calculated in pixels using $d = [(x_2 - x_1)^2 + (y_2 - y_1)^2]^{1/2}$. It was then converted into kilometers using the pixel resolution of the corresponding instruments (Table 4.1).

Table 4.1 Maximum distances, velocities, and time at the maximum velocities of transients of the X17/4B flare of 28 October 2003.

S.N.	Data	Pixel res. (arcsec)	Layer	Max. dist. (Mm)	Max. vel. (km s^{-1})	Time of max. vel. (UT)
1	TRACE UV 284 Å	0.5	TR[1]	15.4±0.3	29±4	11:05:40
2	USO Hα	0.4	Chr[2]	20.0±0.3	38±5	11:06:20
3	RHESSI HXR	4.0	Chr[2]	23.1±0.8	43±9	11:07:03
4	TRACE UV 1600 Å	0.5	TM[3]	28.0±0.3	50±7	11:06:13
5	GONG WL	2.5	Pho[4]	27.3±0.5	45±6	11:06:10
6	MDI Dopplergram	2.0	Pho[4]	29.3±0.5	46±5	11:06:10
7	MDI magnetogram	2.0	Pho[4]	27.9±0.4	43±4	11:06:49

[1]TR: Transition Region, [2]Chr: Chromosphere, [3]TM: Temperature Minimum, [4]Pho: Photosphere

Figure 4.8 (left panel) shows the separation of magnetic/Doppler transients and flare kernels from the neutral line during the impulsive phase, *i.e.*, 11:00-11:15 UT, of the X17/4B flare. Their distances from the reference point E, along AB, increased rapidly during this period, as seen along each row (corresponding to different observations) in the left column of the figure. Thereafter, the rate of increase of separation reduced. Table 4.1 shows an interesting trend in the maximum separation attained by the flare kernels. It was the shortest, *i.e.*, ≈ 15 Mm at the transition layer observed in UV 284 Å (TRACE). Moving toward lower layers, it increased to $\approx$ 20 Mm at the chromosphere (USO Hα), $\approx$ 28 Mm at the temperature minimum region and the photosphere (*cf.* TRACE UV 1600 Å, and GONG and MDI photospheric data). This trend is consistent with the classical flare model of an expanding loop structure with footpoints anchored in the lower atmosphere.

The RHESSI HXR data was available for the X17/4B flare only from 11:06 UT onward. Therefore, we could compute the corresponding distances and separation velocities of HXR sources only for the limited available time, as shown in the third row (from top) of the Figure 4.8. We found that the HXR feature showed a separation of $\approx$ 23 Mm, similar to that observed in the chromospheric Hα. This is consistent with the formation of HXR footpoint sources in the chromosphere or in the lower corona depending on the energy of penetrating particles. The magnetic and Doppler transients, on the other hand, showed a larger separation of $\approx$ 29 Mm as obtained for the photospheric WLF kernels.

The HXR light curve is shown as the dash-dotted line in HXR velocity panel of Figure 4.8. It is evident that the separation velocity of HXR footpoint X_2 (*cf.* Figure 4.10) and the overall HXR flux decreased with time during the post-flare phase, except that there is a small bump in the HXR flux at around 11:12 UT. On examining the HXR images we found that this bump corresponds to an enhancement of HXR flux near the footpoint X_1. It may be noted that the major contribution to the HXR light curve arises from the integrated flux over both the footpoints X_1 and X_2 while the separation velocity plotted here pertains only to the footpoint X_2.

Separation velocities $v(t)$ of MFs and flare ribbons are then obtained by taking the time derivative of fitted distance function $d(t)$. Numerical differentiation was carried out by three point Lagrangian interpolation. Figure 4.8 shows the fitted distances (solid curves) passing through the measured distances marked by "$\times$" symbols (left panel). The derived velocities are also given (right panel). Velocities of flare kernels and magnetic/Doppler transients reached a peak (or maximum)

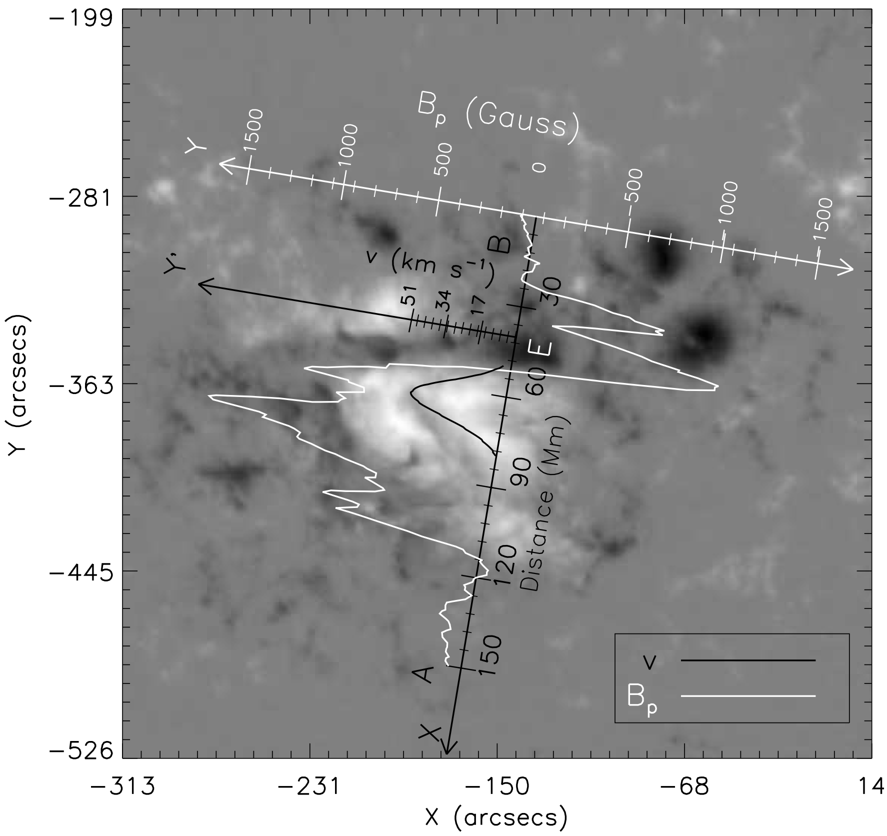

Figure 4.9 Separation velocity profile of the moving "magnetic" feature (black profile) measured along the reference line BA overlaid on the MDI magnetogram (background half-tone image). The magnetic flux variation along the trajectory of motion of the feature is drawn as white profile.

at around 11:06 UT. It is clear from this figure and Table 4.1 that the separation velocity of flare kernels was larger, *i.e.*, 45-50 km s^{-1} at lower atmosphere (temperature minimum region and photosphere). It decreased with increasing height, *i.e.*, 38 km s^{-1} at the chromosphere and 29 km s^{-1} at the transition region.

A systematic increase in separation of Hα flare kernels is the chromospheric signature of magnetic reconnection process occurring progressively at higher levels in the corona. Usually rather small separation velocities in the range of $\approx$ 3-10 km s^{-1} are reported in literature for two ribbon flares that are associated with filament eruptions. As compared to these, we obtained significantly large velocities, in the range of 30-50 km s^{-1}, for the flare ribbons in NOAA 10486 (Table 4.1). Such and even larger separation velocities in the range 20-100 km s^{-1} have been reported during an M9.0 two ribbon flare of 16 March 2000 occurring in a complex AR NOAA 8906 (Qiu *et al.*, 2002).

As the flare ribbons approach the regions of increasing magnetic fields, their speeds are known to decrease. This is observed for the flare kernels and moving magnetic transients during the flare of 28 October 2003. Figure 4.9 shows the separation velocity profile (dark curve) of the moving magnetic feature from the neutral line along the direction BA. It is clear that the separation velocity first increased with magnetic flux (white curve), attained a peak value, then decreased and vanished at the location where the magnetic flux attained a maximum value. This result is consistent with the general behavior of flare ribbons moving toward the region of strong magnetic fields.

4.4.4 Association of MFs with HXR Sources and White-Light Flare Ribbons

Figure 4.10 shows spatial and temporal evolution of the enhanced WLF kernels (red patches) observed in GONG white-light intensity images (green half-tone images) obtained during the impulsive phase of the X17/4B flare of 28 October 2003 (top rows 1-2). Similarly, the evolution of moving magnetic transients (magenta patches) are shown over the same background images in the bottom rows (3-4). White contours represent RHESSI HXR flux in the energy range 100-200 keV associated with the flare during its impulsive phase, *i.e.*, 11:07:03-11:12:03 UT, at 20, 40, 60, 80% levels of the maximum HXR flux. The central maximum of the HXR source (marked by "+" sign in yellow color) was found to be moving in the direction of arrow with separation velocity of 43 km s^{-1} from the reference line, *i.e.*, the solid blue line drawn along the neutral line. Separation velocity of the HXR feature was similar to that of the moving magnetic/Doppler transient and WLF kernels (*cf.* Table 4.1), however, their spatial positions some what differed.

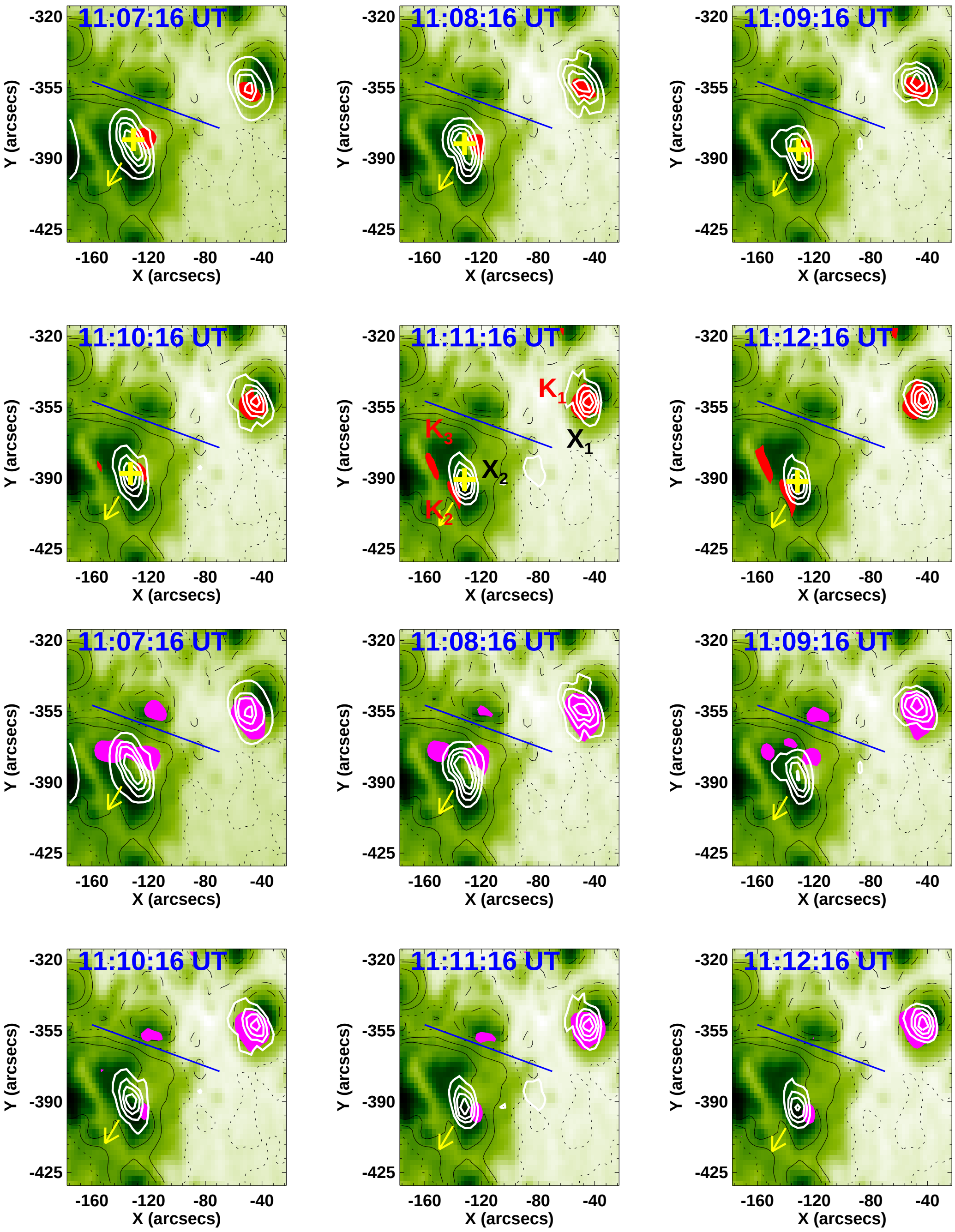

Figure 4.10 A mosaic of white-light intensity images (background green half-tone image) during the impulsive phase of the X17/4B flare - 11:07:16-11:12:16 UT on 28 October 2003. Superimposed dashed (solid) contours represent negative (positive) flux at ±800, ±1500 G levels, while the dotted contours mark the magnetic neutral lines. RHESSI HXR fluxes (white contours) in the energy range 100–200 keV are overlaid at the levels 20, 40, 60, 80% of the maximum value. Red patches mark the enhanced WLF kernels (top rows 1-2) and magenta patches represent the enhanced magnetic transients (bottom rows 3-4).

Figure 4.7 shows that the moving magnetic transients were also the sites where polarity sign reversal occurred. They first appeared around 11:03 UT close to the neutral line, *i.e.*, at a weak magnetic field location. Thereafter, one of these features moved toward the direction of strong magnetic field of the following (positive) polarity umbra. Unfortunately, it is not clear whether HXR source also formed along with MFs near the neutral line as RHESSI HXR data is not available before 11:07:16 UT.

Qiu and Gary (2003) have also reported formation of HXR features during the impulsive phase of the X5.6 flare of 6 April 2001, but in strong magnetic fields of umbral/penumbral regions. They noted that locations of sign-reversal "anomaly" coincided well with HXR footpoints. They suggested the observed anomalous magnetic features to be related to electron precipitation into the lower atmosphere but not with all WLF kernels. They gave the energetics for the reversal of line-profiles in the cooler, strong magnetic field umbral regions as compared to that in the hotter, weak magnetic field locations.

In a partial agreement with Qiu and Gary (2003), in this case we observed that one of the HXR footpoint X_1 formed at the strong magnetic field location of the leading umbra. This HXR source was nearly stationary and matched well with both the WLF kernel K_1 (rows 1-2) and the magnetic transient feature (rows 3-4). On the other hand, the HXR source X_2 did not match well with WLF kernel. We observed that the WLF kernel K_2 first appeared at one edge of the X_2 contours (11:07:16 UT), then decayed and appeared at the opposite edge (11:11:16 UT). Around the same time, WLF kernel K_3 appeared which was not associated with any HXR feature. The moving magnetic feature at X_2 was better associated with HXR than with the WLF kernels. Thus, association of HXR source with anomalous magnetic polarity feature, as reported by Qiu and Gary (2003), does appear to hold in this particular case.

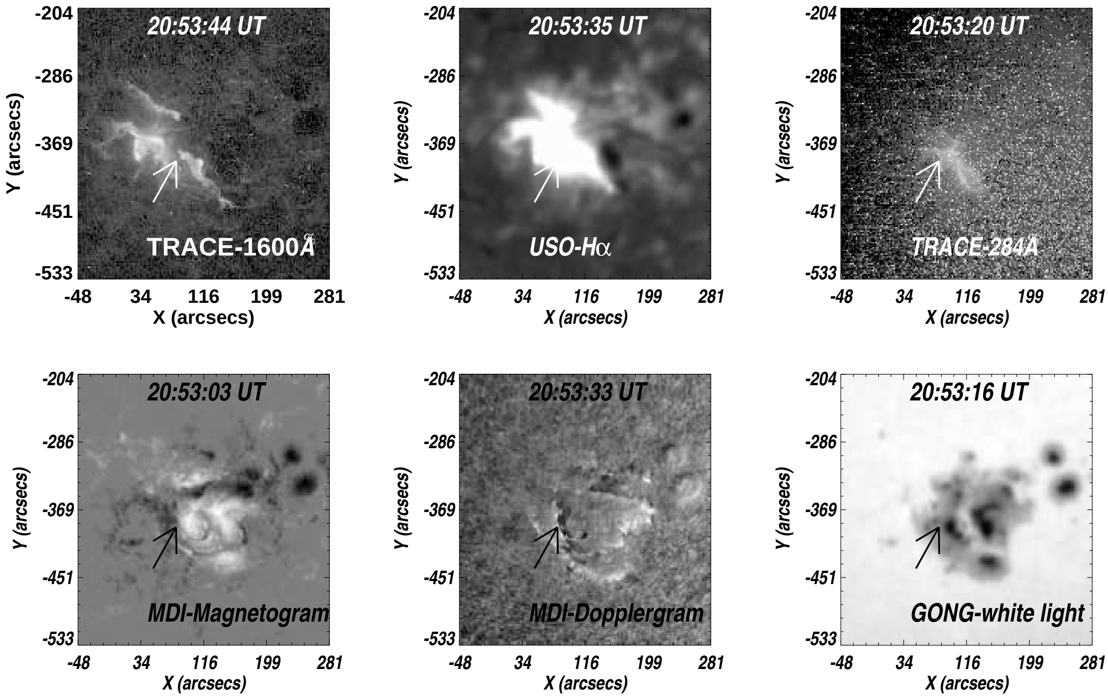

Figure 4.11 A Mosaic of NOAA 10486 images during the white-light X10/2B flare of 29 October 2003 in TRACE UV 1600 Å, MLSO Hα and TRACE UV 284 Å (top row). MDI magnetogram, Dopplergram and GONG white-light image are shown at the peak phase of the flare (bottom row: left to right columns).

4.5 The X10/2B Flare of 29 October 2003

NOAA 10486 had moved to S15W02, closer to the disk center, on 29 October 2003 when another white-light two ribbon X10/2B flare occurred in this SAR. However, its location was different, away from the site of the previous X17/4B flare of 28 October 2003, in the western edge of the AR. GOES observations showed that the flare began at 20:37 UT, reached the peak phase at 20:49 UT and decayed at 21:01 UT while in Hα it ended much later at 22:53 UT.

Figure 4.11 shows a mosaic of flare images as observed in different wavelengths, TRACE UV 1600 Å, Hα and TRACE UV 284 Å (top row). The photospheric magnetogram, Dopplergram and white-light images are shown in the bottom row. Locations of WLF kernels are marked by arrow in each frame of the figure.

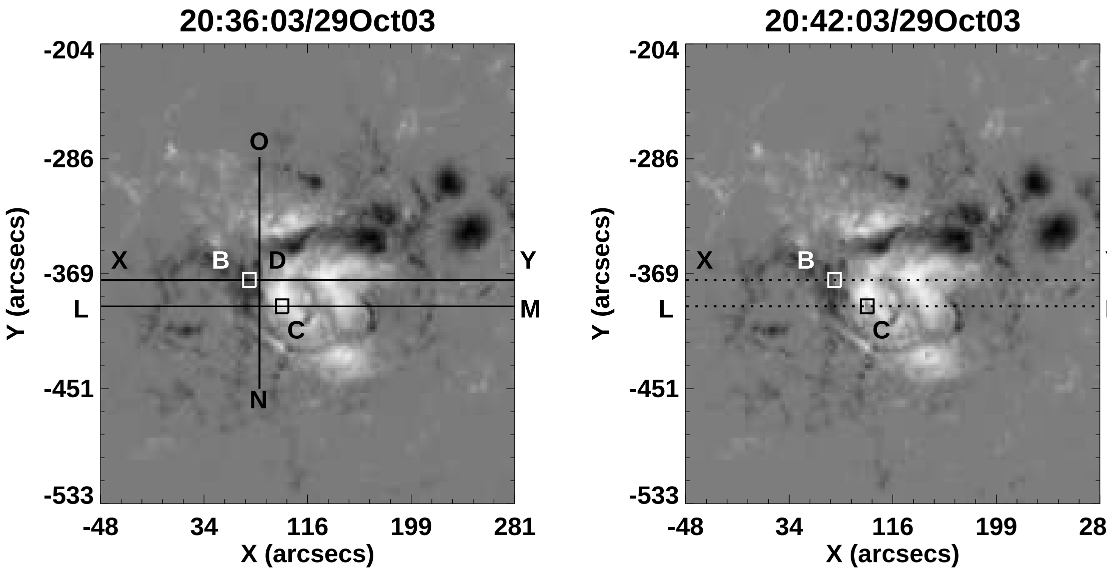

Figure 4.12 Magnetograms of NOAA 10486 taken around the pre- and peak phases of the 29 October 2003 flare at 20:36:03 UT (left panel) and 20:42:03 UT (right panel), respectively.

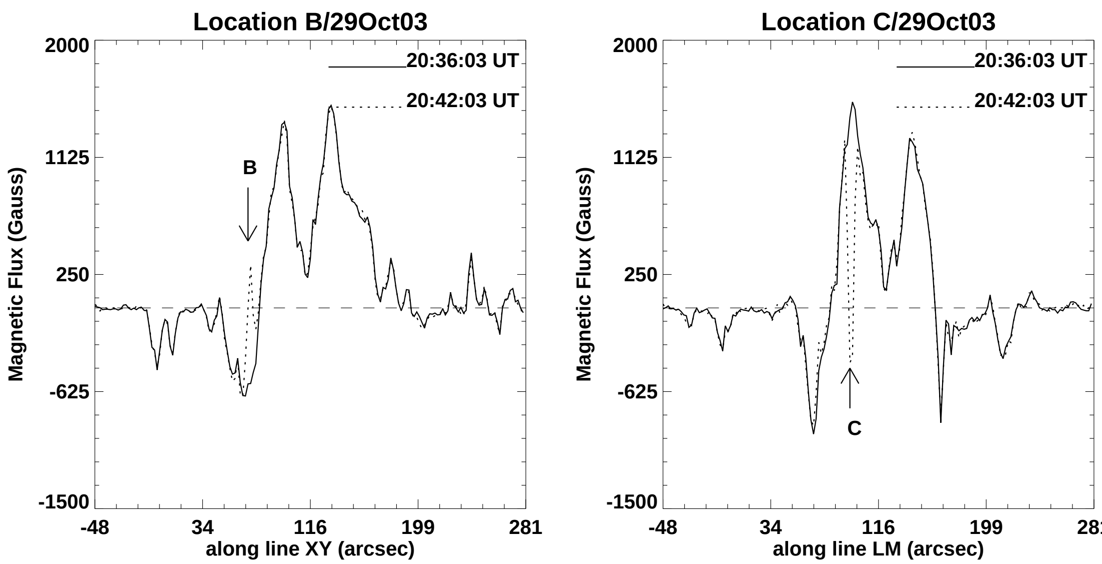

Figure 4.13 Profiles of magnetic flux along the lines XY and LM (as shown in Figure 4.12), where, solid (dotted) profile represents magnetic flux obtained at 20:36:03 UT (20:42:03 UT).

4.5.1 Magnetic Polarity Reversal during the X10/2B Flare

A movie of MDI magnetograms showed magnetic transient features during the impulsive phase of this flare also as observed in the event of the X17 flare. We identified locations of sign reversals in magnetic flux in the AR by using a horizontal raster moving from the bottom to the top of magnetograms selected during the pre-peak and peak phases of the flare (*cf.* Figure 4.12). Magnetic fluxes along XY and LM are plotted in Figure 4.13. Solid and dotted lines in the figure correspond to the times of pre-peak phase (20:36:03 UT) and the peak phase (20:42:03 UT), respectively. It is observed that magnetic flux changed sign at “B” and “C” , *i.e.*, around 20:42:03 UT, while it remained nearly unchanged elsewhere along the lines XY and LM.

4.5.2 Motion of Magnetic/Doppler Transients and Flare Kernels

Spatial and temporal evolution of MFs and flare kernels observed during the flare of 29 October 2003 are illustrated in Figure 4.14. Contour levels were derived from the enhanced images using the same technique (MEM) as used for the event of the previous day, *i.e.*, 28 October 2003. Different sets of images, *i.e.*, photospheric magnetograms (MDI), Dopplergrams (MDI), white-light (GONG), chromospheric Hα (MLSO) and temperature minimum UV 1600 Å (TRACE) are shown from the left to the right columns.

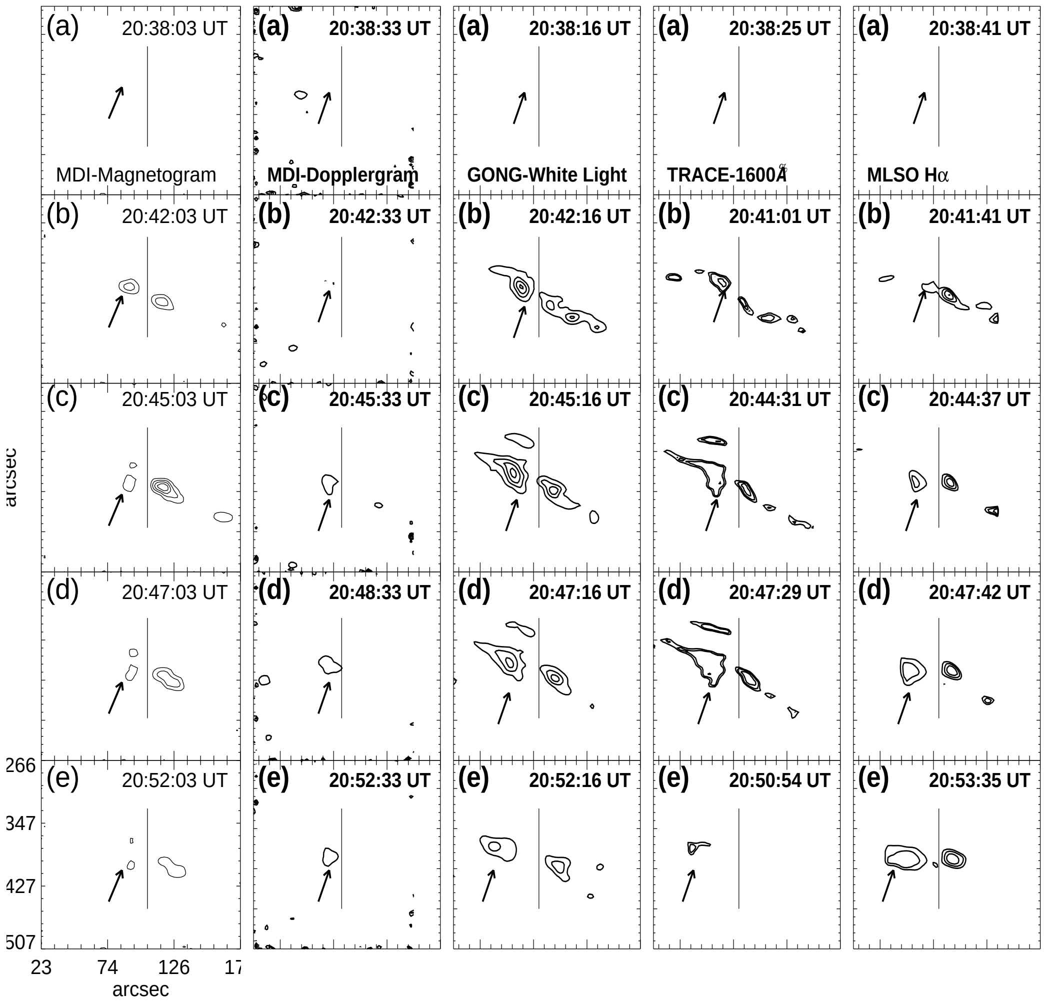

Figure 4.14 A mosaic of magnetograms (MDI), Dopplergrams (MDI), white-light (GONG), UV 1600 Å (TRACE) and Hα (MLSO) (from left to right columns) of NOAA 10486 during the impulsive phase of the X10/2B flare of 29 October 2003. The contours mark the development and motion of the transient feature during the impulsive phase of the flare. Arrows have been drawn at the locations of MF and at corresponding positions in the flare kernels. The solid line is the reference direction with respect to which MF and flare kernel motions were measured.

The magnetic and Doppler transients appeared to be correlated with flare kernels observed in white-light and other wavelengths corresponding to various layers of the solar atmosphere (see Figure 4.14). Temporal evolution of MFs and flare kernels are shown from the top (a) to the bottom (e) rows in each column. A solid line drawn in each frame marks the reference direction perpendicular to which MFs and flare kernels moved, and the arrow shows the location of the MF

Figure 4.15 Separation of flare kernels from the reference line NO during 20:38:40-20:53:35 UT for different observations, Hα (MLSO), HXR (RHESSI), UV 1600 Å (TRACE) and white-light (GONG) marked by symbols □, +, $*$ and △, respectively. The solid lines represent the straight-line fitting through the corresponding data points.

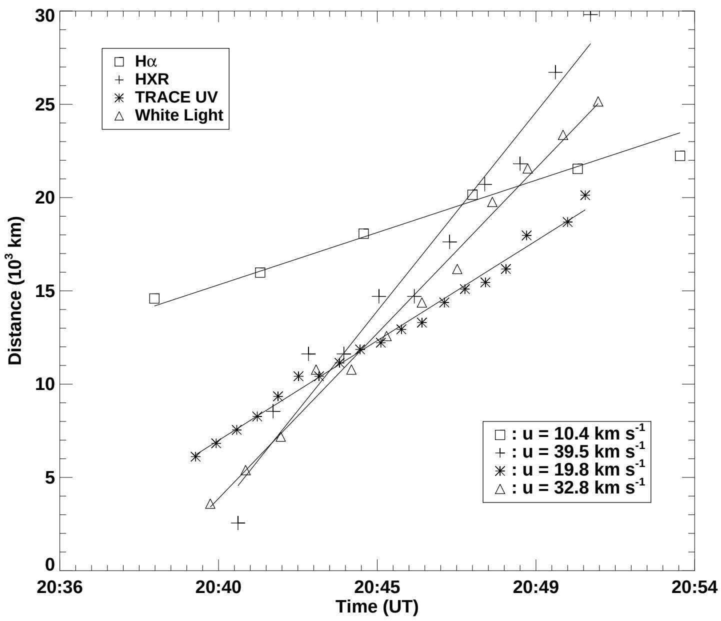

in each set of the observations.

We have determined the distances of flare kernels from the reference line NO along the line DX (*cf.* Figure 4.12) by following the position of the maximum value within a feature of interest. Separations of various flare kernels are shown in Figure 4.14. In order to find the separation speeds of flare kernels, we fitted straight lines (best fitting) through the measured distances. Slopes of these fitted lines provided the respective velocities (Figure 4.15). Maximum distances and velocities are listed in the Table 4.2. Velocities of flare kernels showed similar trend as in the earlier case of the flare of 28 October 2003; it generally increased from the upper to the lower atmospheric layers. However, the magnitudes of separation velocities obtained for this flare were found to be much smaller as compared to that for the X17/4B flare.

Other differences from the event of X17/2B were: (i) the magnetic and Doppler transients remained nearly stationary during this flare, and (ii) the profiles for distance and separation velocity were different in nature. For the event of 28 October 2003, we could do a Boltzmann Sigmoid fitting whereas a straight line fitting was applicable for this flare. It is unlikely that the separation velocity

Table 4.2 Maximum distances and velocities of the flare kernels during the X10/2B flare of 29 October 2003.

S.N.	Data	Pixel res. (arcsec)	Layer	Max. dist. (Mm)	Max. vel. (km s^{-1})
1	USO Hα	0.4	Chr[1]	23.5±0.3	10±5
2	RHESSI HXR	4.0	Chr[1]	28.3±0.9	40±9
3	TRACE UV 1600 Å	0.5	TM[2]	19.3±0.3	20±7
4	GONG WL	2.5	Pho[3]	25.0±0.5	33±6

[1]Chr: Chromosphere, [2]TM: Temperature Minimum, [3]Pho: Photosphere

of flare kernels would remain constant throughout the flare duration as appears to be the case in this event. It is to note that flare kernels became fainter in intensity or got fragmented as they moved away from the reference line, and were generally difficult to identify and follow up after 20:51 UT. For Hα kernel, however, there is an indication that the rate of change of separation decreased after this time.

4.5.3 The Association of HXR Sources and White-Light Flare Ribbons

Figure 4.16 shows the temporal and spatial evolution of HXR sources and WLF. The enhanced WLF kernels obtained from GONG intensity maps are shown as red patches on green half-tone images during the impulsive phase of the X10/2B flare of 29 October 2003 (top rows 1-2). Similarly, evolution of magnetic transients (magenta patches) is shown over the same background intensity images in the bottom rows (3-4). Blue contours represent RHESSI HXR fluxes in the energy range 50-100 keV associated with the flare during its impulsive phase, *i.e.*, 20:40:16-20:50:16 UT, at 20, 40, 60, 80% levels of the maximum flux. The central maximum of the HXR source is marked by "+" sign in blue color. A solid blue line is drawn along the neutral line as a reference to measure the positions of various flare kernels observed to be moving in the direction of the arrow.

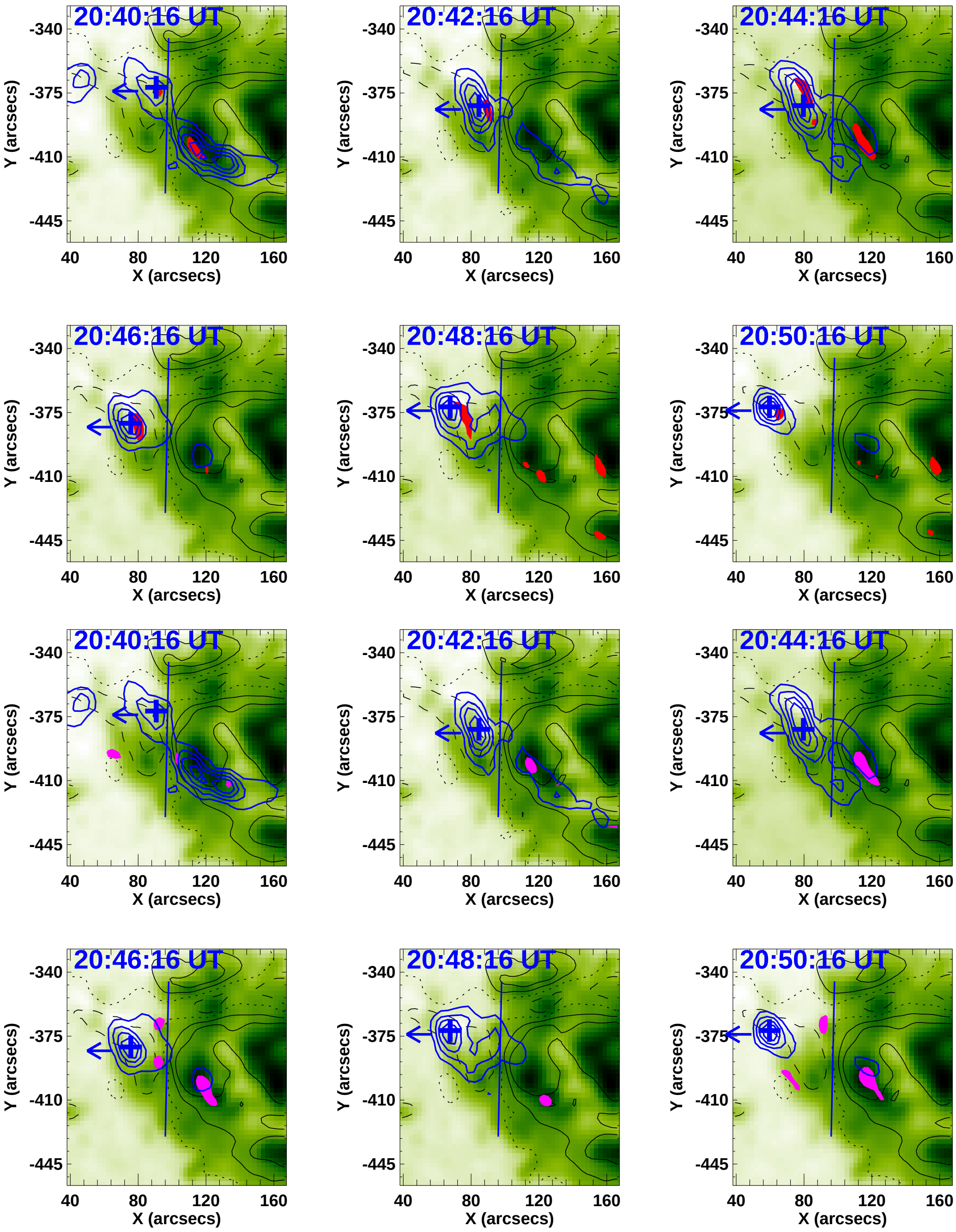

Figure 4.16 A mosaic of white-light intensity images (background half-tone green image) taken during the impulsive phase of the X10/2B flare - 20:40:16-20:50:16 UT on 29 October 2003. Superimposed dashed (solid) contours represent negative (positive) flux levels at ± 800, ± 1500 gauss, and dotted contours mark the magnetic neutral lines. RHESSI HXR fluxes in the energy range 50-100 keV are overlaid at 20, 40, 60, 80% levels of the maximum value (blue contours). Red patches (top rows 1-2) show the positions of WLF kernels, while magenta patches (bottom rows 3-4) mark the magnetic transients.

Xu *et al.* (2004) studied the 1.56 μm near-infrared (NIR) observations corresponding to the white-light flare of 29 October 2003. The NIR images of the region correspond to $\approx$ 50 km below the photosphere at the opacity minimum layer. These images indicated extremely energetic activities associated with this flare as only the most energetic electrons can penetrate this deep in the photosphere. They found that the locations of WLF kernels matched very well with the NIR continuum flare patches. However, not all these WLF kernels were associated with RHESSI HXR sources, as seen in Figure 4.16(top rows 1-2). Also, locations of MFs, where sign-reversal anomaly appeared, did not conform well with these HXR sources except at 20:40:16 UT (first two frames in row 3). Thereafter, the HXR source intensified at the opposite side of the neutral line, where the other part of the two ribbon WLF kernel was located (top rows 1-2), but no magnetic transient feature (magenta patches in rows 3-4) was present.

Interestingly, in disagreement with Qiu and Gary (2003), we note that the strong HXR source (and the WLF kernel) which intensified at the west side of the neutral line was located in a weak field region. On the other hand, the magnetic transient observed at the stronger field positive polarity umbra was generally associated with WLF kernel but no HXR source. This is generally in contrast with the white-light flare of 28 October 2003, and also contradicts the suggested association of sign reversal anomaly with HXR sources. However, it may be noted that for a white-light flare of 30 September 2002, Chen and Ding (2006) found motions of the continuum similar to HXR sources.

4.6 Summary and Conclusions

From our study of multi-wavelength observations of NOAA 10486, we detected moving magnetic and velocity transients during the impulsive phases of both the white-light flares of 28 and 29 October 2003. Sign reversals were also detected by both GONG and MDI instruments during the impulsive phases of the flares of 28 and 29 October 2003.

In the case of the X17/4B flare of 28 October 2003, the two locations of magnetic transients differed in their basic characteristics. The location of sign reversal that occurred in strong magnetic field of the leading (negative) umbra was nearly stationary. Both HXR source and WLF kernel were associated with this feature. The other sign reversal location was observed in a weak field area near the neutral line moved rapidly toward the following (positive) polarity umbra. It was better associated with HXR as compared to the WLF kernels.

On the other hand, magnetic, Doppler transients and sign-reversal anomaly observed during the X10/2B flare on 29 October 2003 did not conform well with the HXR sources. Interestingly, we observed a strong HXR source (and WLF kernel) in weak field region without the corresponding sign reversal anomaly. Also, there was a WLF kernel but no HXR source associated with the magnetic transient observed in strong field location of the positive polarity umbra. This is in contrast with the HXR-magnetic anomaly relation observed for the white-light flare of 28 October 2003, and also in contradiction with the earlier suggestions of Qiu and Gary (2003).

The magnetic/Doppler transients generally followed the usual behavior of separation of flare kernels observed in two ribbon flares. The maximum separation attained for the flare kernels observed in successively lower layers of solar atmosphere showed a trend consistent with the classical flare model of an expanding loop structure with footpoints anchored in the lower atmosphere.

The HXR feature showed separation of $\approx$ 23 Mm, *i.e.*, nearly the same as the separation observed in chromospheric Hα. This is consistent with the formation of footpoint sources in the chromosphere or in the lower corona depending on the energy of particles. Magnetic and Doppler transients, on the other hand, showed a larger separation of $\approx$ 29 Mm which matched the separation obtained for the photospheric WLF kernels.

The flare kernels for the X17/4B flare separated faster in the lower atmosphere (the temperature minimum region and the photosphere) with velocity of 45-50 km s^{-1} as compared to that in the upper atmosphere, *i.e.*, 38 km s^{-1} at the chromosphere, and 29 km s^{-1} at the even higher transition region. However, these were found to be much smaller for the X10/2B flare of 29 October 2003.

Ding, Qiu and Wang (2002), using an atmospheric model, showed that spectral line inversion occurs near sunspot penumbral area if electron density rises significantly. It is to note that a rise in the electron density was found during the impulsive phase of the flare of 28 October 2003 (Klassen *et al.*, 2005), consistent with the RHESSI HXR observations. Therefore, occurrence of the moving transients appears to be related to the process associated with electron-beams and not due to the real changes in photospheric magnetic and Doppler fields. However, no clear conclusions are discernible in the case of the X10/2B flare of 29 October 2003. Also, away from these features, permanent changes in magnetic fluxes from the pre- to post-flare phases have been reported that do not seem to be affected by the WLF or HXR related effects (Ambastha, 2007b).

Finally, association characteristics of the moving magnetic transients (or magnetic anomaly) remain some what ambiguous as a clear and consistent correlation of these features with HXR sources (or WLF kernels) did not emerge from the two extremely complex white-light flares of NOAA 10486.

Chapter 5

Ring-Diagram Analysis and Inversion Techniques

5.1 Introduction

Ring diagram analysis is one of the most powerful tools of local helioseismology. It utilizes Doppler observations for long time series of small patches (typically $16^\circ \times 16^\circ$) centered near the disk center. Thus the ring diagram analysis is a generalization of global helioseismology over a small area as compared to the whole Sun. Basic idea of ring diagram technique is to study the characteristics of photospheric p-mode parameters, *e.g.*, mode amplitude, width, flow, *etc*, at the scale of an AR. Further, inversion of p-mode parameters obtained from ring analysis can be used to understand various physical parameters with depth in the sub-photospheric layers at the local scales.

The technique of ring diagram was first developed by Hill (1988) to infer the horizontal flows and thermodynamic structure underneath the solar photosphere. Using Doppler observations from NSO, they found flows of 100 m s^{-1} from the equator to the pole. From the analysis of four ARs, Hill (1989) found presence of large scale flows with longitudinal variations of about 20 m s^{-1}. Thereafter, several important inferences have been derived using this technique (Antia and Basu, 2007, and references therein). Another important tool of local helioseismology, the time-distance analysis, has also been used extensively to infer sub-photospheric flows of ARs (Duvall *et al.*, 1993b).

Although the ring diagram analysis gives much poorer spatial resolution than the time-distance analysis, it has several advantages over the time-distance helioseismology. Ring diagram analysis is based on the physics of normal modes, which are reasonably well understood, while the interpretation of time-distance analysis depends on the propagation of waves in a dispersive medium; the response functions and properties of which are still being worked out (*e.g.*, Birch *et al.*, 2001; Korzennik, 2001; Gizon and Birch, 2002; Jensen, Duvall and Jacobsen, 2003; Braun and Birch, 2008; Gizon *et al.*, 2009).

Considering the advantages and straightforward approach of the ring diagram technique, we have employed it for our study of photospheric, and sub-photospheric properties of ARs using suitable inversion techniques. In this chapter, we discuss briefly about the methods of ring diagram analysis and inversions. We present a comparison of results obtained using different methods along with estimates of systematic errors involved.

In Section 5.2, we discuss the data requirement. Section 5.3 describes the main steps used in data processing. Section 5.4 discusses the ring-fitting methods and their comparison. Section 5.5 describes the two main tools used in sub-photospheric velocity inversions and their comparison. Finally, Section 5.6 is devoted to the summary and conclusions.

5.2 The Observational Data

The primary data requirement of modern helioseismology are high-resolution uninterrupted, long time series of Doppler images of the Sun's photosphere. These are available from the ground-based GONG and space-borne MDI instruments (for detail please see Chapter 2). Small spatial scale data for carrying out the ring diagram analysis of an AR is extracted from the full disk Doppler images. Data with high spatial and temporal resolutions gives more spatial information of the photosphere as well as beneath it. In order to get high temporal resolution in the data required for the helioseismology, the GONG data obtained from six stations are merged using the method described by Toner *et al.* (2003) adopted for the GONG pipeline (Hill *et al.*, 2003).

5.3 Data Reduction and Power Spectra

The main steps of data processing for ring diagram technique are: *i*) extraction of data cube corresponding to the AR, *ii*) remapping and tracking of the data, *iii*) interpolation and apodization, and *iv*) filtering and three-dimensional Fourier transformation. A schematic diagram giving various steps involved in the technique are illustrated in Figure 5.1. Detailed descriptions are provided in the following sections.

5.3.1 The Data Cube

In order to estimate the p-mode parameters corresponding to a selected area over the Sun, we need to track this area temporally over long time. Such a spatial-temporal area is defined by an array (or data-cube) of dimension $N_x \times N_y \times N_t$, where, first two dimension (N_x, N_y) correspond to the spatial size of the AR along x and y axes, representing zonal and meridional directions, and the third (N_t) to the time t in minutes.

The data-cubes employed by ring diagram analysis have typical 1664 minutes' duration and cover $16^\circ \times 16^\circ$ area centered at the location of interest. This choice of area makes a compromise between the spatial resolution on the Sun, range of depths and resolution in spatial wavenumber of the power spectra. A larger size allows access to deeper sub-photospheric layers, but only with a coarser spatial resolution. On the other hand, a smaller size not only limits the access to the

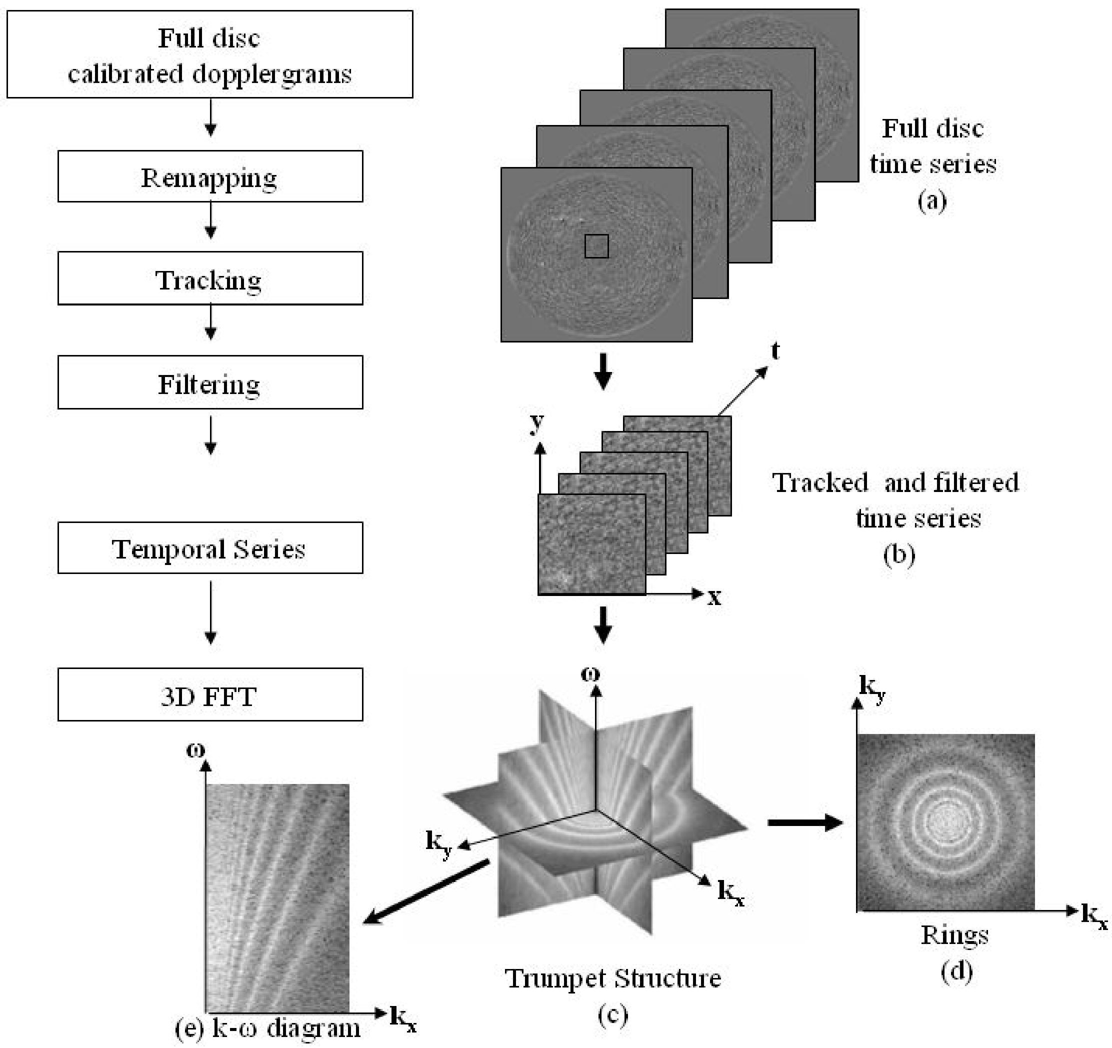

Figure 5.1 Ring diagram analysis data reduction steps: (a) Time series of full disk dopplergrams, (b) Remapped and tracked time series filtered for noise to resolve more modes, (c) Trumpet structure, showing the three-dimensional power spectra of the time series in "b", (d) Rings obtained after slicing the trumpet at a fixed frequency, and (e) Slice of the trumpet at a constant k_y giving the $k_x - \omega$ diagram.

deeper layers but also renders the fitting of rings more difficult. The time duration of 1664 min is the time required by the Sun to rotate about its axis by the spatial size of the patch, *i.e.*, 16°. An angular size of 16° near the disk center corresponds to 128 pixels along the x- and y-axes for both the GONG and MDI data.

5.3.2 Remapping and Tracking

The observational data are essentially the images of solar photosphere as projected onto the sky plane, therefore, the spatial size of a pixel depends on its position in the solar image. Pixels away from the disk center require larger corrections for foreshortening which increases towards the limb. Local helioseismology essentially deals with high degree acoustic waves that are assumed to be plane waves traveling across shallow regions of solar surface and follow great circles.

The three-dimensional Fourier transformation of the data requires equal sampling in temporal and spatial dimensions. Equal time interval is provided by constant image sampling rate Δt but in order to get equidistance in spatial directions, we need to remap them onto another grid. A remapping attempts to transform the spherical surface on a plane. Accurate sampling of surface is essential to provide a good precision in wavelength and direction of propagation of acoustic waves.

Several types of remapping methods, *viz.*, cylindrical, conic, azimuth, *etc.*, are used. The methods used for equidistance for GONG and MDI data are Transverse Cylindrical Equidistance (TCE) and Azimuth Equidistance (AE or Postel's) projections (Richardus and Adler, 1972), respectively. However, there is no accurate method available for remapping as they produce some distortion in the actual data. For small areas of $\sim$16°, GONG and MDI both use similar methods.

As already mentioned, ring diagram analysis utilizes small patches of size 16°×16° for 1664 minutes. Further, we know that the Sun rotates about its axis differentially (Scheiner, 1963), therefore, a given fixed area on the solar disk from the first to the last image of the data cube will involve different portions on the Sun.

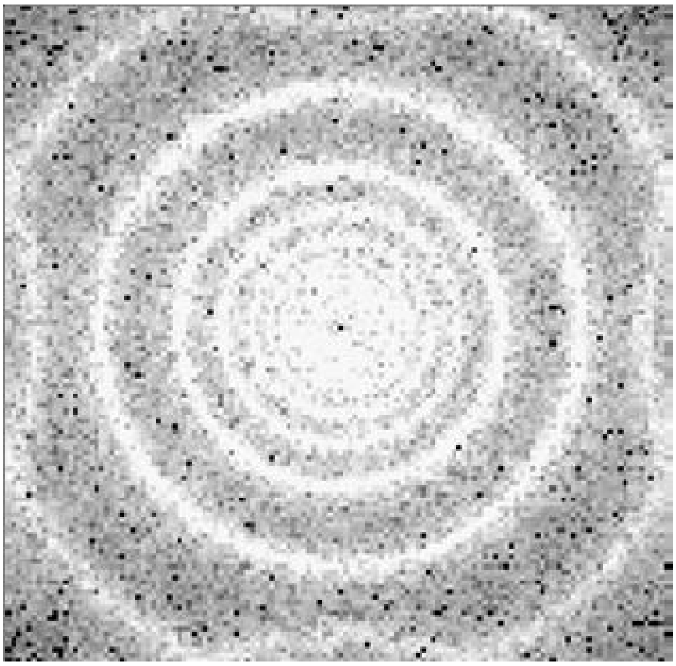

Figure 5.2 Truncation of rings near the edges due to aliasing of higher frequencies toward lower side.

To compensate for this undesired effect, full disk images are tracked with the speed of solar rotation (Snodgrass, 1984) before extracting data cube corresponding to the AR, which would otherwise hide small horizontal and vertical flows of interest.

5.3.3 Interpolation and Apodization

The spatial coordinates of points in the tracked images are not always integer. To apply three-dimensional Fourier transform on tracked data cube, we need to interpolate the coordinates of tracked images to integer values, for which we use sinc interpolation method.

The three-dimensional Fourier transformation of data cube produces truncation of rings near edges due to aliasing of higher frequencies toward lower side (see Figure 5.2). In order to avoid the truncation effects, we apodize the data cube in both the spatial and temporal dimensions. The spatial apodization is obtained by 2D cosine bell method which reduces the $16^\circ \times 16^\circ$ area to a circular patch of radius 15°. Apodization in temporal dimension is carried out by multitaper technique suggested by Fodor and Stark (1998).

5.3.4 Temporal Filtering and Three-Dimensional Power Spectra

Solar photospheric velocity observations include the effects not only of the p-mode oscillations, but also that of the solar rotation (2 km s^{-1}), convective motions (1 km s^{-1}), Earth's rotation (500 m s^{-1}), *etc.* These effects introduce low frequency fluctuations in the power spectrum. Therefore, before starting the three-dimensional Fourier transformation process, we need to filter out these low frequency fluctuations from the tracked images. To filter the time series, tracked images are detrended by subtracting the running mean over 21 neighboring images.

The observed photospheric velocity signal $v(x, y, t)$ in the data cube is a function of position (x, y) and time (t). Let the velocity signal in frequency domain be $f(k_x, k_y, \omega)$, where, k_{x} and k_{y} are spatial frequencies in x and y directions, respectively, and ω the angular frequency of oscillations. Then the data cube $v(x, y, t)$ can be written as,

$$v(x, y, t) = \int\int\int f(k_x, k_y, \omega) \exp[i(k_x x + k_y y + \omega t)]\, dk_x\, dk_y\, d\omega \tag{5.1}$$

The amplitude $f(k_x, k_y, \omega)$ of p-mode oscillations is calculated using the three-dimensional Fourier transformation of Equation 5.1. Hence the power spectrum is given by,

$$P(k_x, k_y, \omega) = |f(k_x, k_y, \omega)|^2 \tag{5.2}$$

The 16° patch consists of 128 pixels, giving a spatial resolution Δx =1.5184 Mm, *i.e.*, the k-number resolution, $\Delta k = 3.2328 \times 10^{-2}$ Mm^{-1}, and a Nyquist value for the harmonic degree, $\ell = 1440$. The corresponding range in k_{x}-k_{y} space is -2.069 to 2.069 Mm^{-1}. The temporal cadence and duration of data-sets give Nyquist

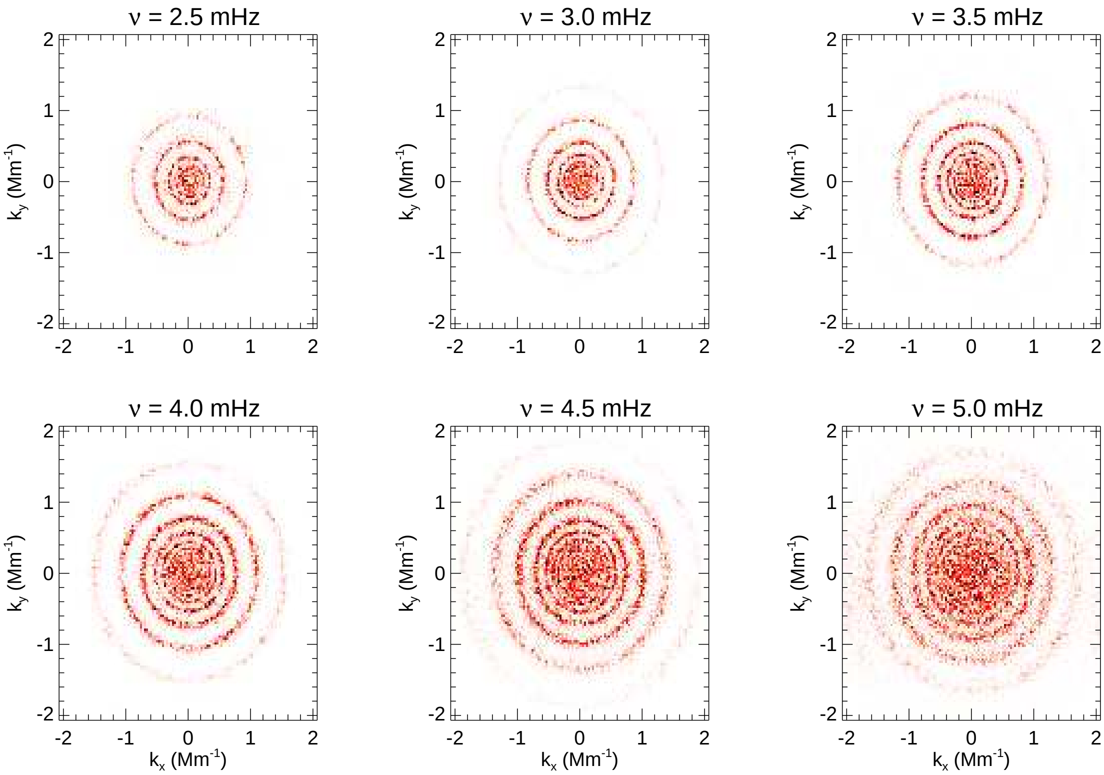

Figure 5.3 Two-dimensional power spectra of Doppler observations as function of k_{y} and k_{y} at different frequencies. The spectrum was computed from a time series of 1 March 2001 consisting of 1664 minutes' long image sequence, centered at the Carrington longitude 165° and latitude +15°.

frequency of 8333 μHz and frequency resolution of 10 μHz, respectively.

A sample data cube of 1 March 2001 obtained from MDI, centered at the Carrington longitude 165° and latitude +15°, is shown in Figure 5.1(c). The three-dimensional power spectrum $P(k_x, k_y, \omega)$ of the data shows a trumpet like structure. For a fixed value of ω, the cross-section of the trumpet yields ring like structures (Figure 5.1d), where concentric rings correspond to p-modes of different radial order, n. The outer most ring corresponds to $n = 0$ (fundamental or f-mode), the next inner ring for $n = 1$, and so on. A sample of rings obtained by slicing the trumpet at different frequencies are shown in Figure 5.3. The ridges are seen to broaden with increasing k, due to a decrease in the lifetime of modes (Hill, 1988). A slice along k_{x} (or k_{y}) renders tilted parabolae providing the k_{x} (or k_{y}) –

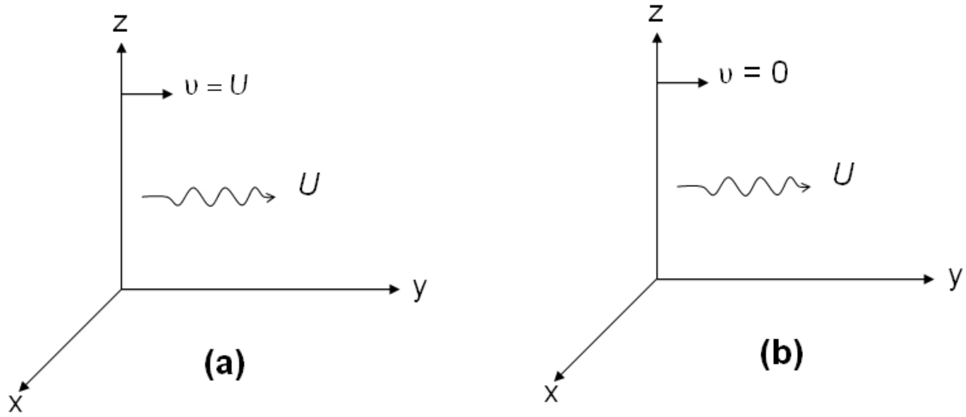

Figure 5.4 Schematic diagram showing a wave propagating in the presence/absence of a mean flow field, where υ and U are absolute velocities of the frame and the fluid, respectively. (a) The frame is moving with fluid, *i.e.*, $\upsilon = U$. (b) The frame is stationary, *i.e.*, $\upsilon = 0$.

ω diagrams (Figure 5.1e).

In order to understand the concepts of ring and trumpet analysis, let us consider the propagation of a wave in the presence of mean flow field, as shown in Figure 5.4a. The phase speed of a wave, seen in the frame (a) moving with the fluid is, $\upsilon_{\phi 0} = \omega/k$, so that the frequency ω is given by

$$\omega = k\,\upsilon_{\phi 0},$$

where, k is magnitude of the wavenumber. From the point of view of a fixed observer (see Figure 5.4b), the phase velocity, υ_ϕ, is augmented by the flow velocity $\mathbf{U}$, *i.e.*, $\upsilon_\phi = \upsilon_{\phi\mathbf{0}} + \mathbf{U}$. Then the observed frequency is

$$\omega' = \mathbf{k} \cdot \upsilon_\phi = \mathbf{k} \cdot (\upsilon_{\phi\mathbf{0}} + \mathbf{U}).$$

Thus the observed frequency of a wave is perturbed by an amount

$$\Delta\omega = \mathbf{k} \cdot \mathbf{U} = k_x U_x + k_y U_y \tag{5.3}$$

where, U_x and U_y are x and y components of velocity $\mathbf{U}$, which represent equatorial or zonal and meridional velocities, respectively.

In the ring diagram analysis, sound waves do not know anything about their horizontal direction of propagation, so the resonant frequencies are independent of the azimuthal angle, $\arctan(k_y/k_x)$. Thus one could obtain the three-dimensional version of Figure 5.1(c) simply by rotating Figure 5.1(e) about the frequency axis (ω). One would then find significant power not along one-dimensional ridges in $k-\omega$ space, but rather along the two-dimensional surfaces in k_x - k_y - ω space. These surface are the trumpets of the ring analysis.

The rings provide information on the characteristic properties of p-modes. Displacements of rings are caused by horizontal flows, while alterations of ring diameters are produced by sound speed perturbations (Hill, 1988). The photospheric p-mode parameters can be derived from these perturbations using appropriate ring fitting techniques.

5.4 Ring-Diagram Fitting

From Figure 5.3, we can see that power corresponding to a given radial order, n, is not concentrated along the rings but is rather distributed over a finite width. The width of rings increases with k from center outwards, which indicates that the modes with higher radial order have shorter lifetime. Similarly, other properties of modes corresponding to different radial order can be obtained by fitting the rings using methods proposed earlier by several researchers (Hill, 1988; Patron *et al.*, 1995, 1997; Basu, Antia and Tripathy, 1999; Basu and Antia, 1999; Haber *et al.*, 2000, 2002). In our study, we fit the three-dimensional power spectra using two main ring-fitting techniques: *i)* Asymmetric Peak Profile (APP) fitting (Basu and Antia, 1999) and *ii)* Dense-Pack (DP) ring fitting (Haber *et al.*, 2002) adopted to the GONG project. These procedures are described in the following.

5.4.1 Asymmetric Peak Profile (APP) Fitting

The solar oscillation power spectra are not symmetric (Duvall *et al.*, 1993a; Nigam and Kosovichev, 1998; Toutain *et al.*, 1998). Therefore, Basu and Antia (1999) proposed an asymmetric peak profile fitting to three-dimensional power spectra. Accordingly, the function to fit the power spectra is given by,

$$P(k_x, k_y, \nu) = \frac{\exp[A_0 + A_1(k - k_0) + A_2(\frac{k_x}{k})^2 + A_3\frac{k_x k_y}{k^2}]S_x}{(1+x)^2} + \frac{e^{B_1}}{k^3} + \frac{e^{B_2}}{k^4} \tag{5.4}$$

where,

$$x = \frac{\nu - ck^p - U_x k_x - U_y k_y}{\Gamma_0 + \Gamma_1(k - k_0)},\ S_x = S^2 + (1 + Sx)^2,\ k^2 = k_x^2 + k_y^2$$

The thirteen parameters A_0, A_1, A_2, A_3, c, p, U_{x}, U_{y}, Γ_0, Γ_1, S, B_1 and B_2 in Equation 5.4 are determined by fitting the spectra using maximum likelihood method (Anderson, Duvall and Jefferies, 1990). Here S is the asymmetry parameter which controls the asymmetry in power. A positive value of S indicates that asymmetry is positive and more power is concentrated on the higher frequency side (Basu and Antia, 1999). For $S = 0$, the Equation 5.4 fits a symmetric Lorentzian profile. Further, k_0 is the central value of k in the fitting interval, p and c are constants, Γ_0 is the mean half width while Γ_1 represent the variation in Γ_0 with k in fitting interval, $\exp(A_0)$ is the mean peak power in the ring while A_1 is the variation in power with k in fitting interval, A_2 and A_3 represent variations in power along the ring, B_1 and B_2 are background powers.

We have applied this fitting technique to the power spectra obtained for the time series of GONG dopplergrams for 27 October 2003 centered at the Carrington longitude 285° and latitude -22.5°. We fitted 800 modes covering $0 \leq n \leq 6$, $200 \leq \ell \leq 1000$ and $1800 \leq \nu \leq 5000\,\mu$Hz for each spectrum. Some of the ring fitted parameters for radial order $n = 0, \ldots, 5$ are shown in Figures 5.5 – 5.6.

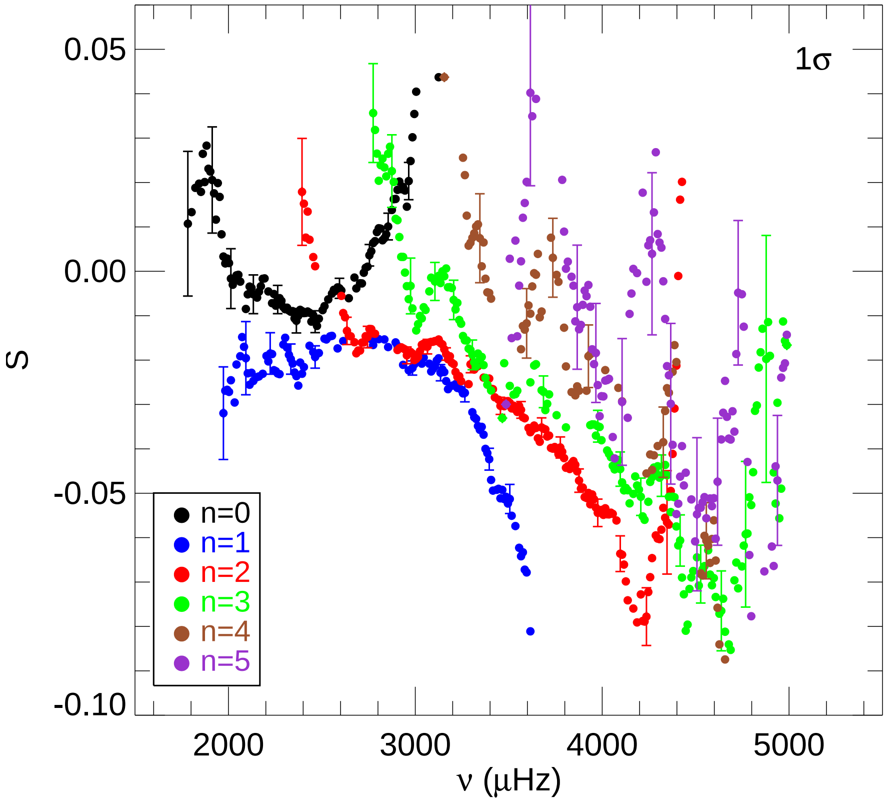

Figure 5.5 Asymmetry parameter (S) obtained from APP fitting for radial order n=0, ..., 5. For clarity, error bars with 1σ are shown only at some points.

Figure 5.5 shows that the asymmetry parameter (S) is mostly negative for all radial orders, n, *i.e.*, most of the power is in the lower frequency side of the peak. This is similar to earlier results obtained for low degree power spectrum (Duvall *et al.*, 1993a; Toutain *et al.*, 1998). The mode amplitude A is larger for higher radial order (Figure 5.6a). However, at a fixed n, it initially increases with frequency then decreases rapidly. The mode width (Γ_0) for a given radial order (n) initially decreases with frequency (ν) and then increases after a certain frequency (Figure 5.6b). Fitted values of surface velocities, $U_{\rm x}$ and $U_{\rm y}$, are shown in Figure 5.6(c)–(d). These provide average flow velocity over the region covered by the power spectrum and the depth range where the corresponding modes are trapped.

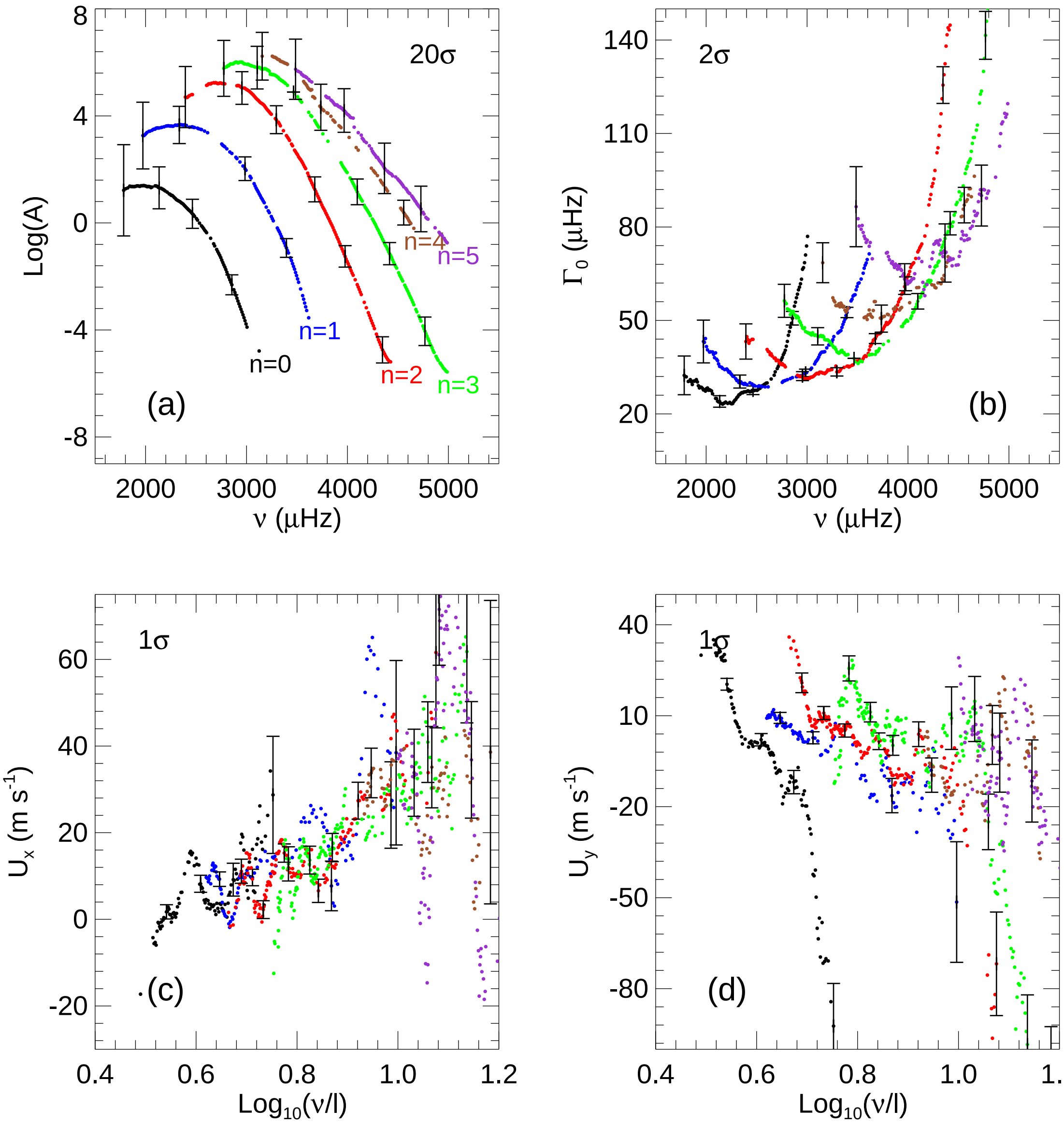

Figure 5.6 Various p-mode parameters obtained from APP fitting of the power spectra of the time series of Doppler data for 27 October 2003 centered at the Carrington longitude 285° and latitude -22°.5. The modes corresponding to different radial order n are shown in different colors. For clarity, error bars with 1σ are shown only at some points.

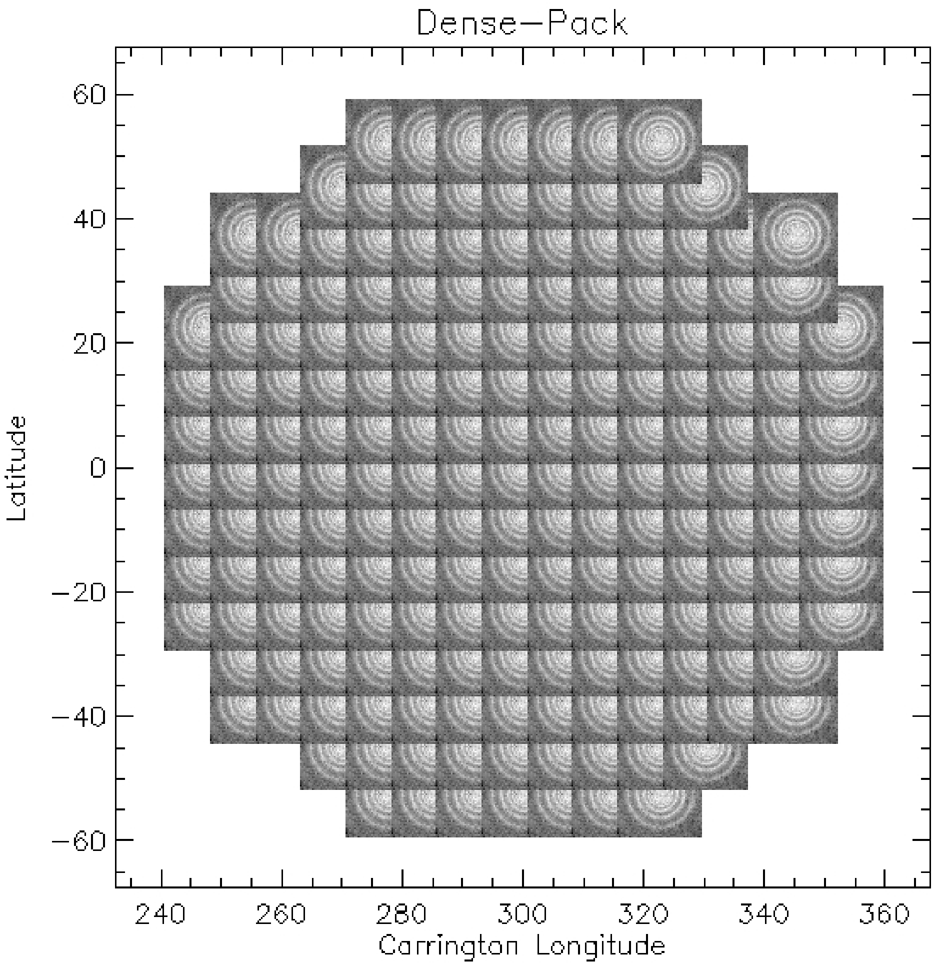

Figure 5.7 Dense-pack ring diagram maps which cover much of the solar disk with centers separated by 7.5°.

5.4.2 Dense-Pack (DP) Fitting

To perform ring diagram analyses at many sites on the solar disk, Haber *et al.* (2002) mapped the flows over much of the solar photosphere. They conducted 189 separate ring diagram analyses filling the solar disk out to 60° from disk center with overlapping analysis regions (Figure 5.7). Each region is 16° (apodized to 15° diameter disks) with their centers separated by 7.5° in latitude and longitude. This arrangement of analysis regions, or tiles, is called a "dense-pack" and allows the horizontal flow to be mapped over a substantial fraction of the solar disk. They fitted the three-dimensional power spectrum using Lorentzian function, given by

$$P(k_x, k_y, \omega) = \frac{A}{(\omega - \omega_0 + k_x U_x + k_y U_y)^2 + \Gamma^2} + \frac{b_0}{k^3} \tag{5.5}$$

Six fit parameters, *viz.*, zonal velocity (U_{x}), meridional velocity (U_{y}), background power (b_0), mode's central frequency (ω_0), mode width (Γ) and amplitude (A) are determined by fitting the spectra using the maximum likelihood approach given by Anderson, Duvall and Jefferies (1990).

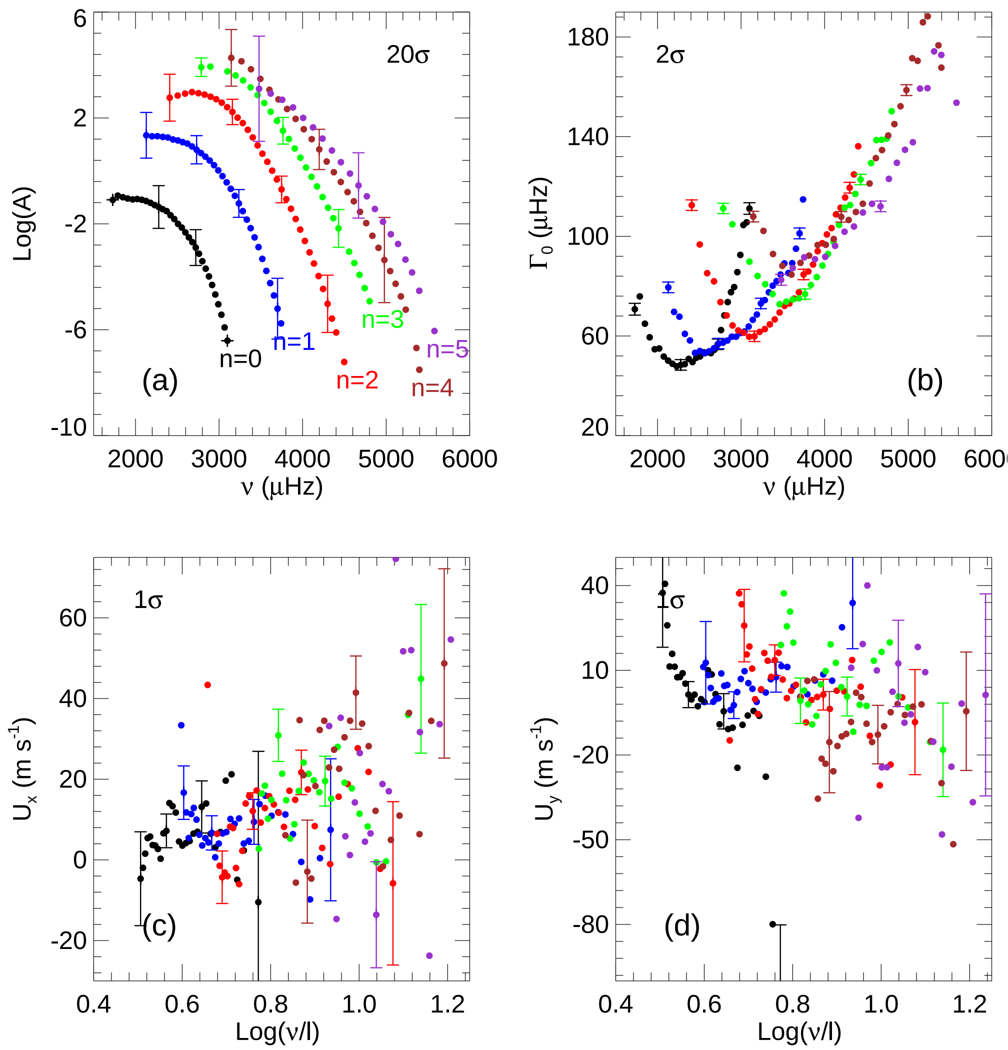

Figure 5.8 Various p-mode parameters obtained from the DP fitting of the same power spectra used in APP fitting (*cf.* Figure 5.6). For clarity, error bars with 1σ are shown only at some points.

Figure 5.9 The $\ell - \nu$ diagram. Blue (red) symbol correspond to the p-mode parameters obtained from the APP(DP) fitting.

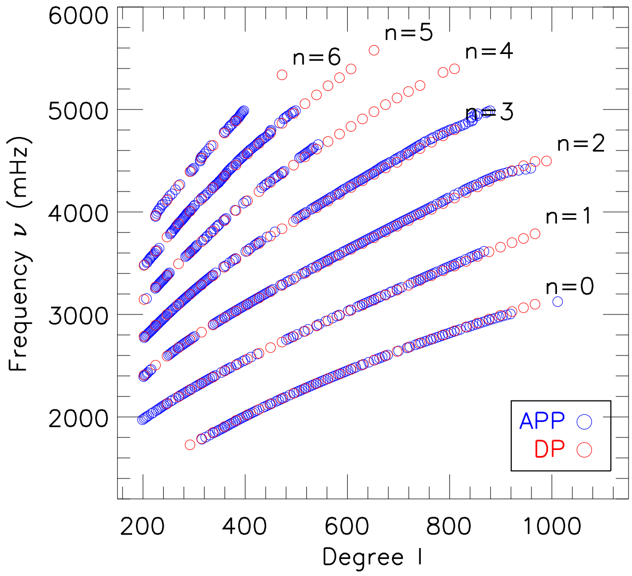

We have applied this fitting to the three-dimensional power spectra which has been used in the APP fitting (Figure 5.6). Some of the ring fitted parameters are shown in Figure 5.8. It is seen that the mode parameters obtained from DP fitting (Figure 5.8) show similar trend as the modes obtained from APP fittings (Figure 5.6). In the following, we describe their comparison in detail.

5.4.3 Comparison of APP and DP Fittings

Ring diagram analysis has been used extensively to find the characteristic of photospheric p-modes and sub-photospheric properties of ARs. Various techniques give similar results, however, a comparison of p-mode parameters obtained from two different ring-fitting techniques generally show systematic errors. The APP and DP methods are two different approaches to determine the properties of photospheric acoustic mode parameters. The APP method assumes asymmetry in power spectra and 13 parameters are used in the fitting. On the other hand DP method fits the spectra for Lorentzian profile with only 6 parameters. The number of modes obtained from APP fitting are found to be 4 times larger than the modes obtained from DP fitting. Hence APP method is computationally more excessive

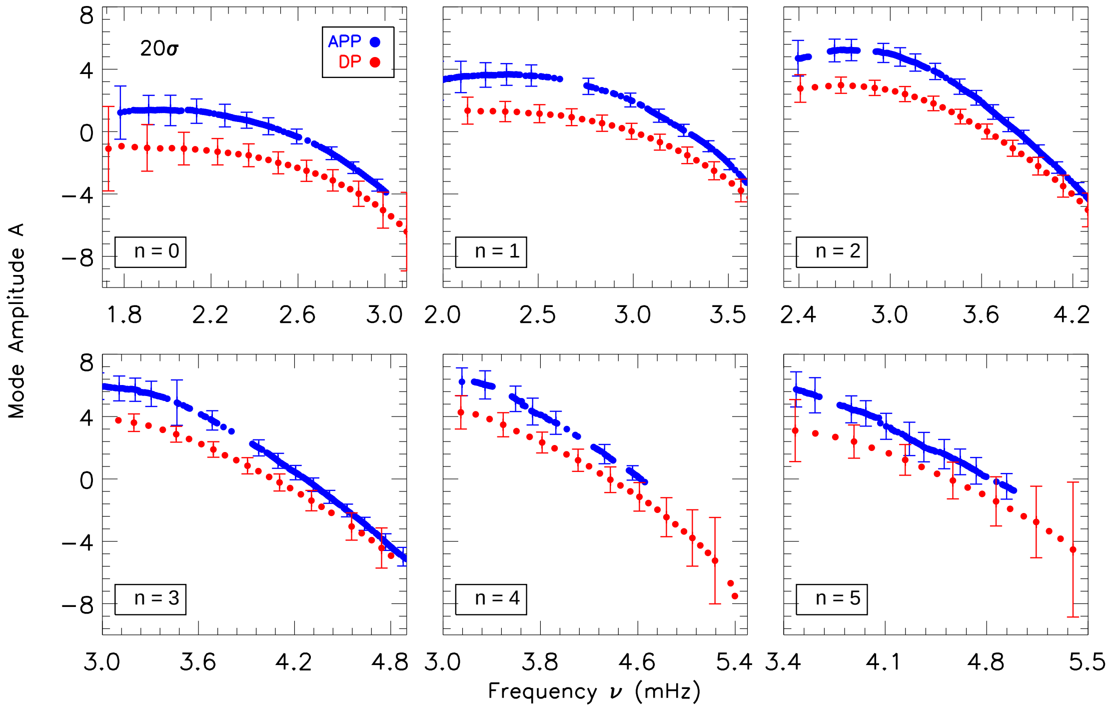

Figure 5.10 The p-mode amplitudes for different n. Blue (red) symbols correspond to the p-mode parameters obtained from the APP (DP) fitting.

compared to DP. However, larger number of modes gives higher signal to noise ratio in inverting the sub-photospheric velocities of ARs. The precision of both methods is equivalent since the errors are of the same order for both methods.

A comparison of p-mode parameters obtained from APP and DP fitting methods are shown in Figures 5.9 – 5.14. Figure 5.9 shows the $\ell - \nu$ diagram, where ridges for radial orders $n = 0, \ldots, 6$ arise due to the dispersion relation of acoustic waves in the solar interior. Blue (red) symbols correspond to the p-mode parameters obtained from the APP (DP) fitting. In this $\ell - \nu$ diagram, any frequency differences are not noticeable as they are too small to show up in the scale used.

Amplitude and Width of p-modes

Mode amplitude A and width Γ for radial orders $n = 0, \ldots, 5$ obtained from APP and DP fittings are shown in Figures 5.10 – 5.11. Values of A obtained from APP method are slightly larger than those obtained from DP method while Γ

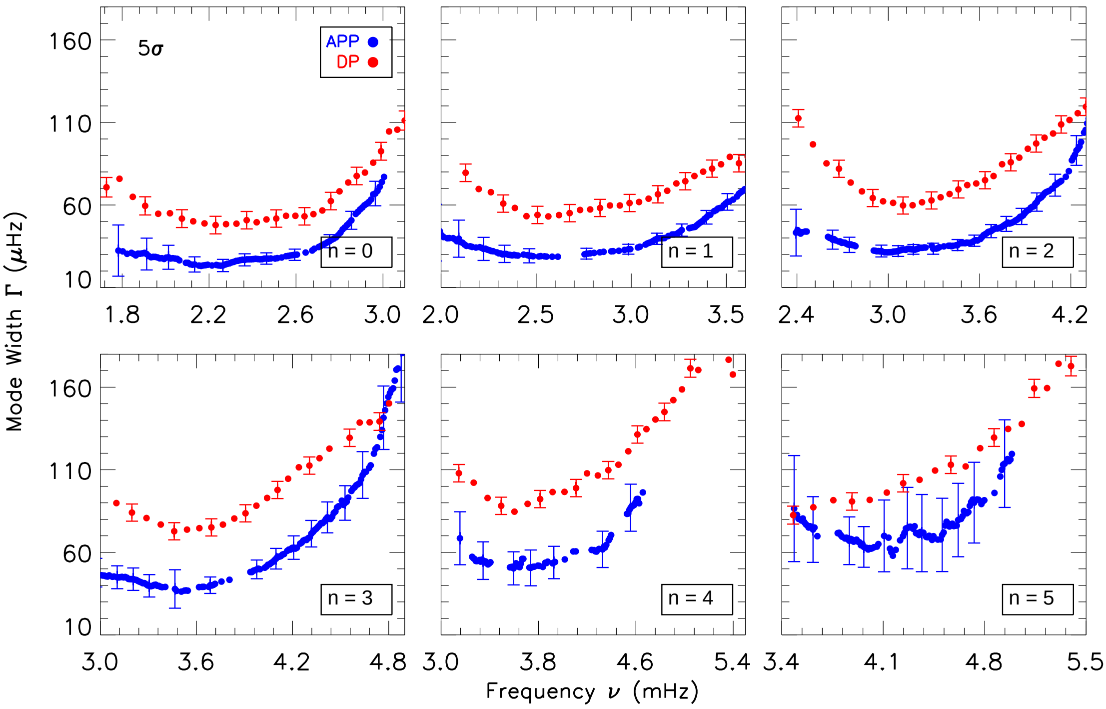

Figure 5.11 Mode widths. Blue (red) symbols correspond to the p-mode parameters obtained from the APP (DP) fitting.

shows a reverse trend at all frequencies and radial orders. The two trends would be expected to be opposite as the total power ($\approx\ A \times \Gamma$) in a mode may be more robust. Amplitude and width can also be affected because of the choice of background. This issue is not well understood and is expected to depend on the region used for fitting of each "mode".

The p-mode Frequency Shift and Flows

Frequency shift $\delta\nu$ and flow parameters U_{x} and U_{y} for radial order $n = 0, \ldots, 5$ obtained from APP and DP methods are shown in Figures 5.12 – 5.14, where mode parameters obtained from APP (DP) method are plotted in blue (red). It can be noted that although U_{x} and U_{y} obtained from the two methods match very well, frequency shifts $\delta\nu$ are different at all frequencies and radial orders. According to Equation 5.3, if parameters U_{x} and U_{y} match with each other, frequency shifts should also match. The problem may be related to the shift induced by the asym-

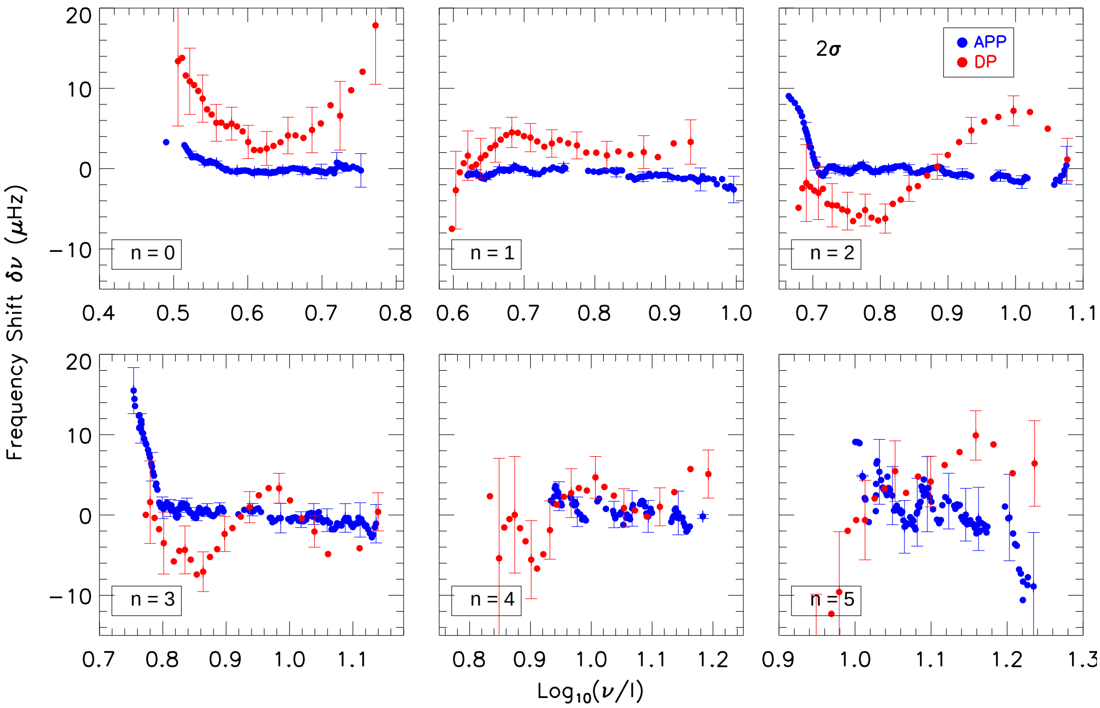

Figure 5.12 Frequency shifts $\delta\nu$. Blue (red) symbols correspond to the p-mode parameters obtained from the APP (DP) fitting.

metry parameter S in APP fitting, which does not appear to affect the velocities (Basu and Antia, 1999).

5.5 Sub-Photospheric Velocity Inversion

The high degree p-modes of different wavelengths are trapped at different depths near the photosphere where they interact with the medium and bear the characteristic properties of the solar interior. Therefore, mode parameters obtained from ring-fittings can be used to determine the near sub-photospheric velocities of ARs.

Velocity parameters U_{ix} and U_{iy}, obtained from ring-fittings, represent weighted average over depths of the components of horizontal flow (u_{x}, u_{y}) fields below the photosphere. Therefore, sub-photospheric velocity components u_{x} and

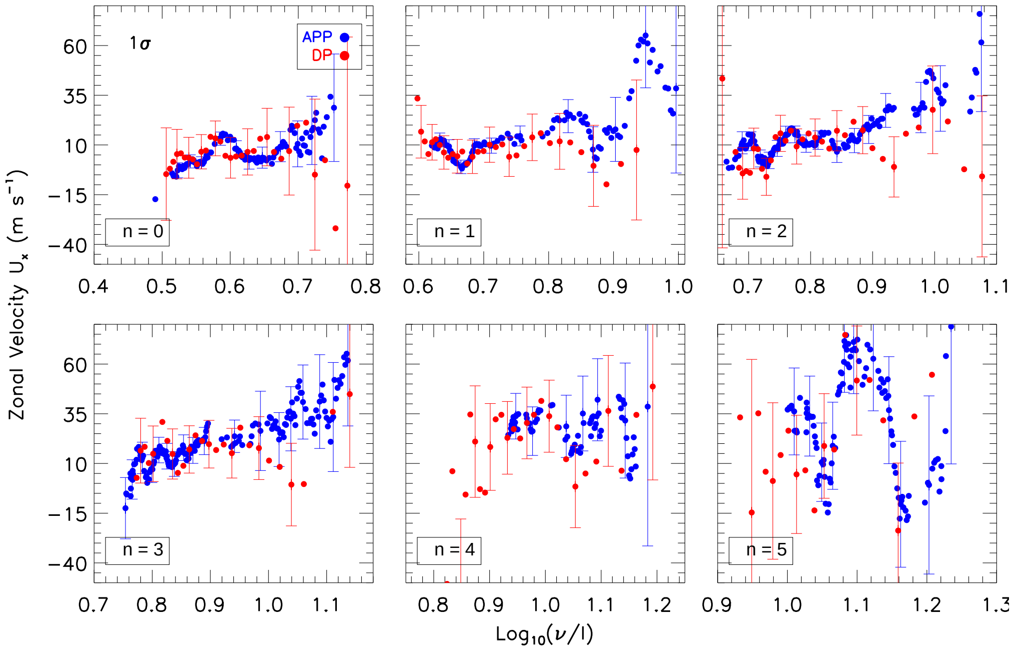

Figure 5.13 Zonal velocities U_x. Blue (red) symbols correspond to the p-mode parameters obtained from the APP (DP) fitting.

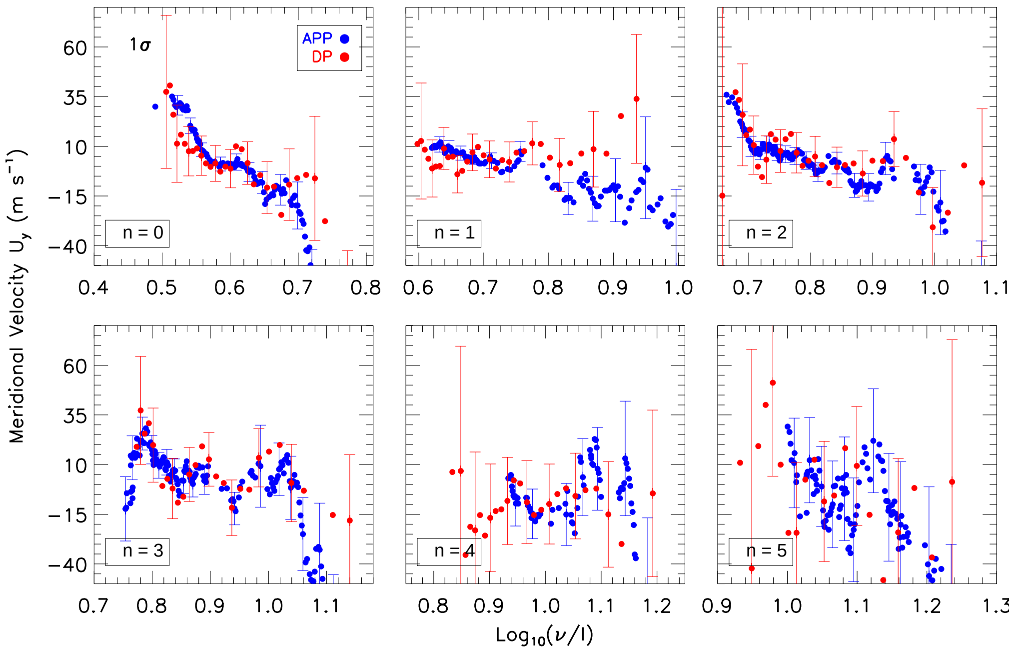

Figure 5.14 Meridional velocities U_y. Blue (red) symbols correspond to the p-mode parameters derived from the APP (DP) fitting.

u_y can be written as,

$$U_i = \int K_i(z) u(z)\, \mathrm{d}z + \varepsilon_i \tag{5.6}$$

where, $i \,\epsilon\, M \equiv (n, l)$ is the set of observed modes. $K_i(z)$ are inversion kernels at the radius $z = r/R_\odot$ which can be calculated using a solar model, and ε_i represent errors in the fitted velocity U_i. Here, for convenience we have dropped the subscripts x (zonal) and y (meridional) for flows at the photosphere and underneath.

The Equation 5.6 is a Fredholm inverse problem of first kind. The corresponding forward problem where $u(z)$ is known can be easily solved to calculate U_i and is generally well conditioned. But the inverse problem of determining $u(z)$ from U_i is generally ill-conditioned. It is clear that using only a finite number of measured quantities U_i, it is not possible to determine the continuous function $u(z)$ uniquely. However, using a finite number of measurements of any quantity at different times, we can try to estimate the values at some other time using interpolation or approximation. The basic assumption in all this is that the required function is sufficiently smooth to be approximated. Similarly, if we assume that the function $u(z)$ in the inverse problem is smooth in some sense, it may be possible to calculate $u(z)$ from the known U_i. Nevertheless, because of smoothing due to integration the problem is ill-conditioned and very high accuracy in U_i will be required to get any reasonable solution.

There are several inversion techniques available to solve such equations, *viz.*, *i)* asymptotic inversion (AI) using spline fitting (Gough, 1984) which is applicable only to lower order p-modes and has been developed for the rotational splitting of the frequencies, *ii)* regularized least-squares (RLS, Gough, 1985; Jeffrey, 1988), *iii)* spectral expansions and annihilator which is used by Backus and Gilbert (1967) for geoseismic inversion and later by Gough (1985) for solar data, *iv)* Optimally Localized Averaging (OLA) developed by Backus and Gilbert (1968, 1970) for geoseismic inversion later used for solar data by Gough (1985) and Brown *et al.*

(1989), *v)* Linearized Asymptotic Inversion (LAI, Gough and Kosovichev, 1993), *vi)* Subtractive Optimally Localized Average (SOLA, Pijpers and Thompson, 1992, 1994) which is a faster formulation of OLA, and *vii)* Non-asymptotic inversion (Antia and Basu, 1994; Antia, 1996). A detailed discussion on methods (i) – (iv) and their comparison is presented by Christensen-Dalsgaard, Schou and Thompson (1990).

From these, SOLA and RLS are two common methods adopted for sub-photospheric inversion of sound speed, flow, *etc.* Initially, these methods were developed for the inversion of internal angular velocity of the Sun. Later, these were also applied for the inversion of sub-photospheric velocities. The two methods are essentially complimentary in nature, therefore, one can be more confident if SOLA and RLS results are in good agreement. For the study of sub-photospheric velocities of ARs, we have used our codes developed on the basis of these two inversion methods. Their procedures are outlined in the following sections.

5.5.1 SOLA Inversion

The SOLA inversion technique attempts to produce a linear combination of data such that the resulting averaging kernel is localized while simultaneously controlling the error estimates. The average velocity u at $z = z_0$ can be written as

$$u(z_0) = \sum_{i \in M} c_i(z_0) U_i \tag{5.7}$$

where, c_i are inversion coefficients to be determined. Using Equation 5.6, we have

$$u(z_0) = \int \bar{K}(z_0, z) U_i(z)\, \mathrm{d}z + \sum_{i \in M} c_i(z_0) \varepsilon_i \tag{5.8}$$

where, the averaging kernel

$$\bar{K}(z_0, z) \equiv \sum_{i \in M} c_i(z_0) K_i(z) \tag{5.9}$$

is presumed to be a function of depth z and the inversion coefficients $c_i(z_0)$ for different modes at $z = z_0$. The coefficients $c_i(z_0)$ are selected such that the resulting averaging kernel is localized around the depth $z = z_0$ and at the same time the error is controlled in the estimated velocity $u(z_0)$,

$$\sigma^2(z_0, u) = \sum_{i \in M} c_i^2(z_0)\sigma^2(U_i). \tag{5.10}$$

The first term on the right hand side of Equation 5.8 represents the $\bar{K}(z_0, z)$ weighted average of U_i over the solar interior and the other term gives error in the inverted velocity $u(z_0)$. The main purpose of this method is to make the averaging kernels resemble to a target form $T(z_0, z)$ and at the same time moderating the effect of data errors by minimizing the function

$$\int [\bar{K}(z_0, z) - T(z_0, z)]^2 \, \mathrm{d}z + \mu \sum_{i,j \in M} E_{ij} c_i c_j \tag{5.11}$$

under the constraint

$$\int \bar{K}(z_0, z) \, \mathrm{d}z = 1. \tag{5.12}$$

Here E is the variance-covariance matrix of errors in U_i. If errors in the data are assumed to be uniform and correlated then $E_{ij} = \sigma_i^2 \delta_{ij}$. The target function T is given by

$$T(z, z_0) = \frac{1}{f} \exp\left[- \left(\frac{z - z_0}{\Delta} \right)^2 \right] \tag{5.13}$$

where, f is a normalization factor to make the total integral of T equal to unity. This function approaches a delta function for small Δ. The parameter μ, used in Equation 5.11, is given by

$$\mu = \mu_0 \left(\sum_{i \in M} \frac{E_{ij}}{\mathtt{M}} \right)^{-1} \tag{5.14}$$

where, $\mathtt{M}$ is the total number of modes in mode set M and μ_0 is a kind of trade-off parameter whose value may be chosen to determine the relative desirability of making the first and second terms in Equation 5.11 small. The inversion coefficients c_{ij} are obtained by solving the matrix equation

$$A\,c(z_0) = v(z_0) \tag{5.15}$$

where, the symmetric matrix A of order $\mathtt{M}+1$ has elements

$$\mathrm{A}_{ij} = \begin{cases} \int K_i K_j \,\mathrm{d}z + \mu E_{ij} & (i,j) \le \mathtt{M} \\ \int K_i \,\mathrm{d}z & (i \le \mathtt{M}, j = \mathtt{M}+1) \\ \int K_j \,\mathrm{d}z & (j \le \mathtt{M}, i = \mathtt{M}+1) \\ 0 & (i = j = \mathtt{M}+1) \end{cases} \tag{5.16}$$

and vectors c and v are given by

$$c = [c_i]\,,\; v = \left[\int K_i T dz\right],\;\; i = 1, \cdots, \mathtt{M}+1 \tag{5.17}$$

The constraint (5.12) has been incorporated with Lagrange multiplier 2λ which gives $(\mathtt{M}+1)^{th}$ elements of vector c and v to λ and 1, respectively.

Equation 5.15 is a system of $\mathtt{M}$+1 linear equations with $\mathtt{M}$+1 unknown coefficients. We solve these equations using singular value decomposition described in Antia (2002).

Test of SOLA Inversion

To test our code of SOLA inversion, we generated artificial data using the forward method (see Equation 5.6). Here, we have assumed that the sub-photospheric velocity u is a sine function of z, given by

$$u(z) = 120.0 + 100\,\sin(250\,z) \tag{5.18}$$

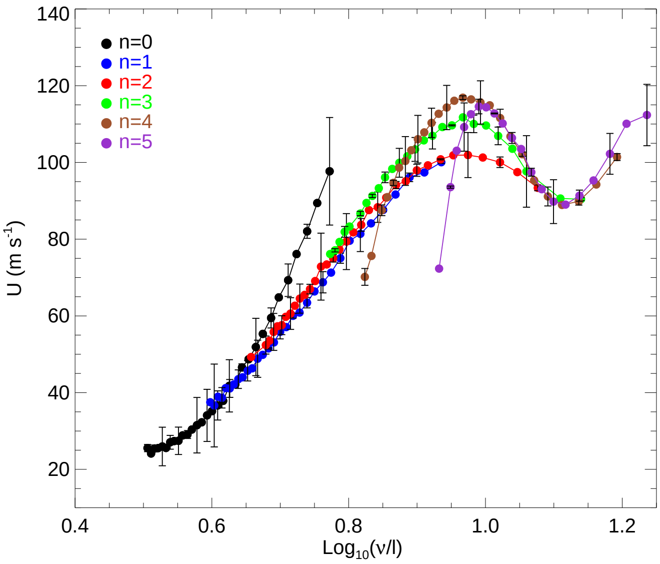

Figure 5.15 Velocities of the photospheric flow obtained using a forward technique. Velocities corresponding to different modes were calculated using the Equation 5.6 and 5.18.

The velocities U_i for modes $n = 0, \ldots, 6$ are calculated using Equations 5.6 and 5.18. In order to simulate the real data, we have added random noise with zero mean and one variance in U_i. Thus, calculated mode parameter U_i corresponding to modes $n = 0, \ldots, 5$ are shown in Figure 5.15. We invert U_i using the SOLA inversion to get back the velocities u at corresponding radius z.

In order to get an accurate value of u at $z_0 = 0.98\, R_\odot$, we calculate averaging kernels at the same z_0 for different values of inversion parameters μ_0 and Δ. A sample of some averaging kernels obtained from SOLA inversion are shown in Figure 5.16. The inversion parameter μ_0 increases from the top to bottom while the parameter Δ increases from the left to right. It is clear from Figure 5.16 that the shape of averaging kernel does not vary much with the parameter μ_0 while it varies largely with the parameter Δ. However, to visualize the localization of every averaging kernel is difficult. Therefore, we define a parameter χ to estimate the nonlocal nature of the averaging kernel by

$$\chi = \int [\bar{K}(z, z_0) - T(z, z_0)]^2 \, \mathrm{d}z \tag{5.19}$$

For well localized averaging kernel the value of χ is small (< 1.0).

Figure 5.16 shows that the value of χ increases with μ_0, *i.e.*, nonlocal behavior

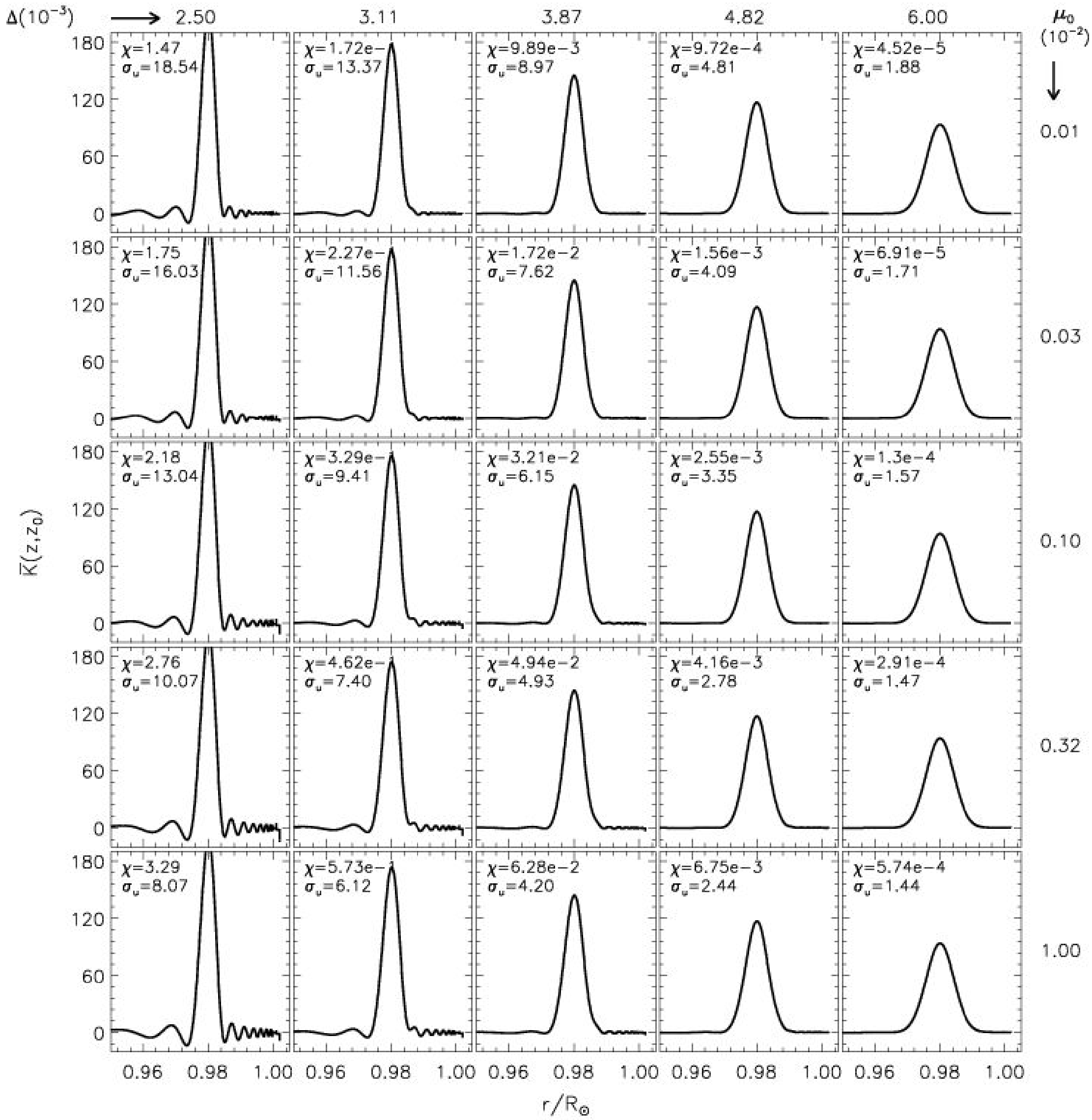

Figure 5.16 SOLA averaging kernels at a target radius $z_0 = 0.98R_\odot$ for different inversion parameters μ_0 and Δ. The values of μ_0 (Δ) increase from the top (left) to bottom (right). χ and σ_u represent the localization of the averaging kernel and error in the inverted velocity, respectively.

Figure 5.17 A trade-off diagram between the error $\sigma(u, z_0)$ and width Δ_{qu} of averaging kernels to obtain the sub-photospheric velocity at target radius $z_0 = 0.98\,R_\odot$. Inversion parameters corresponding to the arrow marked at the trade-off diagram are: $\mu_0 = 2.14 \times 10^{-3}$, $\Delta = 4.69 \times 10^{-3}$.

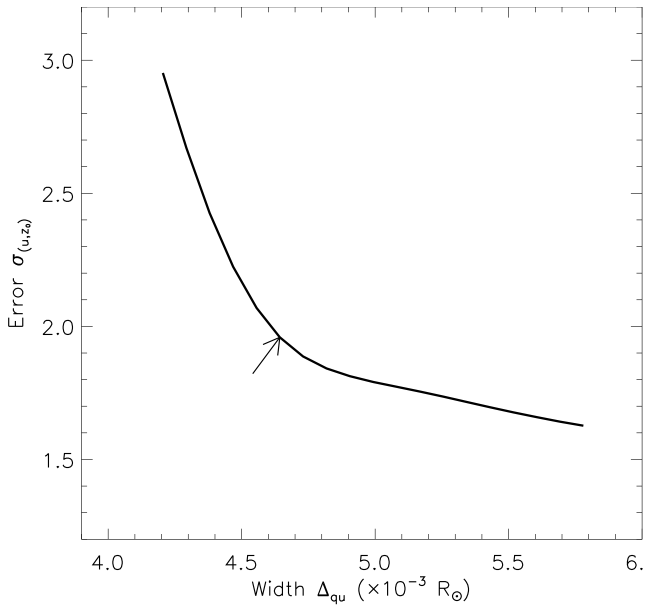

of averaging kernel around the target radius increases with μ_0. The error σ_u in the inverted velocity decreases with increasing μ_0. For a very small value of Δ, the averaging kernel shows oscillatory pattern due to Gibbs phenomenon similar to Fourier series, around the target radius z_0, and hence large value of χ. For a very large value of Δ, the averaging kernel shows large width while choosing the averaging kernel of thinner width renders larger error in u. Thus, the width of the averaging kernel is a measure of depth resolution and simultaneously, it controls the error propagating in the inverted velocity u. Therefore, values of μ_0 and Δ must be chosen such that the averaging kernel localize around the target depth and simultaneously control the estimated error in u. A suitable trade-off diagram between error σ_u and kernel width Δ_{qu}, distance between quartile points, will help in deciding the appropriate values of inversion parameter μ_0 and Δ.

The trade-off diagram for a target radius $z_0 = 0.98R_\odot$ is shown in Figure 5.17. Appropriate values of inversion parameters estimated from the trade-off diagram, corresponding to the arrow marked location, are $\mu_0 = 2.14 \times 10^{-3}$ and $\Delta = 4.69 \times 10^{-3}$.

We calculated velocities u with depth using the above criteria of choosing

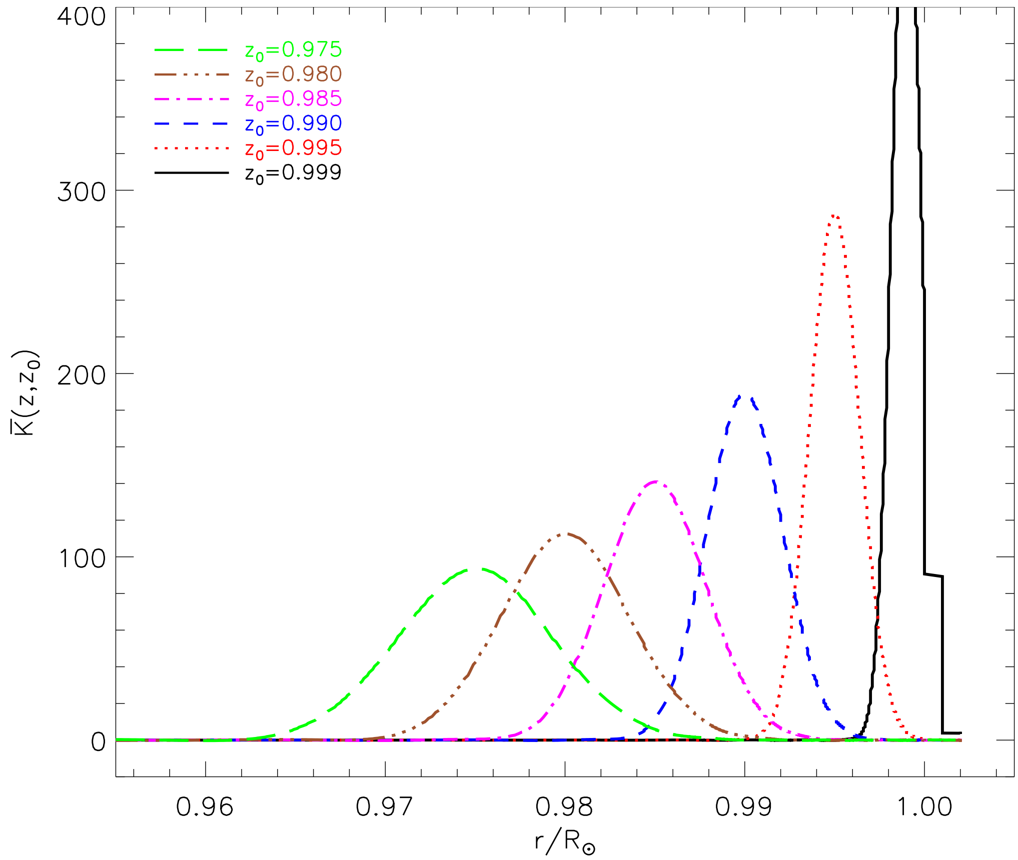

Figure 5.18 SOLA averaging kernels for different depths.

inversion parameters from the trade-off diagram. A set of some averaging kernels for different target radii are shown in Figure 5.18. The width of averaging kernel increases with depth, hence uncertainty increases for target radius at larger depths.

The velocities u at various depths obtained from Equation 5.18 and SOLA inversion are shown in Figure 5.19, where solid curve represents the exact velocity profile obtained from Equation 5.18 and dotted line with error bars drawn only at some points shows the inverted profile obtained from SOLA technique. It is clear from Figure 5.19 that the inverted profile deviates near the photosphere and also at large depths. The error in the inverted velocity is large in these regions because there are only a few modes from these regions which contribute in the inversion. However, the inverted velocity profile matches very well at intermediate depths, giving confidence about the applicability of our code based on SOLA inversion.

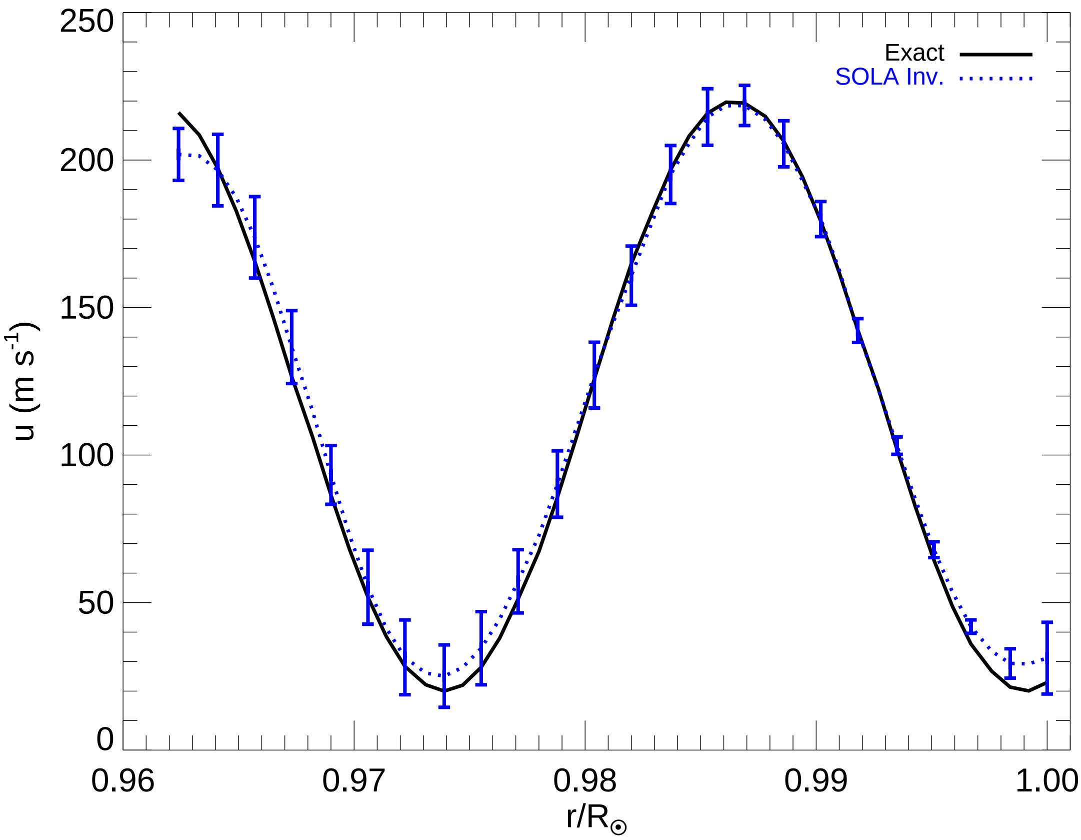

Figure 5.19 Sub-photospheric velocity u estimated from SOLA inversion technique (dotted). The solid curve represents the exact velocity profile calculated from Equation 5.18.

5.5.2 RLS Inversion

The basic idea of this method is to expand the required solution in terms of suitable basis functions and to determine the coefficients of expansion by minimizing the sum of the squared differences between the observations and the adopted model. An additional term is added to ensure smoothness of the solution.

Let $u(z)$ be the estimation function, *i.e.*, average velocity u at radius z. This can be expressed as a linear combination of a chosen set of basis functions $\phi_j(z)$,

$$u(z) = \sum_{j=1}^{N} \upsilon_j \phi_j(z), \qquad j = 1, 2, \ \ldots N \tag{5.20}$$

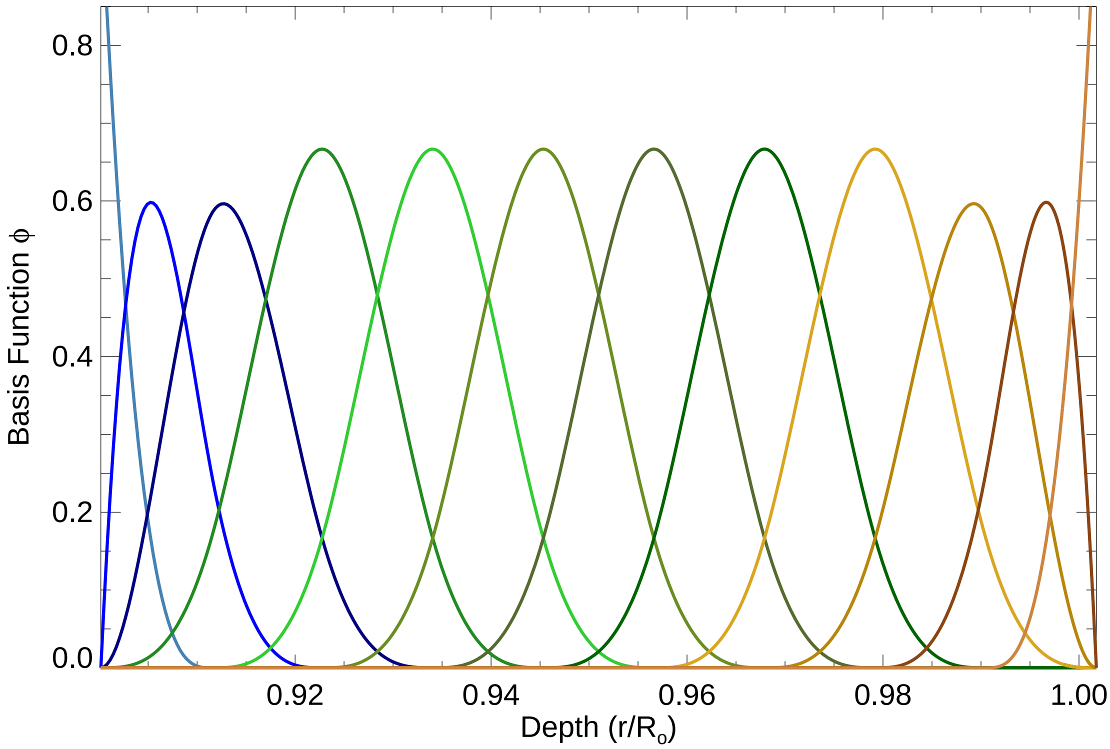

Figure 5.20 The cubic B-splines at ten equally spaced knots.

where, N is the total number of knots (*i.e.*, $z_1, z_2, \ldots, z_N$; in unit of $R_\odot$), and v_j are constants to be determined. The knots are chosen such that,

$$0 = \bar{z}_0 < \bar{z}_1, \bar{z}_2, ..., \bar{z_N} = R_\odot = 1$$

We have used cubic B-spline basis function ϕ_j for our analysis of sub-photospheric flows. A sample of cubic B-splines with ten knots separated equally are shown in Figure 5.20. A variant is to construct $u(z)$ to be continuous and linear on each interval $[\bar{z}_{j-1}, \bar{z}_j]$. Alternatively, one could choose the ϕ_j to be some other set of orthogonal functions.

Using Equations 5.6 and 5.20, we get

$$U_i = \sum_{j=1}^{N} B_{ij} v_j \tag{5.21}$$

Here, we have ignored the error term in Equation 5.6. To make the equations more compact, we define matrix B, as

$$B_{ij} = \int K_i(z)\phi_j(z)\,\mathrm{d}z \tag{5.22}$$

The RLS method seeks the best fit to the data U_i. It is assumed for simplicity that the errors ϵ_i are not only Gaussian but also independent, with variance σ_{U_i} (say σ_i). However, care must be taken because of the ill-conditioned nature of the problem. Basically one would like to choose the constants υ_j by minimizing the χ^2 of the fit in a least-squares sense.

$$\chi^2 = \sum_{i\in M}\frac{1}{\sigma_i^2}\left(U_i - \sum_{j=1}^{N} B_{ij}\upsilon_j\right)^2 \tag{5.23}$$

The minimization of Equation 5.23 yields a system of linear equations with N unknown coefficients (υ_j). If $M > N$ then this gives a system of overdetermined equations which will provide meaningless solution of υ_j as the resulting $u(z)$ will show oscillations on small scale. To resolve this problem, we introduce a smoothness constraint to $u(z)$. The smoothing of Equation 5.23 is performed by adding second derivative regularization,

$$SMT = \lambda \int \left(\frac{\mathrm{d}^2u(z)}{\mathrm{d}z^2}\right)^2 \mathrm{d}z \tag{5.24}$$

where, λ is a free parameter that controls the 'amount' of smoothing as opposed to a direct minimization and resulting procedure is referred as Regularized Least Square (RLS). From Equation A.3, this can be written as

$$SMT = \lambda \sum_{k=1}^{\mathtt{N}} w_i \left(\sum_{j=1}^{N} \upsilon_j \phi_j^{''}\right)^2 \tag{5.25}$$

where, w_i is defined by Equation A.4 and $\mathtt{N}$ is the total number of mesh points to be used for smoothing. Now, the new function to minimize is

$$\sum_{i\in M}\frac{1}{\sigma_i^2}\left(U_i-\sum_{j=1}^{N}B_{ij}\upsilon_j\right)^2+\lambda\sum_{k=1}^{\mathtt{N}}w_i\left(\sum_{j=1}^{N}\upsilon_j\phi_j^{''}\right)^2 \tag{5.26}$$

The parameter λ not only controls the smoothness constraint, but also the trade-off between the resolution and error. If $\lambda = 0$, the solution will reduce to straightforward least square solution. On the other hand, when λ is large the solution will tend to a straight line. Therefore, the values of λ must be chosen carefully to ensure some degree of smoothness in the solution.

The solution of υ_j can be obtained by solving the linear equation

$$A\upsilon(z) = y(z) \tag{5.27}$$

where, elements of matrix A are

$$A = \begin{cases} \frac{B_{ij}}{\sigma_i^2}, & i = 1,\ldots,\mathtt{M},\ \ j = 1,\ldots,N \\ \lambda\, w_i\, \phi_j^{''}, & i = \mathtt{M}+1,\ldots,\mathtt{M}+\mathtt{N},\ \ j = 1,\ldots,N \end{cases}$$

and elements of vector y are

$$y = \begin{cases} \frac{U_i}{\sigma_i^2}, & i = 1,\ldots,\mathtt{M} \\ 0, & i = \mathtt{M}+1,\ldots,\mathtt{M}+\mathtt{N} \end{cases}$$

Equation 5.27 is a system of M+N linear equations with N unknown coefficients. We solve these equations using singular value decomposition described in Antia (2002).

Errors in the inverted profiles that arise due to the errors in the fitted velocities U_i can be estimated using Monte Carlo simulation. For this, we choose an artificial function similar to the inverted profile and generate U_i using the forward problem. We introduce random errors in the fitted parameter U_i as expected in the real data and solve the inverse problem using the same λ as used in the exact

Figure 5.21 The L-curve showing the term SMT plotted with χ^2 of the Equation 5.26 to be minimized. The knee or inflexion value of λ ($= 8.04 \times 10^{-6}$) is the optimum value for the solution of Equation 5.27

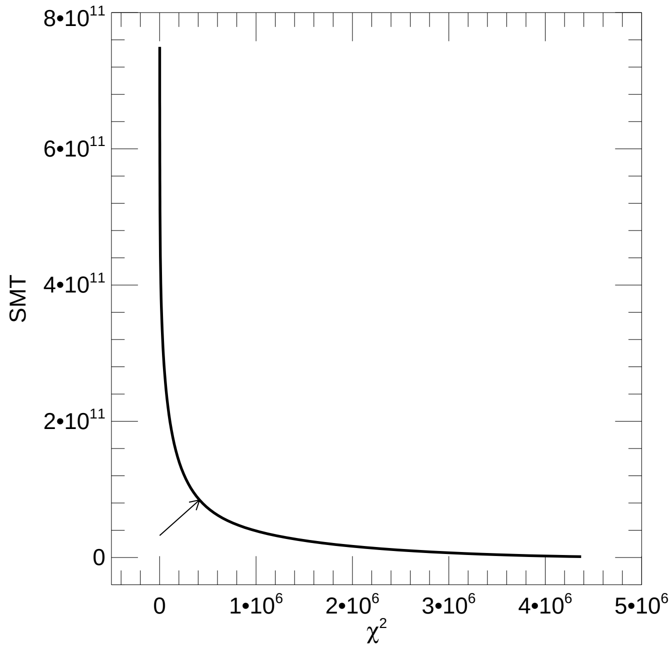

solution. This exercise is repeated for many different realizations of random errors. Finally, using the same set of inverted profiles, we estimate errors $\sigma(u, z)$ at each value of z.

Test of RLS Inversion

To test our code of RLS inversion, we have used the same artificial data as used in the test of SOLA inversion (*cf.* Equation 5.18). We have used 50 uniformly spaced knots to represent the function $u(z)$. We try different values of λ and plot the two terms in Equation 5.26 against each other. The resulting curve has a shape resembling the letter "L" and the values of λ corresponding to the inflexion position would be close to the optimal value. This plot is also known as the L-curve.

In order to find the optimum value of λ, we calculate a large range of values of the first and second terms. A sample of L-curve thus calculated from our code is shown in Figure 5.21. The optimum value of λ corresponding to the arrow marked location is 8.04×10^{-6}.

The inverted profiles $u(z)$ for optimum and other values of λ are shown in Figure 5.22. The solid curve corresponds to the exact profile and the others as

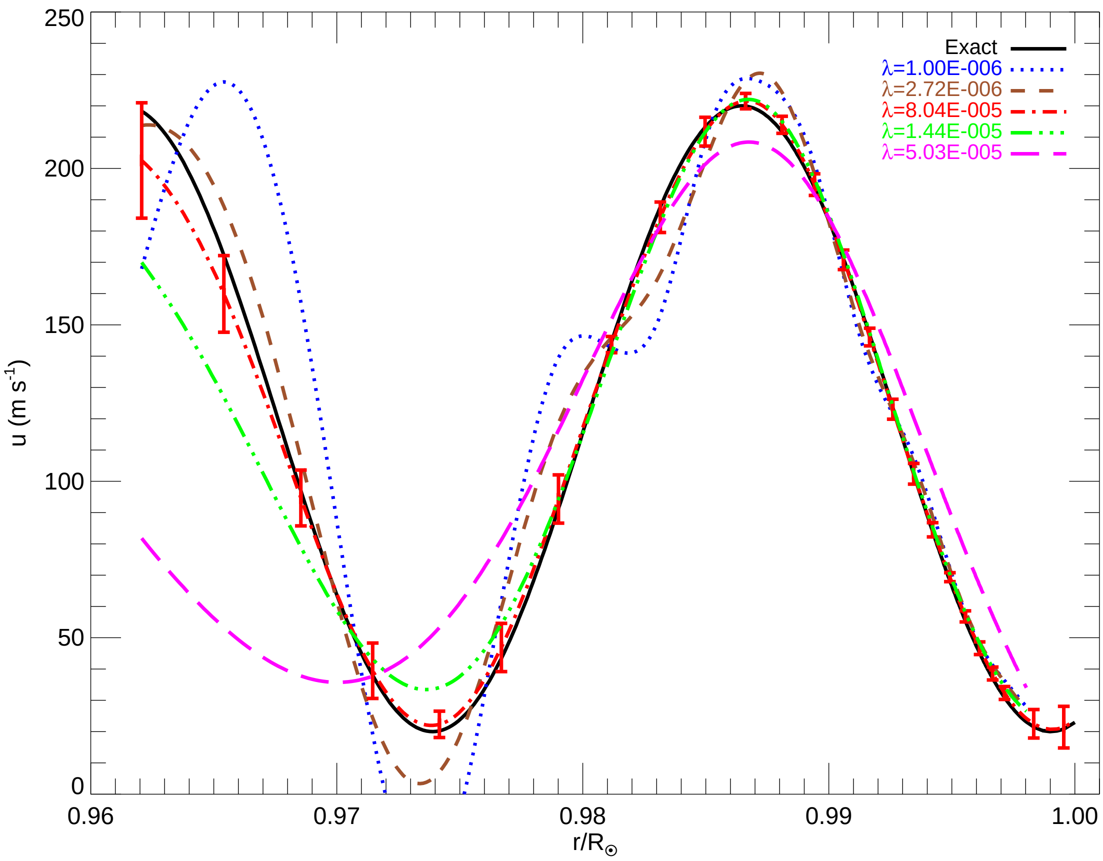

Figure 5.22 Inverted velocity profiles obtained for different values of regularization parameter λ. The solid curve represents the exact velocity profile calculated from the Equation 5.18.

obtained from RLS inversions. For the optimum value of λ, the inverted profile matches with the exact profile. It is clear from Figure 5.22 that when the value of λ is much smaller than the optimum value, the solution shows several oscillations in the interior. For the optimum choice of λ, although the oscillations are suppressed, there is a large departure at the deeper region. For larger values of λ, the solution is smooth but it shows large deviation from exact solution in the deep interior.

Instead of using the L-curve, we can alternatively determine the optimum value of λ using another method. For this, we increase the value of λ until the oscillatory pattern disappears. This criteria also gives similar value of λ for optimal solution. Here, since we know the exact solution, we can try to measure the difference between the inverted and exact solutions. It turns out that the integrated value of squared difference is minimum when λ is close to the value indicated by the L-curve. At large depths, however, the data is not adequate to determine the velocity $u(z)$ correctly, as there are very few modes contributing to U_i.

In the following, we present a comparison of results obtained using the above two independent techniques which provide an estimate of systematic errors involved in the inversion process.

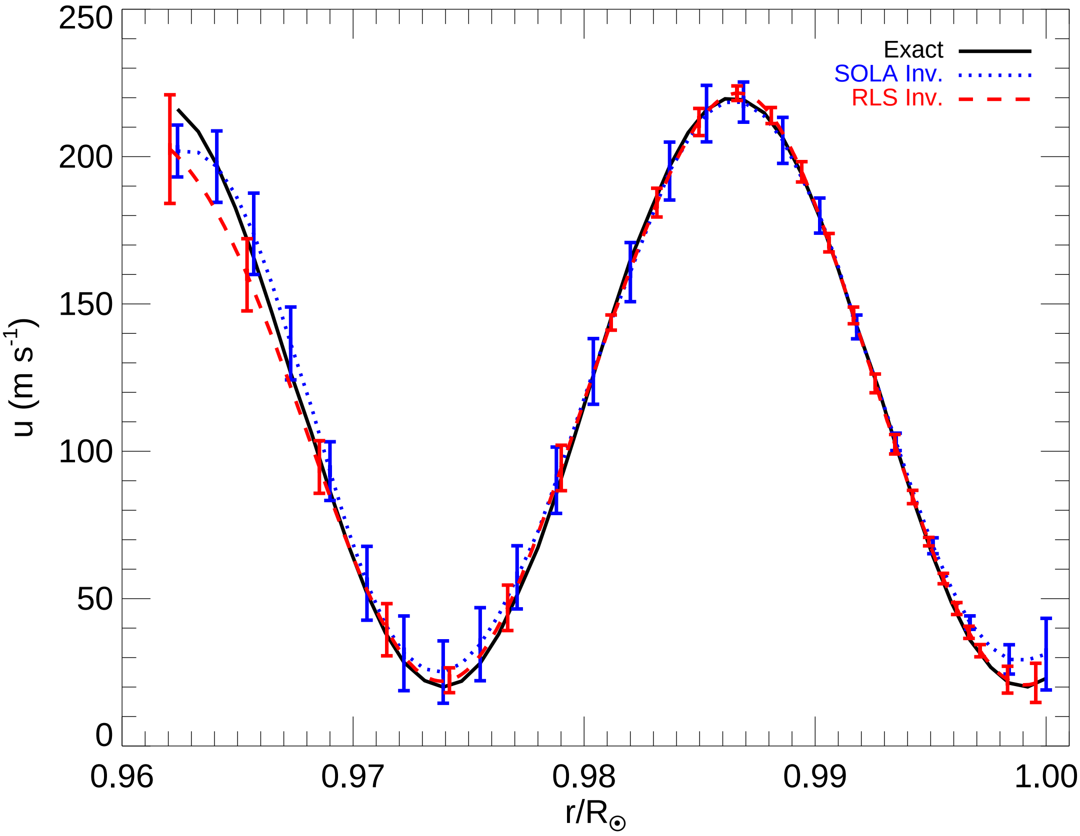

Figure 5.23 A comparison of SOLA (dotted) and RLS (dashed) inverted velocity profiles. The solid curve represents the exact velocity profile calculated from the Equation 5.18.

5.5.3 Comparison of SOLA and RLS Inversions

For the comparison of SOLA and RLS methods, we have plotted the inverted velocity profiles in Figure 5.23, where dotted (dashed) curve corresponds to the

SOLA (RLS) inversion. These profiles were inverted using the same set of data obtained using a forward method (Equation 5.6). The solid curve represents the exact profile obtained from Equation 5.18. The inverted profiles obtained from SOLA and RLS are evidently in good agreement with the exact profile except near the photosphere and at large depths. The error in the inverted profiles is also large very close to the photosphere and the deep interiors. This gives us confidence in the results obtained from our SOLA and RLS inversion codes for the intermediate depths. However, it should be noted that there are large differences in computation methods and also, in the advantages and disadvantages involved in the two methods.

The regularization parameter λ in RLS serves as trade-off similar to the trade-off parameter μ_0 of SOLA. The advantage of SOLA method over RLS is that in this case the relationship between the errors and resolution (measured by width of resulting averaging kernel) comes out more clearly. Thus if we try to reduce the width of averaging kernel the error will increase, and the parameter μ_0 can be chosen to get appropriate balance between the two effects. Disadvantage of the SOLA method is that it requires excessive amount of computation. The RLS method requires the solution of $\mathtt{M}\times\mathtt{N}$ matrix equation while the SOLA technique requires $\mathtt{M}\times\mathtt{M}$ matrix to be solved for value of z_0 at which the solution is desired. The main disadvantage of the RLS technique is that the regularization parameter may be fixed in somewhat arbitrary manner. Consequently, it is difficult to get a realistic determination of errors in the inverted profiles. On the other hand, SOLA technique provides a convenient relation between the resolution and errors which is easier to interpret.

5.6 Summary and Conclusions

We have compared the results of two ring-fitting techniques proposed by Basu and Antia (1999) and Haber *et al.* (2000) for the determination of photospheric p-

mode parameters using three-dimensional power spectra. The first technique uses thirteen parameters to fit the spectra for asymmetric peak profile while the later uses only six parameters to fit the spectra for symmetric Lorentzian profile. For a comparison of results obtained from the two methods, we applied these techniques to the same set of power spectra obtained from GONG. We found that there is a good agreement between the mode velocities $U_{\rm x}$ and $U_{\rm y}$, but other parameters, *e.g.*, mode amplitude A, mode width Γ and frequency shift $\delta\nu$ did not match well. We suggest that the deviations in A and Γ are due to the lower cutoff of background power in the fitting while the deviation in $\delta\nu$ arises due to the contribution of asymmetric parameter S in APP fitting. The APP method fits a large number of modes (~ 800) compared to the DP fitting involving only (~ 200). Therefore, APP fitting takes much longer time compared to the DP fitting. But the advantage of APP fitting is that it gives a good signal to noise ratio in sub-photospheric velocity inversions by providing a larger number of modes.

To determine the sub-photospheric velocities of ARs, we have developed our inversion codes based on SOLA and RLS algorithms. Although SOLA method is computationally excessive as compared to RLS, it provides an option for examining the errors and localization of averaging kernel at the target radius. We tested our inversion codes using artificial data generated from a forward method. We found that the inverted profiles obtained from the two methods deviated in the regions close to the photosphere and the deep interiors. We suggest that this problem may be due to the relatively less number of modes from these regions contributing to inversions. However, results obtained from the two methods are found to be in good agreement at the intermediate depths, which gives us confidence about the correctness and applicability of our codes for these depths beneath ARs.

Chapter 6

Energetic Transients and *p*-Mode Parameters

6.1 Introduction

Energetic transients, *viz.*, flare, CMEs, *etc.*, are believed to occur due to the reconnection of magnetic fields line in the solar corona. Particles are energized at the primary energy release site and then guided along the magnetic field lines downwards to the denser photosphere. Wolff (1972) first suggested that large flares may be able to excite acoustic waves by exerting mechanical impulse of their thermal expansion on the photosphere. They reported that the damping times of the free modes may be longer than a day. Following this, several studies have been carried out to understand the energetic activity related effects on *p*-mode parameters (Haber *et al.*, 1988; Libbrecht and Woodard, 1990; Chaplin *et al.*, 2000; Hindman *et al.*, 2000; Ambastha, Basu and Antia, 2003; Ambastha *et al.*, 2004; Howe *et al.*, 2004).

Excitation of flare-related waves on the solar photosphere have been reported by Kosovichev and Zharkova (1998); Kosovichev (2006) and Donea, Braun and Lindsey (1999); Donea and Lindsey (2005). However, these reports pertain to the traveling waves as opposed to the standing waves which constitute the normal modes of solar oscillations. Chaplin *et al.* (2000) reported that mode amplitudes and solar activity level are anti-correlated for intermediate- and high-degree modes, and strongly depend on the local magnetic fields. Rajaguru, Basu and Antia (2001) found that the intense magnetic fields of sunspots leads to absorption of power associated with solar oscillations. On the other hand, Ambastha, Basu and Antia (2003) have found that the power in high-degree p-mode is amplified during the period of high flare activity as compared to non-flaring regions of similar magnetic fields.

Howe *et al.* (2004) reported strong dependence of the amplitude and lifetime of modes on the local magnetic flux. They found that the amplitude and lifetime decreased in the 5 minute band while a reversed trend was found at high frequencies. Along with other mode parameters, activity related changes in mode frequencies are also reported (Libbrecht, 1988). It is found that the mode frequency changes with local activity along with the solar cycle (Hindman *et al.*, 2000).

Characteristics of the photospheric p-modes in ARs are essentially described by shorter wavelength modes that are trapped near the photosphere. These modes can be studied using the ring diagram analysis. The spatial extent of flares is usually much smaller than the spatial sizes of $16^\circ \times 16^\circ$ used in GONG and SOHO/MDI data-cubes for ring diagram analysis. The temporal extent of flares also is much smaller as compared to the duration (1664 minutes) of these data-cubes. Furthermore, any mode amplification induced by transient flare events has to essentially compete with the absorption effects associated with the intense magnetic fields of sunspots. These are the reasons as to why it has been rather difficult to conclusively detect flare-related effects by the averaging technique involved in ring diagram analysis.

For an estimation of various factors involved, let us estimate the damping time scale of p-modes from the observed mode width. This is generally in the range of 15-100 μHz for high-degree modes which gives a lifetime in the range of 0.5-3 hr assuming that the width is mainly due to the finite life of the modes.

Acoustic waves have been reported to travel outwards from the site of flares with the sound speed ranging from 10 to 50 km s^{-1} for the depths in which the high-degree modes are trapped. Thus, over the damping time of the order of an hour, these waves would travel a distance from 36 to 180 Mm, *i.e.*, comparable to the spatial extent of most ARs. A large fraction of energy dissipation occurs within this region if the flare is temporally located well within the data-cube. From these estimates, we expect that flare-related effects should last over several hours in large events, and possibly be detectable even in the temporal averages as in the ring analysis.

The average properties of p-mode parameters have been studied with magnetic and flare activities by many researchers (Ambastha *et al.*, 2004; Howe *et al.*, 2004; Mason *et al.*, 2006). Ambastha, Basu and Antia (2003) and Ambastha *et al.* (2004) have found the power in p-modes to be larger during the period of high flare activity as compared to that in non-flaring regions of similar magnetic field strength. However, the pre-, peak and post-flare signatures of flares on p-mode parameters, the relationship of energetic events with p-mode energy, and evolution of p-mode parameter of ARs over Carrington rotations are some issues that still require a careful statistical analysis.

To investigate the properties of p-modes and unambiguously establish the results on the flare-related changes, we have considered the highly energetic X17/4B superflare of 28 October 2003 observed in NOAA 10486. The aims of this study are two fold – firstly, we wish to study the flare related variations in p-mode parameters, and secondly, ascertain the nature of variations in p-mode parameters by changing the temporal position of onset time of the flare within the data cube. Further, we carry out a statistical analysis of a sample of 74 ARs of Cycle 23 to further establish the results on the p-mode energy amplification by flares.

In Section 6.2, we describe the variations in p-mode parameters with changing temporal location of flare in the data cube. Section 6.4 discusses the statistical relationship of energetic transients and p-mode energy. Finally, Section 6.5 is devoted to the summary and conclusions of the new findings.

6.2 Flare Associated Changes in the p-Mode Parameters

The method of ring diagram analysis gives average properties of the AR over the temporal length of the data-cubes, which is around 1664 minutes or over a day for MDI and GONG (see Chapter 5). Therefore, the effect of smaller transient events lasting for short periods of time is not expected to be significant or even detectable. But large duration energetic events lasting for several hours should be detectable even in the ring diagram analysis. However, as the effect of flare propagates outward from the flare site, the temporal and spatial location of the flare within the data cube would affect the results. For instance, if the flare onset time lies at the start of the data cube then the post-flare effects will remain entirely within the data-cube. On the other hand, if the flare occurred around the end of the data-cube, then the post-flare effects would have propagated to the subsequent data-cube corresponding to the next day. Also, if several flares occurred within the time-span of the data-cube, the mode properties would contain the net effect of all the flares.

6.2.1 The White-Light Superflare of NOAA 10486

The whitelight (WL) super-flare of 28 October 2003 that occurred in NOAA 10486 was one of the most energetic events ever observed in the Sun. It was classified as X17/4B flare. During the period of the data-sets used in our study, some other C and M class flares also occurred in NOAA 10486, but the X17/4B event was the dominant event during the 24 hr period of October 28, 2003. According to GOES X-ray observations, the flare started at 09:51 UT, reached the maximum phase at 11:10 UT, and decayed at 11:24 UT, *i.e.*, lasting over more than 90 minutes (Figure 6.1). However, it is evident that the integrated X-ray flux remained at a very high level well beyond 11:24 UT. Even if a background corresponding to M1

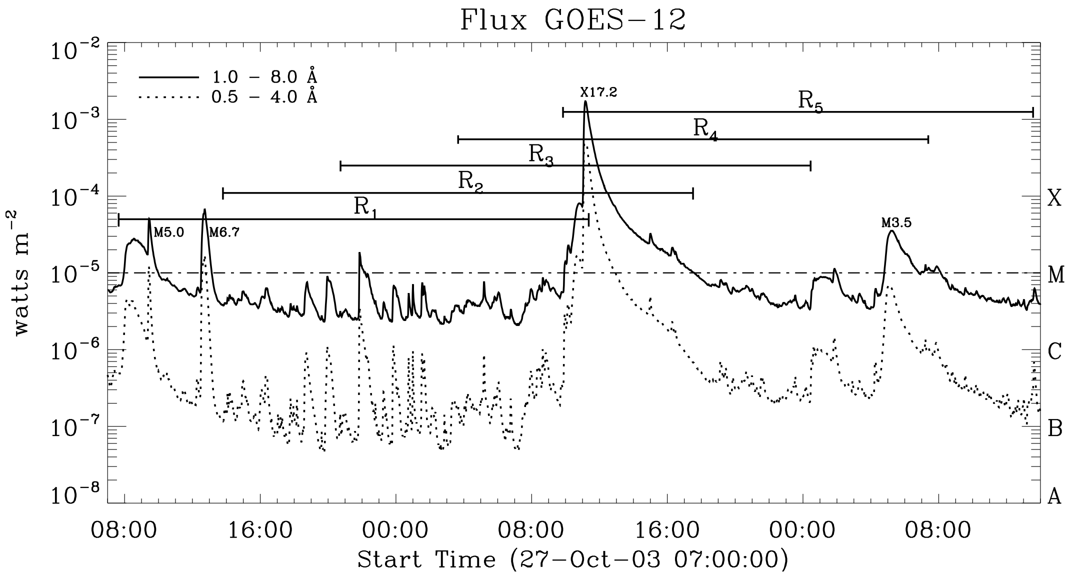

Figure 6.1 GOES-12 integrated X-ray flux in 1.0 - 8.0Å (solid line) and 0.5 - 4.0Å (dotted line). The horizontal lines with labels $R_i, i = 1, \ldots 5$, represent different 1664 min long time periods selected for constructing five data-cubes for ring diagram analysis.

level (10^{-5} watts m^{-2}) is considered, the X-ray flux gradually reduced to this level only around 16:00 UT. In Hα also, the flare was reported to have lasted for more than four hours. Therefore, this extremely energetic, LDE was a particularly well suited case for an investigation of flare-related helioseismic effects.

6.2.2 The Observational Data

We have used high resolution GONG Dopplergrams obtained at one minute cadence. The data-cubes have 1664 minutes' duration and cover 16°×16° area centered at 285° Carrington longitude and -22.5° latitude covering NOAA 10486. The AR was located close to the disc center at the time of this flare, therefore, projection effects did not pose any serious difficulty in the analysis.

As illustrated in Figure 6.1, we constructed five data-cubes of 1664 minutes duration each with different starting time, such that the time of flare onset was placed in the beginning (R_5), one-fourth (R_4), center (R_3), three-fourth (R_2) and end (R_1) of the data-cube's time-line. To determine the photospheric p-modes mode parameters, we have carried out ring diagram analysis using the dense-pack technique (Haber *et al.*, 2002) adapted for GONG data (Corbard *et al.*, 2003; Hill *et al.*, 2003). For detail please see Chapter 5.4.2. The common mode parameters in all sets were corrected for filling factor using a method described in Komm, Howe and Hill (2000a).

6.2.3 Determination of Mode Energy

The total energy (*i.e.*, kinetic and potential energy) of the p-mode is estimated using the formula given by Goldreich and Murray (1994),

$$E_{nl} = M_{nl} < v_{nl}^2 > \tag{6.1}$$

where, $< v_{nl}^2 >$ is the mean square velocity (Komm, Howe and Hill, 2000b) which is the measure of mode area and is given by

$$< v_{nl}^2 >= \frac{\pi}{2} C_{vis} A_{nl} \Gamma_{nl} \tag{6.2}$$

where, $C_{vis} = -3.33$ corrects for the reduced visibility due to leakage (Hill and Howe, 1998). A_{nl} and Γ_{nl} are mode amplitude and width, respectively, obtained from the ring fitting. The mode mass (M_{nl}) is given by

$$M_{nl} = 4\pi M_{\odot} I_{nl} \tag{6.3}$$

where, I_{nl} is the mode inertia. We have used the mode inertia table provided by Antia (private communication) to calculate the total energy in p-modes (Equation 6.1). Figure 6.2 shows normalized mode inertia as a function of frequency for different radial order $n = 0, \ldots, 5$ in the frequency range of interest.

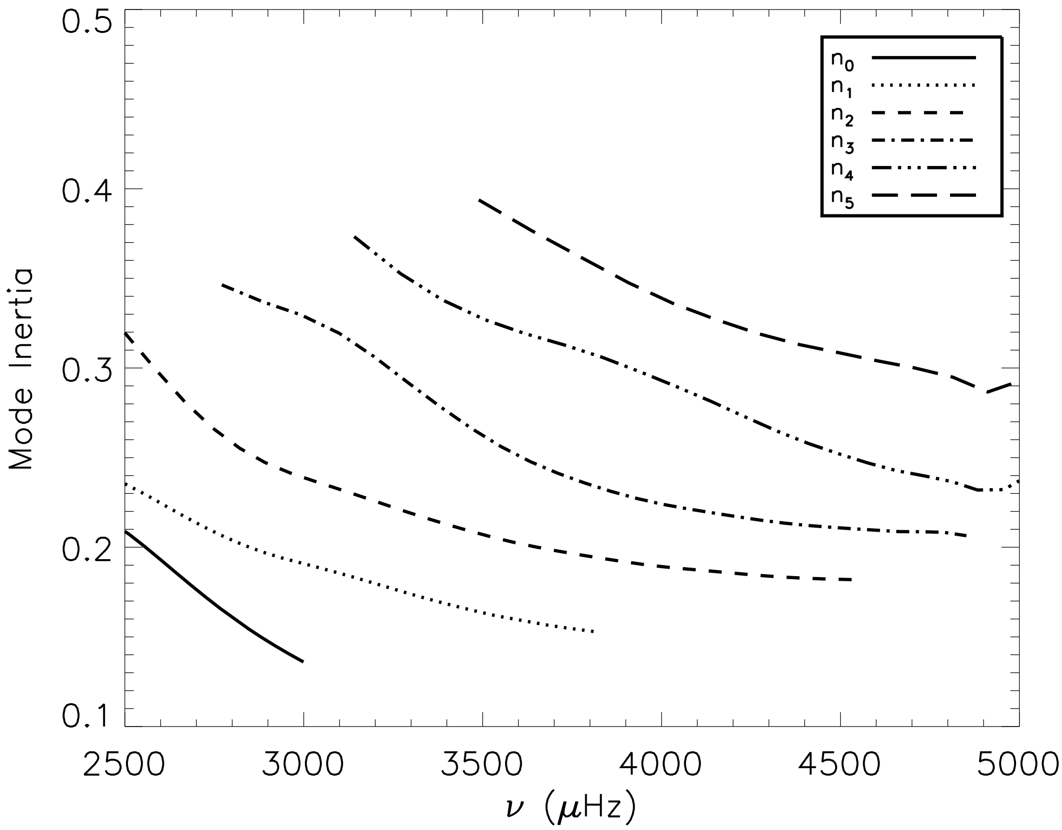

Figure 6.2 Mode inertia as a function of frequency for radial order $n = 0, \ldots, 5$.

6.2.4 Results and Discussions

Figure 6.3 shows the relative difference in p-mode amplitude obtained for data-cubes R_2 to R_5 with reference to R_1. This quantity is found to be the largest for R_5 as compared to that for other data-sets. The difference between the amplitudes increased with frequency $\nu > 2000\,\mu$Hz, and reduced with increasing radial order from $n = 0$ to 5. The large difference of mode amplitude at lower radial orders may be attributed to the flare effect as these modes are confined within a shallow region under the photosphere and hence, are more likely to be affected by photospheric activities.

The flare onset was placed at the beginning in the data-set R_5, hence the overall helioseismic contribution of this energetic LDE, extending from the pre- to the post-flare phase, is expected to remain entirely within this data-cube. Corre-

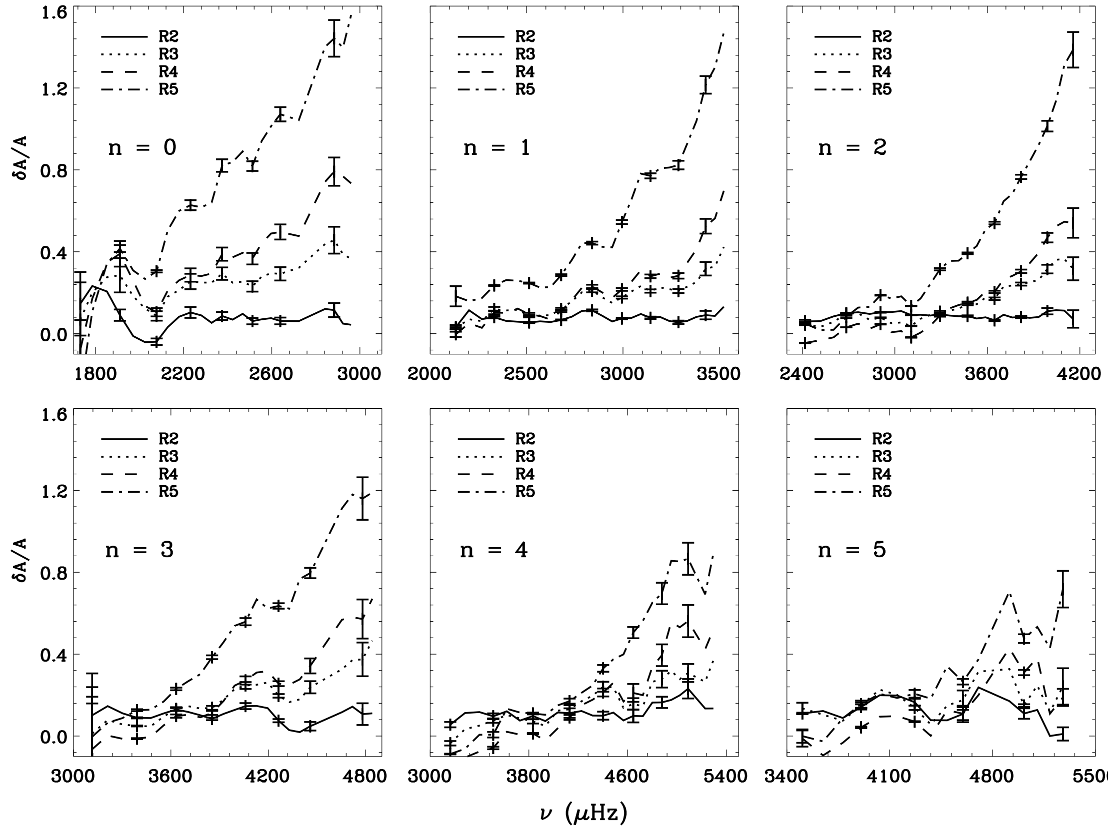

Figure 6.3 Relative differences in mode amplitude for the data-sets R_i, $i = 2, \ldots 5$, for radial orders, $n = 0 - 5$. Here, R_1 is used as the reference.

spondingly, according to the expected effect of flare related amplification, the mode amplitude was found to be the largest in R_5. On the other hand, it was smallest for R_1 where the flare was placed at the end of the data-set. Therefore post-flare effects were not contained within this data-set. It is evident from the systematic decreasing trend of mode amplitude from R_5 to R_1 that the energetic flare indeed gave rise to a significant amplification of mode amplitude.

Mode width is found to be large at all frequencies and radial orders for R_5. The changes are found to be larger at lower frequencies implying that higher-n modes have shorter lifetimes. Duvall, Harvey and Pomerantz (1988) and Burtseva *et al.* (2009) have also found that mode width increased with frequency as well as with degree of the modes. However, care is needed in this interpretation as significant contribution to mode width may arise due to the limitation of available resolutions in wavenumber and frequency. The relative values of mode energy, computed using Equation 6.1, was also found to be large for R_5 at all frequencies.

Using the ring diagram fits, we calculated the horizontal velocities in order to check whether there is any variation in photospheric velocities associated to the flare. Indeed, we found large variations in photospheric zonal and meridional velocities at all frequencies for the radial orders $n = 0$ to 5 from R_1 to R_5. Also, the deviation for both the components of velocity is larger for R_5 as compared to other data-sets indicating the extent of variation in flows from the pre- to post-flare phases.

Thus the above study provides two important inferences: (i) effect of a LDE on p-mode parameters can be assessed using ring diagram analysis of appropriately constructed data cube, and (ii) systematic variations are produced in the photospheric p-mode parameters by the LDE.

In the following, we discuss the results obtained on the evolution of p-mode parameters for NOAA 10486 using ring diagram analysis.

6.3 Evolution of p-Mode Parameters in NOAA 10486

NOAA 10486 was extremely flare productive during its disk passes from 25 October to 1 November 2003. In would be interesting to compare the p-mode characteristics of NOAA 10486 with other dormant and quiet regions, and examine their evolution during the above-mentioned period using ring diagram analysis. For this study, we have computed the mode parameters averaged for radial orders $n = 0$ to $n = 5$ over the Sun in the range (-60, 60) of longitudes and latitudes using dense pack method.

The main results of our analysis are shown in Figure 6.4. In the figure, the vectors correspond to horizontal flows and colors represent the frequency shift in modes averaged over $n = 0$ to $n = 5$. Positive (negative) frequency shifts are shown in red (blue) colors. It is evident that there are large, positive frequency

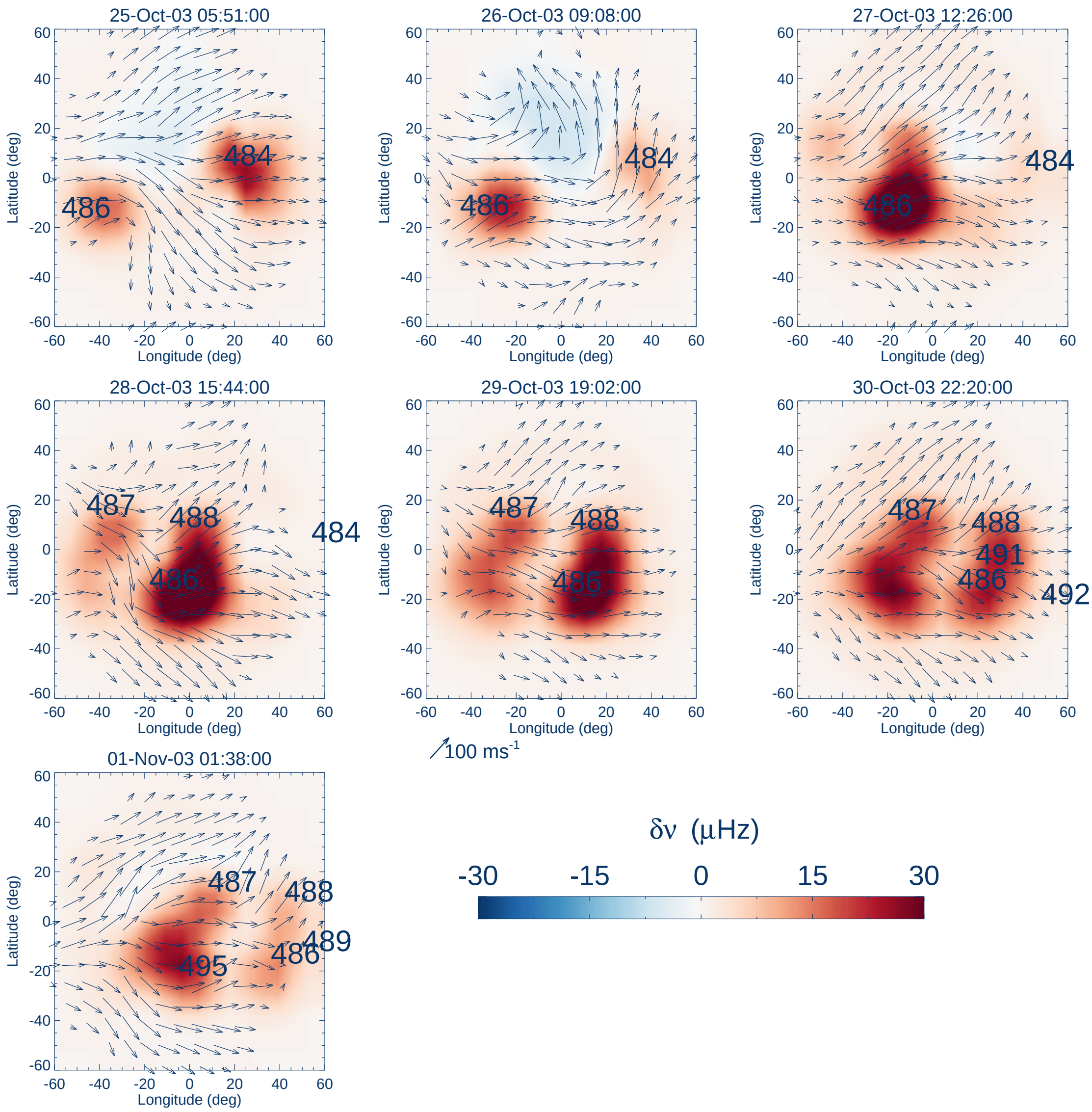

Figure 6.4 Evolution of surface p-mode parameters in the regions, $\pm 60^{\circ}$ centered around the solar disc, from 25 October to 1 November 2003. Horizontal flows are represented by vectors, and positive (negative) frequency shifts in red (blue) color for the modes averaged over $n = 0$ to $n = 5$. The scale for frequency shifts is given by the colorbar. The NOAA numbers of the major ARs are marked in the map at their appropriate positions.

shifts at the AR locations. As the AR evolved, the frequency shift also evolved. For instance, NOAA 10486 was initially associated with smaller positive $\delta\nu$ value on 25 October 2003. It increased thereafter till 29 October 2003 and then decreased again. Interestingly, $\delta\nu$ values reached the maximum around the period 28-29 October 2003 when this AR produced two major flares, *i.e.*, X17/4B and X10/2B events (for detail please see Chapter 4).

Now, if one examines the horizontal flows, it is evident that they showed a large deviation from the general flow pattern around NOAA 10486 on 27 and 28 October 2003. This is clearly seen from the changing direction of vectors at the location of this AR, although the U_{x} and U_{y} components of velocity were obtained from averaging over the modes $n = 0$ to $n = 5$. Since the parameters U_{x} and U_{y} are the weighted averages over depth, this flow pattern reveals highly sheared flows in the interior of NOAA 10486 as compared to other less flare active ARs and the surroundings.

These results provide further confirmation that energetic transients and flare productivity of the AR NOAA 10486 are associated with p-mode parameters, sub-photospheric flows and their changes. More details on these are described in Chapter 7. In the following, we discuss the statistics of flares and and mode energy for several ARs.

6.4 Statistics of Flares and p-Modes Energy

The amplification in p-mode amplitude implies that during an energetic flare, the energy of p-modes must be weighted by the energy of excited modes. We need to carry out study of a large set of flare productive ARs to further establish the results on the p-mode energy amplification by flares. Therefore, we have carried out a statistical analysis of 74 ARs of solar cycle 23.

6.4.1 Flare Productive ARs of Solar Cycle 23

For selecting our sample of the ARs, we have used archived information on ARs and solar activity provided by the web-pages of *Solar Monitor*[1]. We first identified the ARs producing flares of X-ray class > M1.0 using *GOES* database[2] during Carrington rotations 1980–2051 of Solar Cycle 23.

We short-listed ARs lying within the heliocentric location $\pm 40°$ to avoid projection effects and selected 74 ARs, both flaring and relatively dormant, that were well covered by the GONG network. For each flaring AR, we chose a single data set corresponding to the day of maximum flaring activity. A full list of the selected ARs is provided in Table 6.1. The locations and distribution of these 74 ARs over the solar photosphere is illustrated in Figure 6.5, where circles correspond to the logarithmic area of ARs in Millionth of Hemispheric (MH, *i.e.*, 3×10^6 km^2).

6.4.2 The Observational Data and Analysis

Helioseismic data for our statistical study was obtained from the GONG project. The p-mode energy (Equation 6.1) is derived using the p-mode parameters, *i.e.*, mode amplitude and width, obtained from ring diagram analysis, and mode inertia (see Figure 6.2). We examined the relationship of p-mode energy with magnetic activity of ARs using the magnetic index, MI, obtained from SOHO/MDI 96 minutes averaged magnetograms. For this, we extracted the area of interest from the full disk magnetograms corresponding to the $16° \times 16°$ spatial patch used in the ring analysis. Then MI corresponding to the AR was calculated from the averaged absolute values of magnetic fields over the patch. We also calculated the flare index, FI, for each AR by multiplying the X-ray flux, obtained from GOES, with the flare duration and then summing the contributions from all the flares that occurred during the 1664 minutes' period of the data-cube.

[1] http://www.solarmonitor.org

[2] http://www.lmsal.com/SXT/plot_goes.html

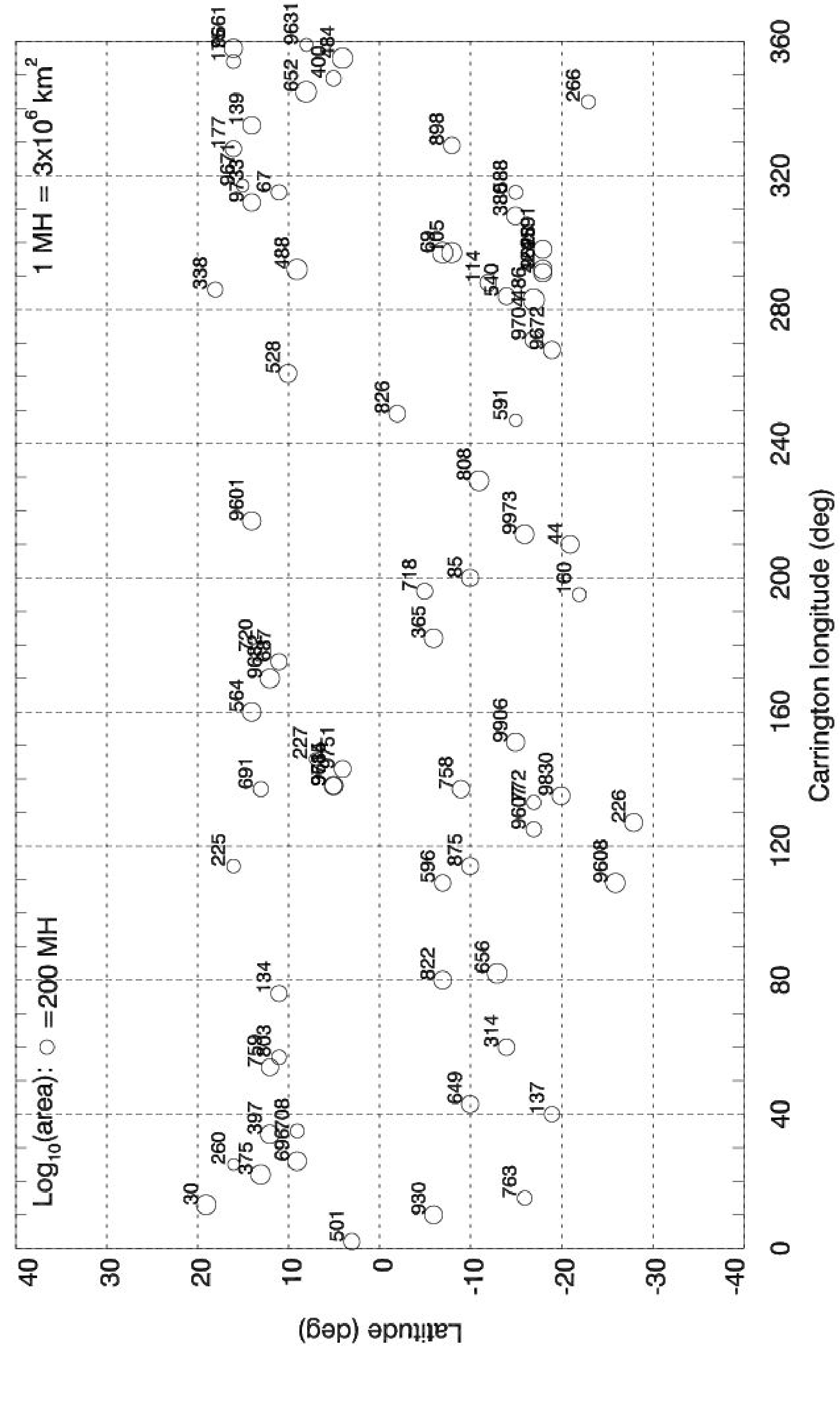

Figure 6.5 A map showing the positions of 74 ARs used in our study. The circle sizes correspond to the logarithm area in millionth of hemisphere (MH).

Table 6.1 shows the characteristics of data cubes (column 2-6) corresponding to ARs (column 1). Column 7 shows magnetic index in the AR while column 8-11 shows flaring activity of the AR during the 1664 minutes of data cube from its starting time (column 6). Columns 9, 10 and 11 represent numbers of X-, M- and C- class flares, respectively, that occurred during the interval of 1664 minutes from the start time of cube (column 6).

Table 6.1 The list of ARs studied using ring diagram analysis.

NOAA No.	Carr. Rot.	CMD Lon. (deg)	Lat. (deg)	Lon. (deg)	Start Date Time	MI (G)	FI 10^{-3} (W m^{-2})	X	M	C
(1)	(2)	(3)	(4)	(5)	(6)	(7)	(8)	(9)	(10)	(11)
9591	1980	337	22.5S	300.0	25-Aug-01 06:17	112.9	1330.1	1	2	4
9601	1980	232	15.0N	217.5	02-Sep-01 05:02	200.3	17.9	0	1	2
9607	1980	142	15.0S	127.5	09-Sep-01 00:35	132.6	25.4	0	1	1
9608	1980	142	22.5S	112.5	09-Sep-01 00:35	163.4	23.7	0	2	2
9628	1981	292	22.5S	292.5	24-Sep-01 22:22	203.3	853.2	0	1	2
9631	1981	352	7.5N	0.0	20-Sep-01 09:16	33.9	18.7	0	1	1
9661	1982	337	22.5N	352.5	18-Oct-01 19:23	88.6	294.3	1	0	2
9671	1982	337	15.0N	315.0	18-Oct-01 19:23	75.4	10.4	0	1	1
9672	1982	262	22.5S	270.0	24-Oct-01 11:52	154.9	363.7	1	0	2
9682	1982	202	15.0N	172.5	29-Oct-01 01:04	142.7	59.3	0	1	3
9684	1982	127	7.5N	135.0	03-Nov-01 17:34	137.2	324.0	1	0	0
9704	1983	247	15.0S	270.0	21-Nov-01 22:29	128.6	33.5	0	1	5
9715	1983	172	7.5N	135.0	27-Nov-01 15:03	103.2	62.1	0	1	0
9733	1984	322	15.0N	315.0	13-Dec-01 13:32	166.0	564.4	1	0	1
9751	1984	127	7.5N	142.5	28-Dec-01 08:48	125.6	14.5	0	1	1
9830	1986	127	22.5S	135.0	21-Feb-02 01:05	113.7	3702.3	0	1	1
9906	1988	157	15.0S	150.0	14-Apr-02 09:07	135.0	95.8	0	1	1
9973	1990	247	15.0S	217.5	01-Jun-02 00:47	138.0	9.9	0	1	0
30	1991	22	22.5N	7.5	15-Jul-02 05:34	152.3	361.6	1	1	8
44	1992	232	22.5S	210.0	26-Jul-02 13:40	175.0	358.2	0	6	7

continued on next page

Table 6.1 – continued from previous page

NOAA	Carr.	CMD	Lat.	Lon.	Start Time	MI	FI	X	M	C
67	1993	352	7.5N	315.0	13-Aug-02 17:15	78.4	41.5	0	1	5
69	1993	322	7.5S	300.0	15-Aug-02 23:43	226.4	318.0	0	2	4
85	1993	232	7.5S	202.5	22-Aug-02 19:09	105.9	29.9	0	1	3
105	1994	337	7.5S	300.0	11-Sep-02 02:28	155.6	21.1	0	1	0
114	1994	277	15.0S	285.0	15-Sep-02 15:32	115.0	11.2	0	1	4
134	1994	112	7.5N	75.0	28-Sep-02 03:33	71.7	38.4	0	1	6
137	1994	37	22.5S	37.5	03-Oct-02 19:58	78.0	107.8	0	5	4
139	1994	22	15.0N	337.5	04-Oct-02 23:15	85.0	164.1	0	3	5
160	1995	187	22.5S	195.0	19-Oct-02 18:01	93.2	33.9	0	2	3
175	1995	37	15.0N	352.5	31-Oct-02 03:00	64.2	20.0	0	1	2
177	1996	352	15.0N	330.0	03-Nov-02 12:54	117.2	56.3	0	1	3
225	1997	157	15.0N	112.5	15-Dec-02 15:30	93.2	28.5	0	1	0
226	1997	97	30.0S	127.5	20-Dec-02 04:49	122.1	199.1	0	1	9
227	1997	142	7.5N	142.5	16-Dec-02 18:50	41.0	23.7	0	1	3
260	1998	37	15.0N	22.5	21-Jan-03 02:12	47.4	24.5	0	1	3
266	1998	7	22.5S	345.0	23-Jan-03 08:53	49.8	72.2	0	2	2
314	2000	37	15.0S	60.0	16-Mar-03 18:14	95.4	252.7	1	0	2
338	2002	277	15.0N	285.0	22-Apr-03 03:17	61.3	125.1	0	1	3
365	2003	172	7.5S	180.0	27-May-03 07:21	108.1	316.1	1	2	3
375	2003	7	15.0N	22.5	08-Jun-03 18:34	166.4	230.2	1	1	21
380	2004	337	15.0S	307.5	11-Jun-03 00:58	142.2	35.6	0	1	0
397	2004	67	15.0N	37.5	01-Jul-03 10:31	101.1	83.3	0	1	4
400	2004	7	7.5N	352.5	05-Jul-03 23:19	48.4	48.0	0	1	2
424	2006	337	15.0S	292.5	04-Aug-03 10:47	101.1	8.2	0	1	0
484	2009	322	7.5N	352.5	26-Oct-03 09:08	189.5	1124.2	1	4	0
486	2009	307	22.5S	285.0	27-Oct-03 12:26	243.3	10227.0	1	2	5
488	2009	307	7.5N	292.5	27-Oct-03 12:26	79.7	41.6	0	1	5
501	2009	7	0.0N	7.5	19-Nov-03 06:32	106.0	182.9	0	3	4
528	2011	247	7.5N	262.5	25-Dec-03 16:47	110.4	79.1	0	1	7
540	2012	277	15.0S	285.0	19-Jan-04 18:11	125.4	91.7	0	3	4
564	2013	157	15.0N	157.5	25-Feb-04 05:04	95.4	169.5	1	0	11

continued on next page

Table 6.1 – continued from previous page

NOAA	Carr.	CMD	Lat.	Lon.	Start Time	MI	FI	X	M	C
588	2015	337	15.0S	315.0	06-Apr-04 04:11	71.3	110.6	0	1	1
591	2015	217	15.0S	247.5	15-Apr-04 06:21	38.0	9.0	0	1	0
596	2015	142	7.5S	112.5	20-Apr-04 22:39	74.5	28.2	0	1	2
649	2018	82	15.0S	37.5	16-Jul-04 02:44	79.0	604.5	3	1	3
652	2018	7	7.5N	345.0	21-Jul-04 18:46	254.8	203.9	0	1	10
656	2019	67	15.0S	82.5	13-Aug-04 11:12	174.6	409.5	1	9	8
687	2022	202	7.5N	172.5	24-Oct-04 01:11	89.5	30.5	0	1	4
691	2022	127	15.0N	142.5	29-Oct-04 17:41	68.2	553.2	1	4	7
696	2022	22	7.5N	22.5	06-Nov-04 16:48	117.5	830.1	1	4	16
708	2023	37	7.5N	37.5	02-Dec-04 20:57	64.8	1250.1	0	1	0
718	2025	187	7.5S	195.0	15-Jan-05 03:29	78.9	59.5	0	1	0
720	2025	172	15.0N	180.0	16-Jan-05 06:50	230.7	4385.8	1	2	8
758	2029	112	7.5S	135.0	10-May-05 01:04	98.5	36.1	0	1	5
759	2029	67	15.0N	52.5	13-May-05 10:45	96.3	366.7	0	1	2
763	2029	37	15.0S	15.0	15-May-05 17:11	63.2	269.5	0	3	11
772	2030	157	15.0S	135.0	02-Jun-05 20:32	57.6	551.7	0	1	3
803	2033	97	7.5N	60.0	28-Aug-05 00:43	70.4	20.3	0	1	0
808	2034	247	15.0S	225.0	12-Sep-05 22:20	146.5	1233.4	2	3	8
822	2036	97	7.5S	82.5	17-Nov-05 21:12	122.0	870.7	0	1	4
826	2037	277	7.5S	255.0	01-Dec-05 12:58	86.1	199.8	0	2	8
875	2042	142	15.0S	120.0	27-Apr-06 08:52	70.3	175.7	0	1	1
898	2045	307	7.5S	330.0	05-Jul-06 12:39	78.5	59.6	0	1	1
930	2051	352	7.5S	7.5	12-Dec-06 17:30	111.5	884.0	1	0	2

6.4.3 Results and Discussions

The results of the analysis of our sample of 74 ARs are shown in Figure 6.6 – 6.7.

Figure 6.6 shows a graph plotted between the mode energy (ME) and magnetic index (MI) of ARs. The straight line fitted using a linear regression model is shown by the solid line while the dashed lines represent 95% confidence levels.

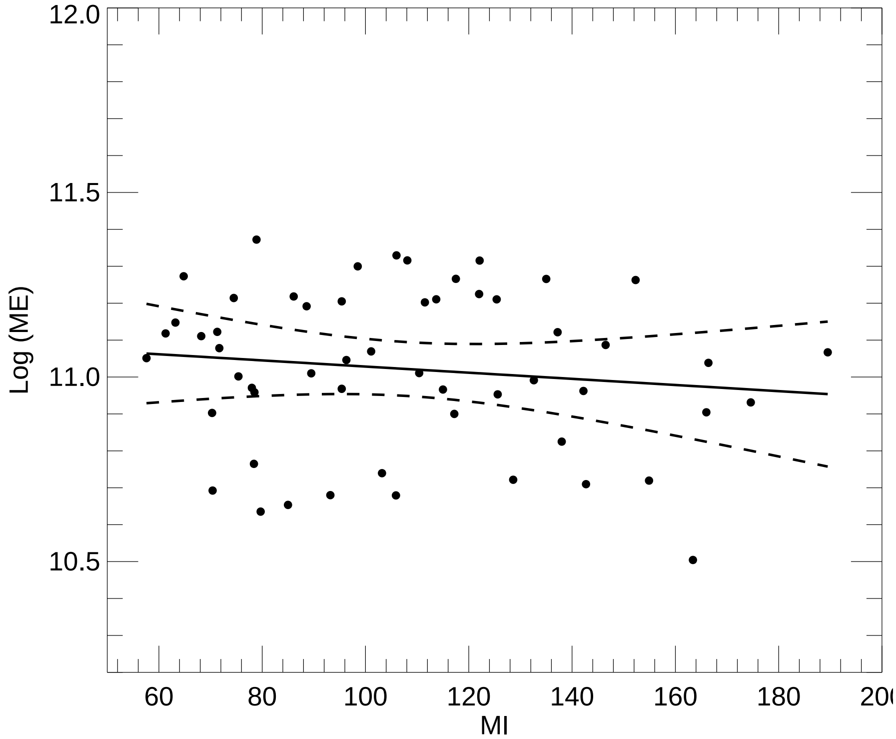

Figure 6.6 Association of mode energy and magnetic index of ARs.

The slope of the linear regression line in this case is a very small negative value, *i.e.*, nearly zero. It is revealed that the energy of the modes very slowly decreased with increasing magnetic index of ARs. This is some what perplexing due to the reason that strong magnetic fields of ARs are expected to absorb p-mode power (Braun, Duvall and Labonte, 1987; Braun, Labonte and Duvall, 1990; Rajaguru, Basu and Antia, 2001; Mathew, 2008). Therefore, mode energy should decrease faster with increasing MI than the rate as inferred by the nearly zero slope in Figure 6.6. However, it is to note that we have computed mode energy for our ARs using the data-cubes corresponding to their maximum flaring periods. These include essentially the net result of the effects of absorption by sunspots and amplification by flares. In ARs of large and strong magnetic fields having large MI but lower flare index (FI), the effect due to absorption would dominate. On the other hand, when the flare energy is larger than the energy absorbed by sunspots, then the amplification effect due to flares would dominate. Therefore, the net energy

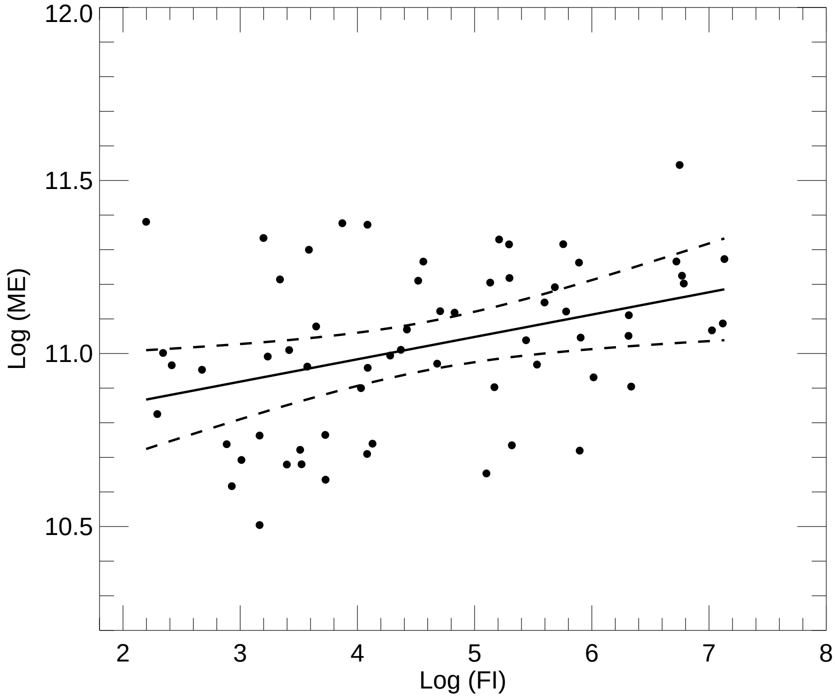

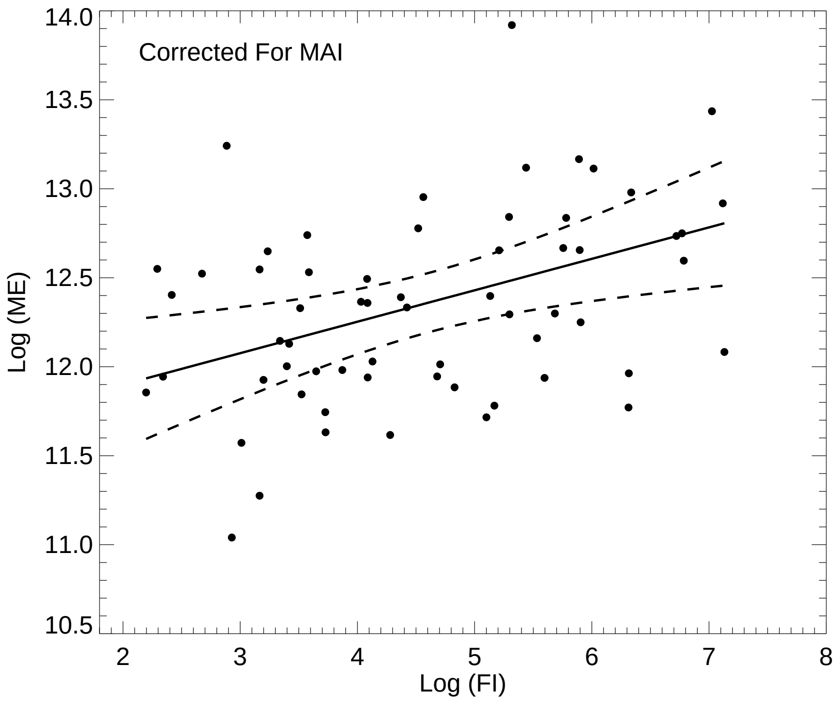

Figure 6.7 Association of p-mode energy (ME) and flare index. The straight line fits using a linear regression model are shown by solid lines while the dashed lines represent 95% confidence levels. Top (bottom) panel shows the uncorrected (corrected) ME for magnetic index for each ARs.

of p-modes would involve relatively substantial flare related effect (as discussed in Section 6.2). We suggest that near zero slope found in the figure, *i.e.*, p-mode energy not showing significant decrease with increasing MI, may be attributed to the flare effects.

In Figure 6.7 (top panel), we have plotted p-mode energy with the flare index of the ARs. The solid and dashed lines have same meaning as in Figure 6.6. The fitted line is given by ME $= (10.72 \pm 0.10) + (0.07 \pm 0.02)$FI. This shows that the slope of the regression line is significant. The positive value of slope indicates an increase in mode energy with flare energy, *i.e.*, mode energy is amplified by flares.

In order to make a better identification of flare-related effects on the mode power, we have corrected it for the sunspot related absorption effects as suggested in Rajaguru, Basu and Antia (2001). The corrected mode energy is plotted in Figure 6.7(bottom panel) which provides the straight line fit corrected to ME $=$ $(11.54 \pm 0.23) + (0.18 \pm 0.05)$FI, showing a further improvement in the association of mode and flare energies.

6.5 Summary and Conclusions

We have examined NOAA 10486 helioseismically using ring diagram analysis during an extremely energetic and long duration X17/4B flare of 28 October 2003. We found clear indication of flare-related variations in the p-mode parameters. We evaluated these parameters by changing the temporal position of the flare within the Doppler data-cubes obtained for the AR, which amounts to changing the level of the pre- and post- effects in the data-set. The ring diagram analysis of different data-sets thus constructed provided the following important results:

- The amplitude of p-modes increased up to 150% in the case of the flare placed in the beginning of the data-set as compared to the case when flare was placed near the end or outside the data-cube. A similar result is obtained for p-mode energy as expected due to its relation to the amplitude, manifesting the rate of energy supplied to the p-modes by the large flare.

- Amplitude and energy of the modes decreased with radial order indicating that the effect of the flare decreased with increasing depth. Furthermore, we found that the amplitude and energy of modes increased with frequency. This suggests that modes with high natural frequencies are amplified more by the flare as compared to the low frequency modes.

- We found a strong evidence of evolutionary and flare related changes in the p-mode parameters in NOAA 10486 during its disk transit.

The statistical study of 74 ARs of solar cycle 23 showed association of p-mode energy with flare energy. This association was found to become stronger after correcting the mode energy for magnetic index of the ARs. These results further support the expected mode excitation by flares.

Chapter 7

Sub-photospheric Flows in Solar Active Regions

7.1 Introduction

Properties of Solar photosphere have been extensively studied during the past decades mostly using the surface observations of magnetic tracers and Doppler measurements. These tracers have revealed that the magnetized regions rotate faster than the surrounding medium of field-free plasma, and their rotation rates depend on the stage of evolution and age. In particular, it is reported that shorter lived small features rotate $\sim 5\%$ more slowly than the long lived ones (Golub and Vaiana, 1978). Using magnetic field observations from NSO, Komm, Howard and Harvey (1993) found a poleward meridional flow of the order of 10 m s^{-1} near the equator. The magnitude of this flow increases with latitude, reaching 13.2 m s^{-1} at mid latitude around 39°, and then decaying slowly at higher latitudes. Doppler measurements show poleward meridional flows at the solar photosphere (Duvall, 1979; Labonte and Howard, 1982; Ulrich *et al.*, 1988). From these results, it was realized that ARs can be used as a tool for sub-photospheric diagnostics (Howard, 1996).

The advent of helioseismology has made it possible to study the sub-photospheric structures and flows (Deubner and Gough, 1984; Gough and Toomre, 1991) by probing the solar interior using acoustic modes of oscillations (Ulrich, 1970; Leibacher and Stein, 1971). Helioseismic studies have revealed that sunspots are rather shallow, near-photospheric phenomena (Kosovichev, Duvall and Scherrer, 2000; Basu, Antia and Bogart, 2004). Local helioseismology has further revealed the sunspots to be locations of large flows at the photosphere (Haber *et al.*, 2002; Braun, Birch and Lindsey, 2004; Zhao and Kosovichev, 2004; Komm *et al.*, 2005b). Recently, using simulations, Schüssler and Rempel (2005) have presented a mechanism for the disconnection of sunspots from their magnetic roots. They suggested that the combination of pressure buildup by the upflows and radiative cooling of the upper layer of a rising flux tube makes the tube weak in the interior at depths of several megameters. Thus advected flux tube is fragmented by convective motions and fluting instability. Using correlation tracking of Doppler features, Švanda, Klvaňa and Sobotka (2009) have reported that a majority of ARs display sudden decrease in rotation speed compatible with dynamic disconnection of sunspots from their parental magnetic roots.

Earlier studies have found that magnetic helicity of ARs follows a hemispheric trend, *i.e.*, it has positive (negative) sign for ARs located in the southern (northern) hemisphere (Pevtsov, Canfield and Latushko, 2001). Such a hemispheric trend is also reported for flows in ARs (Komm *et al.*, 2005b; Zaatri *et al.*, 2006; Komm *et al.*, 2007), *viz.*, the zonal flows exhibit larger amplitudes in southern hemisphere especially at higher latitudes coinciding with larger magnetic activity in that hemisphere. This may be attributed to the inclination of the solar rotation axis (Beck and Giles, 2005). Also, ARs advect poleward at nearly the same rate as the quiet regions (QRs) (Hindman, Haber and Toomre, 2009) and show convergent horizontal flows combined with cyclonic vorticity; counter clockwise in the northern hemisphere (Komm *et al.*, 2004b; Zhao and Kosovichev, 2004).

Activity related variations are reported in solar photospheric flows (Vorontsov *et al.*, 2002; Basu and Antia, 2003; Ambastha *et al.*, 2004; Howe *et al.*, 2005).

It is believed that sheared flows in sub-photospheric layers give rise to sunspot motions that may lead to unstable magnetic topologies, causing reconnection of magnetic field lines required for flares. Basu and Antia (2003) have found that the maximum meridional velocity of sub-photospheric flows is smaller when the Sun is more active. The maximum unsigned zonal and meridional vorticities of ARs are correlated with the total X-ray flare intensity (Mason *et al.*, 2006). Furthermore, steep meridional velocity gradients are found in flaring ARs at the depth range of 4–5 Mm (Ambastha *et al.*, 2004), which decreased after flares.

Relation between photospheric proper motions and flare activity has been studied earlier extensively by Ambastha and Bhatnagar (1988); Fontenla *et al.* (1995) among others. Correlation tracking studies have discovered some cases of small-scale vorticity at the photosphere preceding a flaring event with timescales around an hour (Yang *et al.*, 2004). Sunspot rotation in flaring ARs have also been found (Brown *et al.*, 2003). Relationship of flare activity with some statistical properties of ARs has been studied by Lu (1995) and Abramenko and Longcope (2005), among others. Although internal flows in ARs and QRs have been studied recently (Mason *et al.*, 2006; Komm, Howe and Hill, 2009), their distinctive characteristics in flare productive ARs as compared to that in dormant ARs are not well understood. Further investigations are required to explore the nature of variations in the sub-photospheric flows during flares.

In this chapter, we plan to discuss properties of internal flows in ARs of varying levels of flare productivity and magnetic complexity, observed during the Solar Cycle 23, including large ARs such as NOAA 10030, 10484, 10486, 10070, *etc*, also termed as SARs. These SARs are expected to possess distinctly different characteristics of flows in their interiors as compared to the less productive or dormant ARs. We have addressed important issues on the relationship of flow characteristics with the lifetime of ARs, magnetic and flaring activities and hemispheric trends. We have studied the flow characteristics at both the photospheric and sub-photospheric levels of ARs.

In the section 7.2, we present basic formalism to derive various flow parameters. Section 7.3 describes the three dimensional flow distribution beneath the AR NOAA 10486 and a reference QR. Section 7.4 describes variations in sub-photospheric flows of the AR NOAA 10486 during pre- to post flare phases of a large flare. Section 7.5 presents the association of sub-photospheric flows and energetic transients. We discuss an interesting and important relationship of sub-photospheric flow (vorticity) with the lifetime of ARs. Finally, in Section 7.6 we give the summary and conclusions.

7.2 The Basic Formalism

We derive sub-photospheric zonal and meridional velocities ($u_{\rm x}$, $u_{\rm y}$) as a function of depth under ARs by inversion techniques. For the calculation of these velocities, we use photospheric, surface velocity parameters ($U_{\rm x}$, $U_{\rm y}$) of different modes obtained from ring diagram analysis (for detail, please see Chapter 5). In the following, we formulate some important flow parameters which facilitate our study of sub-photospheric flow topology of ARs.

7.2.1 Gradient, Divergence and Vorticity of Horizontal Flows

Having derived the horizontal component ($u_{\rm x}$, $u_{\rm y}$) of flows with depth, we can calculate some topological parameters to describe the nature of flows, *viz.*, gradient, divergence and vorticity. These parameters further help in understanding the distinctive characteristics of flaring ARs as compared to the dormant ARs and QRs. The radial gradients in horizontal components of flows (*i.e.*, depth derivative) are given by

$$\mathrm{d}'u_x = \frac{\partial u_x}{\partial z}, \qquad \mathrm{d}'u_y = \frac{\partial u_y}{\partial z} \tag{7.1}$$

We have carried out the numerical differentiation in deriving gradients of horizontal component using Lagrange three point interpolation method. The radial gradient of horizontal velocity gives the greatest rate of change of horizontal flow with depth, which is useful in inferring the number of sheared layers underneath an AR.

The divergence of horizontal component of velocity is determined using,

$$\mathrm{div}\, u_h = \frac{\partial u_x}{\partial x} + \frac{\partial u_y}{\partial y} \tag{7.2}$$

A consequence of Gauss' divergence theorem is that the divergence of a vector field is a local measure of the presence of "source" and "sink" in the field. A source is the point where fluid is entering and a sink is the point where the fluid leaves. The positive (negative) value of $\mathrm{div}\, u_\mathrm{h}$ describes the diverging (converging) nature of flows beneath ARs.

Twist in a fluid field can be determined by deriving "circulation". It is a line integral of the fluid velocity around a closed curve. If $\mathbf{u}$ is the fluid velocity and d$\mathbf{l}$ is unit vector along a closed curve C then circulation in fluid velocity around a closed curve C can be written as,

$$\zeta = \oint_C \mathbf{u} \cdot \, \mathrm{d}\mathbf{l} \tag{7.3}$$

From Stoke's theorem it can be written as,

$$\zeta = \oint_C \mathbf{u} \cdot \, \mathrm{d}\mathbf{l} = \oint_S (\nabla \times \mathbf{u}) \cdot \, \mathrm{d}\mathbf{S}$$

or

$$\zeta = \oint_S \omega \cdot \, \mathrm{d}\mathbf{S} \tag{7.4}$$

where, vorticity ω is given by,

$$\omega = \nabla \times \mathbf{u} \tag{7.5}$$

From Equation 7.4, we can say that vorticity is essentially the "circulation" or "rotation" of local angular rate of rotation per unit area taken around an infinitesimal loop, *i.e.*, it is curl of the fluid velocity. It can also be considered as the circulation per unit area at any point of fluid fields. It is a vector quantity having its direction along the axis of fluid rotation. For a two dimensional fluid the magnitude of vorticity can be written as

$$\omega = \frac{\partial u_y}{\partial x} - \frac{\partial u_x}{\partial y} \tag{7.6}$$

Its direction is perpendicular to the plane of fluid which can be described by the right-hand rule, *i.e.*, if a parcel of fluid is rotating clockwise (counterclockwise) it will be negative (positive).

7.2.2 Vertical Component of Flow

The inversion of sub-photospheric flows gives only the horizontal components (u_{x}, u_{y}) of velocity vector. But for the topological study of sub-photospheric flows, we also require the vertical component (u_{z}). It can be determined from the continuity equation as suggested by Komm *et al.* (2004b):

$$\frac{\partial \rho}{\partial t} + \nabla \cdot (\rho \mathbf{u}) = 0 \tag{7.7}$$

where, density ρ and flow velocity $\mathbf{u}$ are functions of position and time, *i.e.*, $\rho \equiv \rho(x, y, z)$, $\mathbf{u} \equiv \mathbf{u}(x, y, z)$. Here, we can drop the time derivative of density $\frac{\partial \rho}{\partial t} \to 0$ because in ring diagram analysis, we use time series of length $t = 1664$ min. Further, the ring diagram analysis gives average flow over the region of small size (16°×16°) as compared to the whole Sun. Therefore, the density can be considered to be constant for all the points (x, y) at a given depth d, *i.e.*, it is only a function of depth, or, $\rho(x, y, z) \to \rho(z)$. Thus, Equation 7.7 can be written as

$$\frac{\partial u_z}{\partial z} + \left(\frac{1}{\rho}\frac{\partial \rho}{\partial z}\right) u_z + \nabla \cdot u_h = 0 \tag{7.8}$$

This is a standard differential equation, and its solution can be written as

$$u_z(d) = -\frac{1}{\rho(d)} \int\limits_0^d \rho \nabla \cdot u_h \, \mathrm{d}z \tag{7.9}$$

Here, we have assumed the vertical velocity at the photosphere, $u_z(0)$, to be zero, which is similar to the assumption as considered by Komm *et al.* (2004b). As we do not have information about the density and horizontal velocities continuously with depth, we can transform the Equation 7.9 into a summation using the Equation A.3.

$$u_z(d) = -\frac{1}{\rho(d)} \sum_{i=0}^{N} w_i \rho(z_i) \, \mathrm{div}\, u_h \tag{7.10}$$

where, w_i is defined by Equation A.4, and N represents total number of mesh points used in deriving the velocity u_z at the depth d. The density ρ in the interior can be taken from a standard solar model, such as, Christensen-Dalsgaard *et al.* (1996), and the divergence ($\mathrm{div}\, u_\mathrm{h}$) of horizontal component can be computed using Equation 7.2.

7.3 Three Dimensional Flow Distribution Beneath NOAA 10486

As mentioned in Chapter 6, NOAA AR 10486 was one of the most flare productive, magnetically complex regions observed during Solar Cycle 23. Therefore, we expect distinctly different kind of flows beneath this SAR as compared to other ARs on the Sun. Figure 7.1 shows a map of the three components of flows in the sub-photospheric region of the Sun over the $\pm 60^\circ$ range of latitudes and longitudes. The dense-packed GONG data-cubes used in deriving the flows started from 12:26/27 October 2003 extending over a temporal length of 1664 minutes. Therefore, this map essentially gives the average flow and also includes information of all the flares occurring in the region during this period. In the figure, the vectors represent magnitude and direction of the horizontal component of velocities while the red (blue) colors represent the upward (downward) flows or vertical velocities. A color bar labeled with u_z velocities is shown at the top for scale. The column in the right marks the depth at which the velocity map is constructed. The NOAA numbers of ARs with areas $> 100\,MH$ observed in the visible face of the Sun on 27-28 October 2003 are marked at their appropriate locations.

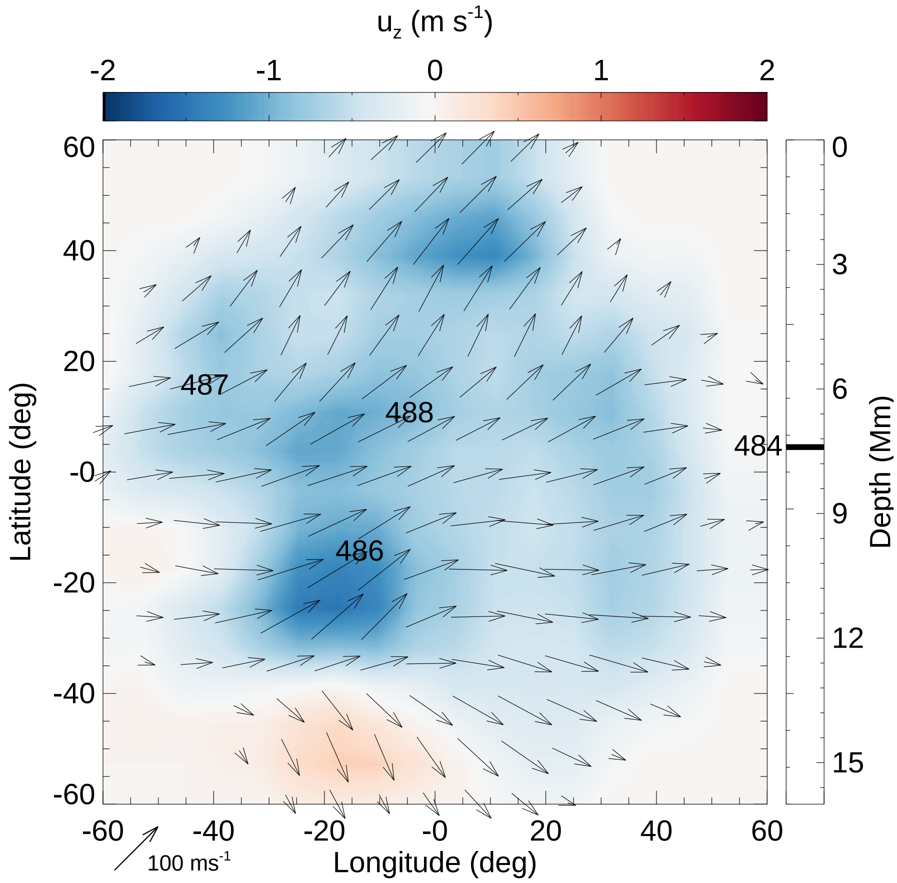

Figure 7.1 A map of solar sub-photospheric flows of 27-28 October 2003. Major ARs observed on the day are marked by their NOAA numbers at appropriate locations. Vectors represent horizontal flows while the color (red/blue) shows vertical (upward/downward) flows.

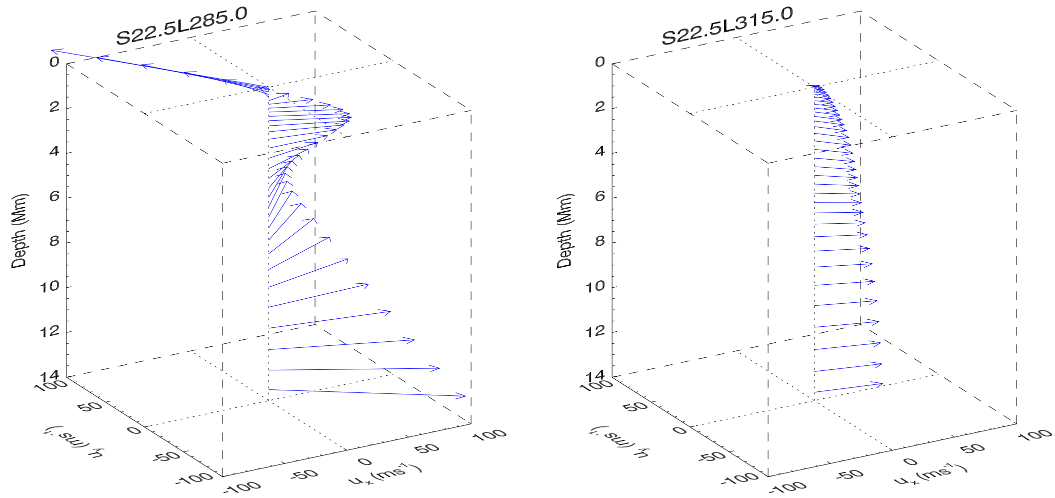

Figure 7.2 A 3-D view of flows with depth for (left panel) NOAA 10486, and (right panel) a QR having same latitude and time but a different longitude.

Figure 7.1 shows strong downward flows at the AR locations as compared to QRs. The horizontal flows at the lower latitudes are generally directed along the equator while at the higher latitudes they are directed towards the poles. This pattern shows a large scale poleward meridional circulation from the equator. Interestingly, the velocity vectors over NOAA 10486 are found to deviate from the general direction of horizontal flows at that latitude. This reveals that the flow fields in the sub-photospheric interior of NOAA 10486 are twisted as compared to its surroundings.

In Figure 7.2, we have shown a 3-D view of flow profiles beneath NOAA 10486 (left panel) as compared to a QR taken for reference (right panel) located at the same latitude (-22.5°) but a different longitude. This figure illustrates that the flow field of the AR, having very complex and strong magnetic fields, possessed a strongly twisted helical structure as compared to the untwisted flows in the QR. It may further be noted that the magnitudes of horizontal velocities are much larger in the depths of AR as compared to the QR.

This AR produced a long duration, extremely energetic event X17/4B on 28 October 2003. Therefore, a study of variations in sub-photospheric flow structure in the pre- and post-flare phases is of particular interest. As the ring diagram analysis provides only the average properties of the region over 1664 minutes, we have used appropriately constructed data cubes for our study by placing the onset time of the flare at different temporal locations within the data cubes (for detail please see Section 6.2). In the following, we give detailed results of this study.

7.4 Variations in Sub-photospheric Flows with a Large Flare

As discussed in Section 7.1, energetic transients are caused by the changes in magnetic field lines which are rooted beneath the photosphere. The sub-photospheric flows result in braiding and intertwining the rising magnetic flux tubes. Therefore, we expect the structural changes in magnetic field configuration to be governed by sub-photospheric flows. In order to investigate this issue, we determine sub-photospheric flows using ring diagram analysis of the data-cubes constructed for pre- and post-flare phases of the X17/4B event of 28 October 2003.

7.4.1 The Observational Data and Analysis

We use the same sets of data used in Chapter 6. The fitted velocities ($U_{\rm x}$, $U_{\rm y}$) for different modes were used to calculate the zonal ($u_{\rm x}$) and meridional ($u_{\rm y}$) velocities as a function of depth (Chapter 5). We compute the vertical component of flows ($u_{\rm z}$) using Equation 7.10. Then, we determined the divergence and vertical vorticity using Equations 7.2 and 7.6, respectively. We also computed the kinetic helicity density (for detail please see Chapter 8) using Equation 8.9.

7.4.2 Results and Discussions

We have found the following important results about the sub-photospheric flows beneath NOAA 10486 with the large flare. The profiles of zonal velocities u_x with

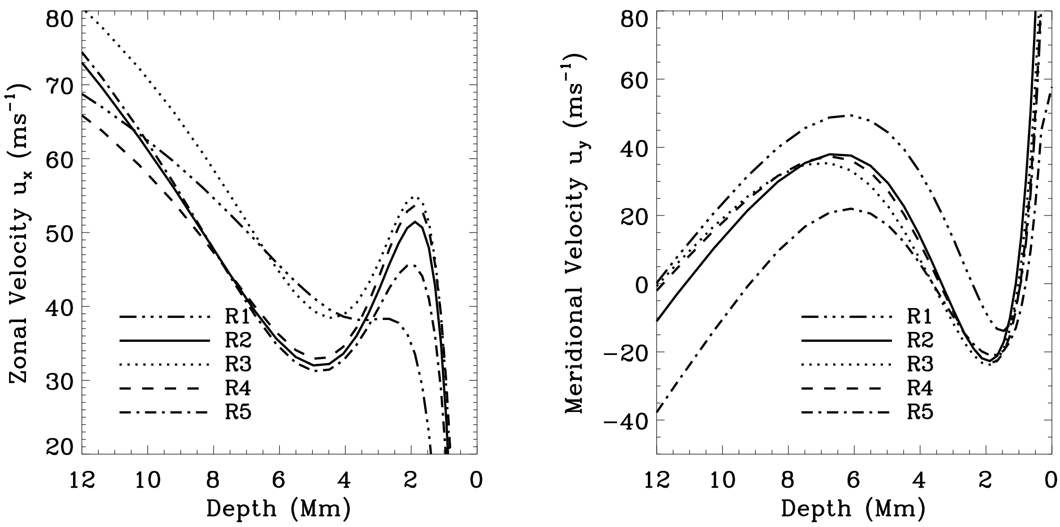

Figure 7.3 Zonal u_x (left panel) and meridional u_y (right panel) velocity profiles with depth from 0 to 12 Mm corresponding to the data-sets of NOAA 10486, $R_i, i = 1, \ldots 5$ (see Section 6.2).

depth are shown for R_1 to R_5 in Figure 7.3 (*left panel*), while the corresponding meridional velocities u_y are shown in Figure 7.3 (*right panel*). Both u_x and u_y exhibited significant systematic changes with changing temporal position of the flare onset in the respective data cubes. A large decrease in zonal velocity around the depth $\approx$4 Mm is a common feature in all cases. However the depth where the minimum of u_x occurred varied from the shallowest for R_1 to the deepest for R_5.

It is found that u_y decreased rapidly from the photosphere to the depth of $\sim$1 Mm for all the data-sets. Thereafter, it increased and attained a peak at $\sim$6 Mm. It is inferred that the gradient in u_y was largest for R_1 (*i.e.*, before the flare) and it decreased systematically from R_2 to R_5 as the post-flare effects increased. This confirms the presence of steep meridional velocity gradient in ARs during the pre-flare phases and subsequent decrease after large flaring activities as reported by Ambastha *et al.* (2004).

Apart from the horizontal component of velocity, we have calculated some other physical quantities of the sub-photospheric flows. These are (a) the divergence of horizontal component of velocity, (b) vertical component of velocity u_z,

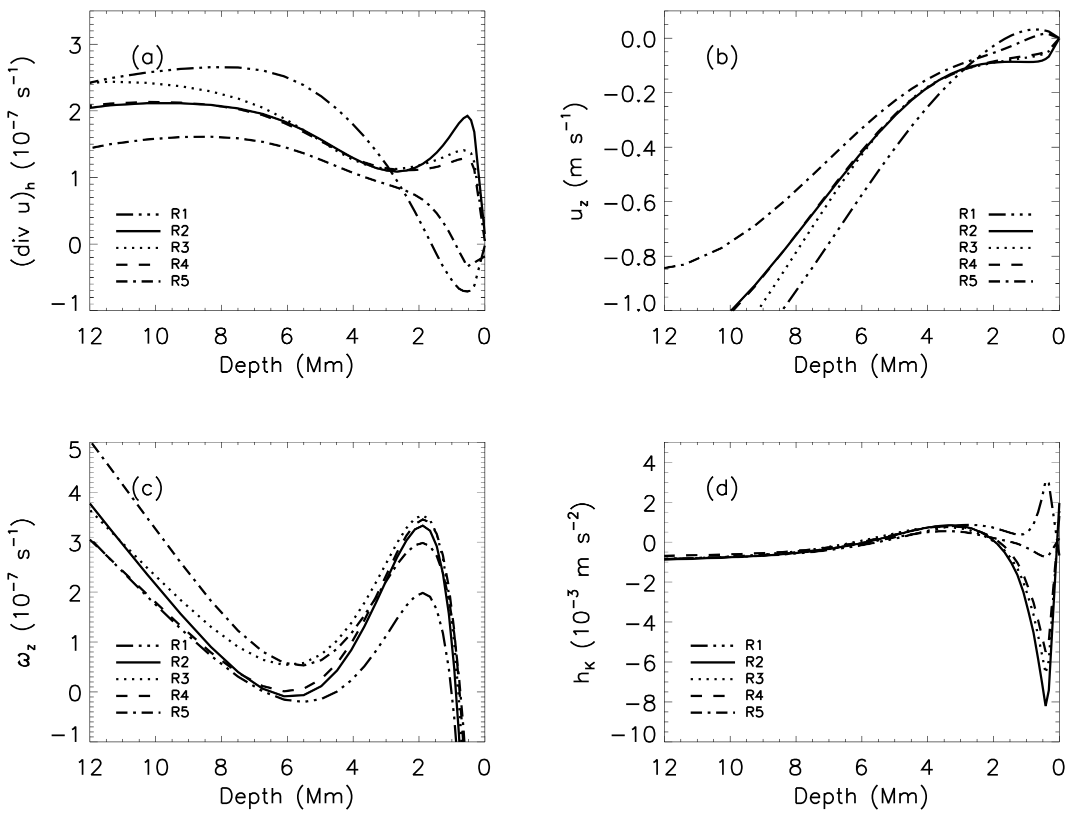

Figure 7.4 Inverted profiles of (a) divergence of horizontal components of velocity, (b) vertical component of velocity u_z, (c) vorticity and (d) kinetic helicity density, with depth from 0 to 12 Mm for the data-sets $R_i, i = 1, \ldots 5$.

(c) vertical vorticity, and (d) kinetic helicity density. These quantities are shown in Figure 7.4(a). It is seen that the divergence of horizontal component of velocity (u_h) at the depth of ≈ 1 Mm changed from a small negative value for R_1 to a large positive value for R_2, and then gradually decreased for R_3 to R_5 (Figure 7.4a). This suggests that the perturbation in the flows at this depth gradually returned back to the initial or pre-flare state after the flare decayed. On the other hand, the magnitude of positive divergence at depths below 3 Mm decreased for R_1 to R_5. This further indicates that the large flows present before the flare onset (*i.e.*, in R_1) changed from converging to diverging during the flare and then reverted back to converging after the flare.

The direction of the vertical component of flow, u_z, at the depth of ≈ 1 Mm changed from the upward in R_1 to downward in R_2, and then back to upward in R_5 through R_3 - R_4 (Figure 7.4b). The u_z profiles converged to the same negative value (≈ -0.1 m s^{-1}) at the depth of $\sim$3 Mm, and then diverged systematically from R_1 to R_5 as the depth increased. The vertical component of vorticity vector, ω_z, is shown in Figure 7.4(c) for R_1 to R_5. The peak in ω_z near 2 Mm and the trough near 6 Mm manifest a bipolar flow structure of the AR.

Similarly, kinetic helicity density, h_k, changed from a small positive value for R_1 to a large negative value for R_2, increasing toward the level of R_1 for R_3 - R_5 (Figure 7.4d). Interestingly, it is observed that flare-related variations in helicity density h_k are confined within a shallow region, from the photospheric to a depth of around 3 Mm. For depths greater than 3 Mm, h_k derived for all the five cases approached toward the same value. These systematic changes in sub-photospheric parameters (u_h, u_z, ω_z and h_k) from R_1 to R_5 provide unambiguous evidence of the systematic variations in sub-photospheric dynamics of the AR related to the large flare in NOAA 10486.

7.5 Sub-photospheric Meridional Flow, Vorticity and the Lifetime of Active Regions

In order to further establish the results obtained for NOAA 10486 as a general feature of flaring ARs, we have carried out a detailed analysis of several flare productive and dormant ARs. We have tried to find whether lifetime of ARs has any association with their sub-photospheric topology. This may help in predicting the life expectancy of ARs. We have attempted to search for hemispheric trends, if any, in the sub-photospheric meridional flows. With these aims, we have obtained statistical properties of sub-photospheric flows for a sample of 74 ARs of Solar Cycle 23. The results are discussed in the following.

7.5.1 The Observational Data and Analysis

For our statistical study of sub-photospheric flows of ARs, we use the same data set as used for the study of p-mode and flare energies described in Section 6.4. We now use these to examine the relationship of internal flows with magnetic and flare activities of ARs (see Section 6.4.2).

The remaining lifetime (τ) of ARs is estimated from the information provided by *solar monitor* for the Earthside and MDI farside imaging as follows. We followed the signature of an AR using magnetograms from the reference, central time t_r of the data cube until the time t_e when the AR disappeared. In case when the AR rotated past the west-limb of the Sun to the farside, we followed up its signature using the acoustic hologram images until its disappearance at time t_e. The remaining lifetime (τ) of an AR is then estimated from the difference $(t_e - t_r)$.

7.5.2 Results and Discussions

The main results of our analysis for the sample of 74 ARs are shown in Figures 7.5–7.8.

Meridional Velocity and Gradients

Meridional velocities, u_y, obtained for two of the ARs of our sample, NOAA 10030 (northern hemisphere) and 10486 (southern hemisphere), are shown by the solid curves in Figure 7.5. The velocities are obtained from the photosphere to a depth of 14 Mm. The data sets used for these ARs correspond to 15 July 2002 and 27 October 2003, respectively. The dash-dotted curves show the greatest rate of change, or the gradient of u_y, along the vertical direction z, *i.e.*, $\mathrm{d}u_y/\mathrm{d}z \equiv \mathrm{d}'u_\mathrm{y}$. It is evident that the magnitudes of u_y and $\mathrm{d}'u_\mathrm{y}$ are more significant as compared to their errors in the depth range from 1.5 to 10 Mm.

The profiles of u_y and $d'u_y$ for the two ARs, located in opposite hemispheres, exhibit opposite trends with depth. The two extrema near P and Q of u_y, however,

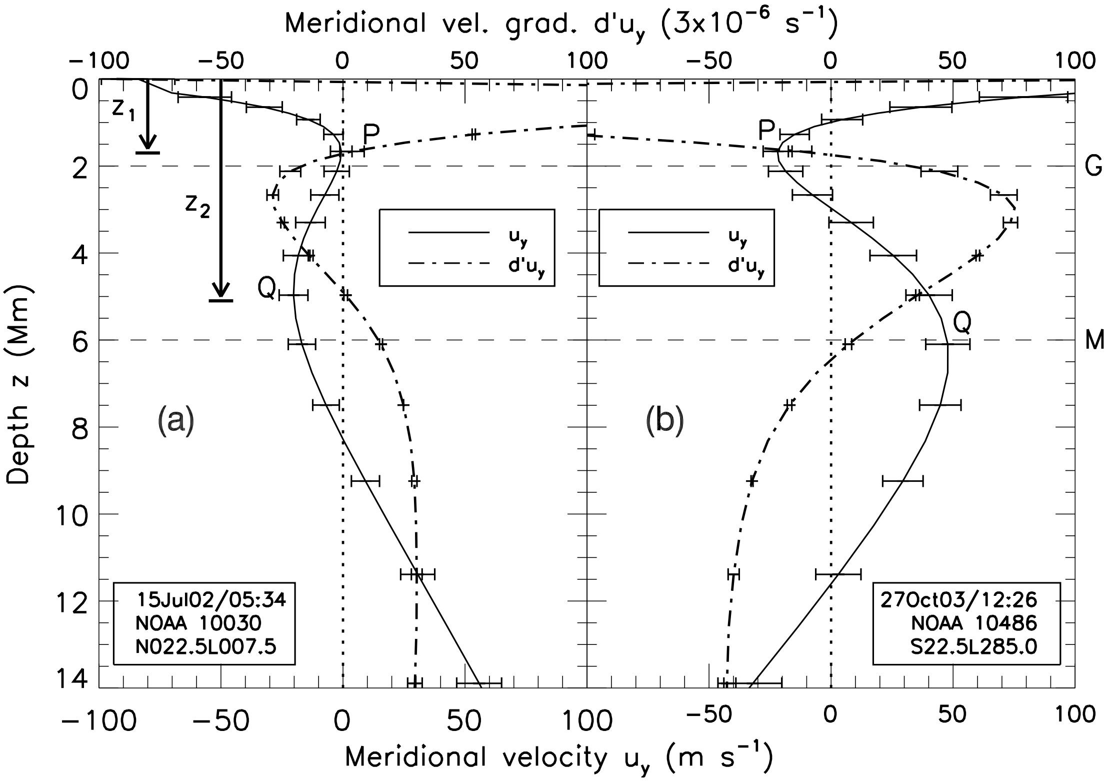

Figure 7.5 Meridional velocity profiles (solid curves) in the depth range 0–14 Mm for two ARs (a) NOAA 10030 (northern hemisphere) and (b) NOAA 10486 (southern hemisphere). The dash-dotted curves correspond to the meridional velocity gradients. Error bars show the corresponding uncertainties at 1σ level. Horizontal dashed lines at the depths of 2 and 6 Mm, marked G and M, correspond to the convective scale sizes of granules and mesogranules, respectively.

occurred at around the same depths for both the ARs. It is found that $d'u_y$ changed sign with increasing depth from the photosphere to a depth of 1.5 Mm where $d'u_y$ is positive (negative) in the northern (southern) hemisphere. Thereafter, it changed sign again in the depth ranges of 1.5–5 Mm and 5–10 Mm. From these sign reversals of u_y and $d'u_y$ profiles, we can infer that there exist three sheared layers in the interior of these two ARs. This appears to be a general feature of all flare productive and complex ARs of our sample. Some more examples of these ARs are shown in Figure 7.6.

We may infer here that the locations of the extrema of u_y occur at the depths of 2 and 6 Mm, marked for reference in Figures 7.5– 7.6 as "G" and "M", respec-

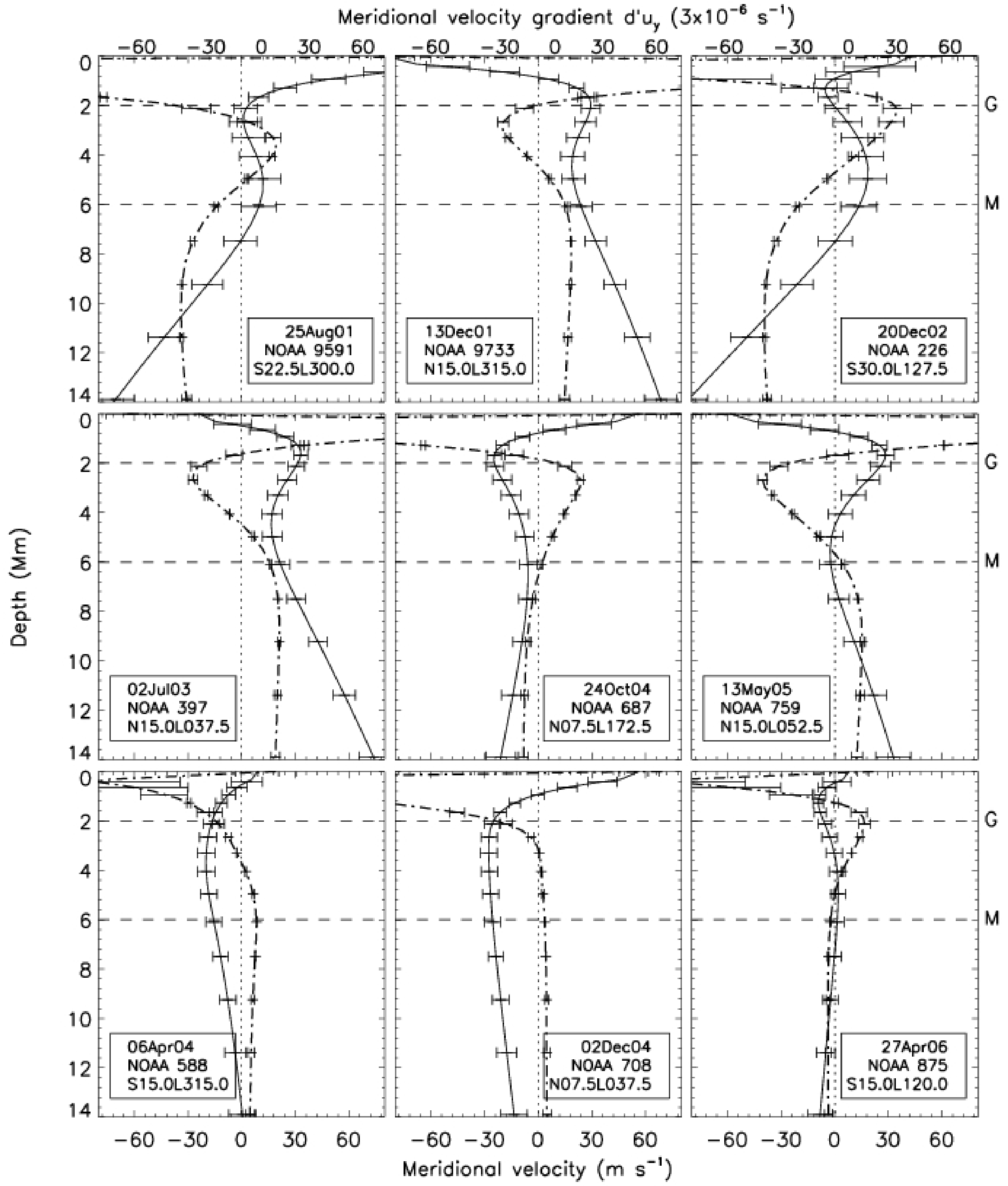

Figure 7.6 Meridional velocity profiles (solid curves) in the depth range 0–14 Mm for nine ARs of our sample. The dash-dotted curves correspond to the meridional velocity gradient. Error bars show the corresponding uncertainties at 1σ level. Horizontal dashed lines at the depths of 2 and 6 Mm, marked G and M, correspond to the convective scale sizes of granules and mesogranules, respectively.

tively. These depths correspond to the convective scale sizes of granulations and mesogranulations. These depths were also referred as the locations of ionization zones of H^+ and He^+ ions by Simon and Leighton (1964) and November *et al.* (1981). However, recently Cattaneo, Lenz and Weiss (2001) and Rast (2003) have shown this argument to be incorrect. Rieutord *et al.* (2000) suggested that mesogranulations result from the non-linear interaction of granules (also Cattaneo, Lenz and Weiss, 2001; Rast, 2003). Rast (2003) suggested that granular scales are determined by a close association between the upflows, which sustain radiative loss, and the downflow plumes, which initiate the upflow motions. A more detailed description of surface convection and scales can be found in a recent review article by Nordlund, Stein and Asplund (2009).

Convective cells are essentially the parcels of fluid moving from the deeper layers to the upper layers and back to the bottom. The vertically rising material must change direction along a horizontal flow at two positions, *i.e.*, the bottom and the top of convective cells. In a depth distribution of the velocity flow, these turning points may be represented by peaks in the velocity profile. The extrema seen in the vertical profiles of u_y, such as the one at "G" in Figure 7.5, may be due to instabilities that drive the convective cells. The reason for convective driving near these depths is not yet clear because it depends on many factors, *e.g.*, physical properties of flux rope and its ambient medium.

We found by examining the u_y profiles in the depth range 0–10 Mm of the 74 ARs of our sample that 44 displayed two extrema while the rest, *i.e.*, 30 possessed a single extremum. A statistical analysis of our sample showed that the ARs that possessed two extrema were, in general, more complex and flare productive. The depths of the two extrema for the ARs were found to be 1.92±0.15 and 4.69±0.30 Mm, respectively. The relatively dormant ARs, on the other hand, possessed only a single extremum located at a shallower depth of 1.66±0.97 Mm, *i.e.*, with larger depth uncertainty. There are some further interesting features associated with the ARs having two extrema as compared to the ARs having only one extremum: i) larger mean magnetic field, ii) nearly twice the mean GOES flux, and iii) nearly twice the mean lifetimes.

The maximum $d'u_y$ of ARs in the two hemispheres exhibited a general trend as evident from their distribution with depths (Figure 7.7a). Most ARs lying in the northern (southern) hemisphere possessed their maximum negative (positive) gradients in the depth range 1.5–6 Mm. There are 24 (70%) out of the 34 ARs located in the northern hemisphere having negative maximum gradients while 29 (74%) out of the 39 ARs located in the southern hemisphere having positive maximum gradients. We noticed that some of those ARs which did not follow this hemispheric trend were new emerging ARs.

It is clear from Figure 7.7(a) that the magnitude of maximum $d'u_y$ decreased with depth. The fits for ARs in northern (southern) hemisphere are drawn in solid (dotted) line. These lines are described by $d'u_y = -1.15 + 0.21z$ for the northern ARs and $d'u_y = 1.05 - 0.19z$ for the southern ARs, where, z represents the depth of the maximum $d'u_y$. We do not clearly understand the reason as to why the maximum $d'u_y$ should have such a linear relationship with depth, as only 25% (21%) of the total variance in $d'u_y$ in the northern (southern) hemisphere is explained by the linear regression model. However, the hemispheric trend is clearly evident from the averages of $d'u_y$ obtained for the northern and southern hemispheres, *i.e.*, $(-5.87{\pm}0.72)\times10^{-4}\,\mathrm{s}^{-1}$ and $(5.86{\pm}0.70)\times10^{-4}\,\mathrm{s}^{-1}$, respectively.

In order to ascertain the hemispheric trend in $d'u_y$, we have computed the probability density function (PDF) for northern and southern hemispheric ARs as shown in Figure 7.7(b). The maximum of PDF for northern (southern) hemispheric ARs lies at -4.0×10^{-6} $(+2.3\times10^{-6})$ $\mathrm{m\,s^{-2}}$. This further confirms the hemispheric trend of $d'u_y$. The larger peak in the PDF of southern ARs is due to large number of ARs lying around the central region.

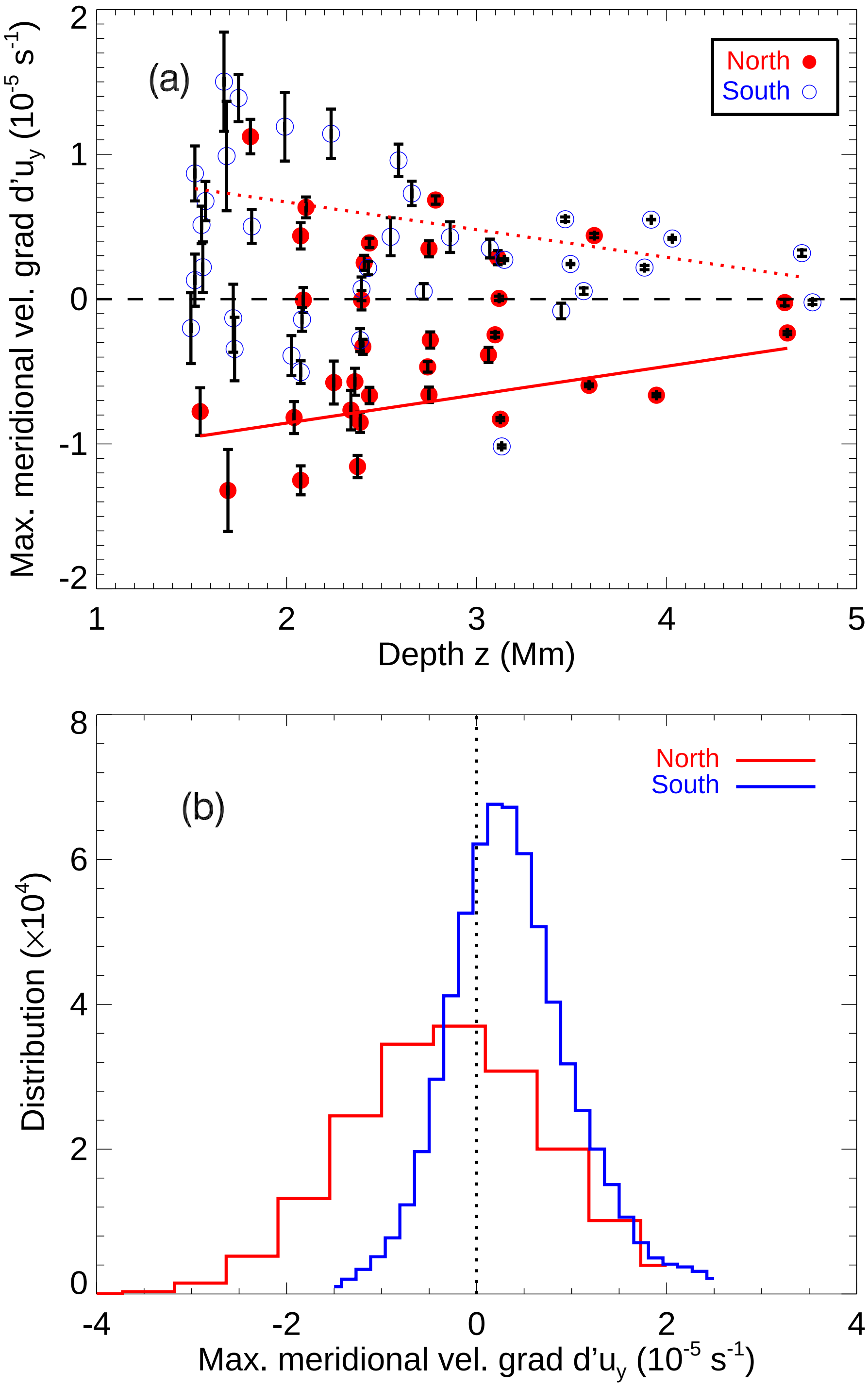

Figure 7.7 Distributions of the maximum meridional velocity gradient $d'u_y$ for 74 ARs with (a) depth z, and (b) Probability density function of maximum $d'u_y$. Filled (open) circles in (a) represent the northern (southern) hemispherical ARs. The solid (dotted) fitted lines drawn through these points indicate the general hemispheric trend of the ARs.

Vertical Vorticity and Lifetime of Active Regions

We have computed the vertical component of vorticity, ω_z, for all the ARs of our sample, however, profiles for only two ARs, NOAA 10030 and 10226, are shown here as typical examples (Figure 7.8, top panel). It is evident that ω_z varies with depth both in sign and magnitude (Figure 7.5). These profiles also show two extrema of opposite signs at the depths near 2 and 6 Mm corresponding to the scales "G" and "M". This implies that flows at these depths are twisted in opposite directions. For NOAA 10030, ω_z changed direction around the depths $\sim$1.8 and $\sim$12 Mm while for NOAA 10226, the corresponding depths are $\sim$2 and $\sim$8 Mm.

Zero vorticity may be considered as a signature of the flux rope being broken at its depths. It is possible that the connection between the magnetic structures at the photosphere and its underlying roots may get broken through a dynamical disassociation process (Fan, Fisher and McClymont, 1994), and photosphere reconnection of the two opposite polarities (Schrijver and Title, 1999). But these mechanisms have been overruled by dynamical disconnection mechanism proposed by Schüssler and Rempel (2005) based upon the buoyant upflow of plasma along the field lines. From the simulation of thin flux tubes, Schüssler and Rempel (2005) found that the disconnection takes place at a depth between 'G" and "M" marked in Figure 7.8(a). We suggest that once the flux ropes in the interior of an AR are disconnected, its remaining lifetime would depend upon the depth at which ω_z vanishes, *i.e.*, $\omega_z = 0$.

We have determined the depth of zero ω_z by a minimization procedure for the ARs. However, it was not possible to accurately approach toward the point of zero vorticity for some of the ARs of our sample due to the limitation of the available spatial resolution of GONG data. For those ARs which did not show zero ω_z in their interior, we took its absolute minimum to relate with the remaining lifetime. Further, in Figure 7.8(b), we have plotted the depths of zero vorticity, d_0, with the remaining lifetime, τ. A good linear trend is evident between the parameters d_0

and τ from the fitted line, $\tau = 6.43 + 0.34\, d_0$, drawn through the boxcar averaged points. The fit is found to be good as 72.65% of the total variance in τ is explained by the linear regression model.

Figure 7.8(b) shows that ARs having zero vorticity at deeper levels last longer. The Pearson correlation coefficient between the depth and lifetime of ARs is ∼85% for ARs in the northern and southern hemispheres. However, for the four SARs, *i.e.*, NOAA 10030, 10044, 10069, 10486, 10488, the remaining lifetimes are found to be >30 days, *i.e.*, much larger than the rest of ARs of our sample. These SARs did not follow a linear relationship with depth unlike the others. This may be attributed to a continuous process of emergence of new flux tubes in these SARs resulting in enhancing their life. Due to their distinct abnormal behaviour, we have excluded these SARs from the fittings.

Activity Related Variations in Sub-photospheric Flows

We have examined the relationship of flare productivity of ARs with the extrema of ω_z. It is found that the depth of first extremum is mildly correlated with the integrated X-ray flux released during the 1664 minutes' period of the data cube obtained for the ARs. The Pearson correlation coefficient calculated between these parameters is 20%. On the other hand, no correlation is found between the second extremum of ω_z and the integrated X-ray flux of the corresponding ARs.

The relationship of $d'u_y$ with magnetic index (MI) of ARs is shown in Figure 7.9. Although the ARs show a rather large scatter, there still appears to be a correlation between these two parameters. The fitted lines drawn for the ARs in the northern and southern hemispheres are given by $d'u_y = -0.22 - 0.31\,\mathrm{MI}$ and $d'u_y = 0.01 + 0.48\,\mathrm{MI}$, respectively. These fits reveal that the maximum $d'u_y$ of ARs increased with MI. The larger slope of the fitted line corresponding to the ARs located in the southern hemisphere indicates larger $d'u_y$ for these as compared to the ARs of similar MI located in the northern hemisphere.

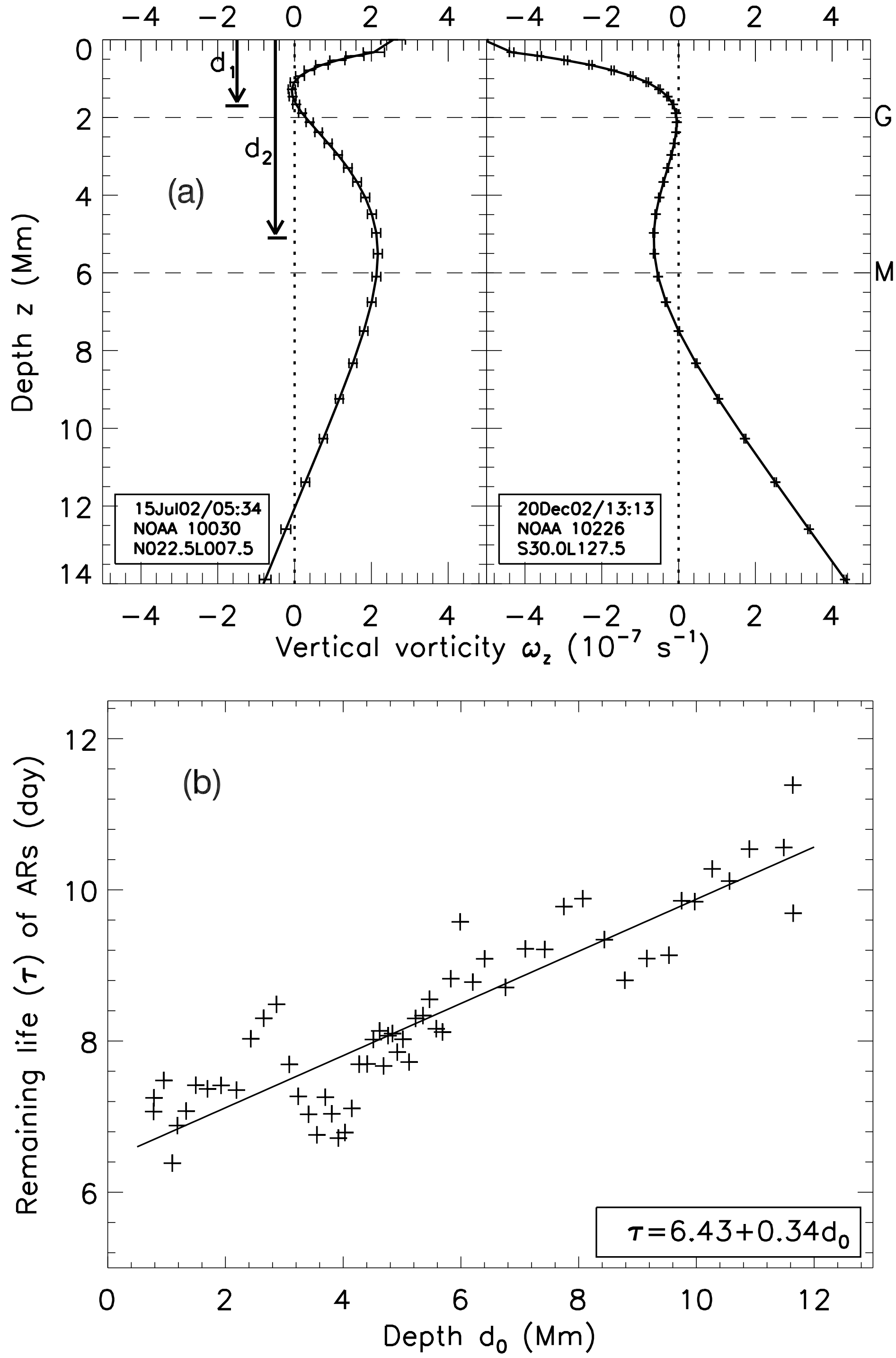

Figure 7.8 (a) Vertical vorticity profiles, with error bars, corresponding to two ARs, NOAA 10030 (northern hemisphere) and NOAA 10226 (southern hemisphere). Horizontal dashed lines at the depths of 2 and 6 Mm, marked G and M, correspond to the convective scale sizes of granules and mesogranules, respectively. (b) The remaining lifetime of the sample of 74 ARs with the depth of deepest zero vertical vorticity.

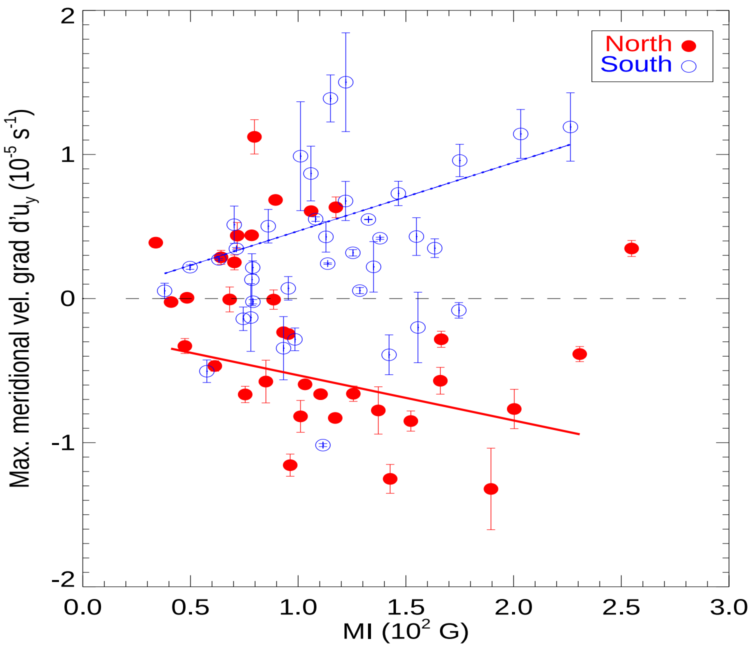

Figure 7.9 Distributions of the maximum meridional velocity gradient $d'u_y$ for 74 ARs with magnetic index MI of the AR. Filled (open) circles represent the northern (southern) hemispherical ARs. The solid (dotted) fitted lines drawn through these points indicate the general hemispheric trend of the ARs.

7.6 Summary and Conclusions

From our study of the sub-photospheric flows beneath AR and QRs, we have found stronger twists in the interior of flaring ARs as compared to the dormant regions and QRs. The sub-photospheric flows of NOAA 10486 show a systematic variation from the pre- to post- flare phases. Furthermore, the steep gradient in meridional velocity observed at the depth range of 2-6 Mm decreased after the flare which manifests a relationship of the flaring activity with the sub-photospheric flows. The vertical component of flow changed to downward direction during the flaring and then returned back later to the pre-flare state. This is an evidence of downward moving flows during the flare.

Divergence of the horizontal component of flow near the photosphere changed from negative to positive and then back to the pre-flare state after the flare. The sub-photospheric flow possessed a bipolar structure with one pole located at the depth of around 2 Mm and the other at 6 Mm. Near the photosphere, the flow was twisted during the pre-flare phase, which relaxed after the flare. The kinetic helicity of sub-photospheric flow around the depth of 1 Mm changed from positive to negative during the flaring phases, and returned back to the pre-flare level in the post-flare phase.

From a study of sub-photospheric flows of 74 ARs, we have discovered statistically significant relationship among the sub-photospheric flow topology, energetics and the remaining lifetime of ARs. We have found the following important results: Three sheared layers in the depth range 0–10 Mm were found to exist in 44 ARs which revealed the complexity of flow structures beneath more complex ARs. The two extrema in u_y and $d'u_y$ profiles of these ARs were found to be located at the depths of 1.92±0.15 and 4.69±0.30 Mm. ARs having two extrema as compared to the ARs having only a single extremum in u_y were found to be more active as they possessed as large as twice the mean magnetic field (MI), mean GOES X-ray flux and mean lifetime.

The extrema of meridional velocity gradients were found to follow a hemispheric trend, *viz.*, in the northern hemisphere, 24 (70%) out of 34 ARs had negative gradients while in the southern hemisphere, 29 (74%) out of 39 ARs had positive gradients. ARs with larger MI possessed steeper gradient in meridional velocity profiles. Flaring activity of an AR is found to be associated with depth of the first extremum of vertical vorticity. ARs having zero vertical vorticity at deeper layers are expected to last longer.

In summary, we detected systematic variations in the sub-photospheric flow topology during a large energetic event using the ring diagram analysis. We have discovered a new hemispheric trend involving the meridional velocity gradient of sub-photospheric flows. More importantly, lifetime of ARs is found to be correlated with the depth of the deepest zero vertical vorticity. This inference may be useful in predicting the expected lifetime of ARs.

Chapter 8

Kinetic and Magnetic Helicities of Solar Active Regions

8.1 Introduction

Large-scale ordering of magnetic field at various layers in ARs are observationally evident. These structures may be produced by a variety of processes, such as, coherent patterns of surface flows (*e.g.*, van Ballegooijen, 1999), subphotospheric flows (*e.g.*, Longcope, Fisher and Pevtsov, 1998), and/or emergence of twisted sub-photospheric fluxes (*e.g.*, Longcope and Welsch, 2000). A photospheric manifestation of these patterns is the large-scale non-potential fields, generally observed in flaring ARs. These are marked by twisted, or sheared, photospheric magnetic fields near flare sites *i.e.*, large departures from a potential configuration (Hagyard *et al.*, 1984).

In more recent years, a topological property called "magnetic helicity" has been used to characterize the observed large-scale magnetic patterns which includes the subset of twisted or sheared fields, and provides a measure of magnetic linking and kinking (Berger and Field, 1984). Magnetic helicity observed at the photosphere is attributed to shear at larger depths and strong turbulence in the convection zone (Pevtsov, Canfield and Metcalf, 1994).

Helicity is a physical quantity which defines the degree of knottedness and twist of field lines. Mathematically, helicity of a vector field $\mathbf{X}$ is the volume integral of the scalar product of the vector field and its curl, given by

$$H = \int_V \mathbf{X} \cdot \mathbf{Y} \, \mathrm{d}V \tag{8.1}$$

where, $\mathbf{Y} = \nabla \times \mathbf{X}$ represents curl or twist of field lines and V is volume. In general, helicity describes what kind of handedness is preferable for the field $\mathbf{X}$, left or right hand screw. If $\nabla \times \mathbf{X}$ is clockwise when viewed from ahead of the body, the helicity is positive; and if counterclockwise, it is negative.

Helicity is a fundamental quantity of magnetic fields in laboratory as well as in astrophysical plasma. It is believed that the main source of the magnetic fields on the solar surface is the dynamo action (Parker, 1955) which located either at the bottom of the convection zone or in a thin region called the overshoot zone; a layer between the convection and radiation zones. The joint action of differential rotation and cyclonic convection vortices contributes to the dynamo (Parker, 1955).

The necessary condition for the kinetic dynamo action is that the underlying velocity field ($\mathbf{u}$) lacks reflection symmetry, *i.e.*, it has handedness (Pouquet, Frisch and Leorat, 1976; Moffatt, 1978; Krause and Raedler, 1980). One of the natural measures of the lack of the reflection symmetry is the kinetic helicity H_k. The kinetic helicity of flow is the volume integral of the scalar product of the velocity ($\mathbf{u}$) and vorticity ω (Moffatt and Tsinober, 1992), given by

$$H_k = \int_V \mathbf{u} \cdot \omega \, \mathrm{d}V \tag{8.2}$$

Another important parameter to describe the flows is vorticity ω which represents circulation per unit area or twist of fluid fields (for detail please see Section 7.2.1). H_k represents extent to which corkscrew-like motion occurs. If a parcel of fluid is moving and rotating about an axis parallel to the direction of motion, it will have positive helicity. The existence of kinetic helicity has been observed in several physical and astrophysical systems often a consequence of differential rotation. Therefore, kinetic helicity provides mechanism for the production of large scale hydrodynamic and magnetic structure, and hence, important to understand the role of the H_k in plasma.

The handedness of the resulting large scale magnetic fields is determined by the handedness of the underlying turbulent flows, defined by

$$H_m = \int_V \mathbf{A} \cdot \mathbf{B} \, \mathrm{d}V \tag{8.3}$$

where, $\mathbf{A}$ is the vector potential of magnetic field $\mathbf{B}$, $\mathbf{B} = \nabla \times \mathbf{A}$. H_m represents the extent to which a magnetic field "wraps around itself". The main source of magnetic helicity observed on the Sun is assumed to be due to kinetic helicity of turbulent flows in the convection zone (Pevtsov, Canfield and Metcalf, 1994). The kinetic helicity of turbulent flows twists the rising flux tube (Longcope, Fisher and Pevtsov, 1998) and creates twist in the magnetic fields observed on the photosphere. The other possibility of twist in the rising tube is dynamo action (Choudhuri, 2003).

There is a third kind of helicity called the "current helicity" which has also been extensively used to study the AR topology. It defines the degree of twist and linkage of electric currents, given by

$$H_c = \int \mathbf{J} \cdot \mathbf{B} \, \mathrm{d}V \tag{8.4}$$

where, $\mathbf{J}$ is current density related with magnetic field by $\mathbf{J} = \frac{1}{\mu_0} \nabla \times B$, $\mu_0 = 4\pi \times 10^{-7} \, \mathrm{Hm}^{-1}$ is the permeability of free space. It is of particular interest for the study of ARs, and transients, *e.g.*, flare, CMEs, *etc.* It is also related to the dynamo-α (Rüdiger, Pipin and Belvedère, 2001). Therefore, it may be possible to use the kinetic helicity measurement in sub-photospheric layers as a proxy of the current helicity.

A large number of studies have been carried out regarding the helicity on the Sun. Earlier researchers have reported that the magnetic/current helicity of solar

ARs have hemispheric trends; it is positive (negative) in the southern (northern) hemisphere. This tendency is called "hemispheric sign rule (HSR)" of helicity. There are some other parameters, *e.g.*, Hα vortices, filament chirality, *etc.*, which have been used to demonstrate the HSR in the solar atmosphere. Table 8.1 shows the results of helicity parameters obtained by previous researchers.

Hα vortices, filaments, *etc.*, are consequence of the chromospheric magnetic structures which are rooted below at the photosphere. From the study of chromospheric Hα images of 51 sunspots from 1901 to 1944, Hale (1927) first reported the preference of hemispheric trend in the Hα vortices. Later, Richardson (1941) included some more sunspots and reported 71% (66%) sunspots with left-handed (right-handed) vortices in the northern (southern) hemisphere. Hemispheric trend has also been reported in the chirality of chromospheric filaments (Martin, Bilimoria and Tracadas, 1994; Pevtsov, Balasubramaniam and Rogers, 2003; Lim and Chae, 2009).

Vector magnetic field observations of ARs on the photosphere have revealed that on the average solar ARs have a small but statistically significant mean twist in current helicity (Seehafer, 1990; Abramenko, Wang and Yurchishin, 1996; Bao and Zhang, 1998) and magnetic helicity (Pevtsov, Canfield and Metcalf, 1995; Longcope, Fisher and Pevtsov, 1998; Bao, Ai and Zhang, 2000) that is left-handed in the northern hemisphere and right-handed in the southern hemisphere. Theoretical analysis of spatial and temporal evolution of helicity has also become possible recently by numerical modeling (Choudhuri, Chatterjee and Nandy, 2004; Yeates, Mackay and van Ballegooijen, 2008). Based on solar dynamo model, Choudhuri, Chatterjee and Nandy (2004) have shown that the sign of helicity tends to be opposite to that of the preferred hemispheric trends during a short interval at the beginning of a cycle. Recently, Tiwari, Venkatakrishnan and Sankarasubramanian (2009) also found opposite hemispheric trend in the global force free parameter α obtained for several sunspots during the minimum and maximum epochs of the 23rd solar cycle.

Reference	**Helicity Parameter**	**North** (-ve) %(no.)	**South** (+ve) %(no.)	**Total** (no.)	**Date**
Hale (1927)	HV	64(16)	50(13)	51	1901-1944
Richardson (1941)	HV	71	66	141	1901-1944
Seehafer (1990)	h_c	92(11)	75(3)	16	SC21-22
Martin, Bilimoria and Tracadas (1994)	FC	100(26)	72(34)	47	SC22
Pevtsov, Canfield and Metcalf (1995)	α_{best}	76(25)	69(25)	69	1991-1995
Abramenko, Wang and Yurchishin (1996)	h_c	79(15)	86(18)	40	Jun88-Sep94
Bao and Zhang (1998)	h_c	84(169)	79(177)	422	1988-1997
Longcope, Fisher and Pevtsov (1998)	α_{best}	62(58)	66(73)	203	1991-1995*
Bao, Ai and Zhang (2000)	α_{best}	59(152)	65(26)	87	Start of SC23
Pevtsov, Balasubramaniam and Rogers (2003)	FC	80(558)	86(633)	2310	2000-2001
Lim and Chae (2009)	FC	95(19)	100(18)	45	1996-2001

Table 8.1 A list of references showing hemispheric trend of helicity parameters.

HV- Hα vortices, FC - Hα filament chirality, SC - Solar Cycle

Kinetic helicity measurement in the solar convection zone may provide a direct inference of α-effect, a mechanism which transforms azimuthal magnetic fields into meridional magnetic fields in solar dynamo model. It has now become possible to measure kinetic helicity in the interior of solar ARs after the advent of local helioseismology. However, local helioseismic measurements of sub-surface flows are limited only within a few Mm depths. Therefore, it is uncertain as to what extent the kinetic helicity measurements will explain the α-effect. In general, the relation between H_k of the underlying flows and H_m of external magnetic fields of ARs remains to be understood.

Using observations from GONG and MDI for the period of 1996-2005, Komm *et al.* (2007) have reported cyclonic vorticity (counter clockwise) in the northern hemisphere. They also found that the kinetic helicity on average is negative (positive) in the northern (southern) hemisphere. Using SOHO/MDI Doppler observations of 88 ARs from April 1997 to March 2000, Zhao (2004) showed that sub-surface kinetic helicity have a preponderance opposite to the current helicity. Topological association of sub-photospheric flows and photospheric magnetic fields have been studied recently by Gao, Zhang and Zhao (2009). Using Huairou Solar Observing Station (HSOS) vector magnetograms and MDI dopplergrams, they studied current and kinetic helicity parameters in 38 ARs from May 1997 to May 2001. They found a significant signature of hemispheric trend in the magnetic field topology parameters similar to the earlier reports, while opposite preponderance in the sub-surface flows topology in agreement with (Zhao, 2004). They suggested that uncertain correlations found between the kinetic helicity of sub-surface flows at 0-12 Mm depths and photospheric current helicity do not support a cause and effect relation between these parameters.

Helicity plays a major role in solar activities, *viz.*, flares and CMEs. It is believed that the flux tubes, created at the base of the convection zone, rise toward the photosphere where turbulent flows braid, intertwine and magnetic energy is eventually released in the flare (Priest and Forbes, 2002). We, therefore, expect the twist in the internal sub-photospheric flows to have a relation with the external twist of observed magnetic fields at the photosphere and higher layers. With this aim, we further explore for any possible relation between the kinetic and magnetic helicities using photospheric vector magnetograms and Dopplergrams observations of a large set of flaring ARs of solar cycle 23.

In Section 8.2, we describe the methodology to determine the helicity parameters. Temporal evolution of twists in NOAA 10930 is discussed in Section 8.3. Section 8.4 is devoted to the statistical analysis of kinetic and magnetic helicities. Finally, we present the summary and conclusions in Section 8.5.

8.2 Measurements of Magnetic and Kinetic Helicities

Magnetic helicity is a global quantity which is defined by Equation 8.3. But one cannot observe a full flux system volume because an AR is extended below and above the visible surface. We therefore use force-free parameter α as another measure of magnetic helicity to get information of twist in the magnetic fields. There are generally two methods for calculating α: *i)* α_{best} which is the best fit single value for the whole AR in a least squares sense (Pevtsov, Canfield and Metcalf, 1995), and *ii)* α^z_{av} which is the average of the vertical component of α over the entire AR. Basically, α^z_{av} has the same sign as magnetic helicity. This has been used by earlier researchers as a representative parameter for the magnetic helicity of solar ARs. For a linear force-free field, rotation of field lines and magnetic field itself, (Pevtsov, Canfield and Metcalf, 1994), it is given by

$$\alpha_z(i,j) = (\nabla \times \mathbf{B})_z / B_z = \left(\frac{\partial B_y}{\partial x} - \frac{\partial B_x}{\partial y} \right) \frac{1}{B_z} \tag{8.5}$$

Numerical derivatives of magnetic field components are determined using Lagrange three point interpolation. While calculating the values of $\alpha_z(i,j)$ in an AR, we selected only those pixels where the measurements were above the accuracy. To get the imbalance of twist (right/left handedness) in an AR, we took average over the entire region. We determined the average value of the vertical component of α using

$$\alpha^z_{av} = \frac{1}{N}\sum_{i,j}\alpha_z(i,j) \tag{8.6}$$

where N represents the total number of points where $\alpha_z(i,j)$ are measured.

Along with the magnetic helicity parameter $\alpha^z_{\rm av}$, we also determined the vertical component of current helicity using

$$(h^z_c)_{av} = \frac{1}{N}\sum\left(\frac{\partial B_y}{\partial x} - \frac{\partial B_x}{\partial y}\right)\frac{1}{B_z} \tag{8.7}$$

For calculating the kinetic helicity in an AR (Equation 8.2), we have determined the complete velocity vector with depth: horizontal components from inversions and the vertical component of velocity u_z from the divergence of horizontal components assuming mass conservation (Equation 7.7). As we do not have the information of flows at each point of the AR, we can derive only the average helicity over the entire area, termed as kinetic helicity density, defined by

$$h_k = \mathbf{u}\cdot\omega = \mathbf{u}\cdot\nabla\times\mathbf{u} \tag{8.8}$$

Equation 8.8 can be written as,

$$h_k = \left(\frac{\partial u_z}{\partial y} - \frac{\partial u_y}{\partial y}\right)u_x + \left(\frac{\partial u_x}{\partial z} - \frac{\partial u_z}{\partial x}\right)u_y + \left(\frac{\partial u_y}{\partial x} - \frac{\partial u_x}{\partial y}\right)u_z \tag{8.9}$$

Vertical and helical fluctuations are an integral part of any turbulent fluid. Therefore, they may have some association with magnetic helicity parameter $\alpha^z_{\rm av}$ defined by Equation 8.6. For this we take only the vertical component of h_k, given by

$$h^z_k = \left(\frac{\partial u_y}{\partial x} - \frac{\partial u_x}{\partial y}\right)u_z \tag{8.10}$$

We have derived the numerical derivatives of sub-photospheric flow components using Lagrange three point interpolation.

8.3 Evolution of Kinetic and Magnetic Helicities in NOAA 10930

NOAA 10930 was a rapidly developing AR during its disk passage from 7 December to 16 December 2006. It produced several flares including two X-class flares, *viz.*, X3.4/4B and X1.5/SF on 13 December and 14 December 2006, respectively. This AR was observed continuously both by GONG and Hinode during its disk passage. We have studied the daily evolution of photospheric and sub-photospheric twist parameters using the computed vertical vorticity and kinetic helicity from 7 December to 15 December 2006. Twist parameters $\alpha^z_{\rm av}$ and $(h^z_c)_{\rm av}$ were determined from vector magnetic fields using Equations given in Section 8.2.

Figure 8.1 shows the daily evolution of photospheric (top panel) and sub-photospheric (middle and bottom panel) twist parameters. Photospheric net magnetic field B_p, twist parameters $\alpha^z_{\rm av}$ and GOES flux are shown in black, blue and red curves, respectively. The dashed (dotted) contours in the $(\omega^z)_{\rm av}$ (middle panel) and $(h^z_{\rm k})_{\rm av}$ (bottom panel) maps are drawn at 20, 40, 60 and 80% of the minimum (maximum) of the color scale.

From the figure, one can see that the average photospheric magnetic flux B_p increased till the day of the X3.4/4B flare (02:40 UT 13 December 2006) and decayed thereafter. The twist parameter $\alpha^z_{\rm av}$ did not vary as smoothly as B_p although there is first a net decrease in the magnitude of $\alpha^z_{\rm av}$ during the post-flare phase and then increase, subsequently. Interestingly, the value of $\alpha^z_{\rm av}$ is found to be mostly negative during the disk passage of the AR. However, according to the usual hemispheric rule, NOAA 10930 located in the southern hemisphere is expected to possess positive value of $\alpha^z_{\rm av}$, therefore, this AR showed an opposite HSR.

The ω_z map (Figure 8.1, middle panel) shows upward vorticity in the depth

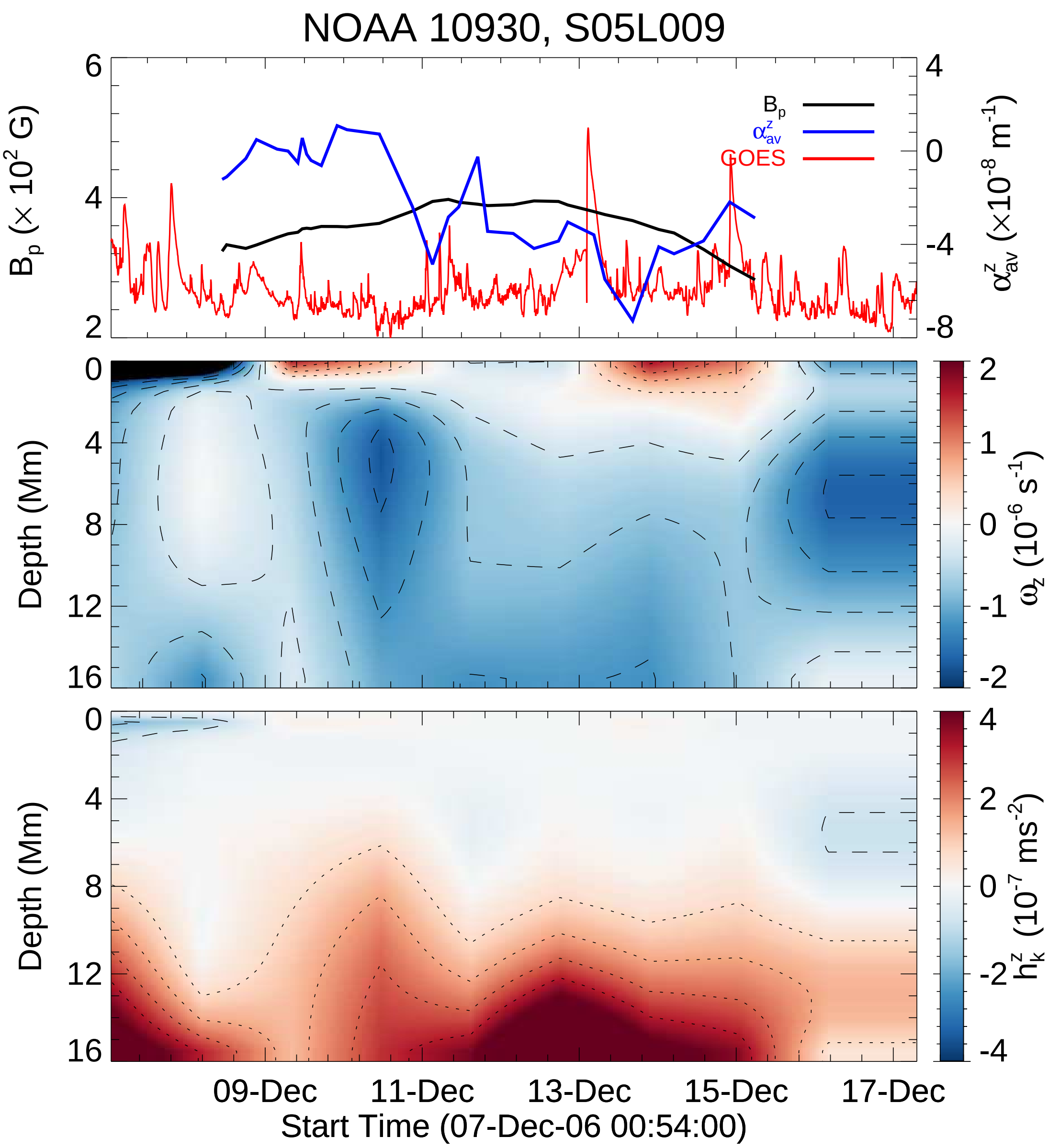

Figure 8.1 Association of vertical component of vorticity and kinetic helicity with magnetic helicity. Top panel shows the average photospheric magnetic flux B_p (black), vertical component of α (blue) and GOES X-ray flux(Red) scaled to the plot range. Middle (bottom) panel shows the daily evolution of vertical vorticity (kinetic helicity) during 7-16 December 2006 with depth beneath NOAA 10930. The dashed (dotted) contours in maps are drawn at 20, 40, 60 and 80% of the minimum (maximum) of the color scale.

range 0-4 Mm during the flaring days (13-15 December 2006), while there was a strong downward vorticity in the depth range 3-12 Mm during the days before (10-11 December) and after (around 16-17 December) the flaring days. No clear relationship is evident between the magnetic helicity parameter $\alpha^z_{\rm av}$ and the vertical component of vorticity $(\omega^z)_{\rm av}$.

The h^z_k map (Figure 8.1, bottom panel) shows a negative vertical kinetic helicity density in the depth range 0-5 Mm, which has the same sign as the magnetic helicity parameter $\alpha^z_{\rm av}$. Therefore, h^z_k in the depth range 0-5 Mm and $\alpha^z_{\rm av}$seem to be associated with each other. There is a strong positive h^z_k, opposite in sign to $\alpha^z_{\rm av}$, seen in the depth range 12-16 Mm during the X3.4/4B flare of 13 December 2006. This represents the alignment of vertical flow $u_{\rm z}$ in the direction of ω_z. Strong kinetic helicity density has also been reported by Komm *et al.* (2004a) in the interior of NOAA 10486 during the X10/2B flare of 29 October 2003. However, it should be noted that errors at these depths are larger $\sim 2.0 \times 10^{-7}$ m s^{-2}.

Thus, from the study of photospheric and sub-photospheric evolution of NOAA 10930, we have found some indication that the twists in photospheric magnetic fields and sub-photospheric flows may be associated and also show a correspondence with flares.

8.4 Statistics of Helicities in Sub-photospheric Flows and Photospheric Magnetic Fields

To get statistical inferences of the above-mentioned findings, we have studied a sample of 91 ARs of solar cycle 23. The results are presented in the following.

8.4.1 The Observational Data and Analysis

Photospheric vector magnetic field measurements provide all the three components of magnetic fields while Doppler observations provide sub-photospheric flow components (Chapter 7). Unfortunately, simultaneous observations of magnetic and

Doppler velocity fields are not available from the same instruments. We therefore use data from different sources, for example, vector magnetograms from MSFC and Hinode data archives, and Doppler observations from the GONG. Good quality vector magnetograms from MSFC are available for the period September 2000 - October 2004 while the Hinode data are available from November 2006 onward. High resolution Doppler observations from GONG are available only from Jul 2001 onward. Therefore, for our study of photospheric and sub-photospheric topology, we selected ARs observed in the period from July 2001 to August 2007.

Our selection of ARs involved the following procedure. First, we selected ARs observed from July 2001 to August 2007, lying within the central longitude and latitude range of (-40, 40). Then we shortlisted ARs depending upon their area and availability of data. We chose one map for each of the AR. Thus we found good data sets for 91 ARs for our analysis. In this sample of 91 ARs, we have MSFC observations for 80 ARs from July 2001 to October 2004. For the rest, *i.e.*, 11 ARs, we have taken data from the Hinode data archives.

Positions of these 91 ARs over the solar photosphere are illustrated in Figure 8.2, where circles correspond to the logarithmic areas of ARs in millionth of hemisphere ($3 \times 10^6\,\mathrm{km}^2$). In our sample of 91 ARs, 59 ARs were located in the southern hemisphere and 32 ARs in the northern hemisphere. Thus the number of ARs for the southern hemisphere is larger as compared to that in the northern hemisphere. However, our results on their hemispheric trends are not expected to be affected because we use percentage values of twist parameters.

The magnetic field components corresponding to the Hinode observations were derived using the method described in Section 2.2.2. We resolved the usual 180°ambiguity in the transverse components of all vector magnetograms using the acute angle method although there are several other methods as reviewed by Metcalf *et al.* (2006). Further, to avoid any projection effects, we transformed the images to the disc center using the method described by Venkatakrishnan and Gary (1989).

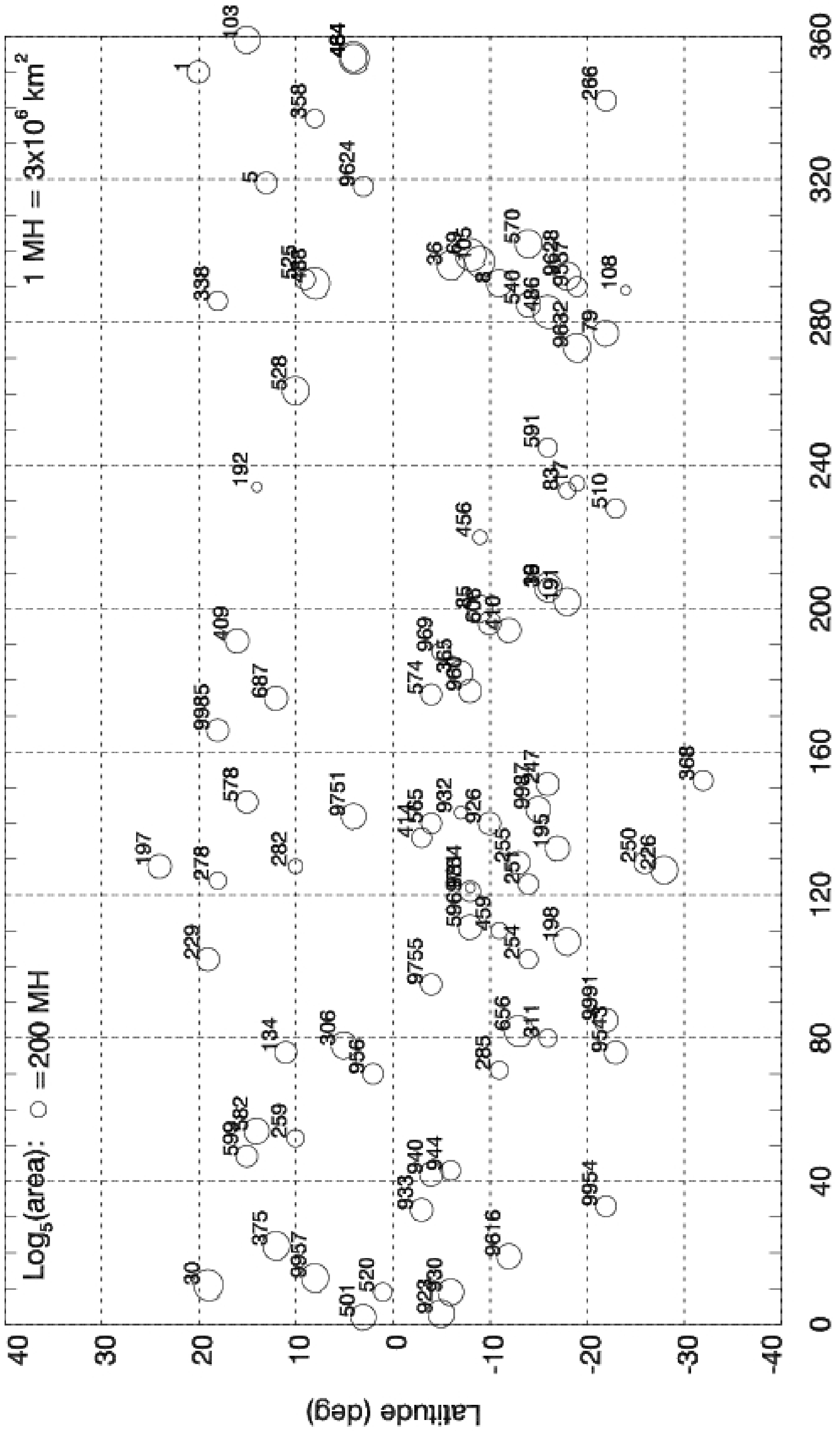

Figure 8.2 Positions of the 91 ARs used in this study are marked by circles where their sizes correspond to the logarithm of AR area in millionth of hemisphere (MH).

Earlier studies (Komm *et al.*, 2005a; Maurya, Ambastha and Tripathy, 2009; Maurya and Ambastha, 2010) have shown bipolar structure of sub-photospheric flows in several ARs. Therefore, two different types of twists are possible in the underlying flows of ARs. To deal with it, we determined vertical vorticity $(\omega_1^z)_{\rm av}$ and $(\omega_2^z)_{\rm av}$ averaged over depths 0.0-2.5 and 2.5-12 Mm, respectively. Similarly, we computed two vertical kinetic helicity densities $(h_{\rm k1}^z)_{\rm av}$ and $(h_{\rm k2}^z)_{\rm av}$ averaged over the two depth ranges.

8.4.2 Twist Parameters of Photospheric Magnetic Fields

Topology of photospheric magnetic fields of 91 ARs has been studied by deriving the twist parameters $\alpha_{\rm av}^z$ and $(h_c^z)_{\rm av}$. In the following, we discuss their latitudinal distribution.

Latitudinal Distribution of Magnetic Helicity

Figure 8.3 shows the latitudinal distribution of magnetic helicity parameter $\alpha_{\rm av}^z$ obtained for our data set of 91 ARs. We found 66%(63%) ARs in the northern hemisphere with negative (positive) $\alpha_{\rm av}^z$in agreement with earlier reports on HSR (Pevtsov, Canfield and Metcalf, 1995; Longcope, Fisher and Pevtsov, 1998; Bao, Ai and Zhang, 2000; Gao, Zhang and Zhao, 2009). We notice that the data points show large scatter in both the hemispheres. Therefore, the following questions arise: Is the hemispheric sign statistically significant? Do the $\alpha_{\rm av}^z$ values have any relation with latitude?

To address these questions, we fit a straight line through the measured data points using a linear regression model. The solid line in Figure 8.3 shows the linear regression line while dashed curves correspond to the 95% confidence ($\sim 2\sigma$) interval, *i.e.*, boundaries of all possible straight lines. In other words, the confidence interval is 95% sure to contain the best fit regression line. The fitted line has a slope such that the magnitude of $\alpha_{\rm av}^z$ increases with latitude.

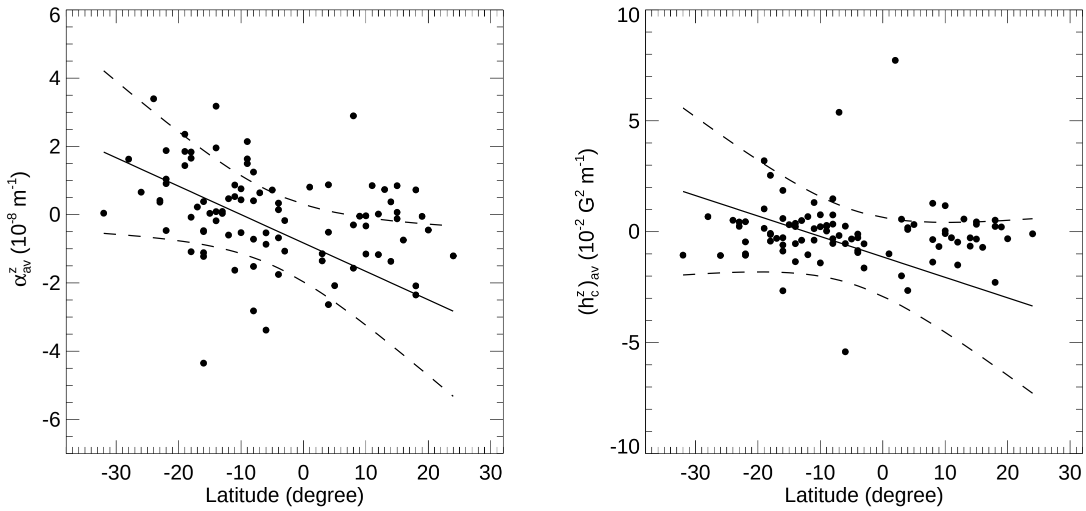

Figure 8.3 Latitudinal distribution of the force-free parameter $\alpha^z_{\rm av}$ (left panel), and the current helicity $(h^z_c)_{\rm av}$ (right panel). Solid line represents the straight line fitted through the data points while the dashed curves correspond to 95% confidence intervals.

This is not fully satisfactory because we do not have any known reason for the straight line to be the appropriate fit. But at the same time, we can not justify higher order polynomials. To give statistical significance of hemispheric trend, we calculated probability density function (PDF) for $\alpha^z_{\rm av}$ which is shown in Figure 8.4 (left panel). The peak of density function for northern (southern) hemisphere lies at $-9.37\times10^{-9}(+1.72\times10^{-9})$ m^{-1}. The average of $\alpha^z_{\rm av}$ for northern (southern) hemisphere is $-1.39 \times 10^{-8}(+3.05 \times 10^{-9})$ m^{-1}. These results confirm the hemispheric trend of the estimated $\alpha^z_{\rm av}$ values for our set of ARs. The FWHM of PDF of $\alpha^z_{\rm av}$ for northern (southern) hemispheric points is $1.03 \times 10^{-7}(2.34 \times 10^{-8})$ m^{-1}. The large width of PDF for northern hemisphere is due to the less number of points in the central region.

Latitudinal Distribution of Current Helicity

Latitudinal distribution of the vertical component of current helicity ($(h^z_c)_{\rm av}$) for the ARs is shown in Figure 8.3 (right panel). The measured values of $(h^z_c)_{\rm av}$ shows a weak hemispheric trend as compared to the force-free parameter $\alpha^z_{\rm av}$ (left panel).

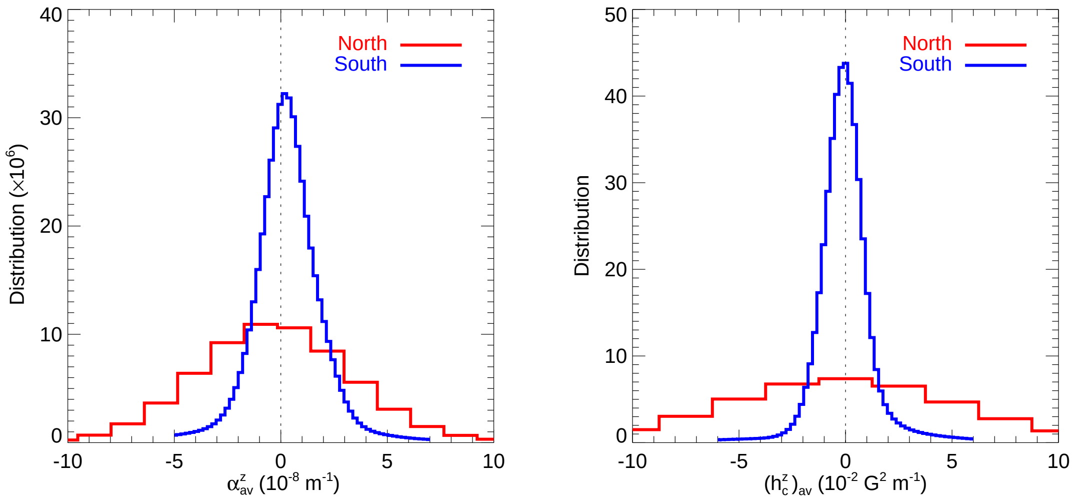

Figure 8.4 Probability density function of the force-free parameter α^z_{av} (left panel) and the current helicity $(h^z_c)_{av}$ parameter (right panel) for 91 ARs.

There are only 56% (47%) points in the northern (southern) hemisphere having negative (positive) sign for $(h^z_c)_{\rm av}$ although the points are much closer to the regression line (solid line) as compared to $\alpha^z_{\rm av}$. Most of the points lie within the confidence band. The regression line has smaller slope as compared to $\alpha^z_{\rm av}$.

The probability density function for $(h^z_c)_{\rm av}$ is shown in Figure 8.4 (right panel). This shows no significant hemispheric trend for $(h^z_c)_{\rm av}$ as the PDF for northern and southern hemispheric points lie at 0.0 $\mathrm{G}^2\,\mathrm{m}^{-1}$. The average $(h^z_c)_{\rm av}$ lies at $-1.93\times10^{-2}(0.00)$ $\mathrm{G}^2\,\mathrm{m}^{-1}$ for northern (southern) hemisphere. Again the FWHM of PDF for northern hemisphere is 0.12 $\mathrm{G}^2\,\mathrm{m}^{-1}$ which is much larger than the FWHM for southern hemisphere 2.12×10^{-2} $\mathrm{G}^2\,\mathrm{m}^{-1}$. This is because of the same reason as for $\alpha^z_{\rm av}$.

8.4.3 Twist Parameters of Sub-photospheric Velocity Fields

Twist in the sub-photospheric velocity fields in our sample of 91 ARs has been studied by deriving the vertical vorticity and kinetic helicity density. In the following we discuss the latitudinal distribution of these parameters.

Latitudinal Distribution of Vertical Vorticity

Figure 8.5 (top panel) shows the latitudinal distribution of the vertical component of vorticity averaged over depth ranges 0.0-2.5 Mm and 2.5-12 Mm. Each point corresponds to a single AR for which twist parameters have been measured from a 1664 minutes' Doppler time series using ring diagram technique (see Chapter 5). Vorticity $(\omega_1^z)_{\rm av}$ averaged over the depth range 0-2.5 Mm shows a hemispheric trend similar to $\alpha_{\rm av}^z$ while it has an opposite trend for the depth 2.5-12 Mm (see Figure 8.3). This is evident from the opposite slopes of linear regression lines passing through the data points. For these two depth ranges, the latitudinal distribution shows 56%(51%) and 41%(39%) ARs in the northern (southern) hemisphere having negative (positive) values of $(\omega_1^z)_{\rm av}$. This is also supported from the flow distribution beneath the AR (Chapter 7).

The probability density function for the vertical vorticity is shown in Figure 8.6 (top panel). For the depth range 0-2.5 Mm the vorticity parameter peaked at $-1.12 \times 10^{-7}(8.62 \times 10^{-9})\,{\rm s}^{-1}$ for the northern (southern) hemisphere. This further confirms the HSR in vertical vorticity. For the depth range 2.5-12 Mm the vertical vorticity peaked at $3.5 \times 10^{-7}(-1.17 \times 10^{-7})\,{\rm s}^{-1}$ for the northern (southern) hemisphere. This confirms an opposite trend of vorticity at the depth range 2.5-12 Mm.

Latitudinal Distribution of Kinetic Helicity

Figure 8.5 (bottom panel) shows the latitudinal distribution of the vertical component of the kinetic helicity density averaged over depth ranges 0.0-2.5 Mm (left panel) and 2.5-12 Mm (right panel). There is no clear hemispheric preference found in the parameter $(h_{\rm k1}^z)_{\rm av}$ as there are 47%(53%) ARs in the northern (southern) hemisphere having negative (positive) values. But the kinetic helicity parameter $(h_{\rm k2}^z)_{\rm av}$ shows a significant signature of the HSR as 69%(56%) ARs in the northern (southern) hemisphere show negative (positive) helicity. To further confirm

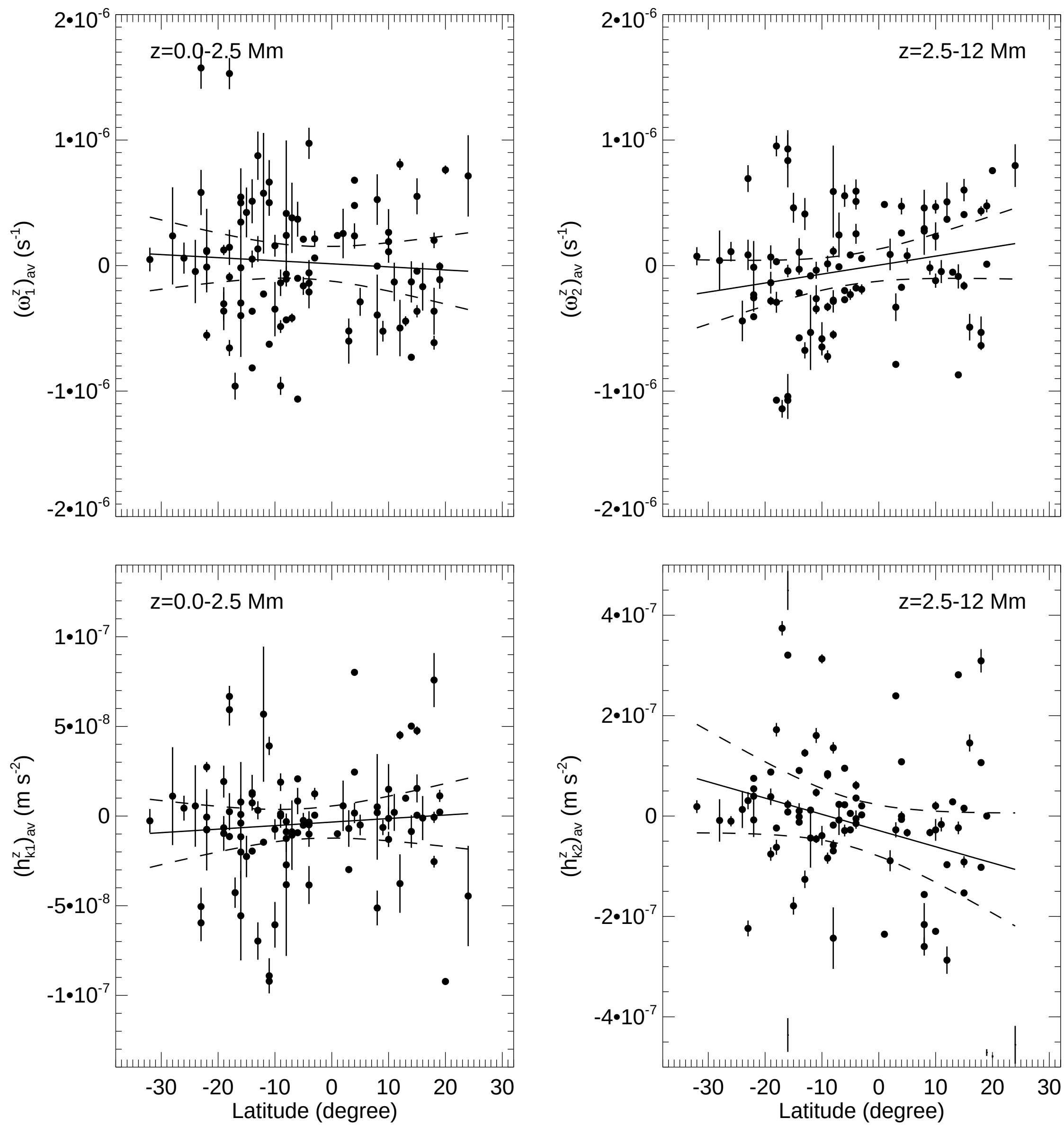

Figure 8.5 Latitudinal distribution of the vertical component of vorticity $(\omega^z)_{\rm av}$ (top panel), and the kinetic helicity density $(h^z_{\rm k})_{\rm av}$ (bottom panel) averaged over depth ranges 0-2.5 Mm (left column) and 2.5-12 Mm (right column). Solid lines represent the straight line fits through the data points while dashed curves correspond to the 95% confidence levels.

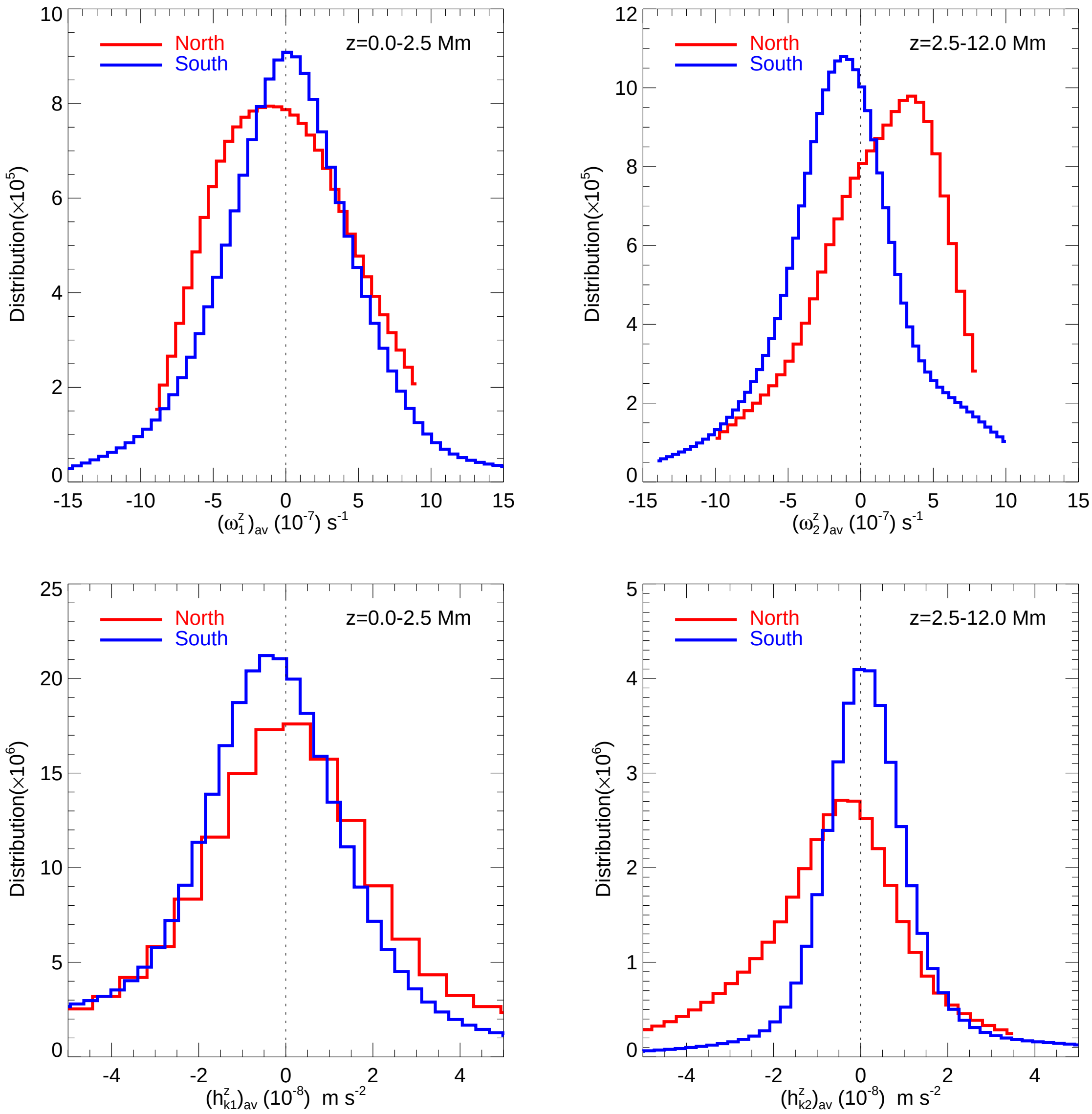

Figure 8.6 Probability density function of the vertical component of vorticity (top panel), and the kinetic helicity density (bottom panel) averaged over depth ranges 0-2.5 Mm (left column) and 2.5-12 Mm (right column).

Table 8.2 Latitudinal distribution of kinetic and magnetic helicities of 91 ARs.

Parameter	**North** (-ve) %(no.)	**South** (+ve) %(no.)	**Total** (no.)
α^z_{av}	66(21)	63(37)	91
$(h^z_c)_{av}$	56(18)	47(28)	91
$(\omega^z_1)_{av}$	56(18)	51(30)	91
$(\omega^z_2)_{av}$	41(13)	39(23)	91
$(h^z_{k1})_{av}$	47(15)	53(23)	91
$(h^z_{k2})_{av}$	69(22)	56(33)	91

the hemispheric sign of kinetic helicity, we have derived the PDF for northern and southern ARs.

Figure 8.6 (bottom panel) shows the PDF of $(h^z_{\mathrm{k1}})_{\mathrm{av}}$ and $(h^z_{\mathrm{k2}})_{\mathrm{av}}$. The left panel shows that the PDF for $(h^z_{\mathrm{k1}})_{\mathrm{av}}$ peaked at $2.5\times10^{-9}(-4.48\times10^{-9})$ m s^{-2} for northern (southern) hemispheric ARs. But the average value for northern (southern) hemisphere was found to be $1.88\times10^{-9}(-7.62\times10^{-9})$ m s^{-2}. This further confirms the opposite hemispheric trend for the parameter $(h^z_{\mathrm{k1}})_{\mathrm{av}}$. Similarly, the PDF for $(h^z_{\mathrm{k2}})_{\mathrm{av}}$ peaked at $-4.4\times10^{-8}(+3.4\times10^{-9})$ m s^{-2} while the average value for northern (southern) hemisphere is $-7.0\times10^{-8}(+1.7\times10^{-8})$ m s^{-2}, which further confirms the HSR for parameter $(h^z_{\mathrm{k2}})_{\mathrm{av}}$.

8.4.4 Relation between Kinetic and Magnetic Helicities

As mentioned in Section 8.1, magnetic field lines are rooted beneath the photosphere where they interact with the sub-photospheric fluid. Therefore, it is expected that the twists of magnetic and velocity fields would be associated with each others. Figure 8.7 shows the correlation between the force-free parameter α^z_{av} and the sub-photosphere twist parameters, *e.g.*, $(\omega^z)_{\mathrm{av}}$, $(h^z_{\mathrm{k}})_{\mathrm{av}}$. We have also shown the correlation between the current helicity and sub-surface flows in Figure 8.8. To get quantitative information of their associations, we have computed the Pearson correlation coefficients among these parameters as listed in Table 8.2.

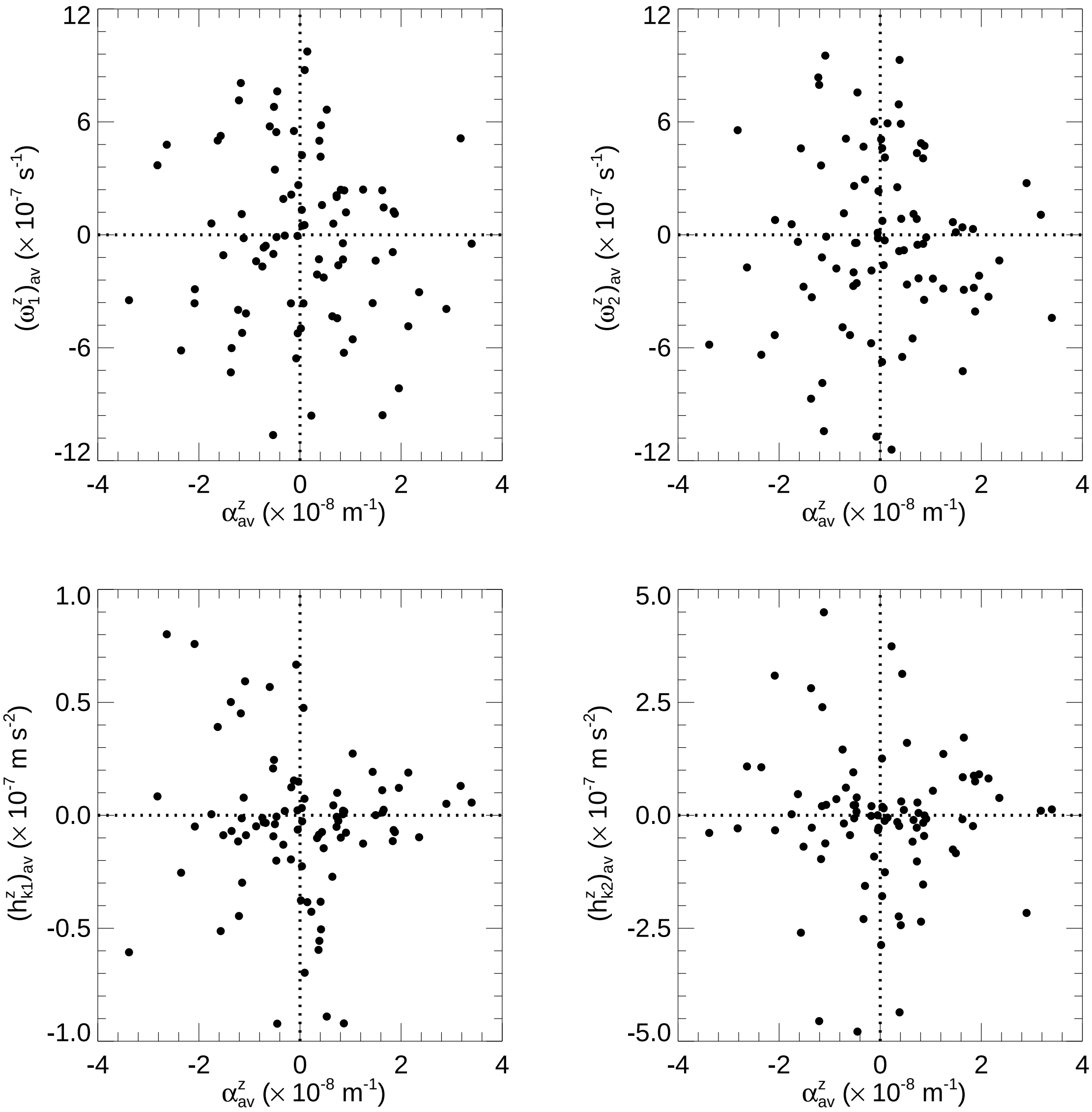

Figure 8.7 Association of magnetic helicity parameter α^z_{av} with the twist parameters of sub-photospheric flows for 91 ARs.

Table 8.3 Correlation table of various twist parameters of 91 ARs.

	$(\omega_1^z)_{\rm av}$	$(\omega_2^z)_{\rm av}$	$(h_{\rm k1}^z)_{\rm av}$	$(h_{\rm k2}^z)_{\rm av}$	$\alpha_{\rm av}^z$	$(h_c^z)_{\rm av}$
$\alpha_{\rm av}^z$	0.11	-0.03	-0.07	0.23	1.00	0.98
$(h_c^z)_{\rm av}$	-0.10	0.04	-0.05	0.26	0.98	1.00
B_p	-0.03	0.05	0.07	0.17	0.32	0.34
GOES	-0.04	0.15	-0.03	0.09	0.04	0.23

The top panel in Figure 8.7 shows scatter plot of the vertical vorticity at the depth ranges 0.0-2.5 Mm and 2.5-12 Mm against $\alpha_{\rm av}^z$, while the bottom panel shows the kinetic helicity density averaged over the same depth as in the top panel. It is clear that there is no significant correlation between the force-free parameter $\alpha_{\rm av}^z$ and the twist of sub-photospheric flows. The correlation table 8.3 shows that the parameter $\alpha_{\rm av}^z$ is anti-correlated with the parameters $(\omega_2^z)_{\rm av}$ and $(h_{\rm k1}^z)_{\rm av}$ and correlated with $(\omega_1^z)_{\rm av}$ and $(h_{\rm k2}^z)_{\rm av}$, although the magnitude of this correlation is not significant.

Figure 8.8 shows correlation between the current helicity and the twist parameter of sub-photospheric flows similar to that in Figure 8.7. Corresponding correlation coefficients are given in Table 8.2. The magnitudes of correlation coefficients are very small, implying that association between the current helicity and the twist of sub-photospheric flows of ARs is not significant.

8.4.5 Activity Related Variation in Twist Parameters

Table 8.3 shows the Pearson correlation coefficients between the GOES flux and twist parameters. The magnitude of the correlations are very small indicating no significant association of GOES flux with sub-photospheric twist. Our previous studies had found that the second maximum vorticity is associated with the GOES flux (Maurya and Ambastha, 2010). However, in this sample of our 91 ARs, we have taken an average over depths diluting the associations. In fact, we find that the correlation coefficients between the twist of photospheric magnetic fields and

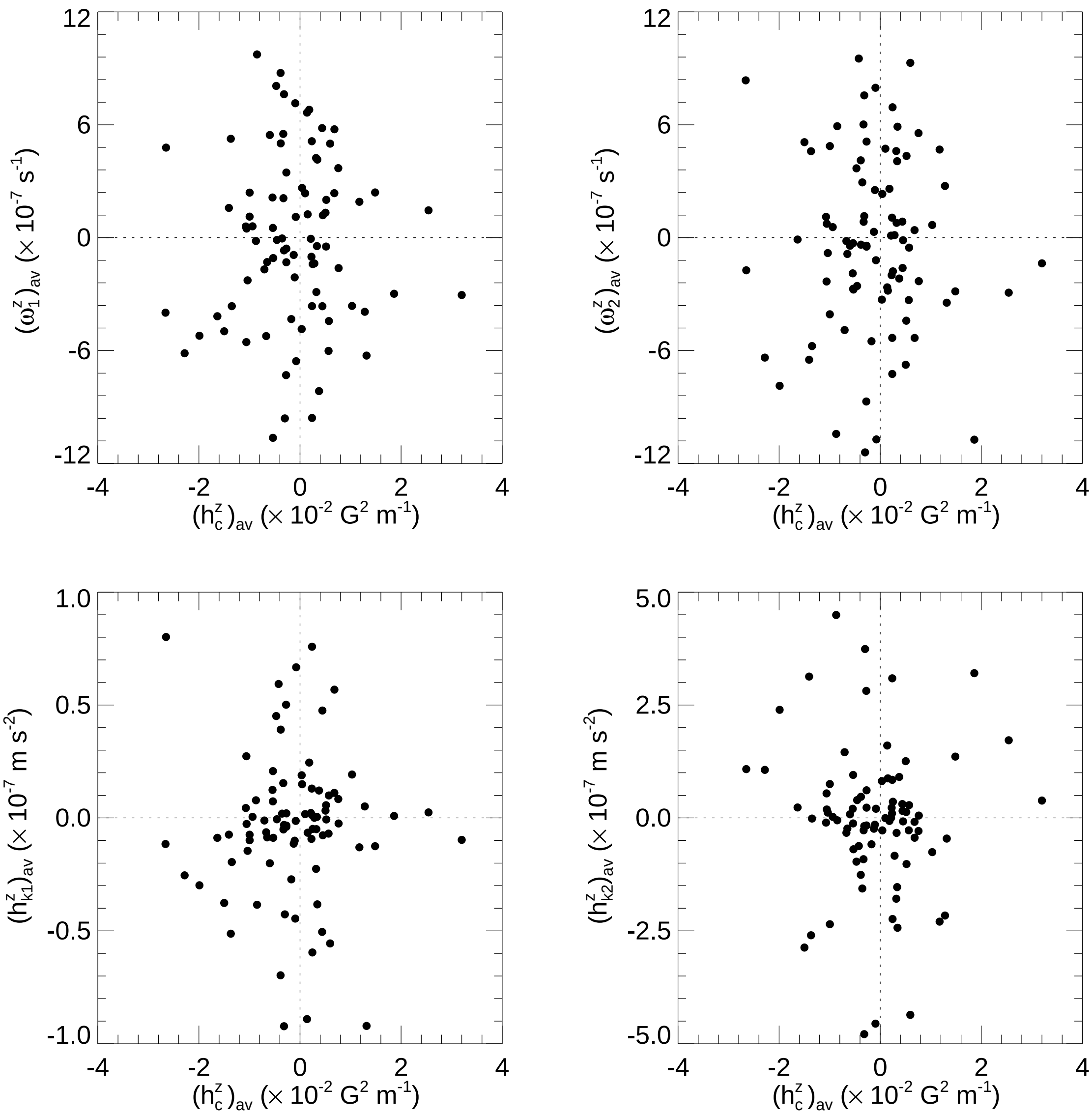

Figure 8.8 Association of current helicity parameter $(h_c^z)_{av}$ with the twist parameters of sub-photospheric flows for 91 ARs.

B_p are more significant as compared to the twist in sub-photospheric flow.

8.5 Summary and Conclusions

Using MSFC/Hinode vector magnetogram and GONG Dopplergram observations, we have studied twists in photospheric magnetic fields and sub-photospheric velocity fields of 91 ARs selected in the period from July 2001 to August 2007. We derived the following conclusions.

- Magnetic helicity parameter α^z_{av} shows a significant hemispheric trend while the current helicity shows only a weak trend, in agreement with the earlier reports.
- The vertical vorticity averaged over the depth range 2.5-12 Mm shows opposite HSR while there is no hemispheric signature found for the depth range 0.0-2.5 Mm.
- There is no clear hemispheric trend for the average vertical kinetic helicity for the depth range 0.0-2.5 Mm while a strong hemispheric trend is discernible for the depth range 2.5-12 Mm.
- We do not find any clear association between the twists of surface magnetic fields and sub-surface flows.
- Absolute mean magnetic field B_p showed a mild correlation with the magnetic field twist while no association was found with the twist of sub-photospheric flows.
- The GOES X-ray flux shows a mild correlation with vertical vorticity averaged over depths 2.5-12 Mm and photospheric current helicity.

In summary, unambiguous, statistically significant association is not found between the topology of photospheric magnetic field and the sub-photospheric flows. This result further supports a recent study involving 38 ARs by Gao, Zhang and Zhao (2009). It should be noted that we have used a single vector magnetogram map corresponding to an AR to derive the photospheric twist while the twist in sub-photospheric flow was derived using the data cube for 1664 minutes. It should also be noted that we have used magnetic and Doppler fields observations obtained from different sources. These factors may be responsible in affecting our results and in reducing correlations of the twist parameters (Xu, Gao and Zhang, 2009). It is expected that these result may improve when high resolution observations are used, such as, from the space borne instrument, Solar Dynamics Observatory (SDO), launched recently in February 2010.

Chapter 9

Summary, Conclusions and Future Plan

The main emphasis of the thesis is to understand the internal and external characteristics of ARs using local oscillations and the observed transient activities. The ARs are three-dimensional magnetic structures extending from the sub-photospheric interiors to the corona. Energetic solar transients primarily originate at the coronal region as a result of the changes in magnetic topology brought about by photospheric flux motions. The release of energy in the transient activities energizes the particles which are guided along the magnetic field lines and propagate toward the denser, lower layers of the solar atmosphere. Eventually they produce the observed flare ribbons and affect the characteristics of photospheric p-modes.

We have attempted to understand the variations in magnetic and Doppler velocity fields of ARs associated with the extremely energetic energetic transients that occurred in NOAA 10486 on October 28-29, 2003. From the study of local oscillations of ARs, we derived the photospheric p-mode parameters and sub-photospheric flows. We tried to understand the association of energetic transients with p-modes and sub-photospheric flows. We have studied the association of sub-photospheric flow topology of ARs with their observed photospheric magnetic fields and the lifetimes.

We have discussed solar oscillations and their importance in the study of solar interior in Chapter 1, and outlined the work carried out by previous researchers using local and global oscillations of the Sun. We discussed the motivation of our study and gave a brief introduction to the chapters of this thesis. Here, we provide the summary and conclusions of the work carried out in Section 9.1. Section 9.2 gives some limitations of the tools used in our study and the scope for improvements. We also discuss in Section 9.3 some new problems which we expect to address in the future.

9.1 Present Work

In the following, we summarize the work carried out in this thesis.

9.1.1 Determination of Flare Ribbon Separation

In Chapter 2, we have presented a technique for automatic determination of flare ribbon separation and energy release during the course of two ribbon flares. We have used chromospheric Hα filtergrams and photospheric LOS magnetograms to analyze flare ribbon separation and magnetic field structures, respectively. flare ribbons were first enhanced and then extracted by the technique of "region growing", *i.e.*, a morphological operator, to help resolve the flare ribbons. Separation of flare ribbons was then estimated from magnetic polarity reversal line using an automatic technique implemented into IDL platform. In addition to flare ribbons, this method may be applied to measure the motion of any feature of interest (*e.g.*, intensity, magnetic, Doppler) from a given point of reference.

Further, we gave a formulation of flare energy release based on the flare ribbon separation speed and the observed photospheric magnetic fields. We applied this technique to the extensively observed X17/4B flare of 28 October 2003. Velocities of different parts of flare ribbons were used to determine the rate of energy release.

The estimated flare energy was found to be sufficient to account for the production of observed hard X-ray (HXR) sources.

9.1.2 Transient Magnetic and Doppler Features Related to the White-Light Flares in NOAA 10486

The energetic transients, such as flares and CMEs, derive their energy from the stressed magnetic fields (Patterson and Zirin, 1981; Ambastha, Hagyard and West, 1993; Chen *et al.*, 1994; Hagyard, Stark and Venkatakrishnan, 1999). Flare/CME associated effects on the observed magnetic field parameters have been reported. However, there are questions about the observed changes as the magnetic field measurements are known to be affected by flare-induced line profile variations (Harvey, 1986; Qiu and Gary, 2003). Edelman *et al.* (2004) simulated the GONG and MDI observations for solar flares and concluded that as compared to Doppler velocity measurements the magnetic field measurements are less sensitive to the line shape changes. In addition, their numerical simulation also showed that the observed transient sign reversal may be produced when the Ni I 6768Å line profile turns into emission as a result of non-thermal beam impact on the atmosphere in regions of strong magnetic fields.

While examining the observational characteristics of the AR NOAA 10486, we discovered some magnetic and Doppler features moving away from the sites of its energetic flares. These moving features were conspicuous during the impulsive phases of the X17.2/4B and X10/2B superflares of October 28 and 29, 2003, respectively (Maurya and Ambastha, 2008, 2009). Observation of such dynamic features in magnetograms is perplexing and needs an explanation. Interestingly, these were also found to be associated with sign reversals in magnetic and Doppler velocity fields.

We examined the origin of these features and their relationship with various aspects of the flares, *viz.*, hard X-ray (HXR) emission sources and flare kernels observed at different layers. In some cases, the transients in NOAA 10486 were found to occur near the magnetic neutral line, *i.e.*, away from strong field site of umbra/penumbra. This finding contradicts with the suggestion of Qiu and Gary (2003). In particular, the moving transients appear to be related to the process associated with electron-beams and not to the line profile changes by any thermal changes.

9.1.3 Ring-Diagram Analysis and Inversion Techniques

Ring diagram technique is one of the most powerful tools to study the photospheric p-mode characteristics of ARs. In ring diagram analysis we construct the data cube by tracking a small area of size $16^\circ \times 16^\circ$ for a day to derive the p-modes by ring-fittings. We have compared the results obtained from two different techniques: *i)* Asymmetric Peak Profile (APP) fitting (Basu and Antia, 1999) and *ii)* Dense-Pack (DP) ring fitting (Haber *et al.*, 2002). The first technique involves thirteen parameters while the later requires only six parameters to fit the power spectra. The APP fitting also gives the asymmetry in the p-mode power.

From a comparison of results obtained from the two techniques, we found that there is a good agreement between the mode velocities U_x and U_y, but other parameters, *e.g.*, mode amplitude A, mode width Γ and frequency shift $\delta\nu$ do not match well. We suggested that the deviation in the parameters A and Γ are due to the lower cutoff of the background power in the fittings while the deviation in the parameter $\delta\nu$ arises due to the contribution of the asymmetric parameter S in the APP fitting.

Further, properties in the interior of ARs were derived by inversions using the p-modes. To determine the sub-photospheric velocities, we developed two different inversion codes based on SOLA and RLS methods. We tested these codes by a simulated data obtained from a forward method. The results obtained from both the methods were compared and found to be in reasonably good agreement.

However, the first method is computationally excessive as compared to the later, although it provides a way to check the inverted errors and target depths.

9.1.4 Variations in p-Mode Parameters with Changing Onset Time of a Large Flare

Wolff (1972) had first suggested that energetic flares may be able to excite acoustic waves by exerting mechanical impulse of the thermal expansion of the flare on the photosphere. Subsequently, sunspot related mode power absorption effects on p-mode parameters were reported by several researchers (Libbrecht and Woodard, 1990; Chaplin *et al.*, 2000; Hindman *et al.*, 2000; Rajaguru, Basu and Antia, 2001). Ambastha, Basu and Antia (2003) found p-mode power to be larger during the period of high flare activity as compared to that in non-flaring regions of similar magnetic fields. However, the changes in p-mode parameters and sub-photospheric flows during these energetic events are not well studied although some efforts have been made to examine the difference between flare productive ARs and QRs (Mason *et al.*, 2006).

We have studied the long duration, energetic X17.2/4B flare of October 28, 2003 in NOAA 10486 by placing the flare at different temporal positions in appropriately constructed GONG data-cubes (*cf.* Figure 6.1). We found a strong evidence of flare-related changes in p-mode parameters and sub-photospheric flows. When the flare onset was located at the start of the data cube constructed for this region, the contribution of the flare to the mode power, during and after the flare, remained entirely within the data cube. This resulted in significant enhancement of the mode amplitude. However, when the flare onset time was kept at the end of the data cube, the mode power was found to have the smallest magnitude compared to other cases where the flare was placed well within the data cube. The amplitude of p-mode power was found to be amplified as much as by 150% at radial order $n = 0$; decreasing for higher n. We suggested that smaller amplification in amplitude for higher n is due to the trapping of modes in larger depths. It increased with frequency > 2000 μHz. Other parameters, *e.g.*, mode width, zonal flows, *etc*, were also found to change systematically as the flare time was changed within the data cubes. These results essentially manifest the helioseismic influences related to the large flare X17.2/4B (Ambastha, Basu and Antia, 2003).

9.1.5 Three-dimensional Flow Distribution Beneath the Active Regions

In an attempt to obtain generalized statistical results on the characteristics of sub-photospheric flows beneath ARs and QRs, we applied the technique of ring diagram analysis to a large sample (74 ARs) of data sets obtained from GONG. This sample of ARs is selected from Carrington rotations 1980–2052 covering the period of August 2001-January 2007. We found that the flare productive ARs possessed stronger twisted flows, *i.e.*, large zonal/meridional velocities, in sub-photospheric depths as compared to QRs. This is in good agreement with earlier studies (Haber *et al.*, 2002; Braun, Birch and Lindsey, 2004; Zhao and Kosovichev, 2004). In flare productive ARs, we discovered the presence of steep meridional velocity gradients in depths ranging from 1.5 to 5 Mm. This supports the results obtained earlier by Ambastha *et al.* (2004). These gradients showed an interesting hemispheric trend of negative (positive) signs in the northern (southern) hemisphere. We have discovered the presence of three sheared layers in the depth range 0–10 Mm of 44 ARs which revealed the complexity of flow structures beneath the surface of more complex and flare productive ARs. The two extrema in meridional velocity profiles of these ARs were found to be located at the depths of 1.92±0.15 and 4.69±0.30 Mm. The ARs having two extrema as compared to the ARs having only a single extremum in meridional velocity were found to be more active as they possessed as large as twice the mean magnetic field (MI) and mean GOES X-ray flux. ARs having larger MI showed steeper gradients in their meridional velocity profiles.

The flaring productivity of an AR is found to be associated with the depth of first extremum of vertical vorticity.

9.1.6 Topology of Sub-photospheric Flows and the Lifetime of Active Regions

Solar sub-photospheric fluid topology provides an indirect approach to determine the internal characteristics of ARs. Helioseismic studies have revealed that sunspots are rather shallow, near-photospheric phenomena (Kosovichev, Duvall and Scherrer, 2000; Basu, Antia and Bogart, 2004; Couvidat, Birch and Kosovichev, 2006), and their rotation rate with depth depends on the stage of evolution and age. Švanda, Klvaňa and Sobotka (2009) have reported that a majority of ARs display sudden decrease in the rotation speed; compatible with dynamic disconnection of sunspots from their parental magnetic roots. It is possible that the connection between the magnetic structures at the photosphere and its underlying roots may get broken through a dynamical disconnection mechanism proposed by Schüssler and Rempel (2005) based upon the buoyant upflow of plasma along the field lines. From the simulation of thin flux tubes, Schüssler and Rempel (2005) showed that the disconnection takes place at a depth between 2 and 6 Mm.

Using the results obtained for our sample of 74 ARs of solar cycle 23, we suggested that zero vertical vorticity (ω_z) of sub-photospheric flows is a signature of the flux rope being broken at these depths. Once the flux ropes in the interior of an AR are disconnected, its remaining lifetime would depend upon the depth where ω_z vanishes, *i.e.*, $\omega_z = 0$. Further, we have found a linear relationship between the depth (d_0) of zero vertical vorticity and the remaining lifetime (τ) of ARs given by, $\tau = 6.43 + 0.34\, d_0$. The fit is found to be good as 72.65% of the total variance in τ is explained by the linear regression model. This suggests that the ARs having zero vertical vorticity at the deeper layers are expected to last longer. This inference is expected to be useful in predicting the lifetime of ARs.

9.1.7 Kinetic and Magnetic Helicities of Solar Active Regions

Solar energetic transients, *viz.*, flares and CMEs, are associated with rapid changes in magnetic and velocity field topologies in solar atmosphere (Patterson and Zirin, 1981; Ambastha, Hagyard and West, 1993; Chen *et al.*, 1994; Hagyard, Stark and Venkatakrishnan, 1999). These changes are essentially brought about by magnetic fields that are rooted beneath the photosphere where they interact and get affected by sub-photosphere flows. Recent theories suggest that the flux tube created at the base of the convection zone rises toward the photosphere where turbulent flows braid, intertwine and eventually, magnetic energy is released in the flare (Priest and Forbes, 2002). Therefore, we expect the twist in sub-photospheric flows to have a correlation with the observed twist of magnetic fields at the photosphere and higher layers.

In order to examine the correlation, if any, we have derived the kinetic helicity of sub-photosphere flows using ring diagram analysis and the magnetic helicity using photospheric vector magnetograms for 91 ARs of Solar Cycle 23. However, we did not find a statistically significant association between the topology of photospheric magnetic field and sub-photospheric flows. Kinetic helicity of ARs in the depth range 2.5-12 Mm shows an hemisphere trend; it is positive (negative) in southern (northern) hemisphere similar to the trend observed for magnetic helicity by Pevtsov, Canfield and Metcalf (1994).

9.2 Limitations of the Techniques

The method of ring diagram analysis has become an important tool in the study of the interior of ARs, although it has some limitations. First, it provides only the spatially averaged properties over the entire patch $16^\circ \times 16^\circ$ of the size of ARs. Thus it is not suitable for spatially resolved study of the p-modes. Secondly, it only provides temporally averaged properties of the ARs over a day. Therefore, effects of small transients lasting over short durations are diluted and hence the detection of their role in p-mode amplification is rather difficult.

The first limitation can be resolved by the use of small scale ring analysis (Hindman, Haber and Toomre, 2006) which provides more detailed information with spatial resolution of 2°. The later problem can be addressed by the use of time-distance method (Duvall *et al.*, 1993b). We are planning to apply these tools in our future studies.

9.3 Future Directions

We plan to address the following problems in the future:

9.3.1 Association of Photospheric p-Mode Parameters with Energetic Transients

In Chapter 6, we determined the characteristic properties of p-mode parameters using GONG data by applying the ring diagram technique to three-dimensional power spectra obtained for AR NOAA 10486 during the long-duration energetic X17/4B flare of 28 October 2003. In order to further establish our results statistically, we plan to study a larger sample of flares in SARs using high resolution data from instruments such as SDO-HMI. Such a statistical study is expected to help in our understanding of the mechanism of p-mode amplification by energetic transients. Further, we hope to enhance our understanding of the penetration of flare energy beneath the photosphere by studying the mode amplification with radial order n of p-modes.

9.3.2 Association of Sub-photospheric Flows with Energetic Transients

A study of sub-photospheric flows beneath NOAA 10486 has revealed systematic variations in the flow parameters from the pre- to post-flare phases of X17/2B flare of 28 October 2003. A statistical study of ARs of varying complexities is expected to reveal association of sub-photospheric flow parameters with flare productivity. We wish to further enhance the scope of our study by using small ring technique (Hindman, Haber and Toomre, 2006) for obtaining spatially resolved structures at the photosphere and in the interior of ARs. For a better resolution of sub-photospheric flows, we also plan to use time-distance techniques. This may also help in resolving the problem of photospheric magnetic and Doppler transients as discussed in Chapter 4.

9.3.3 Sub-photospheric Fluid Topology and the Lifetime of Active Regions

As mentioned earlier, active region seismology using ring diagram analysis gives poor spatial and temporal resolutions. Hence, it is not possible to precisely locate the depth of zero vertical vorticity in some ARs. The ring analysis gives flow characteristics averaged for a day; therefore, changes in the sub-photospheric fluid structure within a day are not resolved. Secondly, it is not possible to analyze as to how the fluid is spatially distributed over the entire region $16^\circ \times 16^\circ$. To resolve these problems and get more accurate inferences on the sub-photospheric structure beneath ARs, we plan to apply the "small scale" ring analysis and time-distance techniques. Once the exact relation of sub-photosphere structure with lifetime of the AR is established, it can be used in predicting their life more accurately.

9.3.4 Long Term Evolution of Super Active Regions

We plan to extend our study of selected ARs having long lifetimes covering at least two or three Carrington rotations, in order to compare the change in their properties from birth to maturity and eventual decay. It would be of particular importance to study those ARs which produced most energetic flares. For example, NOAA 6555, 6559 of solar cycle 22, and NOAA 9393, 10486 of solar cycle 23, are such few rare candidates, deserving to be termed as SARs. NOAA 10486 stood unrivaled as it produced flares of unprecedented magnitude, such as X17/4B, X10/3B and X28 in quick succession. Occurrence of flares of such magnitude at this rate evidently requires extremely rapid energy buildup mechanism. Therefore, from their energetic considerations, these SARs are expected to possess distinctly different sub-surface flows as compared to less productive ARs. Study of such ARs is expected to provide important insights in our understanding of flare productivity, characterization of ARs, and in space-weather predictions.

9.3.5 Chromospheric Oscillations

Another important aspect of solar oscillations, which needs to be further explored and established, is the chromospheric oscillations. Different researchers have found a variety of periodicities in the chromosphere. Understanding of chromospheric oscillations is not yet as complete as the photospheric ones, due in part to the inhomogeneity of the chromosphere (arising from the influence of magnetic fields) which makes the observation and theoretical interpretation more complicated. Major questions are: (i) Are oscillations the prime structuring agent of the quiet Sun inter-network chromosphere, or do inter-network magnetic fields or thermal inhomogeneities also play a role? (ii) What sources drive chromospheric oscillations? Are they localized, identifiable pistons in the photosphere, such as 5 minute amplitude peaks (Fleck and Schmitz, 1993)? (iii) what are the dynamics of magnetic elements in the chromosphere? In particular, what motions constitute the low-frequency power of network elements? (iv) How a flare affects the oscillations? These questions remain yet to be addressed in a satisfactory manner. To give statistically significant answers to the above questions, we plan to study ARs involving a large set of solar flares with a particular emphasis to identify how the flares may affect the chromospheric oscillations.

Appendix A

A New Method of Trapezoidal Integration

The integration of a continuous function $f(x)$ between two abscissa points, say x_1 and x_2, can be written as

$$A = \int_{x_1}^{x_n} f(x)\,\mathrm{d}x \tag{A.1}$$

In practices we do not have continuous observations of $f(x)$ and it is possible to compute (Equation A.1) only by numerical integration methods. The methods such as Simpson's rule, Newton-Cotes assume that the abscissa points are equally spaced. For unequally spaced points, numerical integration is carried out by Gaussian quadrature and trapezoidal methods.

In the trapezoidal (also known as trapezium) rule of integration, we split the area of integration into many trapeziums. As illustrated in the Figure A.1, we split the area under the curve $f(x)$ and x-axis into $n-1$ parts. Then the total area under the curve can be calculated by adding areas of each trapezium,

Figure A.1 Graphic illustration of trapezoidal rule, where area under the curve and x-axis (from x_1 to x_n) is divided into n-1 trapeziums.

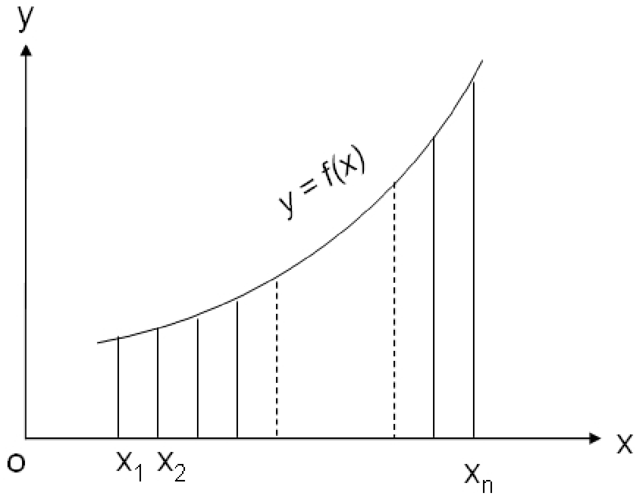

$$\int_{x_1}^{x_n} f(x)\,\mathrm{d}x = \frac{1}{2}(x_2 - x_1)[f(x_1) + f(x_2)] + \frac{1}{2}(x_3 - x_2)[f(x_2) + f(x_3)] + \cdots + \frac{1}{2}(x_n - x_{n-1})[f(x_{n-1}) + f(x_n)] \tag{A.2}$$

We can write the Equation A.2 as,

$$\int_{x_1}^{x_n} f(x)\,\mathrm{d}x = \sum_{i=1}^{n} w_i f(x_i) \tag{A.3}$$

where, w_i is given by

$$w_i = \frac{1}{2}\begin{cases} x_2 - x_1, & i = 1 \\ x_{i+1} - x_{i-1}, & i = 2, \ldots, n-1 \\ x_n - x_{n-1}, & i = n \end{cases} \tag{A.4}$$

The Equation A.3 is very useful for simplifying the integral equation into summation and provides an easy way for numerical integration of unequally spaced data points.

Bibliography

Aboudarham, J., Scholl, I., Fuller, N., Fouesneau, M., *et al.*: 2008, Automatic detection and tracking of filaments for a solar feature database. *Ann. Geophys.* **26**(2), 243 – 248.

Abramenko, V.I., Baranovsky, E.A.: 2004, Flare-related changes in the profiles of six photospheric spectral lines. *Solar Phys.* **220**, 81 – 91.

Abramenko, V.I., Longcope, D.W.: 2005, Distribution of the magnetic flux in elements of the magnetic field in active regions. *Astrophys. J.* **619**, 1160 – 1166.

Abramenko, V.I., Wang, T., Yurchishin, V.B.: 1996, Analysis of electric current helicity in active regions on the basis of vector magnetograms. *Solar Phys.* **168**, 75 – 89.

Ambastha, A.: 2006, Photospheric, chromospheric and helioseismic signatures of a large flare in super-active region NOAA 10486. *J. Astrophys. Astron.* **27**, 255 – 265.

Ambastha, A.: 2007a, Evolution of magnetic and velocity fields in super-active region noaa10486 and the large 4B/X17.2 flare of October 28, 2003. *Sun Geosph.* **2**, 13 – 18.

Ambastha, A.: 2007b, Signatures of large flares on photospheric magnetic and velocity fields. *Bul. Astron. Soc. India* **35**, 419 – 426.

Ambastha, A.: 2008, Helioseismic effects of energetic transients. *J. Astrophys. Astron.* **29**, 93 – 101.

Ambastha, A., Antia, H.M.: 2006, Possibility of excitation of low-ℓ p-modes by energetic solar transients. *Solar Phys.* **238**, 219 – 230.

Ambastha, A., Bhatnagar, A.: 1988, Sunspot proper motions in active region NOAA 2372 and its flare activity during SMY period of 1980 April 4-13. *J. Astrophys. Astron.* **9**, 137 – 154.

Ambastha, A., Basu, S., Antia, H.M.: 2003, Flare-induced excitation of solar p-modes. *Solar Phys.* **218**, 151 – 172.

Ambastha, A., Hagyard, M.J., West, E.A.: 1993, Evolutionary and flare-associated magnetic shear variations observed in a complex, flare-productive active region. *Solar Phys.* **148**, 277 – 299.

Ambastha, A., Basu, S., Antia, H.M., Bogart, R.S.: 2004, Solar p-mode characteristics associated with superactive-regions observed during Oct – Nov 2003. In: Danesy, D. (ed.) *SOHO 14 Helio- and Asteroseismology: Towards a Golden Future*, *(ESA SP-559, Noordwijk:ESA)*, 293 – 296.

Anderson, E.R., Duvall, T.L. Jr., Jefferies, S.M.: 1990, Modeling of solar oscillation power spectra. *Astrophys. J.* **364**, 699 – 705.

Antia, H.M.: 1996, Nonasymptotic helioseismic inversion: Iterated seismic solar model. *Astron. Astrophys.* **307**, 609 – 623.

Antia, H.M.: 2002, *Numerical methods for scientists and engineers*, 2nd edn. Hindustan Book Agency, New Delhi, India.

Antia, H.M., Basu, S.: 1994, Nonasymptotic helioseismic inversion for solar structure. *Astron. Astrophys. Suppl.* **107**, 421 – 444.

Antia, H.M., Basu, S.: 2007, Local helioseismology using ring diagram analysis. *Astron. Nachr.* **328**, 257 – 263.

Asai, A., Yokoyama, T., Shimojo, M., Masuda, S., *et al.*: 2004, Flare ribbon expansion and energy release rate. *Astrophys. J.* **611**, 557 – 567.

Asai, A., Yokoyama, T., Shimojo, M., Masuda, S., Shibata, K.: 2006, Flare ribbon expansion and energy release. *J. Astrophys. Astron.* **27**, 167 – 173.

Backus, G., Gilbert, F.: 1968, The resolving power of gross Earth data. *Geophys. J. Int.* **16**, 169 – 205.

Backus, G., Gilbert, F.: 1970, Uniqueness in the inversion of inaccurate gross Earth data. *Roy. Soc. Phil. Tran. Ser. London* **266**, 123 – 192.

Backus, G.E., Gilbert, J.F.: 1967, Numerical applications of a formalism for geophysical inverse problems. *Geophys. J. Int.* **13**, 247 – 276.

Bahcall, J.N., Pinsonneault, M.H., Basu, S., Christensen-Dalsgaard, J.: 1997, Are standard solar models reliable? *Phys. Rev. Lett.* **78**, 171 – 174.

Bao, S., Zhang, H.: 1998, Patterns of current helicity for the twenty-second solar cycle. *Astrophys. J.* **496**, L43 – L46.

Bao, S.D., Ai, G.X., Zhang, H.Q.: 2000, The hemispheric sign rule of current helicity during the rising phase of cycle 23. *J. Astrophys. Astron.* **21**, 303 – 306.

Basu, S., Antia, H.M.: 1999, Large-scale flows in the solar interior: Effect of asymmetry in peak profiles. *Astrophys. J.* **525**, 517 – 523.

Basu, S., Antia, H.M.: 2003, Changes in solar dynamics from 1995 to 2002. *Astrophys. J.* **585**, 553 – 565.

Basu, S., Antia, H.M., Bogart, R.S.: 2004, Ring-diagram analysis of the structure of solar active regions. *Astrophys. J.* **610**, 1157 – 1168.

Basu, S., Antia, H.M., Tripathy, S.C.: 1999, Ring diagram analysis of near-surface flows in the Sun. *Astrophys. J.* **512**, 458 – 470.

Beck, J.G., Giles, P.: 2005, Helioseismic determination of the solar rotation axis. *Astrophys. J.* **621**, L153 – L156.

Berger, M.A., Field, G.B.: 1984, The topological properties of magnetic helicity. *J. Fluid Mech.* **147**, 133 – 148.

Birch, A.C., Kosovichev, A.G., Price, G.H., Schlottmann, R.B.: 2001, The accuracy of the born and ray approximations in time-distance helioseismology. *Astrophys. J.* **561**, L229 – L232.

Braun, D.C., Birch, A.C.: 2008, Surface-focused seismic holography of sunspots: I. Observations. *Solar Phys.* **251**, 267 – 289.

Braun, D.C., Fan, Y.: 1998, Helioseismic measurements of the subsurface meridional flow. *Astrophys. J.* **508**, L105 – L108.

Braun, D.C., Lindsey, C.: 1999, Helioseismic images of an active region complex. *Astrophys. J.* **513**, L79 – L82.

Braun, D.C., Lindsey, C.: 2001, Seismic imaging of the far hemisphere of the Sun. *Astrophys. J.* **560**, L189 – L192.

Braun, D.C., Birch, A.C., Lindsey, C.: 2004, Local helioseismology of near-surface flows. In: Danesy, D. (ed.) *SOHO 14 Helio- and Asteroseismology: Towards a Golden Future*, *(ESA SP-559, Noordwijk:ESA)*, 337 – 341.

Braun, D.C., Duvall, T.L. Jr., Labonte, B.J.: 1987, Acoustic absorption by sunspots. *Astrophys. J.* **319**, L27 – L31.

Braun, D.C., Labonte, B.J., Duvall, T.L. Jr.: 1990, The spatial distribution of p-mode absorption in active regions. *Astrophys. J.* **354**, 372 – 381.

Brown, D.S., Nightingale, R.W., Alexander, D., Schrijver, C.J., *et al.*: 2003, Observations of rotating sunspots from TRACE. *Solar Phys.* **216**, 79 – 108.

Brown, J.C.: 1971, The deduction of energy spectra of non-thermal electrons in flares from the observed dynamic spectra of hard X-ray bursts. *Solar Phys.* **18**, 489 – 502.

Brown, T.M., Christensen-Dalsgaard, J., Dziembowski, W.A., Goode, P., *et al.*: 1989, Inferring the Sun's internal angular velocity from observed p-mode frequency splittings. *Astrophys. J.* **343**, 526 – 546.

Bruls, J.H.M.J.: 1993, The formation of helioseismology lines. IV - The Ni I 676.8 nm intercombination line. *Astron. Astrophys.* **269**, 509 – 517.

Burtseva, O., Hill, F., Kholikov, S., Chou, D.: 2009, Lifetimes of high-degree p-modes in the quiet and active Sun. *Solar Phys.* **258**, 1 – 11.

Cattaneo, F., Lenz, D., Weiss, N.: 2001, On the origin of the solar mesogranulation. *Astrophys. J.* **563**, L91 – L94.

Chaplin, W.J., Elsworth, Y., Isaak, G.R., Miller, B.A., New, R.: 2000, Variations in the excitation and damping of low-ℓ solar p-modes over the solar activity cycle. *Mon. Not. Roy. Astron. Soc.* **313**, 32 – 42.

Chen, J., Wang, H., Zirin, H., Ai, G.: 1994, Observations of vector magnetic fields in flaring active regions. *Solar Phys.* **154**, 261 – 273.

Chen, Q.R., Ding, M.D.: 2006, Footpoint motion of the continuum emission in the 2002 September 30 white-light flare. *Astrophys. J.* **641**, 1217 – 1221.

Choudhuri, A.R.: 2003, On the connection between mean field dynamo theory and flux tubes. *Solar Phys.* **215**, 31 – 55.

Choudhuri, A.R., Chatterjee, P., Nandy, D.: 2004, Helicity of solar active regions from a dynamo model. *Astrophys. J.* **615**, L57 – L60.

Christensen-Dalsgaard, J., Schou, J., Thompson, M.J.: 1990, A comparison of methods for inverting helioseismic data. *Mon. Not. Roy. Astron. Soc.* **242**, 353 – 369.

Christensen-Dalsgaard, J., Dappen, W., Ajukov, S.V., Anderson, E.R., *et al.*: 1996, The current state of solar modeling. *Science* **272**, 1286 – 1292.

Corbard, T., Thompson, M.J.: 2002, The subsurface radial gradient of solar angular velocity from MDI f-mode observations. *Solar Phys.* **205**, 211 – 229.

Corbard, T., Toner, C., Hill, F., Hanna, K.D., *et al.*: 2003, Ring-diagram analysis with GONG++. In: Sawaya-Lacoste, H. (ed.) *SOHO12/GONG+ 2002 Local and Global Helioseismology: the Present and Future*, *(ESA SP-517, Noordwijk:ESA)*, 255 – 258.

Couvidat, S., Birch, A.C., Kosovichev, A.G.: 2006, Three-dimensional inversion of sound speed below a sunspot in the born approximation. *Astrophys. J.* **640**, 516 – 524.

Deubner, F.L.: 1975, Observations of low wavenumber nonradial eigenmodes of the Sun. *Astron. Astrophys.* **44**, 371 – 375.

Deubner, F., Gough, D.: 1984, Helioseismology: Oscillations as a daignostic of the solar interior. *Ann. Rev. Astron. Astrophys.* **22**, 593 – 619.

Ding, M.D., Fang, C.: 1989, A semi-empirical model of sunspot penumbra. *Astron. Astrophys.* **225**, 204 – 212.

Ding, M.D., Qiu, J., Wang, H.: 2002, Non-LTE calculation of the Ni I 676.8 nanometer line in a flaring atmosphere. *Astrophys. J.* **576**, L83 – L86.

Donea, A.C., Lindsey, C.: 2005, Seismic emission from the solar flares of 2003 October 28 and 29. *Astrophys. J.* **630**, 1168 – 1183.

Donea, A., Braun, D.C., Lindsey, C.: 1999, Seismic images of a solar flare. *Astrophys. J.* **513**, L143 – L146.

Duvall, T.L. Jr.: 1979, Large-scale solar velocity fields. *Solar Phys.* **63**, 3 – 15.

Duvall, T.L. Jr., Harvey, J.W., Pomerantz, M.A.: 1988, Intermediate degree solar oscillations. In: Christensen-Dalsgaard, J., Frandsen, S. (eds.) *Advances in Helio- and Asteroseismology*, *IAU Symposium* **123**, 37 – 40.

Duvall, T.L. Jr., Harvey, J.W., Jefferies, S.M., Pomerantz, M.A.: 1991, Measurements of high-frequency solar oscillation modes. *Astrophys. J.* **373**, 308 – 316.

Duvall, T.L. Jr., Jefferies, S.M., Harvey, J.W., Osaki, Y., Pomerantz, M.A.: 1993a, Asymmetries of solar oscillation line profiles. *Astrophys. J.* **410**, 829 – 836.

Duvall, T.L. Jr., Jefferies, S.M., Harvey, J.W., Pomerantz, M.A.: 1993b, Time-distance helioseismology. *Nature* **362**, 430 – 432.

Edelman, F., Hill, F., Howe, R., Komm, R.: 2004, The effect of spectral line shape changes on GONG observations of oscillations and flares. In: Danesy, D. (ed.) *SOHO 14 Helio- and Asteroseismology: Towards a Golden Future*, *(ESA SP-559, Noordwijk:ESA)*, 416 – 419.

Emslie, A.G.: 1978, The collisional interaction of a beam of charged particles with a hydrogen target of arbitrary ionization level. *Astrophys. J.* **224**, 241 – 246.

Evans, J.W., Michard, R.: 1962, Observational study of macroscopic inhomogeneities in the solar atmosphere. I. Velocity displacements of Fraunhofer lines as a function of line strength and position on disk. *Astrophys. J.* **135**, 812 – 822.

Fan, Y., Fisher, G.H., McClymont, A.N.: 1994, Dynamics of emerging active region flux loops. *Astrophys. J.* **436**, 907 – 928.

Fernandez Borda, R.A., Mininni, P.D., Mandrini, C.H., Gómez, D.O., *et al.*: 2002, Automatic solar flare detection using neural network techniques. *Solar Phys.* **206**, 347 – 357.

Fleck, B., Schmitz, F.: 1993, On the interactions of hydrodynamic shock waves in stellar atmospheres. *Astron. Astrophys.* **273**, 671 – 683.

Fletcher, L., Hudson, H.: 2001, The magnetic structure and generation of EUV flare ribbons. *Solar Phys.* **204**, 69 – 89.

Fodor, I.K., Stark, P.B.: 1998, Multitaper spectrum estimates. In: Korzennik, S. (ed.) *Structure and Dynamics of the Interior of the Sun and Sun-like Stars, (ESA SP-418, Noordwijk:ESA)*, 171 – 176.

Fontenla, J.M., Ambastha, A., Kalman, B., Csepura, G.: 1995, The magnetic evolution of AR 6555 which led to two impulsive, relatively compact, X-type flares. *Astrophys. J.* **440**, 894 – 906.

Forbes, T.G., Lin, J.: 2000, What can we learn about reconnection from coronal mass ejections? *J. Atmos. Sol. Terr. Phys.* **62**, 1499 – 1507.

Forbes, T.G., Priest, E.R.: 1984, Numerical simulation of reconnection in an emerging magnetic flux region. *Solar Phys.* **94**, 315 – 340.

Fu, G., Shih, F.Y., Wang, H.: 2007, Automatic detection of prominence eruption using consecutive solar images. *IEEE Transactions on Circuits and Systems for Video Technology* **17**(1), 79 – 85.

Gabriel, A.H., Grec, G., Charra, J., Robillot, J., *et al.*: 1995, Global oscillations at low frequency from the SOHO mission (GOLF). *Solar Phys.* **162**, 61 – 99.

Gao, Y., Zhang, H., Zhao, J.: 2009, Comparison of photospheric current helicity and subsurface kinetic helicity. *Mon. Not. Roy. Astron. Soc.* **394**, L79 – L83.

García, R.A., Régulo, C., Turck-Chièze, S., Bertello, L., *et al.*: 2001, Low-degree low-order solar *p*-modes as seen by GOLF on board SOHO. *Solar Phys.* **200**, 361 – 379.

García, R.A., Turck-Chièze, S., Jiménez-Reyes, S.J., Ballot, J., *et al.*: 2007, Tracking solar gravity modes: The dynamics of the solar core. *Science* **316**, 1591 – 1593.

Giovanelli, R.G.: 1939, The relations between eruptions and sunspots. *Astrophys. J.* **89**, 555 – 567.

Gizon, L., Birch, A.C.: 2002, Time-distance helioseismology: The forward problem for random distributed sources. *Astrophys. J.* **571**, 966 – 986.

Gizon, L., Schunker, H., Baldner, C.S., Basu, S., *et al.*: 2009, Helioseismology of sunspots: A case study of NOAA region 9787. *Space Sci. Rev.* **144**, 249 – 273.

Goldreich, P., Murray, N.: 1994, The effects of scattering on solar oscillations. *Astrophys. J.* **424**, 480 – 490.

Golub, L., Vaiana, G.S.: 1978, Differential rotation rates for short-lived regions of emerging magnetic flux. *Astrophys. J.* **219**, L55 – L57.

Gonczi, G., Roddier, F.: 1969, A fourier spectrum analysis of long samples of solar line oscillations. *Solar Phys.* **8**, 255 – 259.

Gonzalez, R.C., Woods, R.E.: 2008, *Digital image processing*, 3rd edn. PHI Learning, New Delhi, India.

Gough, D.: 1985, Inverting helioseismic data. *Solar Phys.* **100**, 65 – 99.

Gough, D., Toomre, J.: 1991, Seismic observations of the solar interior. *Ann. Rev. Astron. Astrophys.* **29**, 627 – 685.

Gough, D.O.: 1984, On the rotation of the Sun. *Roy. Soc. Phil. Tran. Ser. London* **313**, 27 – 38.

Gough, D.O., Kosovichev, A.G.: 1993, The influence of low-degree p-mode frequencies on the determination of the structure of the solar interior. *Mon. Not. Roy. Astron. Soc.* **264**, 522.

Gough, D.O., Kosovichev, A.G., Toomre, J., Anderson, E., *et al.*: 1996, The seismic structure of the Sun. *Science* **272**, 1296 – 1300.

Haber, D.A., Toomre, J., Hill, F., Gough, D.O.: 1988, Local effects of a major flare on solar five-minute oscillations. In: Rolfe, E.J. (ed.) *Seismology of the Sun and Sun-Like Stars*, *(ESA SP-286, Noordwijk:ESA)*, 301 – 304.

Haber, D.A., Hindman, B.W., Toomre, J., Bogart, R.S., *et al.*: 2000, Solar shear flows deduced from helioseismic dense-pack samplings of ring diagrams. *Solar Phys.* **192**, 335 – 350.

Haber, D.A., Hindman, B.W., Toomre, J., Bogart, R.S., *et al.*: 2002, Evolving submerged meridional circulation cells within the upper convection zone revealed by ring-diagram analysis. *Astrophys. J.* **570**, 855 – 864.

Hagyard, M.J., Stark, B.A., Venkatakrishnan, P.: 1999, A search for vector magnetic field variations associated with the M-class flares of 10 June 1991 in AR 6659. *Solar Phys.* **184**, 133 – 147.

Hagyard, M.J., Teuber, D., West, E.A., Smith, J.B.: 1984, A quantitative study relating observed shear in photospheric magnetic fields to repeated flaring. *Solar Phys.* **91**, 115 – 126.

Hale, G.E.: 1927, The fields of force in the atmosphere of the Sun. *Nature* **119**, 708 – 714.

Handy, B.N., Acton, L.W., Kankelborg, C.C., Wolfson, C.J., *et al.*: 1999, The transition region and coronal explorer. *Solar Phys.* **187**, 229 – 260.

Harvey, J.: 1986, Small-scale photospheric magnetic fields: Observational methods and limitations. In: Deinzer, W., Knölker, M., Voigt, H.H. (eds.) *Small Scale Magnetic Flux Concentrations in the Solar Photosphere*, 25.

Harvey, J.: 1995, Sounding out the Sun. *Physics Today*, 32 – 38.

Harvey, J., Abdel-Gawad, K., Ball, W., Boxum, B., *et al.*: 1988, The GONG instrument. In: Rolfe, E.J. (ed.) *Seismology of the Sun and Sun-Like Stars, (ESA SP-286, Noordwijk:ESA)*, 203 – 203.

Hill, F.: 1988, Rings and trumpets - three-dimensional power spectra of solar oscillations. *Astrophys. J.* **333**, 996 – 1013.

Hill, F.: 1989, Solar oscillation ring diagrams and large-scale flows. *Astrophys. J.* **343**, L69 – L71.

Hill, F.: 1995, Local probes of the solar interior. In: Hoeksema, J., Domingo, V., Fleck, B., Battrick, B. (eds.) *Helioseismology*, *(ESA SP-376, Noordwijk:ESA)*, 63 – 75.

Hill, F., Howe, R.: 1998, Calculating the GONG leakage matrix. In: Korzennik, S. (ed.) *Structure and Dynamics of the Interior of the Sun and Sun-like Stars, (ESA SP-418, Noordwijk:ESA)*, 225 – 230.

Hill, F., Bolding, J., Toner, C., Corbard, T., *et al.*: 2003, The GONG++ data processing pipeline. In: Sawaya-Lacoste, H. (ed.) *GONG+ 2002. Local and Global Helioseismology: the Present and Future*, *(ESA SP-517, Noordwijk:ESA)*, 295 – 298.

Hindman, B.W., Haber, D.A., Toomre, J.: 2006, Helioseismically determined near-surface flows underlying a quiescent filament. *Astrophys. J.* **653**, 725 – 732.

Hindman, B.W., Haber, D.A., Toomre, J.: 2009, Subsurface circulations within active regions. *Astrophys. J.* **698**, 1749 – 1760.

Hindman, B., Haber, D., Toomre, J., Bogart, R.: 2000, Local fractional frequency shifts used as tracers of magnetic activity. *Solar Phys.* **192**, 363 – 372.

Hirayama, T.: 1974, Theoretical model of flares and prominences. I: Evaporating flare model. *Solar Phys.* **34**, 323 – 338.

Howard, R., Labonte, B.J.: 1980, The Sun is observed to be a torsional oscillator with a period of 11 years. *Astrophys. J.* **239**, L33 – L36.

Howard, R.F.: 1996, Solar active regions as diagnostics of subsurface conditions. *Ann. Rev. Astron. Astrophys.* **34**, 75 – 110.

Howe, R., Komm, R.W., Hill, F., Haber, D.A., Hindman, B.W.: 2004, Activity-related changes in local solar acoustic mode parameters from michelson doppler imager and global oscillations network group. *Astrophys. J.* **608**, 562 – 579.

Howe, R., Christensen-Dalsgaard, J., Hill, F., Komm, R., *et al.*: 2005, Solar convection-zone dynamics, 1995-2004. *Astrophys. J.* **634**, 1405 – 1415.

Hudson, H.S., Acton, L.W., Hirayama, T., Uchida, Y.: 1992, White-light flares observed by Yohkoh. *Pub. Astron. Soc. Japan* **44**, L77 – L81.

Hurford, G.J., Schmahl, E.J., Schwartz, R.A., Conway, A.J., *et al.*: 2002, The RHESSI imaging concept. *Solar Phys.* **210**, 61 – 86.

Isobe, H., Yokoyama, T., Shimojo, M., Morimoto, T., *et al.*: 2002, Reconnection rate in the decay phase of a long duration event flare on 1997 May 12. *Astrophys. J.* **566**, 528 – 538.

Jeffrey, W.: 1988, Inversion of helioseismology data. *Astrophys. J.* **327**, 987 – 992.

Jensen, J.M.: 2003, Time-distance: What does it tell us? In: Sawaya-Lacoste, H. (ed.) *GONG+ 2002. Local and Global Helioseismology: the Present and Future, (ESA SP-517, Noordwijk:ESA)*, 61 – 70.

Jensen, J.M., Duvall, T.L. Jr., Jacobsen, B.H.: 2003, Noise propagation in inversion of helioseismic time-distance data. In: Sawaya-Lacoste, H. (ed.) *GONG+ 2002. Local and Global Helioseismology: the Present and Future, (ESA SP-517, Noordwijk:ESA)*, 315 – 318.

Jones, W.L.: 1969, Non-divergent oscillations in the solar atmosphere. *Solar Phys.* **7**, 204 – 209.

Karoff, C., Kjeldsen, H.: 2008, Evidence that solar flares drive global oscillations in the Sun. *Astrophys. J.* **678**, L73 – L76.

Klassen, A., Krucker, S., Kunow, H., Müller-Mellin, R., *et al.*: 2005, Solar energetic electrons related to the 28 October 2003 flare. *J. Geophys. Res.* **110**, 9 – 14.

Komm, R., Howe, R., Hill, F.: 2009, Emerging and decaying magnetic flux and subsurface flows. *Solar Phys.* **258**, 13 – 30.

Komm, R.W., Howard, R.F., Harvey, J.W.: 1993, Meridional flow of small photospheric magnetic features. *Solar Phys.* **147**, 207 – 223.

Komm, R.W., Howe, R., Hill, F.: 2000a, Solar-cycle changes in GONG p-mode widths and amplitudes 1995-1998. *Astrophys. J.* **531**, 1094 – 1108.

Komm, R.W., Howe, R., Hill, F.: 2000b, Width and energy of solar p-modes observed by global oscillation network group. *Astrophys. J.* **543**, 472 – 485.

Komm, R., Howe, R., González Hernández, I., Hill, F., *et al.*: 2004a, Searching for subsurface signatures of X-class flares. In: Danesy, D. (ed.) *SOHO 14 Helio- and Asteroseismology: Towards a Golden Future*, *(ESA SP-559, Noordwijk:ESA)*, 158 – 163.

Komm, R., Corbard, T., Durney, B.R., González Hernández, I., *et al.*: 2004b, Solar subsurface fluid dynamics descriptors derived from global oscillation network group and michelson doppler imager data. *Astrophys. J.* **605**, 554 – 567.

Komm, R., Howe, R., Hill, F., González Hernández, I., Toner, C.: 2005a, Kinetic helicity density in solar subsurface layers and flare activity of active regions. *Astrophys. J.* **630**, 1184 – 1193.

Komm, R., Howe, R., Hill, F., González-Hernández, I., *et al.*: 2005b, Ring analysis of solar subsurface flows and their relation to surface magnetic activity. *Astrophys. J.* **631**, 636 – 646.

Komm, R., Howe, R., Hill, F., Miesch, M., *et al.*: 2007, Divergence and vorticity of solar subsurface flows derived from ring-diagram analysis of MDI and GONG data. *Astrophys. J.* **667**, 571 – 584.

Kopp, R.A., Pneuman, G.W.: 1976, Magnetic reconnection in the corona and the loop prominence phenomenon. *Solar Phys.* **50**, 85 – 98.

Korzennik, S.G.: 2001, On the diagnostic potential of time-distance helioseismology. In: Wilson, A, Pallé, P. L. (eds.) *SOHO 10/GONG 2000 Workshop: Helio- and Asteroseismology at the Dawn of the Millennium*, *(ESA SP-464, Noordwijk:ESA)*, 149 – 156.

Kosovichev, A.G.: 2006, Properties of flares-generated seismic waves on the Sun. *Solar Phys.* **238**, 1 – 11.

Kosovichev, A.G., Zharkova, V.V.: 1998, X-ray flare sparks quake inside Sun. *Nature* **393**, 317 – 318.

Kosovichev, A.G., Zharkova, V.V.: 1999, Variations of photospheric magnetic field associated with flares and CMEs. *Solar Phys.* **190**, 459 – 466.

Kosovichev, A.G., Zharkova, V.V.: 2001, Magnetic energy release and transients in the solar flare of 2000 July 14. *Astrophys. J.* **550**, L105 – L108.

Kosovichev, A.G., Duvall, T.L..J., Scherrer, P.H.: 2000, Time-distance inversion methods and results. *Solar Phys.* **192**, 159 – 176.

Krause, F., Raedler, K.: 1980, *Mean-field magnetohydrodynamics and dynamo theory*, 1st edn. Oxford, Pergamon Press.

Labonte, B.J., Howard, R.: 1982, Solar rotation measurements at Mount Wilson. III - Meridional flow and limbshift. *Solar Phys.* **80**, 361 – 372.

Lee, J., Gary, D.E., Qiu, J., Gallagher, P.T.: 2002, Electron transport during the 1999 August 20 flare inferred from microwave and hard X-ray observations. *Astrophys. J.* **572**, 609 – 625.

Leibacher, J.W., Stein, R.F.: 1971, A new description of the solar five-minute oscillation. *Astrophys. Lett.* **7**, 191 – 192.

Leighton, R.B., Noyes, R.W., Simon, G.W.: 1962, Velocity fields in the solar atmosphere. I. Preliminary report. *Astrophys. J.* **135**, 474 – 499.

Libbrecht, K.G.: 1988, Solar p-mode phenomenology. *Astrophys. J.* **334**, 510 – 516.

Libbrecht, K.G., Woodard, M.F.: 1990, Solar-cycle effects on solar oscillation frequencies. *Nature* **345**, 779 – 782.

Lim, E., Chae, J.: 2009, Chirality of intermediate filaments and magnetic helicity of active regions. *Astrophys. J.* **692**, 104 – 108.

Lin, J., Forbes, T.G.: 2000, Effects of reconnection on the coronal mass ejection process. *J. Geophys. Res.* **105**, 2375 – 2392.

Lin, R., Dennis, B.R., Hurford, G.J., Smith, D.M., *et al.*: 2002, The Reuven Ramaty High-Energy Solar Spectroscopic Imager (RHESSI). *Solar Phys.* **210**, 3 – 32.

Lindsey, C., Braun, D.C.: 1990, Helioseismic imaging of sunspots at their antipodes. *Solar Phys.* **126**, 101 – 115.

Lindsey, C., Braun, D.C., Jefferies, S.M.: 1993, Local helioseismology of subsurface structure. In: Brown, T.M. (ed.) *GONG 1992. Seismic Investigation of the Sun and Stars*, *Astron. Soc. Pac. Conf. Ser.* **42**, 81 – 84.

Litvinenko, Y.E., Somov, B.V.: 1995, Relativistic acceleration of protons in reconnecting current sheets of solar flares. *Solar Phys.* **158**, 317 – 330.

Liu, Y., Norton, A.A.: 2001, MDI measurement errors: The magnetic perspective/SOI-technical note. Technical Report 01-144.

Longcope, D.W., Welsch, B.T.: 2000, A model for the emergence of a twisted magnetic flux tube. *Astrophys. J.* **545**, 1089 – 1100.

Longcope, D.W., Fisher, G.H., Pevtsov, A.A.: 1998, Flux-tube twist resulting from helical turbulence: The sigma-effect. *Astrophys. J.* **507**, 417 – 432.

Lu, E.T.: 1995, The statistical physics of solar active regions and the fundamental nature of solar flares. *Astrophys. J.* **446**, L109 – L112.

Machado, M.E., Avrett, E.H., Vernazza, J.E., Noyes, R.W.: 1980, Semiempirical models of chromospheric flare regions. *Astrophys. J.* **242**, 336 – 351.

Martens, P.C.H., Young, A.: 1990, Neutral beams in two-ribbon flares and in the geomagnetic tail. *Astrophys. J. Sup. Ser.* **73**, 333 – 342.

Martin, S.F., Bilimoria, R., Tracadas, P.W.: 1994, Magnetic field configurations basic to filament channels and filaments. In: Rutten, R.J., Schrijver, C.J. (eds.) *Solar Surface Magnetism*, 303.

Mason, D., Komm, R., Hill, F., Howe, R., *et al.*: 2006, Flares, magnetic fields, and subsurface vorticity: A survey of GONG and MDI data. *Astrophys. J.* **645**, 1543 – 1553.

Masuda, S., Kosugi, T., Hudson, H.S.: 2001, A hard X-ray two-ribbon flare observed with Yohkoh/HXT. *Solar Phys.* **204**, 55 – 67.

Mathew, S.K.: 2008, Enhanced p-mode absorption seen near the sunspot umbral penumbral boundary. *Solar Phys.* **251**, 515 – 522.

Maurya, R.A., Ambastha, A.: 2008, Magnetic and velocity field variations in the active regions NOAA 10486 and NOAA 10488. *J. Astrophys. Astron.* **29**, 103 – 105.

Maurya, R.A., Ambastha, A.: 2009, Transient magnetic and Doppler features related to the white-light flares in NOAA 10486. *Solar Phys.* **258**, 31 – 52.

Maurya, R.A., Ambastha, A.: 2010, Sub-surface meridional flow, vorticity and the life time of solar active regions. *Astrophys. J.* **714**, L196 – L201.

Maurya, R.A., Ambastha, A., Tripathy, S.C.: 2009, Variations in p-mode parameters with changing onset time of a large flare. *Astrophys. J.* **706**, L235 – L239.

Metcalf, T.R., Alexander, D., Hudson, H.S., Longcope, D.W.: 2003, TRACE and Yohkoh observations of a white-light flare. *Astrophys. J.* **595**, 483 – 492.

Metcalf, T.R., Leka, K.D., Barnes, G., Lites, B.W., *et al.*: 2006, An overview of existing algorithms for resolving the 180° ambiguity in vector magnetic fields: Quantitative tests with synthetic data. *Solar Phys.* **237**, 267 – 296.

Meyer, F., Schmidt, H.U.: 1967, Die erzeugung von schwingungen in der sonnenatmosphäre durch einzelne granula. *Zeits. Astrophys.* **65**, 274 – 298.

Moffatt, H.K.: 1978, *Magnetic field generation in electrically conducting fluids*, 1st edn. Cambridge University Press.

Moffatt, H.K., Tsinober, A.: 1992, Helicity in laminar and turbulent flow. *Annual Review of Fluid Mechanics* **24**, 281 – 312.

Narayan, R., Nityananda, R.: 1986, Maximum entropy image restoration in astronomy. *Ann. Rev. Astron. Astrophys.* **24**, 127 – 170.

Narukage, N., Shibata, K.: 2006, Statistical analysis of reconnection inflows in solar flares observed with SOHO/EIT. *Astrophys. J.* **637**, 1122 – 1134.

Neidig, D.F., Kane, S.R.: 1993, Energetics and timing of the hard and soft X-ray emissions in white light flares. *Solar Phys.* **143**, 201 – 204.

Nigam, R., Kosovichev, A.G.: 1998, Measuring the Sun's eigenfrequencies from velocity and intensity helioseismic spectra: Asymmetrical line profile-fitting formula. *Astrophys. J.* **505**, L51 – L54.

Nordlund, Å., Stein, R.F., Asplund, M.: 2009, Solar surface convection. *Liv. Rev. Solar Phys.* **6**, 2 – 116.

November, L.J., Toomre, J., Gebbie, K.B., Simon, G.W.: 1981, The detection of mesogranulation on the Sun. *Astrophys. J.* **245**, L123 – L126.

Noyes, R.W., Leighton, R.B.: 1963, Velocity fields in the solar atmosphere. II. The oscillatory field. *Astrophys. J.* **138**, 631 – 647.

Orrall, F.Q.: 1965, Observational study of macroscopic inhomogeneities in the solar atmosphere.VI. Photospheric oscillations and chromospheric structure. *Astrophys. J.* **141**, 1131 – 1138.

Ossendrijver, M.: 2003, The solar dynamo. *Astron. Astrophys. Rev.* **11**, 287 – 367.

Parker, E.N.: 1955, Hydromagnetic dynamo models. *Astrophys. J.* **122**, 293 – 314.

Patron, J., Hill, F., Rhodes, E.J. Jr., Korzennik, S.G., Cacciani, A.: 1995, Ring diagram analysis of Mt. Wilson data: Velocity fields within the solar convection zone. In: Ulrich, R. K., Rhodes Jr., E. J., Dappen, W. (eds.) *GONG 1994. Helio- and Astro-Seismology from the Earth and Space*, Astron. Soc. Pac. Conf. Ser. **76**, 208 – 211.

Patron, J., Gonzalez Hernandez, I., Chou, D., Sun, M., *et al.*: 1997, Comparison of two fitting methods for ring diagram analysis of very high-ℓ solar oscillations. *Astrophys. J.* **485**, 869 – 874.

Patterson, A.: 1984, Flares in Hale 17760 - magnetic transients in the 1981 July 27 flare. *Astrophys. J.* **280**, 884 – 886.

Patterson, A., Zirin, H.: 1981, Transient magnetic field changes in flares. *Astrophys. J.* **243**, L99 – L101.

Pevtsov, A.A., Balasubramaniam, K.S., Rogers, J.W.: 2003, Chirality of chromospheric filaments. *Astrophys. J.* **595**, 500 – 505.

Pevtsov, A.A., Canfield, R.C., Latushko, S.M.: 2001, Hemispheric helicity trend for solar cycle 23. *Astrophys. J.* **549**, L261 – L263.

Pevtsov, A.A., Canfield, R.C., Metcalf, T.R.: 1994, Patterns of helicity in solar active regions. *Astrophys. J.* **425**, L117 – L119.

Pevtsov, A.A., Canfield, R.C., Metcalf, T.R.: 1995, Latitudinal variation of helicity of photospheric magnetic fields. *Astrophys. J.* **440**, L109 – L112.

Pijpers, F.P., Thompson, M.J.: 1992, Faster formulations of the optimally localized averages method for helioseismic inversions. *Astron. Astrophys.* **262**, L33 – L36.

Pijpers, F.P., Thompson, M.J.: 1994, The SOLA method for helioseismic inversion. *Astron. Astrophys.* **281**, 231 – 240.

Pouquet, A., Frisch, U., Leorat, J.: 1976, Strong MHD helical turbulence and the nonlinear dynamo effect. *J. Fluid Mech.* **77**, 321 – 354.

Priest, E.R., Forbes, T.G.: 2002, The magnetic nature of solar flares. *Astron. Astrophys. Rev.* **10**, 313 – 377.

Qiu, J., Gary, D.E.: 2003, Flare-related magnetic anomaly with a sign reversal. *Astrophys. J.* **599**, 615 – 625.

Qiu, J., Lee, J., Gary, D.E., Wang, H.: 2002, Motion of flare footpoint emission and inferred electric field in reconnecting current sheets. *Astrophys. J.* **565**, 1335 – 1347.

Qu, M., Shih, F., Jing, J., Wang, H.: 2004a, Automated solar flare detection and characterization. *Bul. American Astron. Soc.* **36**, 760.

Qu, M., Shih, F., Jing, J., Wang, H.: 2004b, Automatic solar flare tracking using image-processing techniques. *Solar Phys.* **222**, 137 – 149.

Qu, M., Shih, F.Y., Jing, J., Wang, H.: 2005, Automatic solar filament detection using image processing techniques. *Solar Phys.* **228**, 119 – 135.

Rabello-Soares, M.C., Korzennik, S.G., Schou, J.: 2001, The determination of MDI high-degree mode frequencies. In: Wilson, A, Pallé, P. L. (eds.) *SOHO 10/GONG 2000 Workshop: Helio- and Asteroseismology at the Dawn of the Millennium, (ESA SP-464, Noordwijk:ESA)*, 129 – 136.

Rachkowsky, D.N.: 1967, *Izv. Krymsk. Astrofiz. Obs.* **37**, 56.

Rajaguru, S.P., Basu, S., Antia, H.M.: 2001, Ring diagram analysis of the characteristics of solar oscillation modes in active regions. *Astrophys. J.* **563**, 410 – 418.

Rast, M.P.: 2003, The scales of granulation, mesogranulation, and supergranulation. *Astrophys. J.* **597**, 1200 – 1210.

Rhodes, E.J. Jr., Ulrich, R.K., Simon, G.W.: 1977, Observations of nonradial p-mode oscillations on the Sun. *Astrophys. J.* **218**, 901 – 919.

Richardson, R.S.: 1941, The nature of solar hydrogen vortices. *Astrophys. J.* **93**, 24 – 28.

Richardus, P., Adler, R.K.: 1972, *Map projections for geodesists, cartographers and geographers.*, North Holland Publishing, Amsterdam.

Rieutord, M., Roudier, T., Malherbe, J.M., Rincon, F.: 2000, On mesogranulation, network formation and supergranulation. *Astron. Astrophys.* **357**, 1063 – 1072.

Rüdiger, G., Pipin, V.V., Belvedère, G.: 2001, Alpha-effect, helicity and angular momentum transport for a magnetically driven turbulence in the solar convection zone. *Solar Phys.* **198**, 241 – 251.

Rust, D.M., Hegwer, F.: 1975, Analysis of the August 7, 1972 white light flare - light curves and correlation with hard X-rays. *Solar Phys.* **40**, 141 – 157.

Sakurai, T.: 1982, Green's function methods for potential magnetic fields. *Solar Phys.* **76**, 301 – 321.

Sakurai, T., Makita, M., Shibasaki, K.: 1985, Observation of magnetic field vector in solar active regions. *MPA Rep.* **212**, 312 – 315.

Scherrer, P.H., Bogart, R.S., Bush, R.I., Hoeksema, J.T., *et al.*: 1995, The solar oscillations investigation - Michelson Doppler Imager. *Solar Phys.* **162**, 129 – 188.

Schmidt, H.U., Zirker, J.B.: 1963, On the oscillations of the solar atmosphere. *Astrophys. J.* **138**, 1310 – 1311.

Schrijver, C.J., Title, A.M.: 1999, Active regions losing their moorings by subsurface reconnection. *Solar Phys.* **188**, 331 – 344.

Schrijver, C.J., Title, A.M., Berger, T.E., Fletcher, L., *et al.*: 1999, A new view of the solar outer atmosphere by the transition region and coronal explorer. *Solar Phys.* **187**, 261 – 302.

Schüssler, M., Rempel, M.: 2005, The dynamical disconnection of sunspots from their magnetic roots. *Astron. Astrophys.* **441**, 337 – 346.

Seehafer, N.: 1990, Electric current helicity in the solar atmosphere. *Solar Phys.* **125**, 219 – 232.

Serra, J.: 1983, *Image analysis and mathematical morphology*, Academic Press, New York.

Shih, F.Y., Kowalski, A.J.: 2003, Automatic extraction of filaments in Hα solar images. *Solar Phys.* **218**, 99 – 122.

Simon, G.W., Leighton, R.B.: 1964, Velocity fields in the solar atmosphere. III. Large-scale motions, the chromospheric network, and magnetic fields. *Astrophys. J.* **140**, 1120 – 1149.

Skilling, J., Bryan, R.K.: 1984, Maximum entropy image reconstruction - general algorithm. *Mon. Not. Roy. Astron. Soc.* **211**, 111 – 124.

Snodgrass, H.B.: 1984, Separation of large-scale photospheric doppler patterns. *Solar Phys.* **94**, 13 – 31.

Sturrock, P.A.: 1966, Model of the high-energy phase of solar flares. *Nature* **211**, 695 – 697.

Thompson, M.J., Christensen-Dalsgaard, J., Miesch, M.S., Toomre, J.: 2003, The internal rotation of the Sun. *Ann. Rev. Astron. Astrophys.* **41**, 599 – 643.

Tiwari, S.K., Venkatakrishnan, P., Sankarasubramanian, K.: 2009, Global twist of sunspot magnetic fields obtained from high-resolution vector magnetograms. *Astrophys. J.* **702**, L133 – L137.

Toner, C.G., Haber, D., Corbard, T., Bogart, R., Hindman, B.: 2003, An image merge for GONG+. In: Sawaya-Lacoste, H. (ed.) *GONG+ 2002. Local and Global Helioseismology: the Present and Future*, *(ESA SP-517, Noordwijk:ESA)*, 405 – 407.

Toutain, T., Appourchaux, T., Fröhlich, C., Kosovichev, A.G., *et al.*: 1998, Asymmetry and frequencies of low-degree *p*-modes and the structure of the Sun's core. *Astrophys. J.* **506**, L147 – L150.

Ulmschneider, P.H.: 1968, Possible explanation of the 300-second type oscillation in the solar chromosphere. *Astrophys. J.* **152**, 349 – 350.

Ulrich, R.K.: 1970, The five-minute oscillations on the solar surface. *Astrophys. J.* **162**, 993 – 1012.

Ulrich, R.K., Boyden, J.E., Webster, L., Padilla, S.P., Snodgrass, H.B.: 1988, Solar rotation measurements at mount wilson. V. Reanalysis of 21 years of data. *Solar Phys.* **117**, 291 – 328.

Unno, W., Kato, S.: 1962, On the generation of acoustic noise from the turbulent atmosphere. *Pub. Astron. Soc. Japan* **14**, 417 – 430.

Švanda, M., Klvaňa, M., Sobotka, M.: 2009, Large-scale horizontal flows in the solar photosphere. V. Possible evidence for the disconnection of bipolar sunspot groups from their magnetic roots. *Astron. Astrophys.* **506**, 875 – 884.

van Ballegooijen, A.A.: 1999, Photospheric motions as a source of twist in coronal magnetic fields. *American Geophys. Union Geophys. Monograph Ser.* **111**, 213 – 220.

Venkatakrishnan, P., Gary, G.A.: 1989, Off disk-center potential field calculations using vector magnetograms. *Solar Phys.* **120**, 235 – 247.

Venkatakrishnan, P., Hagyard, M.J., Hathaway, D.H.: 1988, Elimination of projection effects from vector magnetograms - the pre-flare configuration of active region AR 4474. *Solar Phys.* **115**, 125 – 131.

Venkatakrishnan, P., Kumar, B., Uddin, W.: 2008, Co-spatial evolution of photospheric Doppler enhancements and Hα flare ribbons observed during the solar flare of 2003 October 28. *Mon. Not. Roy. Astron. Soc.* **387**, L69 – L73.

Vernazza, J.E., Avrett, E.H., Loeser, R.: 1981, Structure of the solar chromosphere. III. Models of the EUV brightness components of the quiet-Sun. *Astrophys. J. Sup. Ser.* **45**, 635 – 725.

Vorontsov, S.V., Christensen-Dalsgaard, J., Schou, J., Strakhov, V.N., Thompson, M.J.: 2002, Helioseismic measurement of solar torsional oscillations. *Science* **296**, 101 – 103.

Wang, H.: 2006, Rapid changes of photospheric magnetic fields around flaring magnetic neutral lines. *Astrophys. J.* **649**, 490 – 497.

Wang, H., Varsik, J., Zirin, H., Canfield, R.C., *et al.*: 1992, Joint vector magnetograph observations at BBSO, Huairou station and Mees solar observatory. *Solar Phys.* **142**, 11 – 20.

Whitney, C.A.: 1958, Granulation and oscillations of the solar atmosphere. *Smiths. Contrib. Astrophys.* **2**, 365 – 376.

Wolff, C.L.: 1972, Free oscillations of the Sun and their possible stimulation by solar flares. *Astrophys. J.* **176**, 833 – 842.

Xie, W., Zhang, H., Wang, H.: 2009, Study of ribbon separation and magnetic reconnection rates in a two-ribbon flare. *Solar Phys.* **254**, 271 – 283.

Xu, H., Gao, Y., Zhang, H.: 2009, Some basic questions on helicity inferred from vector magnetograms. *Science in China: Phys. Astron.* **52**, 1749 – 1753.

Xu, Y., Cao, W., Liu, C., Yang, G., *et al.*: 2004, Near-infrared observations at 1.56 microns of the 2003 October 29 X10 white-light flare. *Astrophys. J.* **607**, L131 – L134.

Yang, G., Xu, Y., Cao, W., Wang, H., *et al.*: 2004, Photospheric shear flows along the magnetic neutral line of active region 10486 prior to an X10 flare. *Astrophys. J.* **617**, L151 – L154.

Yeates, A.R., Mackay, D.H., van Ballegooijen, A.A.: 2008, Evolution and distribution of current helicity in full-Sun simulations. *Astrophys. J.* **680**, L165 – L168.

Yokoyama, T., Akita, K., Morimoto, T., Inoue, K., Newmark, J.: 2001, Clear evidence of reconnection inflow of a solar flare. *Astrophys. J.* **546**, L69 – L72.

Zaatri, A., Komm, R., González Hernández, I., Howe, R., Corbard, T.: 2006, North south asymmetry of zonal and meridional flows determined from ring diagram analysis of GONG++ data. *Solar Phys.* **236**, 227 – 244.

Zhang, Y., Liu, J.H., Zhang, H.Q.: 2005, The relationship between photospheric magnetic field evolution and major flares. In: Dere, K., Wang, J., Yan, Y. (eds.) *Coronal and Stellar Mass Ejections*, *IAU Symposium* **226**, 229 – 232.

Zhao, J.: 2004, Inference of solar subsurface flows by time-distance helioseismology. PhD thesis, Stanford University.

Zhao, J., Kosovichev, A.G.: 2004, Torsional oscillation, meridional flows, and vorticity inferred in the upper convection zone of the Sun by time-distance helioseismology. *Astrophys. J.* **603**, 776 – 784.

Zharkov, S., Zharkova, V., Ipson, S., Benkhalil, A.: 2005, Technique for automated recognition of sunspots on full-disk solar images. *J. Appl. Sig. Proc.* **2005**, 2573 – 2584.

Zharkova, V.V., Zharkov, S.I.: 2007, On the origin of three seismic sources in the proton-rich flare of 2003 October 28. *Astrophys. J.* **664**, 573 – 585.

Zharkova, V., Ipson, S., Benkhalil, A., Zharkov, S.: 2005, Feature recognition in solar images. *Artif. Intell. Rev.* **23**(3), 209 – 266.

Zhou, T., Ji, H., Huang, G.: 2008, Converging motion of conjugate flaring kernels during two large solar flares. *Adv. Spa. Res.* **41**, 1195 – 1201.

Zirin, H., Tanaka, K.: 1981, Magnetic transients in flares. *Astrophys. J.* **250**, 791 – 795.

List of Publications

I. Research Papers in Scientific Journals:

1. *Transient Magnetic and Doppler Features Related to the White-light Flares in NOAA 10486*, **R. A. Maurya** and A. Ambastha, *Solar Phys.*, **258**, 31 (2009).

2. *Variations in p-Mode Parameters with Changing Onset Time of a Large Flare*, **R. A. Maurya** and A. Ambastha, *Astrophys. J. Lett.*, **706**, 235 (2009).

3. *A Technique for Automated Determination of Flare Ribbon Separation and Energy Release*, **R. A. Maurya** and A. Ambastha, *Solar Phys.*, **262**, 314 (2010).

4. *Sub-surface Meridional Flow, Vorticity and the Life Time of Solar Active Regions*, **R. A. Maurya** and A. Ambastha, *Astrophys. J. Lett.*, **714**, 196 (2010).

II. Papers in Proceedings:

1. *Magnetic and Velocity Field Variations in the Active Regions NOAA 10486 and NOAA 10488*, **R. A. Maurya** and A. Ambstha, *J. Astrophys. Astron.*, **29**, 103 (2008).

2. *Hα Intensity Oscillations in Large Flares*, **R. A. Maurya** and A. Ambstha, *J. Astrophys. Astron.*, **29**, 249 (2008).

3. *Flows in Flare Productive and Dormant Active Regions*, In. Hasan, S.; Rutten, R. J. (Eds.) Magnetic Coupling between the Interior and Atmosphere of the Sun (ASSP, Springer-Verlag), **R. A. Maurya** and A. Ambastha, 516 (2010)

4. *Magnetic and Velocity Field Changes Related to Solar Flares of October 28 and 29, 2003*, In. Hasan, S.; Rutten, R. J. (Eds.) Magnetic Coupling Between the Interior and Atmosphere of the Sun (ASSP, Springer-Verlag), **R. A. Maurya** and A. Ambastha, 517 (2010)

The Astrophysical Journal, 706:L235–L239, 2009 December 1 doi:10.1088/0004-637X/706/2/L235

VARIATIONS IN *p*-MODE PARAMETERS WITH CHANGING ONSET TIME OF A LARGE FLARE

R. A. Maurya[1], A. Ambastha[1], and S. C. Tripathy[2]
[1] Udaipur Solar Observatory, Physical Research Laboratory, Udaipur-313001, India
[2] National Solar Observatory, 950 N. Cherry Avenue, Tucson, AZ 85719, USA; ramajor@prl.res.in, ambastha@prl.res.in, stripathy@noao.edu
Received 2009 September 10; accepted 2009 October 27; published 2009 November 12

ABSTRACT

It is expected that energetic solar flares releasing a large amount of energy at the photosphere may be able to excite the acoustic (*p*-) modes of oscillations. We have determined the characteristic properties of mode parameters by applying the ring diagram technique to three-dimensional power spectra obtained for solar active region NOAA 10486 during the long-duration energetic X17.2/4B flare of 2003 October 28. Strong evidence of substantial increase in mode amplitude and systematic variations in sub-surface flows, i.e., meridional and zonal components of velocity, kinetic helicity, and vorticity, is found from comparison of the pre- to the post-flare phases.

Key words: Sun: activity – Sun: flares – Sun: helioseismology

1. INTRODUCTION

Leighton et al. (1962) discovered solar five-minute oscillations while measuring Doppler shifts in photospheric spectral lines. Ulrich (1970) and Leibacher & Stein (1971) later interpreted these oscillations to be due to acoustic (or *p*-) modes trapped in the sub-photospheric layers. Accurate determination of these modes provides a powerful diagnostic tool for probing the solar interior. It is generally believed that these modes may be either intrinsically overstable or stochastically excited by turbulent convection.

Characteristics of the surface *p*-modes and sub-surface flows are essentially described by shorter wavelength modes that are trapped near the surface. These modes can be studied using the ring diagram analysis which uses three-dimensional data cubes ($16^\circ \times 16^\circ \times 1664$, as generally used by Global Oscillation Network Group (GONG) and *SOHO*/MDI instruments). The first two dimensions correspond to the spatial size of the active region (AR) and the third is time in minutes (Hill 1988). Other techniques of local helioseismology, generally used for studying various aspects of sub-photospheric characteristics of AR interiors, are time–distance analysis (Zhao & Kosovichev 2004), and seismic holography (Braun et al. 2004).

Wolff (1972) first suggested that energetic flares may be able to excite acoustic waves by exerting mechanical impulse of the thermal expansion of the flare on the photosphere. They estimated the damping times to be longer than a day for the free modes. Subsequently, AR-related effects on *p*-mode parameters have been reported by several researchers (Libbrecht & Woodard 1990; Chaplin et al. 2000; Hindman et al. 2000; Rajaguru et al. 2001; Ambastha et al. 2003, 2004; Howe et al. 2004). Kosovichev & Zharkova (1998, 1999) and Donea et al. (1999) have also reported excitation of flare-related waves on the solar surface, however, these pertain to traveling waves as opposed to standing waves which constitute the normal modes of solar oscillations.

The spatial extent of flares is usually much smaller than the spatial sizes of $16^\circ \times 16^\circ$ used in GONG and *SOHO*/MDI data cubes for ring diagram analysis. Also, any mode amplification induced by transient flare events has to essentially compete with the absorption effects associated with the intense magnetic fields of sunspots. Therefore, it is expected to be rather difficult to conclusively resolve flare-related effects by averaging techniques. Here one can estimate the damping timescale of *p*-modes from the observed mode width, generally in the range of 15–100 μHz for high-degree modes. This gives a lifetime in the range of 0.5–3 hr assuming that the width is mainly due to the finite life of the modes. Acoustic waves travel outward from the site of flare ribbons with the speed of sound varying in the range from 10 km s^{-1} to 50 km s^{-1} for the depths in which the high-degree modes are trapped. Thus, over the damping time of the order of 1 hr, these waves would travel a distance from 36 Mm to 180 Mm, i.e., comparable to the spatial extent of the AR. A large fraction of energy dissipation occurs within this region if the flare is temporally located well within the data cube. Therefore, it is expected that flare-related effects would last over several hours and should be detectable in the temporal averages carried out over a day as in the ring analysis. However, if the flare occurred around the end time of the data cube, the flare effects would not be detectable as they would be contained mostly in the subsequent data cube.

The relation between photospheric motions and flare activity has been studied previously. For example, correlation tracking studies have discovered a few cases of small-scale vorticity at the surface preceding a flaring event with timescales around 1 hr (Yang et al. 2004). Some cases of sunspot rotation in flaring ARs have also been found (Brown et al. 2003). The relationship of flare activity to some statistical properties of ARs has been studied by Lu (1995) and Abramenko & Longcope (2005) among others. It is believed that twisted flows in the sub-surface layers cause footpoint motions of sunspots observed at the photospheric layer leading to unstable magnetic topologies in the overlying regions.

Although the average properties of *p*-mode parameters and sub-surface flows have been studied with magnetic/flare activities by many researchers (Ambastha et al. 2004; Howe et al. 2004; Komm et al. 2005b, 2005a; Mason et al. 2006), the change of *p*-mode parameters and sub-surface flows during flares is not well understood. Some efforts have been made to examine the difference between flare productive and quiet regions to infer any activity-related effects (Mason et al. 2006). Ambastha et al. (2003, 2004) have found that power in *p*-modes appears to be larger during the period of high flare activity as compared to that in non-flaring regions of similar magnetic field strength. However, the pre-, peak-, and post-flare signatures of flares on *p*-mode parameters and sub-surface flows still require careful analysis. We have studied the long duration, energetic X17.2/

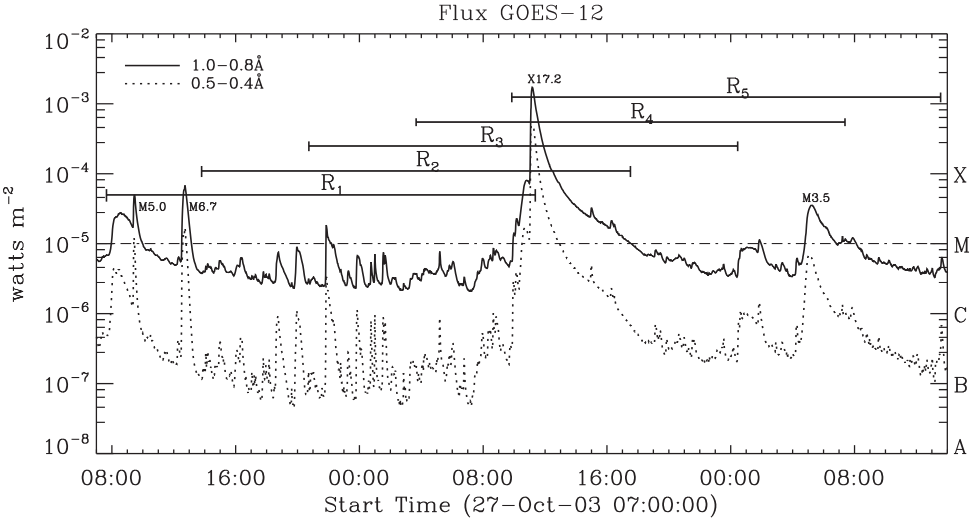

Figure 1. *GOES*-12 integrated X-ray flux for 1.0–0.8 Å (solid line) and 0.5–0.4 Å (dotted line). The horizontal lines with labels R_i, $i = 1, \ldots, 5$, represent different time periods taken for constructing the five data sets.

4B flare of 2003 October 28 in NOAA 10486. We found strong evidence of flare-related changes in p-mode parameters and sub-surface flows by placing the flare at different temporal positions in appropriately constructed data cubes.

2. THE WHITE LIGHT FLARE OF NOAA 10486

In order to determine any flare-related effects on p-mode parameters, we have considered the white light (WL) super-flare of 2003 October 28 that occurred in NOAA 10486. This flare, classified as X17.2/4B, was one of the most energetic events ever observed in the Sun. During the period of the data sets used in our study, some other C and M class flares also occurred in NOAA 10486, but the X17.2/4B super-flare was the dominant event during the 24 hr period. According to *Geostationary Operations Environmental Satellite* (*GOES*) X-ray observations, this flare started at 09:51 UT, reached the maximum phase at 11:10 UT, and decayed at 11:24 UT, i.e., lasted over more than 90 minutes (Figure 1). However, it is evident that the integrated X-ray flux remained at a very high level well beyond 11:24 UT. Even if a background corresponding to the M1 level (10^{-5} watts m^{-2}) is considered, the X-ray flux gradually reduced to this level only around 16:00 UT. In Hα also, it is reported to have lasted for more than 4 hr. Therefore, this energetic, long duration event (LDE) was a particularly well suited case for an investigation of flare-related helioseismic effects.

3. THE DATA AND ANALYSIS

We have used high resolution GONG Dopplergrams obtained at 1 minute cadence. The data cubes have 1664 minutes' duration and cover $16^\circ \times 16^\circ$ area centered at 285° Carrington longitude and $-22\overset{\circ}{.}5$ latitude covering NOAA 10486. The choice of area makes a compromise between spatial resolution, range of depths, and resolution in spatial wavenumber in the power spectra. A larger size will allow access to the deeper sub-surface layers, but only with coarser spatial resolution. On the other hand, a smaller size will not allow access to the deeper layers and also render the fitting of rings more difficult. The AR was located close to the disk center at the time of this flare, therefore, projection effects did not pose any serious difficulty in the analysis.

The three-dimensional Fourier transform of the data cube gives a trumpet-like structure in the frequency domain (k_x, k_y, ω). A slice at fixed frequency ω of this structure gives power concentrated in concentric rings (Hill 1988). These rings provide the characteristic properties of p-modes and sub-surface flows. The phase velocity of the acoustic wave is augmented by flow velocity (**U**) causing change in frequencies ($\Delta\omega = \mathbf{k}\cdot\mathbf{U}$) that perturbs the center and shape of the rings. Surface flows are derived from this perturbation using ring fitting. The p-modes of different wavelengths are trapped at different depths beneath the surface. Therefore, flows derived at the surface are weighted averages over depths. Inverting these characteristics of the modes gives flows in the interior.

As illustrated in Figure 1, we constructed five data sets of 1664 minutes duration each with different starting times, such that the flare onset was placed in the beginning (R_5), one-fourth (R_4), center (R_3), three-fourth (R_2), and end (R_1) of the data cube's time-line. The 16° patch consists of 128 pixels, giving a spatial resolution of $\Delta x = 1.5184$ Mm, i.e., the k-number resolution, $\Delta k = 3.2328 \times 10^{-2}$ Mm^{-1}, and a Nyquist value for the harmonic degree, $l = 1440$. The corresponding range in (k_x, k_y) space is from -2.069 Mm^{-1} to 2.069 Mm^{-1}. The temporal cadence and duration of data sets give a Nyquist frequency of 8333 μHz and a frequency resolution of 10 μHz, respectively.

To determine the surface mode parameters of p-modes, we have carried out ring-diagram analysis using the dense-pack technique (Haber et al. 2002) adapted for GONG data (Corbard et al. 2003; Hill et al. 2003). Images were remapped around the central position (285°, $-22\overset{\circ}{.}5$) using transverse cylindrical projection to obtain the equidistance spatial sampling interval required for Fourier transformation. To remove the effect of differential rotation, the remapped images were tracked with a differential rotation rate of the Sun (Snodgrass 1984). The tracked image cubes are apodized before being Fourier transformed. The main ring-fitted parameters (i.e., surface acoustic mode parameters) determined in our study are radial order (n), degree (l), mode amplitude (A), mode width (Γ), zonal velocity (U_x), and meridional velocity (U_y). The common mode parameters in all sets were corrected for filling factor using a method described in Komm et al. (2000). Zonal (u_x) and meridional (u_y) components of sub-surface flows were derived

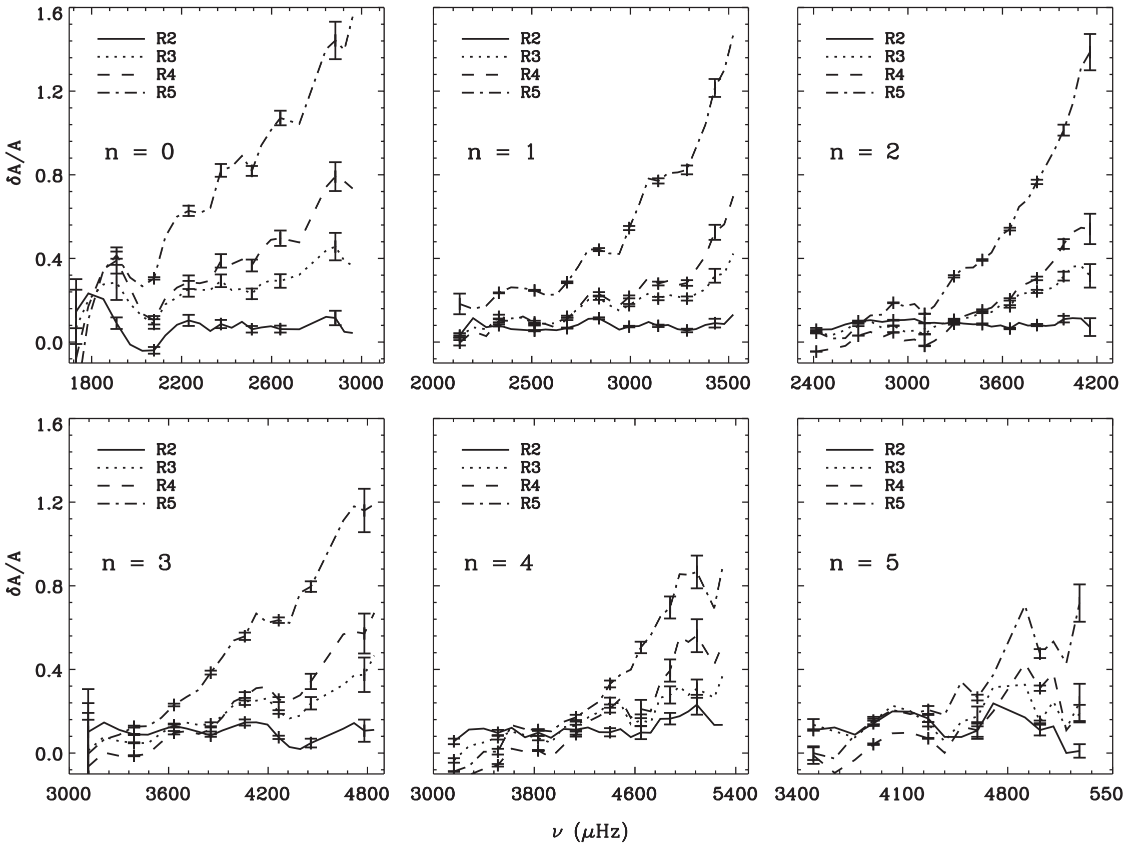

Figure 2. Relative difference in mode amplitude for the data sets R_i, $i = 2, \ldots, 5$, for radial orders, $n = 0$–5. Here, R_1 is used as the reference.

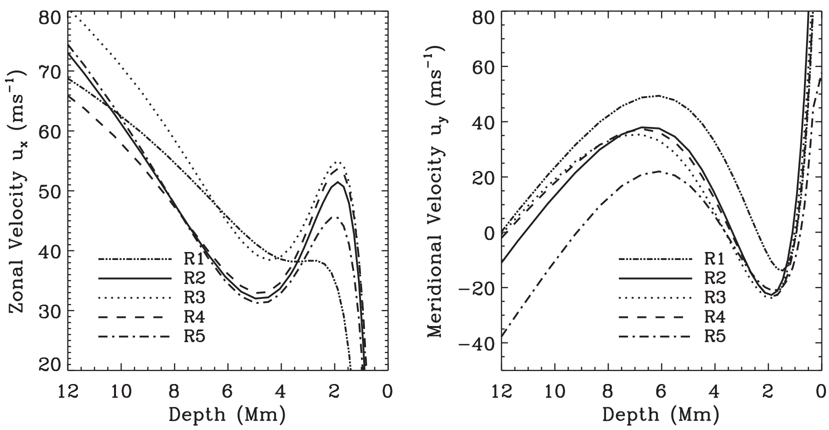

Figure 3. Zonal u_x (left panel) and meridional u_y (right panel) velocity profiles with depth from 0 to 12 Mm for the data sets R_i, $i = 1, \ldots, 5$.

by regularized least square (RLS) inversion from the surface to a depth of ∼20 Mm (Thompson et al. 1996; Haber et al. 2002).

The topology of fluid is measured by kinetic helicity. It is defined as the volume integral of the dot product of the velocity (**u**) and vorticity (ω) of the flows (Moffatt & Tsinober 1992):

$$H_{\mathrm{K}} = \int_V \mathbf{u} \cdot \omega \, dV,$$

where, $\omega = \nabla \times \mathbf{u}$ is the vorticity vector. It is a measure of circulations per unit area, i.e., twist of the flow, while its dot product with velocity gives the variation of the twist with flows. We estimated the vertical component of velocity u_z from the divergence of horizontal components assuming mass conservation (Komm et al. 2005a). Now, having all three components of flows with depths, we can derive kinetic helicity. As we do not have the flows at each point of the AR from ring analysis, we can derive only the average helicity over the entire area, termed as helicity density ($h_K = \mathbf{u} \cdot \nabla \times \mathbf{u}$). The numerical derivatives of flows are derived using Lagrange three-point interpolation.

4. RESULTS AND DISCUSSIONS

Mode parameters are obtained for the five data sets as shown in Figure 1 for comparison of the flare-related effects. Surface acoustic mode parameters and the corresponding inverted parameters for these data sets are shown in Figures 2–4.

Figure 2 shows the relative differences in mode amplitude obtained for R_2 to R_5 where R_1 is used as the reference. This

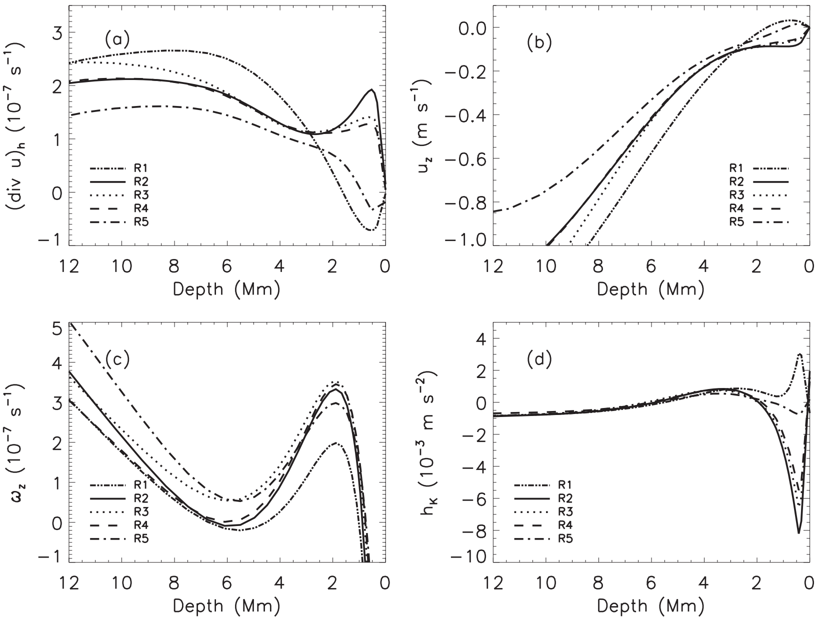

Figure 4. Inverted profiles of (a) divergence of horizontal components of velocity, (b) vertical component of velocity u_z, (c) vorticity, and (d) helicity density, with depth from 0 to 12 Mm for the data sets $R_i, i = 1, \ldots, 5$.

quantity is found to be the largest for R_5 as compared to that for other sets. The difference between the amplitudes increased with frequency $\nu > 2000$ μHz, and reduced with increasing radial order from $n = 0$ to 5. The large difference of mode amplitude at lower radial orders may be attributed to the flare effect as these modes are confined near the surface and hence, more likely to be affected by the surface activity.

The flare was placed at the beginning in R_5; thus the overall helioseismic contribution of this energetic LDE, extending from the pre- to post-flare phase, is expected to remain entirely within this data cube. Correspondingly, the mode amplitude was found to be the largest in R_5 as expected. However, it was smallest in R_1 where the flare was placed at the end of the data cube, therefore post-flare effects were not covered by this data set. From the systematic trend of variations in the mode amplitude from R_5 to R_1, it is evident that the energetic flare indeed gave rise to a significant amplification of mode amplitude.

Mode width is also found to be large at all frequencies and radial orders for R_5. The changes are found to be larger at lower frequencies implying that higher-n modes have shorter life times. Duvall et al. (1988) and Burtseva et al. (2009) have also found that mode width increased with frequency as well as with degree of the modes. However, care is needed in this interpretation as significant contribution to mode width may arise due to the available limited resolutions in wavenumber and frequency.

Using the ring diagram fits, we have calculated the horizontal velocities in order to check if there is any variation in surface velocities due to flares. We found large variations in surface zonal and meridional velocities at all frequencies for the radial orders $n = 0$ to 5 from R_1 to R_5. Also, the deviation for both the components of velocity is larger for R_5 as compared to other data sets indicating the variation in flows from the pre- to post-flare phases.

The fitted velocities for each mode can be inverted to calculate the zonal (u_x) and meridional (u_y) components of velocity as a function of depth. These were derived by RLS inversion from the surface to a depth of 20 Mm (Thompson et al. 1996; Haber et al. 2002). Both u_x and u_y exhibited significant systematic changes with the flare. The profiles of zonal velocities u_x with depth are shown for R_1 to R_5 in Figure 3 (left panel). A large decrease in zonal velocity around the depth ≈ 4 Mm is common in all cases. However, the depth where the minimum of u_x occurred varied from the shallowest for R_1 to the deepest for R_5. Figure 3 (right panel) shows the corresponding changes in meridional velocities u_y for R_1 to R_5. It is found that u_y decreased rapidly from the surface to the depth of $\sim$1 Mm for all the data sets. Thereafter, it increased and attained a peak at $\sim$6 Mm. It is inferred that the gradient in u_y is largest for R_1 (i.e., before the flare) and it decreased systematically from R_2 to R_5 as the post-flare effects increased. This confirms the earlier reports about meridional velocity gradient by Ambastha et al. (2004).

Figure 4 shows the profiles with depth of (a) divergence of horizontal components of velocity, (b) vertical component of velocity u_z, (c) vertical vorticity, and (d) helicity density. Interestingly, it is observed that flare-related variations in helicity density h_k are confined within a shallow region from the surface to a depth of around 3 Mm. For depths greater than 3 Mm, h_k derived for all the five cases approached toward the same value.

Changes in the topology of sub-surface flows during pre- to post-flare phases are illustrated in Figures 4(a)–(d). In R_1, the divergence of horizontal component (u_h) near a depth of ≈ 1 Mm changed from a small negative to a large positive value for R_2, and decreased from R_3 to R_5 (Figure 4(a)). This suggests that the perturbation in the flows at this depth gradually returned back to the initial or pre-flare state after the flare decayed. On the other hand, the large positive divergence observed at depths below 3 Mm decreased in magnitude from R_1 to R_5.

The vertical component of flows (u_z) changed from upward direction in R_1 to downward direction in R_2 at a depth of ≈ 1 Mm, and then back to the upward direction in R_5 through R_3–R_4 (Figure 4(b)). The u_z profiles converged to the same negative value (≈ -0.1 ms^{-1}) at a depth of $\sim$3 Mm, and then diverged systematically from R_1 to R_5 with increasing depth. The vertical component of the vorticity vector (ω_z) is shown in Figure 4(c) for R_1 to R_5. The peak in ω_z near 2 Mm and the trough near 6 Mm manifest the bipolar structure of the AR. Kinetic helicity (h_K)

changed from a small positive value for R_1 to a large negative value for R_2, increasing toward the level of R_1 for R_3–R_5 (Figure 4(d)). However, it remained nearly constant for all the data sets at depths below ∼3 Mm. These systematic changes in sub-surface parameters (u_h, u_z, ω_z, and h_K) from R_1 to R_5 provide unambiguous evidence of the relationship of the large flare with sub-surface dynamics of the AR.

5. CONCLUSIONS

This study of an extremely energetic and long-duration X17.2/4B flare in NOAA 10486 gives a clear indication of flare-related variations in the p-mode parameters and sub-photospheric flows in NOAA 10486. Changing the temporal position of the flare within the Doppler data cubes obtained for the AR amounts to the changing level of the pre- and post-effects in the data set. The ring diagram analysis of different data sets thus constructed provides the following important results:

1. The amplitude of p-modes increased up to 150% in the case of the flare placed in the beginning of the data set as compared to the case when the flare was placed near the end or outside the data cube. A similar result is obtained for p-mode energy also as expected due to its relation with the amplitude, manifesting the rate of energy supplied to the p-modes by the flare.
2. The amplitude and the energy of the modes decreased with radial order indicating that the effect of the flare decreased with increasing depth. Furthermore, we found that the amplitude and the energy of modes increased with frequency. This suggests that modes with high natural frequencies are amplified more by the flare as compared to the low frequency modes.
3. The gradient in meridional velocity observed at depths 2–6 Mm decreased with the flare which manifests the relationship of the flare activity with the sub-surface flows.
4. The vertical component of the flow changed to the downward direction during the flare and then returned back to the pre-flare state. This is an evidence of downward moving material during the flare.
5. Divergence of the horizontal component of flow near the surface changed from negative to positive and then back to the pre-flare state after the flare.
6. The sub-surface flow possessed a bipolar structure with one pole located at the depth of around 2 Mm and the other at 6 Mm. Near the surface, the flow was twisted during the pre-flare phase, which relaxed after the flare.
7. The kinetic helicity of sub-surface flow around the depth of 1 Mm changed from positive to negative during the pre- to the peak phases, and returned back to the pre-flare level after the post-flare phase.

In summary, this study provides strong evidence about the role of a large flare in modifying various acoustic mode parameters. Depending upon the temporal location of the large flare in NOAA 10486, systematic variations in mode parameters have been found for different data sets with varying levels of pre- and post-flare effects. These results also suggest that flare-related changes in the acoustic mode parameters are detectable by ring diagram analysis provided that the pre- and post-flare phases of the flare (or flares) are well covered by the data cube. Finally, we conclude that the sub-surface flow topology can be used as a proxy for flare forecasting.

This work utilizes data obtained by the GONG program operated by AURA, Inc. and managed by the National Solar Observatory under a cooperative agreement with the National Science Foundation, USA. The integrated X-ray flux data were obtained from *GOES* which is operated by National Oceanic and Atmospheric Administration, USA. The authors thank H.M. Antia for many useful discussions during the course of this work and providing mode inertia table for computing mode energy. One of the authors (S.C.T.) acknowledges support from NASA Grant NNG 08EI54I.

REFERENCES

Abramenko, V. I., & Longcope, D. W. 2005, ApJ, 619, 1160
Ambastha, A., Basu, S., & Antia, H. M. 2003, Sol. Phys., 218, 151
Ambastha, A., Basu, S., Antia, H. M., & Bogart, R. S. 2004, in Helio- and Asteroseismology: Towards a Golden Future, ed. D. Danesy (ESA SP-559; Noordwijk: ESA), 293
Braun, D. C., Birch, A. C., & Lindsey, C. 2004, in Helio- and Asteroseismology: Towards a Golden Future, ed. D. Danesy (ESA SP-559; Noordwijk: ESA), 337
Brown, D. S., Nightingale, R. W., Alexander, D., Schrijver, C. J., Metcalf, T. R., Shine, R. A., Title, A. M., & Wolfson, C. J. 2003, Sol. Phys., 216, 79
Burtseva, O., Hill, F., Kholikov, S., & Chou, D.-Y. 2009, Sol. Phys., 258, 1
Chaplin, W. J., Elsworth, Y., Isaak, G. R., Miller, B. A., & New, R. 2000, MNRAS, 313, 32
Corbard, T., et al. 2003, in Local and Global Helioseismology: The Present and Future, ed. H. Sawaya-Lacoste (ESA SP-517; Noordwijk: ESA), 255
Donea, A.-C., Braun, D. C., & Lindsey, C. 1999, ApJ, 513, L143
Duvall, Jr., T. L., Harvey, J. W., & Pomerantz, M. A. 1988, in IAU Symp. 123, Advances in Helio- and Asteroseismology, ed. J. Christensen-Dalsgaard & S. Frandsen (Dordrecht: Kluwer), 37
Haber, D. A., Hindman, B. W., Toomre, J., Bogart, R. S., Larsen, R. M., & Hill, F. 2002, ApJ, 570, 855
Hill, F. 1988, ApJ, 333, 996
Hill, F., et al. 2003, in Local and Global Helioseismology: The Present and Future, ed. H. Sawaya-Lacoste (ESA SP-517; Noordwijk: ESA), 295
Hindman, B., Haber, D., Toomre, J., & Bogart, R. 2000, Sol. Phys., 192, 363
Howe, R., Komm, R. W., Hill, F., Haber, D. A., & Hindman, B. W. 2004, ApJ, 608, 562
Komm, R., Howe, R., Hill, F., González Hernández, I., & Toner, C. 2005a, ApJ, 630, 1184
Komm, R., Howe, R., Hill, F., González-Hernández, I., Toner, C., & Corbard, T. 2005b, ApJ, 631, 636
Komm, R. W., Howe, R., & Hill, F. 2000, ApJ, 531, 1094
Kosovichev, A. G., & Zharkova, V. V. 1998, Nature, 393, 317
Kosovichev, A. G., & Zharkova, V. V. 1999, Sol. Phys., 190, 459
Leibacher, J. W., & Stein, R. F. 1971, Astrophys. Lett., 7, 191
Leighton, R. B., Noyes, R. W., & Simon, G. W. 1962, ApJ, 135, 474
Libbrecht, K. G., & Woodard, M. F. 1990, Nature, 345, 779
Lu, E. T. 1995, ApJ, 446, L109
Mason, D., Komm, R., Hill, F., Howe, R., Haber, D., & Hindman, B. W. 2006, ApJ, 645, 1543
Moffatt, H. K., & Tsinober, A. 1992, Annu. Rev. Fluid Mech., 24, 281
Rajaguru, S. P., Basu, S., & Antia, H. M. 2001, ApJ, 563, 410
Snodgrass, H. B. 1984, Sol. Phys., 94, 13
Thompson, M. J., et al. 1996, Science, 272, 1300
Ulrich, R. K. 1970, ApJ, 162, 993
Wolff, C. L. 1972, ApJ, 176, 833
Yang, G., Xu, Y., Cao, W., Wang, H., Denker, C., & Rimmele, T. R. 2004, ApJ, 617, L151
Zhao, J., & Kosovichev, A. G. 2004, ApJ, 603, 776

The Astrophysical Journal Letters, 714:L196–L201, 2010 May 10 doi:10.1088/2041-8205/714/2/L196

SUB-SURFACE MERIDIONAL FLOW, VORTICITY, AND THE LIFETIME OF SOLAR ACTIVE REGIONS

R. A. Maurya and A. Ambastha
Udaipur Solar Observatory, Physical Research Laboratory, Udaipur-313 001, India; ramajor@prl.res.in, ambastha@prl.res.in
Received 2009 November 23; accepted 2010 March 29; published 2010 April 12

ABSTRACT

Solar sub-surface fluid topology provides an indirect approach to examine the internal characteristics of active regions (ARs). Earlier studies have revealed the prevalence of strong flows in the interior of ARs having complex magnetic fields. Using the Doppler data obtained by the Global Oscillation Network Group project for a sample of 74 ARs, we have discovered the presence of steep gradients in meridional velocity at depths ranging from 1.5 to 5 Mm in flare productive ARs. The sample of these ARs is taken from the Carrington rotations 1980–2052 covering the period 2001 August–2007 January. The gradients showed an interesting hemispheric trend of negative (positive) signs in the northern (southern) hemisphere, i.e., directed toward the equator. We have discovered three sheared layers in the depth range of 0–10 Mm, providing evidence of complex flow structures in several ARs. An important inference derived from our analysis is that the location of the deepest zero vertical vorticity is correlated with the remaining lifetime of ARs. This new finding may be employed as a tool for predicting the life expectancy of an AR.

Key words: Sun: activity – Sun: flares – Sun: helioseismology

1. INTRODUCTION

Solar surface flows have been studied over the last three decades using mostly the surface observations such as the photospheric magnetic tracers and Doppler measurements. These tracers revealed that the magnetized regions rotate faster than the surrounding medium of field-free plasma (Golub & Vaiana 1978; Komm et al. 1993; Howard 1996). Doppler measurements have shown poleward meridional flows at the solar surface (Duvall 1979; Labonte & Howard 1982; Ulrich et al. 1988). More recently, it has become possible to study sub-surface structures and flows subsequent to the advent of helioseismology (Deubner & Gough 1984; Gough & Toomre 1991), which probes the solar interior using acoustic modes of oscillations (Ulrich 1970; Leibacher & Stein 1971). Helioseismic studies have revealed that sunspots are rather shallow, near-surface phenomena (Kosovichev et al. 2000; Basu et al. 2004; Couvidat et al. 2006), and their rotation rate with depth depends on the stage of evolution and age. Švanda et al. (2009a) have reported that a majority of active regions (ARs) displays sudden decrease in the rotation speed, compatible with dynamic disconnection of sunspots from their parental magnetic roots. Local helioseismology has further revealed the sunspots to be the locations of large flows near the surface (Haber et al. 2002; Braun et al. 2004; Zhao & Kosovichev 2004).

Earlier studies have found that magnetic helicity of ARs follows a hemispheric rule, i.e., positive (negative) in southern (northern) hemisphere (Pevtsov et al. 2001). Such a hemispheric trend is also reported for flows in ARs (Komm et al. 2005, 2007; Zaatri et al. 2006). Zonal flows exhibit larger amplitudes in southern hemisphere especially at higher latitudes, coinciding with larger magnetic activity in that hemisphere. This may be attributed to the inclination of the solar rotation axis (Beck & Giles 2005). Also, ARs advect poleward at nearly the same rate as the quiet regions (QRs; Hindman et al. 2009) and show convergent horizontal flows combined with cyclonic vorticity, counterclockwise in the northern hemisphere (Komm et al. 2004; Zhao & Kosovichev 2004).

Activity-related variations are also reported in solar surface flows (Vorontsov et al. 2002; Basu & Antia 2003; Ambastha et al. 2004; Howe et al. 2005; Maurya et al. 2009). It is believed that sheared flows in sub-surface layers cause sunspot motions that may lead to unstable magnetic topologies, causing reconnection of magnetic field lines required for flares. Basu & Antia (2003) have found that the maximum meridional velocity of sub-surface flows is smaller when the Sun is more active. The maximum unsigned zonal and meridional vorticities of ARs are correlated with the total X-ray flare intensity (Mason et al. 2006). Furthermore, steep meridional velocity gradients are found in flaring ARs at the depth range of 4–5 Mm (Ambastha et al. 2004; Maurya et al. 2009), which decreased after flares.

Although internal flows in ARs and QRs have been studied (Mason et al. 2006; Komm et al. 2009; Maurya & Ambastha 2010), an understanding of their distinctive characteristics in flare productive ARs as compared to that in dormant ARs requires further investigation. In this Letter, we report on the properties of internal flows in ARs of varying levels of flare productivity and magnetic complexity observed during the Solar Cycle 23, including large ARs, such as NOAA 10030, 10484, 10486, 10070, etc., termed as super-active regions (SARs). These SARs are found to possess distinctly different characteristics of flows in their interiors as compared to the less productive or dormant ARs. We have addressed important issues on the relationship of flow characteristics with the lifetime of ARs, magnetic and flaring activities, and hemispheric trends.

2. THE DATA AND ANALYSIS

For selecting our sample of the ARs, we have used archived information on ARs and solar activity provided by the Web site of *Solar Monitor*.[1] We first identified the ARs producing flares of X-ray class > M1.0 using *GOES* database[2] during Carrington rotations 1980–2052 of Solar Cycle 23. Then, we short-listed the ARs within the heliocentric location $\pm 40^\circ$ to avoid projection effects and selected 74 ARs, both flaring and relatively dormant, that were well covered by the Global Oscillation Network Group (GONG) network. For each flaring AR, we chose a single data set corresponding to the day of maximum flaring activity. (A

[1] http://www.solarmonitor.org
[2] http://www.lmsal.com/SXT/plot_goes.html

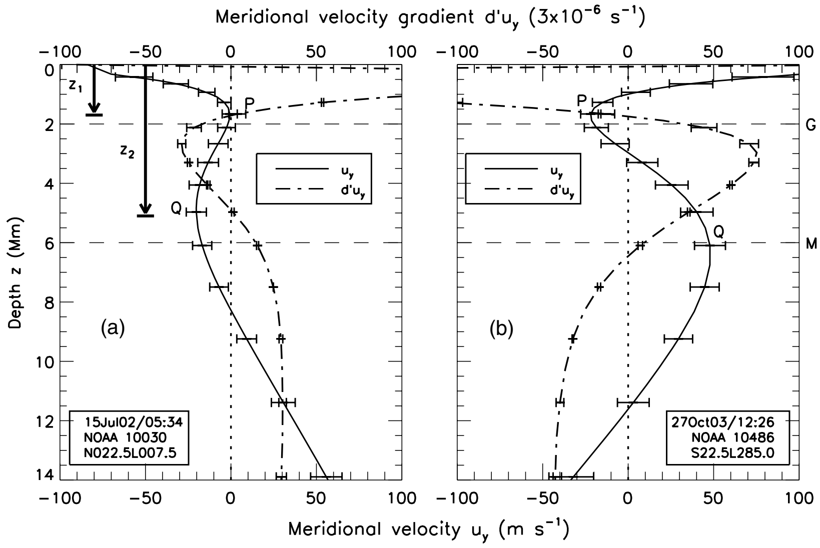

Figure 1. Meridional velocity profiles (solid curves) in the depth range 0–14 Mm for two ARs: (a) NOAA 10030 (northern hemisphere) and (b) NOAA 10486 (southern hemisphere). The dash-dotted curves correspond to the meridional velocity gradients. Error bars show the corresponding uncertainties at 1σ level. Horizontal dashed lines at the depths of 2 and 6 Mm, marked G and M, correspond to the convective scale sizes of granules and mesogranules, respectively.

full list of the selected ARs is not provided here because of the space limitation.)

We examined the sub-surface flows in the interior of the ARs using the ring data products provided by GONG (Hill et al. 2003). It utilizes $16^\circ \times 16^\circ \times 1664$ minutes data cubes, where the first two quantities correspond to the spatial dimensions in degrees and the third is the time duration in minutes. The three-dimensional Fourier transform of the data cube gives the power spectrum which exhibits a trumpet-like structure in the $[k_x, k_y, \omega]$ space. Slices of the trumpet at given frequencies ω render concentric rings in the $[k_x, k_y]$ plane corresponding to different p modes (Hill 1988). A wave propagating through the medium with horizontal flow is advected to increased (decreased) frequency depending on its propagation along (opposite) the flow. The frequency shift $\Delta\omega$ for acoustic waves, $\Delta\omega = \mathbf{U}\cdot\mathbf{K}$, gives the distortion in the shape of the rings. Using a proper fitting technique, this distortion can be estimated and the corresponding flow velocity is determined. As the modes of different wavelengths are trapped at different depths, the flow patterns derived at the surface are the weighted average over depths. This concept is used for deriving the flow beneath the surface using regularized least-square (RLS) inversion (Gough 1985) adopted for GONG data (Corbard et al. 2003).

We can derive vertical vorticity, ω_z, to describe the circulation in ARs, as follows:

$$\omega_z = (\nabla \times u)_z = \frac{\partial u_y}{\partial x} - \frac{\partial u_x}{\partial y}.$$

Here, u_x and u_y are the zonal and meridional components of flow, respectively, and ω_z is the vertical vorticity, which is a physical measure of vertical twist in the flow. In order to ascertain its significance as flow characteristic, we carried out an analysis of ARs with corresponding QRs located at the same latitude and time, but different longitudes. We found that the relative values of u_y and ω_z in ARs were indeed significantly larger than in the QRs. It has been shown observationally (Švanda et al. 2008, 2009a) as well as theoretically (Jouve & Brun 2009) that Maxwell stresses play a significant role in modifying horizontal flows. Švanda et al. (2009b) have also shown that flow parameters obtained for ARs are mainly influenced by their magnetic fields as compared to QRs where the flows correspond to supergranular structures. Therefore, it is clear that the flows below ARs are influenced "magnetically" that are otherwise driven purely by hydrodynamical processes, i.e., Reynolds stress and pressure gradient.

We examined the relationship of internal flow with magnetic activity of ARs using the magnetic index, MI, obtained from *Solar and Heliospheric Observatory*/Michelson Doppler Imager (MDI) 96 minutes averaged magnetograms. For this, we extracted the area of interest from the full disk magnetograms corresponding to the $16^\circ \times 16^\circ$ spatial patch used in the ring analysis. Then MI corresponding to the AR is calculated from the averaged absolute values of magnetic fields over the patch. We also calculated the flare index, FI, for each AR by multiplying the X-ray flux, obtained from *GOES*, with the flare duration and then summing the contributions from all the flares that occurred during the 1664 minutes' period of the data cube.

We estimated the remaining lifetimes (τ) of ARs from the information provided by *solar monitor* for the Earthside and MDI farside imaging as follows. We followed the signature of an AR using magnetograms from the reference, central time t_r of the data cube until the time t_e when the AR disappeared. In case when the AR rotated past the west limb of the Sun to the farside, we followed up its signature using the acoustic hologram images until its disappearance at time t_e. The remaining lifetime (τ) of an AR is then estimated from the difference ($t_e - t_r$).

3. RESULTS AND DISCUSSIONS

The main results of our analysis for the sample of ARs are presented in Figures 1–4. Meridional velocities, u_y, obtained for two of the ARs, NOAA 10030 (northern hemisphere) and 10486 (southern hemisphere), are shown by the solid curves in Figure 1. The velocities are obtained from the surface to a depth of 14 Mm. The data sets used for these ARs correspond to 2002 July 15 and 2003 October 27, respectively. The dash-dotted curves show the greatest rate of change, or the gradient of u_y, along the vertical direction z, i.e., $du_y/dz \equiv d'u_y$. The magnitudes of u_y and $d'u_y$ are evidently more significant as compared to the errors in the depth range from 1.5 to 10 Mm.

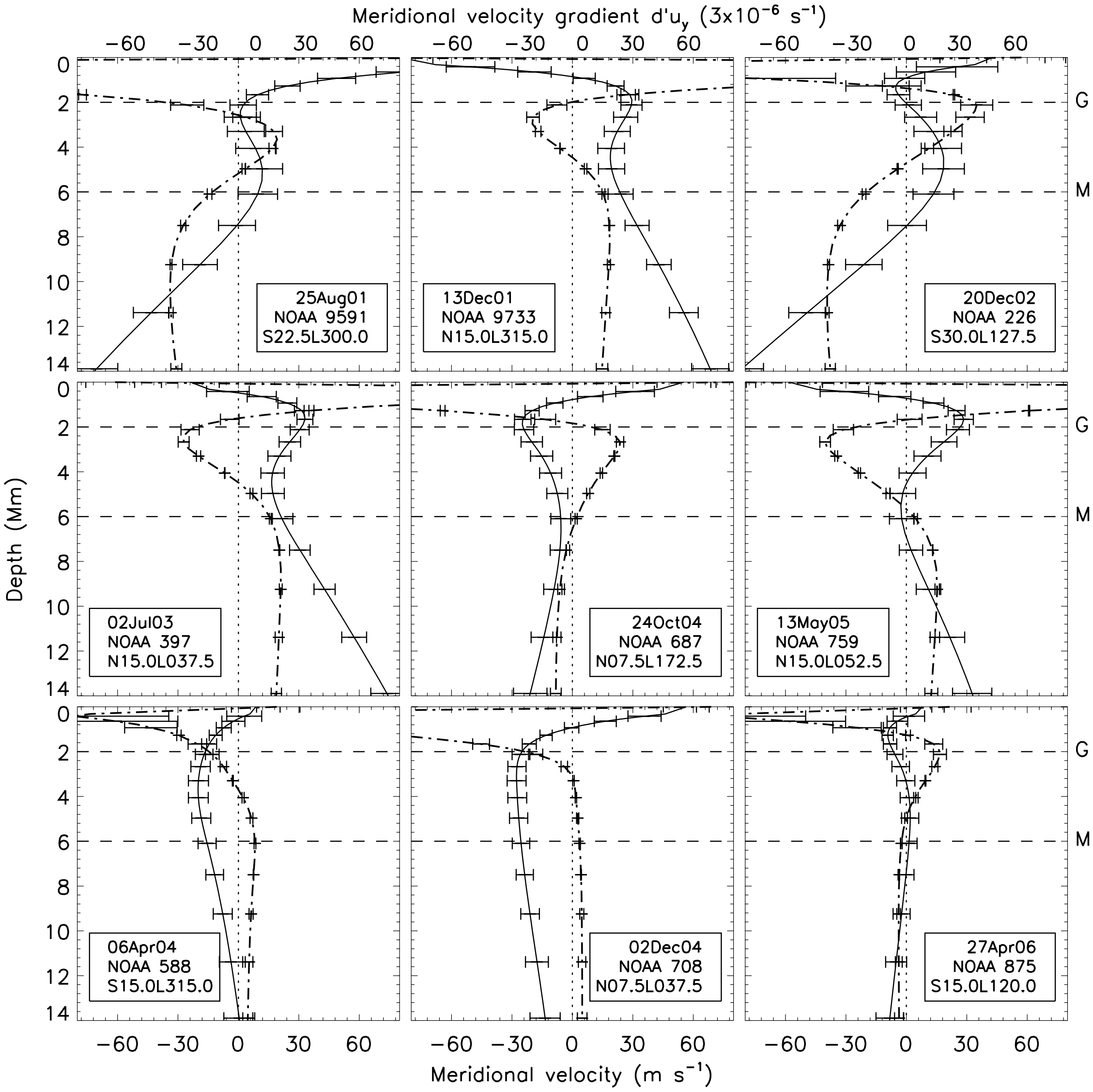

Figure 2. Meridional velocity profiles (solid curves) in the depth range 0–14 Mm for nine ARs of our sample. The dash-dotted curves correspond to the meridional velocity gradient. Error bars show the corresponding uncertainties at 1σ level. Horizontal dashed lines at the depths of 2 and 6 Mm, marked G and M, correspond to the convective scale sizes of granules and mesogranules, respectively.

The profiles of u_y and $d'u_y$ for the two ARs, located in opposite hemispheres, exhibit opposite trends with depth. The two extrema near P and Q of u_y, however, occurred at around the same depths for both the ARs. Evidently, $d'u_y$ changed sign with increasing depth from the surface to a depth of 1.5 Mm where $d'u_y$ is positive (negative) in the northern (southern) hemisphere. Thereafter, it changed sign again in the depth ranges of 1.5–5 Mm and 5–10 Mm. From these sign reversals of u_y and $d'u_y$ profiles, we can infer that there exist three sheared layers in the interior of these two ARs. This appears to be a general feature of flare productive and complex ARs of our sample, some more of which are shown in Figure 2.

We may infer that the depths of 2 and 6 Mm near which the extrema of u_y are located correspond to the convective scale sizes of granulation and mesogranulation. For reference, these depth levels are marked in Figures 1 and 2 as "G" and "M," respectively. These depths were also referred as the locations of ionization zones of H^+ and He^+ ions by Simon & Leighton (1964) and November et al. (1981). However, recently, Cattaneo et al. (2001) and Rast (2003) have shown this argument to be incorrect. Rieutord et al. (2000) suggested that mesogranulations result from the nonlinear interaction of granules (also Cattaneo et al. 2001; Rast 2003). Rast (2003) suggested that granular scales are determined by a close association between the upflows, which sustain radiative loss, and the downflow plumes, which initiate the upflow motions. A more detailed description of surface convection and scales can be found in the recent review article by Nordlund et al. (2009).

Convective cells are parcels of fluid moving from the deeper layers to the upper layers and back to the bottom. The vertically rising material must change direction along a horizontal flow at two positions, i.e., the bottom and the top of convective cells. In a depth distribution of the velocity flow, these turning points may be represented by peaks in the velocity profile. The extrema seen in the vertical profiles of u_y, such as the one at "G" in Figure 1, may be due to instabilities that drive the convective cells. The reason for convective driving near these depths is not clear because it depends on many

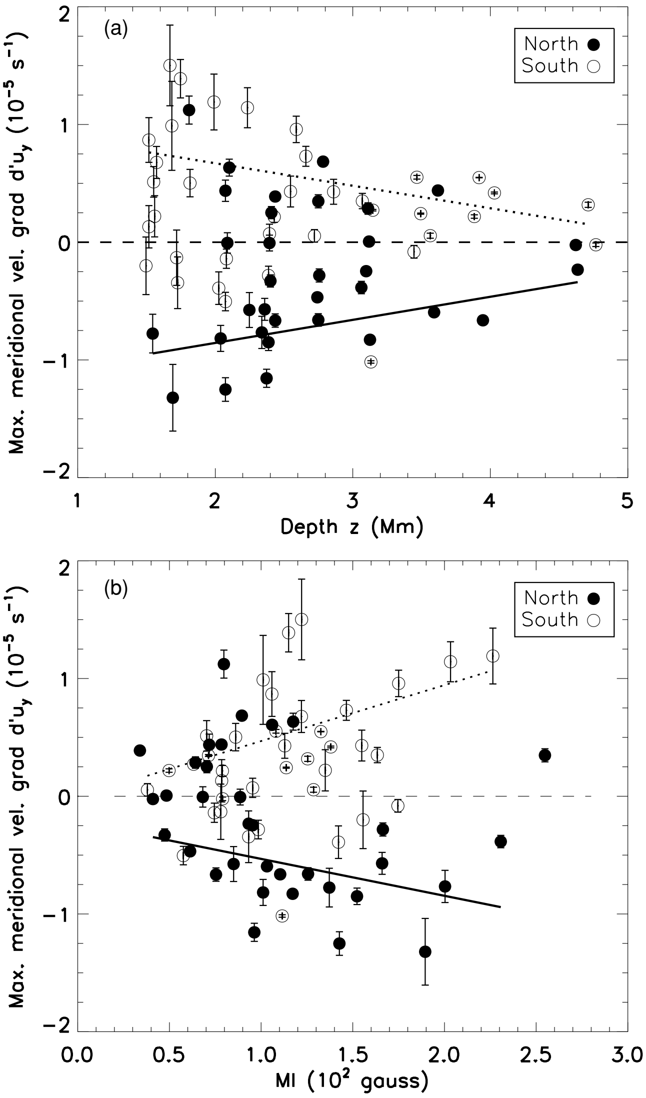

Figure 3. Distributions of the maximum meridional velocity gradient $d'u_y$ for 74 ARs with (a) depth z and (b) magnetic index MI of the AR. Filled (open) circle represents the northern (southern) hemispherical ARs. The solid (dotted) fitted lines drawn through these points indicate the general hemispheric trend of the ARs.

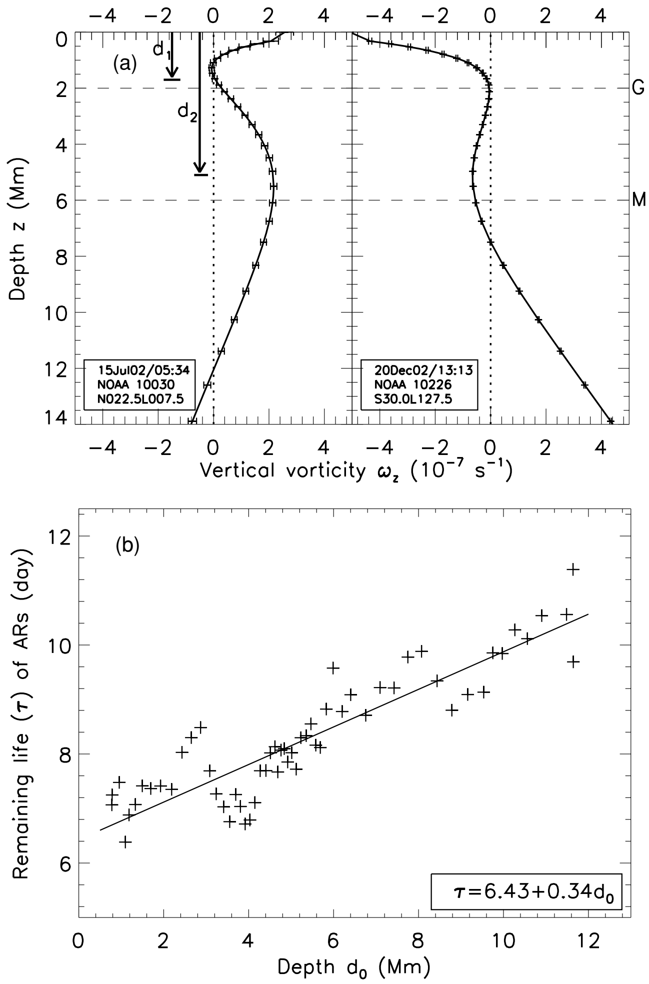

Figure 4. (a) Vertical vorticity profiles, with error bars, corresponding to two ARs: NOAA 10030 (northern hemisphere) and NOAA 10226 (southern hemisphere). Horizontal dashed lines at the depths of 2 and 6 Mm, marked G and M, correspond to the convective scale sizes of granules and mesogranules, respectively. (b) Variation of the remaining lifetime of the sample of 74 ARs with the depth of deepest zero vertical vorticity.

factors, e.g., physical properties of flux rope and its ambient medium.

From our sample we found that 44 ARs displayed two extrema in their u_y profiles while the rest, i.e., 30 ARs possessed a single extremum in the depth range 0–10 Mm. A statistical analysis of these ARs showed that more complex and flare productive ARs possessed two extrema, located at depths of 1.92 ± 0.15 and 4.69 ± 0.30 Mm, respectively. On the other hand, relatively dormant ARs possessed a single extremum located at a shallower depth of 1.66 ± 0.97 Mm, i.e., with large depth uncertainty. There are some further interesting features associated with the ARs having two extrema as compared to the ARs having only one extremum: (1) larger mean magnetic field, (2) nearly twice the mean *GOES* flux, and (3) nearly twice the mean lifetimes.

The maximum $d'u_y$ of ARs in the two hemispheres exhibited a general trend, as evident from their distribution with depths (Figure 3(a)). Most ARs lying in the northern (southern) hemisphere possessed their maximum negative (positive) gradients in the depth range 1.5–6 Mm. There are 24 (70%) out of the 34 ARs located in the northern hemisphere having negative maximum gradients, while 29 (74%) out of the 39 ARs located in the southern hemisphere having positive maximum gradients. We also noticed that some of those ARs which did not follow this hemispheric trend were new emerging ARs.

It is clear from Figure 3(a) that the magnitude of maximum $d'u_y$ decreased with depth. The fits for ARs in northern (southern) hemisphere are drawn in solid (dotted) line. These lines are described by $d'u_y = -1.15 + 0.21z$ for the northern ARs and $d'u_y = 1.05 - 0.19z$ for the southern ARs, where z represents the depth of the maximum $d'u_y$. We do not clearly understand the reason as to why the maximum $d'u_y$ should have such a linear relationship with depth, as only 25% (21%) of the total variance in $d'u_y$ in the northern (southern) hemisphere is explained by the linear regression model. However, the hemispheric trend is clearly evident from the averages of $d'u_y$ obtained for the northern and southern hemispheres, i.e., $(-5.87 \pm 0.72) \times 10^{-4}\,\mathrm{s}^{-1}$ and $(5.86 \pm 0.70) \times 10^{-4}\,\mathrm{s}^{-1}$, respectively.

The relationship of $d'u_y$ with magnetic index (MI) of ARs is shown in Figure 3(b). Although the ARs show a rather large scatter, there still appears to be a correlation between these two parameters. The fitted lines drawn for the ARs in the northern and southern hemispheres are given by $d'u_y = -0.22 - 0.31$ MI and $d'u_y = 0.01 + 0.48$ MI, respectively. These fits reveal that the maximum $d'u_y$ of ARs increased with MI. The larger slope of the fitted line corresponding to the ARs located in the southern hemisphere indicates larger $d'u_y$ for these as compared to the ARs of similar MI located in the northern hemisphere.

We have computed the vertical component of vorticity, ω_z, for all the ARs of our sample, but show the profiles only for two ARs: NOAA 10030 and 10226 (Figure 4, top panel). It is evident that ω_z varies with depth both in sign and magnitude as the flow parameters shown in Figure 1. These profiles also show two extrema of opposite signs at the depths near 2 and 6 Mm corresponding to the scales "G" and "M." This implies that the flows at these depths are twisted in opposite directions. For NOAA 10030, ω_z changed direction around the depths ∼1.8 and ∼12 Mm, while for NOAA 10226 the corresponding depths are ∼2 and ∼8 Mm.

Zero vorticity may be a signature of the flux rope being broken at these depths. It is possible that the connection between the magnetic structures at the surface and its underlying roots may get broken through a dynamical disassociation process (Fan et al. 1994), and surface reconnection of the two opposite polarities (Schrijver & Title 1999). But these mechanisms have been overruled by dynamical disconnection mechanism proposed by Schüssler & Rempel (2005) based upon the buoyant upflow of plasma along the field lines. From the simulation of thin flux tubes, Schüssler & Rempel (2005) found that the disconnection takes place at a depth between 2 and 6 Mm, which correspond with the depths "G" and "M" marked in Figure 4(a). We suggest that once the flux ropes in the interior of an AR are disconnected, its remaining lifetime would depend upon the depth where ω_z vanishes, i.e., $\omega_z = 0$.

We have determined the depth of zero ω_z by a minimization procedure. However, it was not possible to accurately approach toward the point of zero vorticity for some of the ARs of our sample due to the limitation of the available spatial resolution of GONG data. For those ARs which did not show zero ω_z in their interior, we took its absolute minimum to relate with the remaining lifetime. Further, in Figure 4(b), we have plotted the depths of zero vorticity, d_0, with the remaining lifetime, τ. A good linear trend is evident between the parameters d_0 and τ from the fitted line, $\tau = 6.43 + 0.34\, d_0$, drawn through the boxcar-averaged points. The fit is found to be good as 72.65% of the total variance in τ is explained by the linear regression model.

Figure 4(b) shows that ARs having zero vorticity at deeper levels last longer. The Pearson correlation coefficient between the depth and lifetime of ARs is ∼85% for ARs in the northern and southern hemispheres. However, for the five SARs, i.e., NOAA 10030, 10044, 10069, 10486, 10488, the remaining lifetimes are found to be >30 days, i.e., much larger than the rest of ARs of our sample. These SARs did not follow a linear relationship with depth unlike the others. This may be attributed to a continuous process of emergence of new flux tubes in these SARs resulting in enhancing their life. Due to their distinct abnormal behavior, we have excluded these SARs from the fittings.

We have examined the relationship of flare productivity of ARs with the extrema of ω_z. It is found that the depth of first extremum is mildly correlated with the integrated X-ray flux released during the 1664 minutes' period of the data cube obtained for the ARs. The Pearson correlation coefficient calculated between these parameters is 20%. On the other hand, no correlation is found between the second extremum of ω_z and the integrated X-ray flux of the corresponding ARs.

4. CONCLUSIONS

From our study of the 74 ARs observed during 2001 August–2007 January of Cycle 23, we have discovered statistically significant relationship among the sub-surface flow topology, energetics, and the remaining lifetime of ARs. We have found the following important results.

1. Three sheared layers in the depth range 0–10 Mm were found to exist in 44 ARs which revealed the complexity of flow structures beneath the surface of more complex ARs. The two extrema in u_y and $d'u_y$ profiles of these ARs were found to be located at the depths of 1.92 ± 0.15 and 4.69 ± 0.30 Mm.
2. The ARs having two extrema as compared to the ARs having only a single extremum in u_y were found to be more active as they possessed as large as twice the mean magnetic field (MI), mean *GOES* X-ray flux, and mean lifetime.
3. The extrema of meridional velocity gradients were found to follow a hemispheric trend, viz., in the northern hemisphere, 24 (70%) out of 34 ARs had negative gradients while in the southern hemisphere, 29 (74%) out of 39 ARs had positive gradients.
4. ARs of larger MI possessed steeper gradient in meridional velocity profiles.
5. Flaring activity of an AR is found to be associated with the depth of the first extremum of vertical vorticity.
6. ARs having zero vertical vorticity at deeper layers are expected to last longer.

In summary, we have discovered a new hemispheric trend involving the meridional velocity gradient of sub-surface flows. More importantly, lifetime of ARs appears to be correlated with the depth of the deepest zero vertical vorticity. This inference may be useful in predicting the expected lifetime of ARs.

This work utilizes data obtained by the Global Oscillation Network Group (GONG) program and the Solar Oscillations Investigation/Michelson Doppler Imager (SOI/MDI) on the *Solar and Heliospheric Observatory* (*SOHO*). Solar Monitor Data were used to find the correct location of the ARs. We thank the referees for their comments and important suggestions that helped to improve the Letter.

REFERENCES

Ambastha, A., Basu, S., Antia, H. M., & Bogart, R. S. 2004, in Helio- and Asteroseismology: Towards a Golden Future, ed. D. Danesy (ESA SP-559; Noordwijk: ESA), 293
Basu, S., & Antia, H. M. 2003, ApJ, 585, 553
Basu, S., Antia, H. M., & Bogart, R. S. 2004, ApJ, 610, 1157
Beck, J. G., & Giles, P. 2005, ApJ, 621, L153
Braun, D. C., Birch, A. C., & Lindsey, C. 2004, in Helio- and Asteroseismology: Towards a Golden Future, ed. D. Danesy (ESA SP-559; Noordwijk: ESA), 337
Cattaneo, F., Lenz, D., & Weiss, N. 2001, ApJ, 563, L91
Corbard, T., Toner, C., Hill, F., Hanna, K. D., Haber, D. A., Hindman, B. W., & Bogart, R. S. 2003, in GONG+ 2002. Local and Global Helioseismology: the Present and Future, ed. H. Sawaya-Lacoste (ESA SP-517; Noordwijk: ESA), 255
Couvidat, S., Birch, A. C., & Kosovichev, A. G. 2006, ApJ, 640, 516
Deubner, F.-L., & Gough, D. 1984, ARA&A, 22, 593

Duvall, T. L., Jr. 1979, Sol. Phys., 63, 3
Fan, Y., Fisher, G. H., & McClymont, A. N. 1994, ApJ, 436, 907
Golub, L., & Vaiana, G. S. 1978, ApJ, 219, L55
Gough, D. 1985, Sol. Phys., 100, 65
Gough, D., & Toomre, J. 1991, ARA&A, 29, 627
Haber, D. A., Hindman, B. W., Toomre, J., Bogart, R. S., Larsen, R. M., & Hill, F. 2002, ApJ, 570, 855
Hill, F. 1988, ApJ, 333, 996
Hill, F., et al. 2003, in GONG+ 2002. Local and Global Helioseismology: the Present and Future, ed. H. Sawaya-Lacoste (ESA SP-517; Noordwijk: ESA), 295
Hindman, B. W., Haber, D. A., & Toomre, J. 2009, ApJ, 698, 1749
Howard, R. F. 1996, ARA&A, 34, 75
Howe, R., Christensen-Dalsgaard, J., Hill, F., Komm, R., Schou, J., & Thompson, M. J. 2005, ApJ, 634, 1405
Jouve, L., & Brun, A. S. 2009, ApJ, 701, 1300
Komm, R., Corbard, T., Durney, B. R., González Hernández, I., Hill, F., Howe, R., & Toner, C. 2004, ApJ, 605, 554
Komm, R. W., Howard, R. F., & Harvey, J. W. 1993, Sol. Phys., 143, 19
Komm, R., Howe, R., & Hill, F. 2009, Sol. Phys., 258, 13
Komm, R., Howe, R., Hill, F., González-Hernández, I., Toner, C., & Corbard, T. 2005, ApJ, 631, 636
Komm, R., Howe, R., Hill, F., Miesch, M., Haber, D., & Hindman, B. 2007, ApJ, 667, 571
Kosovichev, A. G., Duvall, T. L. J., & Scherrer, P. H. 2000, Sol. Phys., 192, 159
Labonte, B. J., & Howard, R. 1982, Sol. Phys., 80, 361
Leibacher, J. W., & Stein, R. F. 1971, ApJ, 7, 191
Mason, D., Komm, R., Hill, F., Howe, R., Haber, D., & Hindman, B. W. 2006, ApJ, 645, 1543
Maurya, R. A., & Ambastha, A. 2010, in Astrophys. Space Sci. Proc., Magnetic Coupling between the Interior and the Atmosphere of the Sun, ed. S. S. Hasan & R. J. Rutten (Berlin: Springer), 516
Maurya, R. A., Ambastha, A., & Tripathy, S. C. 2009, ApJ, 706, L235
Nordlund, Å., Stein, R. F., & Asplund, M. 2009, Living Rev. Sol. Phys., 6, 2
November, L. J., Toomre, J., Gebbie, K. B., & Simon, G. W. 1981, ApJ, 245, L123
Pevtsov, A. A., Canfield, R. C., & Latushko, S. M. 2001, ApJ, 549, L261
Rast, M. P. 2003, ApJ, 597, 1200
Rieutord, M., Roudier, T., Malherbe, J. M., & Rincon, F. 2000, A&A, 357, 1063
Schrijver, C. J., & Title, A. M. 1999, Sol. Phys., 188, 331
Schüssler, M., & Rempel, M. 2005, A&A, 441, 337
Simon, G. W., & Leighton, R. B. 1964, ApJ, 140, 1120
Švanda, M., Klvaňa, M., & Sobotka, M. 2009a, A&A, 506, 875
Švanda, M., Klvaňa, M., Sobotka, M., & Bumba, V. 2008, A&A, 477, 285
Švanda, M., Klvaňa, M., Sobotka, M., Kosovichev, A. G., & Duvall, T. L. 2009b, New Astron., 14, 429
Ulrich, R. K. 1970, ApJ, 162, 993
Ulrich, R. K., Boyden, J. E., Webster, L., Padilla, S. P., & Snodgrass, H. B. 1988, Sol. Phys., 117, 291
Vorontsov, S. V., Christensen-Dalsgaard, J., Schou, J., Strakhov, V. N., & Thompson, M. J. 2002, Science, 296, 101
Zaatri, A., Komm, R., González Hernández, I., Howe, R., & Corbard, T. 2006, Sol. Phys., 236, 227
Zhao, J., & Kosovichev, A. G. 2004, ApJ, 603, 776